UNIVERSITÀ DEGLI STUDI DI CAMERINO

School of Advanced Studies

DOCTORAL COURSE IN

Science and Technology – Theoretical and Experimental Physics

XXXII cycle

STRONG CORRELATIONS IN THE NORMAL PHASE OF AN ATTRACTIVE FERMI GAS

PhD Student

Michele Pini

Supervisors

Prof. Pierbiagio Pieri

Prof. Giancarlo Calvanese Strinati

Abstract

The purpose of this thesis is the study of an attractive Fermi gas in the normal phase throughout the BCS-BEC crossover by means of diagrammatic approaches based on the t-matrix approximation. More specifically, the calculation is implemented by including different degrees of self-consistency in the t-matrix equations, from the non-self-consistent to the fully self-consistent (or Luttinger-Ward) approach.

In the first part of the thesis, we perform a systematic and unbiased comparative study of all the five variants of the t-matrix approach with different degrees of self-consistency considered thus far in the literature. The analysis is performed by calculating several thermodynamic and dynamical quantities of the spin-balanced Fermi gas in the normal phase within all the approaches. We also compare these results with the available quantum Monte Carlo (QMC), diagrammatic Monte Carlo (DMC) and experimental data. In the comparison, the fully self-consistent t-matrix approach turns up to be the best to describe thermodynamic quantities, however for dynamical quantities partially or non-self-consistent approaches appear to work better.

In the second part of the thesis, we investigate pairing correlations in the normal phase of the spin-balanced system within the fully self-consistent t-matrix approach. We first calculate the pair correlation function $g_{\uparrow\downarrow}(\boldsymbol{\rho})$ and the pair coherence length ξ_{pair} for various couplings and temperatures. We then develop a new approach, based on the two-body Green's function formalism, to calculate the number of preformed pairs in the normal phase. The approach is used to describe the experimental data on this quantity by the group of Prof. Denschlag in Ulm. In order to compare our calculation with the experiment, the fully self-consistent t-matrix approach is extended to consider a Fermi gas in a harmonic trapping potential. In general, very good agreement is found with experimental data.

In the final part of the thesis, we present some preliminary results for the spin-imbalanced Fermi gas, focusing on the temperature-coupling-polarization phase diagram and on $T = 0$ and finite T thermodynamic quantities. In this analysis, we show that the Luttinger theorem for an imbalanced Fermi gas at $T = 0$ is satisfied within the fully self-consistent t-matrix approach, and we present the extension of the calculation of the pair correlation function $g_{\uparrow\downarrow}(\boldsymbol{\rho})$ to the spin-imbalanced case.

Contents

Chapter 1

Introduction

The microscopic explanation of the phenomenon of superconductivity (discovered in 1911 by Kamerlingh Onnes [1]) came in 1957, when Bardeen, Cooper and Schrieffer (BCS) developed their theory of superconductivity [2]. In the BCS theory, the superconducting system is described in terms of a coherent state of Cooper pairs, i.e. pairs of electrons with opposite spin and zero total momentum, generated by phonon-mediated attractive interactions between the electrons. These pairs are of size of the order of 10^3 times the inter-particle distance for typical superconductors. For this reason, the superconducting transition in metals does not correspond to a Bose-Einstein condensation (BEC) of non-overlapping composite bosons, as initially theorized by Schafroth, Butler and Blatt [3].

For some time, BCS superconductivity and Bose-Einstein condensation of bosonic pairs have been considered as disjoint theories to be applied to different physical systems. However, it turns out that Cooper pairs and composite bosons are in fact two faces of the same coin, and can be considered as two limiting (BCS and BEC) situations of the same theory. In the crossover between the BCS and BEC regimes, the Fermi system smoothly goes through an intermediate region where the dimension of the pairs is of the same order of the inter-particle spacing. This aspect was first underlined in 1969 in the work by Eagles [4] in the context of superconducting semiconductors and the connection of the two theories was then derived by Leggett in 1980 [5] for an attractive Fermi gas at $T = 0$.

In these works, it is shown that the BCS-BEC crossover is driven by the form of the interaction potential $V(\boldsymbol{r})$ between the fermions as well as by their number density n. In particular, for short-range potentials and at low temperatures, the crossover is described in terms of a single parameter: the dimensionless *coupling* $(k_F a)^{-1}$, where a is the scattering length associated to the interaction potential $V(\boldsymbol{r})$ and $k_F = (3\pi^2 n)^{1/3}$ is the Fermi wave vector. If the potential $V(\boldsymbol{r})$ is varied across the critical strength for the formation of a two-particle bound state, the coupling $(k_F a)^{-1}$ increases smoothly from negative to positive values as the strength of the potential increases from just below the critical value for binding to just above it (that is, a is negative for no binding, tends to ∞ at the onset of the bound state, and is positive when the bound state exists).

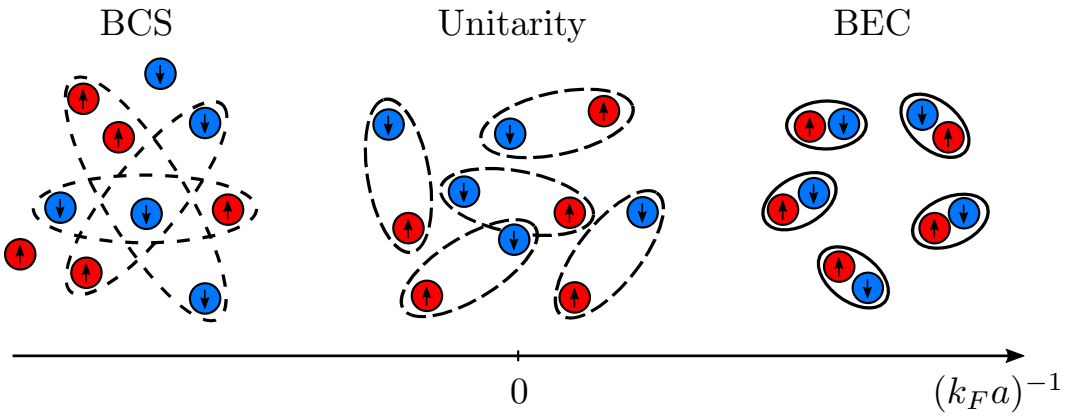

Figure 1.1: Two-component Fermi gas in the broken-symmetry phase across the BCS-BEC crossover.

In Figure 1.1, a graphical representation of a Fermi gas in the broken-symmetry phase along the BCS-BEC crossover is given as a function of the coupling $(k_F a)^{-1}$. For large and negative couplings ($(k_F a)^{-1} \ll -1$), corresponding to the weak-coupling (or BCS) regime, the Fermi system at sufficiently low temperature is well described as a gas of weakly bound overlapping Cooper pairs; instead, for large and positive couplings ($(k_F a)^{-1} \gg 1$), corresponding to the strong-coupling (or BEC) regime, the system is well described as a gas of strongly bound non-overlapping composite bosons. The intermediate region $(k_F a)^{-1} = 0$, where pairs have a dimension that is comparable to the average inter-particle spacing, is usually called "unitary regime" or "unitarity".

At first, the theory of the BCS-BEC crossover found some applications in the description of high-temperature (cuprate) superconductors [6–11] and in nuclear physics [12]. It was however in 2003 that the interest in this field really exploded, when the BCS-BEC crossover was experimentally observed in ultracold Fermi gases of ^{40}K at JILA [13] and ^{6}Li at Innsbruck [14, 15] and MIT [16]. Note that, for ultracold Fermi gases, the fermions involved in pairing are neutral atoms (and not charged particles, as electrons in superconductors), so in this case the ordered phase is *superfluid*, rather then superconducting. The presence of this superfluid phase was confirmed by the observation of the momentum distribution of pairs [17], an excitation gap [18] and the formation of vortices [19]. Quite unexpectedly, it turned out that the unitary regime is experimentally stable due to Pauli suppression of three-body recombination processes, so all the regions of the BCS-BEC crossover are actually accessible in ultracold Fermi gases experiments (for a general experimental overview on the BCS-BEC crossover in ultracold Fermi gases, see Ref. [20]).

In fact, ultracold Fermi gases offer an incredible benchmark for the experimental realization of the BCS-BEC crossover, because they are easily accessible and the strength of the interaction between the fermions is controllable by means of an external uniform

magnetic field through a Fano-Feshbach resonance, i.e. a condition where the zero-energy scattering state of the two hyperfine species (which together define the "open" channel) is degenerate with the most weakly bound molecular state of a second pair of hyperfine species (the "closed" channel) [21]. In particular, we will be interested in "broad" Fano-Feshbach resonances, where the atoms remain mainly within the open channel and the effects of the closed channel can be simply reabsorbed in a single-channel model with magnetic-field-dependent potential $V(\boldsymbol{r})$ [22].

Alongside the first experimental observations in ultracold Fermi gases, the study of the BCS-BEC crossover has strongly developed also on the theory side. Many theoretical methods, like many-body diagrammatic techniques [23–77], quantum Monte Carlo (QMC) [78–89], diagrammatic Monte Carlo (DMC) [90–94], functional-renormalization-group [95, 96], epsilon [97] and virial expansions [98–100], have been extensively used to describe the crossover, with particular emphasis on the unitary region where no analytic or perturbative solutions exist (for a general overview of the theoretical approaches to the BCS-BEC crossover, see Refs. [101, 102]).

In this thesis, we will mainly focus on diagrammatic techniques based on the t-matrix approximation. In the context of a (dilute) Fermi gas with an attractive inter-particle interaction, this theoretical approach appears as a natural candidate to describe the system while it evolves throughout the BCS-BEC crossover. In fact, in the BCS limit it correctly recovers Galitskii's leading correction to the thermodynamic quantities due to the weakly attractive interaction [103], while in the BEC limit it recovers the description in terms of non-interacting composite bosons. Moreover, it smoothly interpolates between the two (BCS and BEC) limits and, at high temperatures, it recovers the virial expansion up to the second order in all regions of the crossover [43, 100].

The first pioneering approach in this respect goes back to the work by Nozières and Schmitt-Rink (NSR) [23], where a simplified version of the non-self-consistent t-matrix approximation proved sufficient to highlight the main features of the crossover physics in the normal phase above the superfluid critical temperature. Later on, the NSR approach was extended, either to improve on the treatment of the non-self-consistent t-matrix approximation [24, 31, 70, 71], or to include various degrees of self-consistency within this approximation, ranging from partial [28, 60, 65] to full [26, 27] self-consistency.

As expected, depending on the degree of self-consistency different numerical results were obtained for thermodynamic and dynamical physical quantities. However, direct comparison among the results obtained with various degrees of self-consistency has been hindered by the (sometimes even drastic) numerical approximations that were introduced in the calculations on top of a specific choice about the degree of self-consistency [29]. For these reasons, it appears that a systematic comparison of the results obtained by adopting various degrees of self-consistency on the t-matrix approximation is still lacking, especially when this comparison would be made in an unbiased way by retaining the same level of numerical accuracy for all different approaches.

The aim of the first part of this thesis is to fill this gap, by undertaking the above systematic study on all the five degrees of self-consistency that have been considered thus far in the literature within the t-matrix approximation in the normal phase above

the superfluid critical temperature [26–28, 31, 60, 65]. Although the present study may not lead to definite conclusions about which one of the above five approximations could account best for the properties of a (dilute) Fermi gas in the BCS-BEC crossover, it appears that for thermodynamic properties the self-consistent t-matrix approach is the one that better agrees with the available QMC, DMC and experimental data (at least at unitarity), while for dynamical properties non-self-consistent or partially self-consistent approaches seem to provide physically more sensible results with respect to the fully self-consistent one.

In addition, the high precision of the numerical calculations that we have implemented has enabled us to accurately check how the two distinct (BCS and BEC) limits of the crossover are recovered by the alternative t-matrix approaches. Specifically, in the BEC limit the residual interaction among composite bosons extracted from our numerical calculations turns out to be in excellent agreement with the analytic estimates that we also provide (which correct a previous analytic estimate obtained in Ref. [26] within the fully self-consistent t-matrix approach). In the BCS limit, on the other hand, we have found that a partially self-consistent t-matrix approach, developed in Ref. [28] and often utilized in the literature, breaks down when one avoids using the set of approximations that normally accompanies its implementation.

In the second part of the thesis, instead, we focus on the phenomenon of pairing in the normal phase of the spin-balanced attractive Fermi gas. In fact, as it was already pointed out by Eagles in Ref. [4], on the BEC side of the crossover there is a wide temperature range where pairing occurs above the critical temperature.

Within the formalism of the fully self-consistent t-matrix approach, we first investigate the pair correlation function $g_{\uparrow\downarrow}(\boldsymbol{\rho})$, which describes the correlations of fermions with opposite spin at a distance $\boldsymbol{\rho}$, and the pair coherence length $\xi_{\rm pair}$, which represent the typical length of the pair correlations.[1] We then develop a theoretical approach, based on the formalism of two-body Green's functions, to describe a recent experimental measurement of the number of preformed pairs in a spin-balanced gas of ^{6}Li in the normal phase by the group of Prof J. H. Denschlag in Ulm, Germany [105]. In order to extend this theoretical approach to the whole BCS-BEC crossover, the preformed pairs are not simply interpreted in terms of independent bosonic molecules (as this interpretation is valid only in the BEC limit), but rather in terms of correlations established between fermions of opposite spins, which are embodied in the pair correlation function $g_{\uparrow\downarrow}(\boldsymbol{\rho})$.

Moreover, in order to directly compare with the experimental data, the fully self-consistent t-matrix approach is extended to the case of a harmonic trapping potential by means of a local density approximation. Within this approach, we also calculate the critical temperature in the trap (which was previously available in the literature only at unitarity [50]) for the whole BCS-BEC crossover.

Finally, we present some preliminary results for the spin-imbalanced Fermi gas, focusing on its temperature-coupling-polarization phase diagram and on its $T = 0$ and finite T thermodynamic properties in the normal phase. In particular, we show that the

[1] In the past, these quantities where already used to describe pair correlations in the broken-symmetry phase within various theoretical approaches [10, 66, 104].

Luttinger theorem [106] for an imbalanced Fermi gas at $T = 0$ is satisfied within the fully self-consistent t-matrix approach, consistently with what was analytically proved in Ref. [107]. We also present an extension of the calculation of the pair correlation function $g_{\uparrow\downarrow}(\boldsymbol{\rho})$ to the spin-imbalanced case.

The thesis is organized as follows. In Chapter 2 we review the many-body diagrammatic formalism and introduce the t-matrix approach for the attractive Fermi gas throughout the BCS-BEC crossover. In Chapter 3 we present and compare the results for both thermodynamic and dynamical quantities for a spin-balanced homogeneous Fermi gas in the normal phase calculated within various t-matrix approaches with different degrees of self-consistency. In Chapter 4 we show how the calculation can be extended to a system within a harmonic trapping potential and we present some results for thermodynamic quantities in the trapped system. In Chapter 5 the pair correlations in the normal phase of a spin-balanced Fermi gas are studied in terms of the pair correlation function $g_{\uparrow\downarrow}(\boldsymbol{\rho})$ and the pair coherence length ξ_{pair}. In Chapter 6, a theory for the fraction of preformed pairs in the normal phase, in order to describe the experimental data of Ref. [105], is developed. Finally, in Chapter 7 some preliminary results for thermodynamic properties of a Fermi gas with imbalanced spin populations are reported.

Chapter 2

Many-body approach to the BCS-BEC crossover

In this chapter, we give a general introduction of the theoretical approach used in this thesis. We start by introducing the finite temperature Green's functions diagrammatic formalism. We then focus on the attractive Fermi gas, starting with the theory of two-body scattering and then presenting the t-matrix approximation for the many-body system, first in its non-self-consistent form and then with the inclusion of various degrees of self-consistency. Finally, we include some considerations on conserving approximations and Tan's contact, and we introduce the formalism of two-particle Green's functions needed for the calculation of the physical quantities of Chapters 5 and 6.

2.1 Finite temperature Green's functions formalism

To describe the whole BCS-BEC crossover at finite temperature within a single theory, it is necessary to consider an approach that goes beyond the BCS mean-field approach and includes pair fluctuations. This can be done within the formalism of finite temperature Green's functions. In this formalism, two different kinds of Green's functions are defined: the *temperature* Green's function G, which describes the equilibrium thermodynamic properties, and the *real-time* Green's function $\bar{G}$, which instead describes the excitation properties of the system. In the following sections, we will introduce the formalism for both of them and show how they are connected.[1] For simplicity, we will assume $\hbar = 1$.

2.1.1 Temperature Green's function

Let us consider a system of N particles described by the Hamiltonian $\hat{H}$ at thermal equilibrium at the temperature T. As we work at finite temperature, it is useful to describe the system in the grand canonical ensemble and introduce the grand canonical Hamiltonian

$$\hat{K} = \hat{H} - \mu\hat{N}, \tag{2.1}$$

[1] For a more detailed introduction, see Ref. [108].

where μ is the chemical potential and $\hat{N}$ is the number operator. We can then introduce the following modified $\hat{K}$-Heisenberg picture for the field operators $\hat{\psi}_\alpha$

$$\begin{aligned}\hat{\psi}_{K\alpha}(\boldsymbol{x}\tau) &= e^{\hat{K}\tau}\hat{\psi}_\alpha(\boldsymbol{x})e^{-\hat{K}\tau},\\ \hat{\psi}^\dagger_{K\alpha}(\boldsymbol{x}\tau) &= e^{\hat{K}\tau}\hat{\psi}^\dagger_\alpha(\boldsymbol{x})e^{-\hat{K}\tau},\end{aligned} \tag{2.2}$$

where τ is the imaginary time and α is the spin index. The *single-particle temperature Green's function* (also called single-particle propagator) is defined in terms of these field operators as [108]

$$G_{\alpha\beta}(\boldsymbol{x}_1\tau_1, \boldsymbol{x}_2\tau_2) = -\left\langle T_\tau[\hat{\psi}_{K\alpha}(\boldsymbol{x}_1\tau_1)\hat{\psi}^\dagger_{K\beta}(\boldsymbol{x}_2\tau_2)]\right\rangle, \tag{2.3}$$

where T_τ is the time-ordering operator, which brings the field operators with the smaller τ on the right (including a factor $(-1)^P$ where P is the number of permutations of fermion operators), and the symbol $\langle\cdots\rangle$ represents the thermal average of an operator

$$\langle\hat{\mathcal{O}}\rangle = \mathrm{Tr}[\hat{\rho}_G\hat{\mathcal{O}}] = \sum_n \langle\psi_n|\hat{\rho}_G\hat{\mathcal{O}}|\psi_n\rangle\,. \tag{2.4}$$

Here, the symbol of trace represents the sum of the expectation values over the states $|\varphi_n\rangle$ of a complete basis set for the Hilbert space of the system. The operator $\hat{\rho}_G$ is the grand canonical statistical weight operator and is defined as

$$\hat{\rho}_G = \frac{1}{\mathcal{Z}}\, e^{-\beta\hat{K}} \tag{2.5}$$

where $\beta = 1/(k_B T)$ and $\mathcal{Z}$ is the grand canonical partition function

$$\mathcal{Z} = \mathrm{Tr}[e^{-\beta\hat{K}}] = \sum_n \langle\varphi_n|e^{-\beta\hat{K}}|\varphi_n\rangle\,. \tag{2.6}$$

If the Hamiltonian $\hat{H}$ is time-independent and the system is homogeneous, the temperature Green's function (2.3) is a function of only $\boldsymbol{x} = \boldsymbol{x}_1 - \boldsymbol{x}_2$ and $\tau = \tau_1 - \tau_2$. We can then introduce its Fourier transform to momentum space

$$G_{\alpha\beta}(\boldsymbol{k}, \tau) = \int d\boldsymbol{x}\, e^{-i\boldsymbol{x}\cdot\boldsymbol{k}}\, G_{\alpha\beta}(\boldsymbol{x}, \tau) \tag{2.7}$$

and the corresponding anti-Fourier transform

$$G_{\alpha\beta}(\boldsymbol{x}, \tau) = \int \frac{d\boldsymbol{k}}{(2\pi)^3}\, e^{i\boldsymbol{x}\cdot\boldsymbol{k}}\, G_{\alpha\beta}(\boldsymbol{k}, \tau). \tag{2.8}$$

Moreover, for fermions (bosons), the temperature Green's function is antiperiodic (periodic) in the τ variable with period β

$$G_{\alpha\beta}(\boldsymbol{k}, \tau + \beta) = \pm G_{\alpha\beta}(\boldsymbol{k}, \tau) \tag{2.9}$$

where the upper (lower) sign refers to bosons (fermions). The imaginary time τ can then be taken only in the interval $(0, \beta)$ without loss of generality. Using these periodicity properties, the bosonic and fermionic Green's functions can be expanded in Fourier series as

$$G_{\alpha\beta}(\boldsymbol{k}, \tau) = \frac{1}{\beta} \sum_n e^{-i\omega_n \tau} G_{\alpha\beta}(\boldsymbol{k}, \Omega_\nu), \tag{2.10}$$

where ω_n are the Matsubara frequencies defined as

$$\begin{aligned} \omega_n &= \frac{(2n+1)\pi}{\beta} \quad \text{for fermions} \\ \omega_n &= \frac{2n\,\pi}{\beta} \quad \text{for bosons} \end{aligned} \tag{2.11}$$

with n integer. The Fourier coefficients in the series (2.10) are given by

$$G_{\alpha\beta}(\boldsymbol{k}, \omega_n) = \int_0^\beta d\tau\, e^{i\omega_n \tau} G_{\alpha\beta}(\boldsymbol{k}, \tau). \tag{2.12}$$

2.1.2 Relation to observables

The single-particle temperature Green's function (2.3) includes informations about the thermal average of all the single-particle observables of the system. To see this, let us consider a single-particle operator, that can in general be written in the form

$$\hat{J} = \int d\boldsymbol{x}\, \hat{\mathcal{J}}(\boldsymbol{x}) = \int d\boldsymbol{x} \sum_{\alpha,\beta} \hat{\psi}^\dagger_\beta(\boldsymbol{x}) J_{\beta\alpha}(\boldsymbol{x}) \hat{\psi}_\alpha(\boldsymbol{x}), \tag{2.13}$$

where $\hat{\mathcal{J}}(\boldsymbol{x})$ is the second-quantized density of the first-quantized operator $J_{\beta\alpha}(\boldsymbol{x})$. Its thermal average can then be written as

$$\begin{aligned} \langle \hat{J} \rangle &= \sum_{\alpha\beta} \int d\boldsymbol{x}\, J_{\beta\alpha}(\boldsymbol{x}) \,\mathrm{Tr}[\hat{\rho}_G\, \hat{\psi}^\dagger_\beta(\boldsymbol{x}) \hat{\psi}_\alpha(\boldsymbol{x})] \\ &= \mathcal{Z}^{-1} \sum_{\alpha\beta} \int d\boldsymbol{x}\, J_{\beta\alpha}(\boldsymbol{x}) \,\mathrm{Tr}[e^{-\beta\hat{K}} e^{-\hat{K}\tau} \hat{\psi}^\dagger_{K\beta}(\boldsymbol{x}, \tau) \hat{\psi}_{K\alpha}(\boldsymbol{x}, \tau) e^{\hat{K}\tau}] \\ &= \mathcal{Z}^{-1} \sum_{\alpha\beta} \int d\boldsymbol{x}\, J_{\beta\alpha}(\boldsymbol{x}) \,\mathrm{Tr}[e^{-\beta\hat{K}} \hat{\psi}^\dagger_{K\beta}(\boldsymbol{x}, \tau) \hat{\psi}_{K\alpha}(\boldsymbol{x}, \tau)] \\ &= \mp \int d\boldsymbol{x} \lim_{\boldsymbol{x}' \to \boldsymbol{x}} \lim_{\tau' \to \tau^+} \sum_{\alpha\beta} J_{\beta\alpha}(\boldsymbol{x}) G_{\alpha\beta}(\boldsymbol{x}, \tau, \boldsymbol{x}', \tau'), \end{aligned} \tag{2.14}$$

where $\tau^+ = \tau + \eta$ with $\eta \to 0^+$. In the derivation, the cyclic property of the trace has been used, together with the definitions of field operators in the $\hat{K}$-Heisenberg picture (2.2), of the temperature Green's function (2.3) and of thermal average (2.4). This means that the thermal average of any single-particle operator $\hat{J}$ can be obtained by operating

with its first-quantized version $J_{\beta\alpha}(\boldsymbol{x})$ on the Green's function and then summing over the spin indices and integrating on $\boldsymbol{x}$. As an example, let us consider the number operator

$$\hat{N} = \int d\boldsymbol{x} \sum_{\alpha} \hat{\psi}^{\dagger}_{\alpha}(\boldsymbol{x})\hat{\psi}_{\alpha}(\boldsymbol{x}), \tag{2.15}$$

where the first quantized operator is simply the identity matrix $J_{\beta\alpha} = \delta_{\beta\alpha}$. The thermal average of the number of particles is then given by:

$$N = \langle \hat{N} \rangle = \mp \int d\boldsymbol{x} \lim_{\tau' \to \tau^+} \sum_{\alpha} G_{\alpha\alpha}(\boldsymbol{x}, \tau, \boldsymbol{x}, \tau'). \tag{2.16}$$

For a homogeneous system in a volume V, it is useful to use the Fourier transformations (2.7) and (2.12) and write the previous number equation in transformed space

$$n = \mp \int \frac{d\boldsymbol{k}}{(2\pi)^3} \frac{1}{\beta} \sum_{n} e^{i\omega_n \eta} \sum_{\alpha} G_{\alpha\alpha}(\boldsymbol{k}, \omega_n), \tag{2.17}$$

where $n = N/V$ is the density of the system and the parameter $\eta \to 0^+$ comes from the imaginary-time ordering. In the simple case of a non-interacting system, the Green's function in transformed space is

$$G_0(\boldsymbol{k}, \omega_n) = \frac{1}{i\omega_n - \xi_{\boldsymbol{k}}}, \tag{2.18}$$

where $\xi_{\boldsymbol{k}} = \boldsymbol{k}^2/(2m) - \mu$, with m the mass of the particles. In this case, the sum over the Matsubara frequencies can be carried out analytically [108] and the density equation (2.17) simply reduces to the the integral on $\boldsymbol{k}$ of the Bose/Fermi distribution

$$n = (2s+1) \int \frac{d\boldsymbol{k}}{(2\pi)^3} \frac{1}{e^{\beta\xi_{\boldsymbol{k}}} \mp 1}, \tag{2.19}$$

where s is the spin of the particles.

2.1.3 Perturbation theory

One of the main reasons to use Green's functions is that perturbation theory is easier to perform in this formalism. Without going into the details of the derivation (see Ref. [108]), we state here the practical rules for perturbation theory. For simplicity, we consider the case of fermions in an homogeneous system and we work in the momentum-frequency space. We also limit ourself to the most common situation of a self-coupled field with two-body interactions, where the Hamiltonian $\hat{H}$ can be written as the sum of a one-body term $\hat{H}_0$ and a two-body term $\hat{H}_1$, so that the grand canonical Hamiltonian is

$$\hat{K} = \hat{H}_0 + \hat{H}_1 - \mu\hat{N} \tag{2.20}$$

with

$$\hat{H}_0 = \sum_\alpha \int d\boldsymbol{x}_1 \, \hat{\psi}^\dagger_\alpha(\boldsymbol{x}_1) \Big[-\frac{\nabla^2_{\boldsymbol{x}_1}}{2m} \Big] \hat{\psi}_\alpha(\boldsymbol{x}_1), \tag{2.21}$$

$$\hat{H}_1 = \frac{1}{2} \sum_{\alpha,\beta} \int d\boldsymbol{x}_1 d\boldsymbol{x}_2 \, \hat{\psi}^\dagger_\alpha(\boldsymbol{x}_1) \hat{\psi}^\dagger_\beta(\boldsymbol{x}_2) V(\boldsymbol{x}_1 - \boldsymbol{x}_2) \hat{\psi}_\beta(\boldsymbol{x}_2) \hat{\psi}_\alpha(\boldsymbol{x}_1). \tag{2.22}$$

For simplicity, we have considered a spin-independent potential $V(\boldsymbol{x})$. As the system is homogeneous, we are going to work in terms of its Fourier transform

$$V(\boldsymbol{k}) = \int \frac{d\boldsymbol{k}}{(2\pi)^3} \, e^{i\boldsymbol{x}\cdot\boldsymbol{k}} \, V(\boldsymbol{x}). \tag{2.23}$$

First of all, it is useful express the Green's function $G_{\alpha\beta}(\boldsymbol{k}, \omega_n)$ in terms of another quantity, the *self-energy* $\Sigma_{\alpha\beta}(\boldsymbol{k}, \omega_n)$, through the *Dyson equation*

$$G_{\alpha\beta}(\boldsymbol{k}, \omega_n) = [G^0_{\alpha\beta}(\boldsymbol{k}, \omega_n)^{-1} - \Sigma(\boldsymbol{k}, \omega_n)]^{-1}, \tag{2.24}$$

or, equivalently,

$$G_{\alpha\beta}(\boldsymbol{k}, \omega_n) = G^0_{\alpha\beta}(\boldsymbol{k}, \omega_n) + G^0_{\alpha\beta}(\boldsymbol{k}, \omega_n) \Sigma_{\alpha\beta}(\boldsymbol{k}, \omega_n) G_{\alpha\beta}(\boldsymbol{k}, \omega_n). \tag{2.25}$$

In this expressions, $G^0_{\alpha\beta}$ is the Green's function for the non-interacting system

$$G^0_{\alpha\beta}(\boldsymbol{k}, \omega_n) = \frac{\delta_{\alpha\beta}}{i\omega_n - \xi_{\boldsymbol{k}}}, \tag{2.26}$$

where $\xi_{\boldsymbol{k}} = \boldsymbol{k}^2/(2m) - \mu$. The Dyson equation (2.24) is a powerful tool because it allows to perform perturbation theory directly on the self-energy $\Sigma_{\alpha\beta}$ and to automatically consider all the diagrams that are formed by repetitions of the self-energy connected by a single particle line $G^0_{\alpha\beta}$. We are now ready to enunciate the *Feynman rules* for the n-th order contribution to the self-energy $\Sigma_{\alpha\beta}(\boldsymbol{k}, \omega_n)$:

1. Draw all the topologically distinct connected Feynman diagrams with n interaction lines and $2n-1$ directed particle lines that cannot be separated into two independent parts by cutting one particle line.

2. Assign an arbitrary direction to each interaction line. Assign a wave vector and a frequency with each line and conserve each quantity at every vertex.

3. Associate a factor $G^0_{\alpha\beta}(\boldsymbol{k}, \omega_n)$ (as defined in 2.26) with each particle line.

4. Associate a factor $V(\boldsymbol{k})$ (as defined in 2.23) with each interaction line.

5. Integrate all n independent internal wave vectors and sum over all n independent internal frequencies.

6. The spin-indices form a matrix product along any continuous particle line. Evaluate all matrix sums.

7. Multiply everything by a factor $[-\beta(2\pi)^3]^{-n}(-1)^F$, where F is the number of closed fermionic loops.

8. Whenever a particle line either closes on itself or is joined by the same interaction line, insert a convergence factor $e^{i\omega_n\eta}$, with $\eta \to 0^+$.

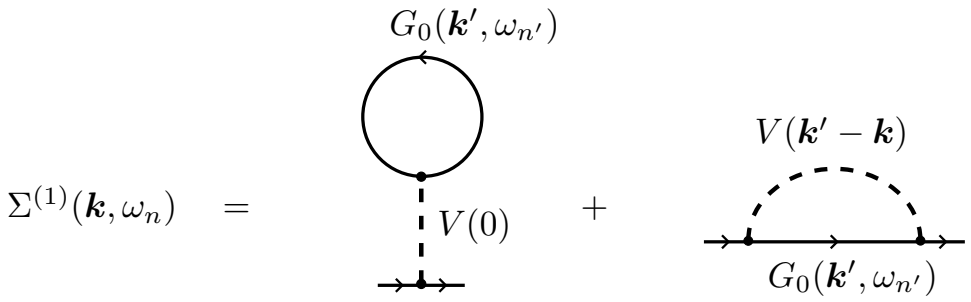

Figure 2.1: First order diagrammatic contribution to the self-energy: Hartree-Fock diagrams.

For example, once we summed over all the spin indices, the first order contribution to the self-energy, represented in Figure 2.1, is given by the Hartree and Fock contributions

$$\begin{aligned}\Sigma^{(1)}(\boldsymbol{k},\omega_n) \equiv \Sigma^{(1)}(\boldsymbol{k}) = \\ -\frac{1}{\beta}\sum_{n'} e^{i\omega_{n'}\eta}\int\frac{d\boldsymbol{k}'}{(2\pi)^3}[-(2s+1)V(0)+V(\boldsymbol{k}'-\boldsymbol{k})]G_0(\boldsymbol{k}',\omega_{n'}),\end{aligned} \tag{2.27}$$

where we have assumed that we can write

$$\begin{aligned}G^0_{\alpha\beta}(\boldsymbol{k},\omega_n) &= \delta_{\alpha\beta}\, G_0(\boldsymbol{k},\omega_n) \\ \Sigma_{\alpha\beta}(\boldsymbol{k},\omega_n) &= \delta_{\alpha\beta}\,\Sigma(\boldsymbol{k},\omega_n)\end{aligned} \tag{2.28}$$

because of the spin-independent interaction, and the factor $(2s+1)$ in the Hartree term comes from the sum over the spin indices $\sum_\alpha \delta_{\alpha\alpha} = 2s+1$.

2.1.4 Real-time Green's function and linear response

The previous formalism can be used to calculate thermodynamic properties of our system at finite temperature, however it does not give any information on dynamical properties.

To complete the description, we need to introduce the *real-time single-particle Green's function*:

$$\bar{G}_{\alpha\beta}(\boldsymbol{x}_1 t_1, \boldsymbol{x}_2 t_2) = -i \langle T_t[\hat{\psi}_{K\alpha}(\boldsymbol{x}_1 t_1)\hat{\psi}^\dagger_{K\beta}(\boldsymbol{x}_2 t_2)]\rangle \,. \tag{2.29}$$

Note that this definition is similar to the one of the temperature Green's function (2.3), however now t is a real time, T_t is the time-ordering operator for the real times and $\hat{\psi}_{K\alpha}$ is a true Heisenberg field operator with respect to the grand canonical Hamiltonian $\hat{K}$:

$$\hat{\psi}_{K\alpha}(\boldsymbol{x}t) = e^{i\hat{K}t}\hat{\psi}_\alpha(\boldsymbol{x})e^{-i\hat{K}t}. \tag{2.30}$$

In the case of a homogeneous system with a time-independent Hamiltonian, the Green's function (2.29) depends only on the differences $\boldsymbol{x} = \boldsymbol{x}_1 - \boldsymbol{x}_2$ and $t = t_1 - t_2$ and can be Fourier transformed to the momentum-frequency space:

$$\bar{G}_{\alpha\beta}(\boldsymbol{k}, \omega) = \int d\boldsymbol{x}\, e^{-i\boldsymbol{k}\cdot\boldsymbol{x}} \int dt\, e^{i\omega t}\bar{G}_{\alpha\beta}(\boldsymbol{x}, t). \tag{2.31}$$

This real-time Green's function contains information on the excitations of the system related to the addition or the removal of a particle. Let us focus on a system of fermions and let us assume for simplicity that the Green's function is diagonal in the spin indices: $\bar{G}_{\alpha\beta} = \bar{G}\delta_{\alpha\beta}$ (this is always true for a spin-balanced Fermi gas in the normal phase). It is possible to show that, in general, the real-time Green's function has the following spectral representation [108]

$$\bar{G}(\boldsymbol{k}, \omega) = \int_{-\infty}^{\infty} d\omega' A(\boldsymbol{k}, \omega')\left[\frac{1 - f(\omega)}{\omega - \omega' + i\eta} + \frac{f(\omega)}{\omega - \omega' - i\eta}\right] \tag{2.32}$$

where $\eta \to 0^+$ and $f(\omega) = (e^{\beta\omega} + 1)^{-1}$ is the Fermi distribution. In the square brackets, The $f(\omega)$ term is related to excitations of energy ω due to the removal a particle from the system (hole-like excitations), while the $1 - f(\omega)$ term is related to excitations of frequency ω due to the addition of a particle to the system (particle-like excitations). All the physical information of the system is contained in the *single-particle spectral function* $A(\boldsymbol{k}, \omega)$, that represents the probability density to excite eigenstates with energy ω (with respect to the ground state energy) and momentum $\boldsymbol{k}$ in the system with $N \pm 1$ particles. As it is a probability, it is positive definite

$$A(\boldsymbol{k}, \omega) \geq 0 \quad \text{for each } \boldsymbol{k},\, \omega \tag{2.33}$$

and it satisfies the sum rule

$$\int_{-\infty}^{\infty} d\omega\, A(\boldsymbol{k}, \omega) = 1. \tag{2.34}$$

If one integrates $A(\boldsymbol{k}, \omega)$ over all momenta $\boldsymbol{k}$, one obtains the *density of states*

$$N(\omega) = \frac{dn(\omega)}{d\omega} = \int \frac{d\boldsymbol{k}}{(2\pi)^3} A(\boldsymbol{k}, \omega), \tag{2.35}$$

so that $N(\omega)d\omega$ is the number of available states with energies between ω and $\omega + d\omega$.

As we have seen, the real-time Green's function $\bar{G}$ of equation (2.29) contains some relevant informations, however most of the finite temperature calculations are performed just in terms of the temperature Green's function G of equation (2.3). Luckily, it is possible to draw a connection between the two. In fact, also the temperature Green's function presents a spectral representation [108], given by

$$G(\boldsymbol{k}, \omega_n) = \int_{-\infty}^{\infty} d\omega' \, \frac{A(\boldsymbol{k}, \omega')}{i\omega_n - \omega'}. \tag{2.36}$$

where $A(\boldsymbol{k}, \omega)$ is the same weight function that was introduced in (2.32). If now we define the following function of complex argument z

$$\tilde{G}(\boldsymbol{k}, z) = \int_{-\infty}^{\infty} d\omega' \, \frac{A(\boldsymbol{k}, \omega')}{z - \omega'} \tag{2.37}$$

we see that both the temperature and real-time Green's functions can be related to the evaluation of the function $\tilde{G}$ on the imaginary axis (at the discrete points $z = i\omega_n$) or just off the real axis (at $z = \omega \pm i\eta$):

$$G(\boldsymbol{k}, \omega_n) = \tilde{G}(\boldsymbol{k}, i\omega_n), \tag{2.38}$$

$$\bar{G}(\boldsymbol{k}, \omega) = (1 - f(\omega))\, \tilde{G}(\boldsymbol{k}, \omega - i\eta) + f(\omega)\, \tilde{G}(\boldsymbol{k}, \omega + i\eta). \tag{2.39}$$

Also, by using the property $(x - i\eta)^{-1} - (x + i\eta)^{-1} = 2\pi i \delta(x)$, the equation (2.37) can be inverted to find $A(\boldsymbol{k}, \omega)$ in terms of the *retarded* Green's function $G^{\mathrm{R}}(\boldsymbol{k}, \omega) = \tilde{G}(\boldsymbol{k}, \omega + i\eta)$:

$$A(\boldsymbol{k}, \omega) = -\frac{1}{2\pi i}\big(\tilde{G}(\boldsymbol{k}, \omega + i\eta) - \tilde{G}(\boldsymbol{k}, \omega - i\eta)\big) = -\frac{1}{\pi} \operatorname{Im}\big[G^{\mathrm{R}}(\boldsymbol{k}, \omega)\big]. \tag{2.40}$$

What is done in practice in our calculations is then the following:

1. We start by calculating the temperature Green's function $G(\boldsymbol{k}, \omega_n)$, that corresponds to the values of the function $\tilde{G}(\boldsymbol{k}, z)$ at the discrete points $z = i\omega_n$ on the imaginary z axis.

2. We perform an (approximate) analytical continuation to retrieve the $\tilde{G}(\boldsymbol{k}, z)$ on the whole z complex plane. This analytical continuation is done, in our case, with the method of Padé approximants (see Section 3.2).

3. We evaluate the analytically continued function $\tilde{G}(\boldsymbol{k}, z)$ just above the real axis at the values $z = \omega + i\eta$, and we obtain the single-particle spectral function $A(\boldsymbol{k}, \omega)$ by means of (2.40).

2.2 Ladder diagrams and t-matrix approximation

In any practical situation, it is impossible to evaluate all the infinite diagrams of perturbation theory, so we have to perform an approximation and select certain classes of diagrams that are relevant to our physical system. In this thesis, the class of self-energy diagrams

selected to study the attractive Fermi gas in the BCS-BEC crossover is composed by diagrams with repeated particle-particle interactions which are called *ladder diagrams*, and the method is called the *t-matrix approximation*. An important aspect of this approach is that it does not stop at a certain perturbation order, but rather selects some diagrams at each perturbation order. This, as we will see, is crucial to correctly recover both the BCS and the BEC analytical limits of the theory.

As a note, the many-body formalism presented in this section refers to the normal phase of the Fermi gas up to the critical temperature of the superfluid transition. To study the superfluid phase, the formalism must be extended to take into account off-diagonal terms of the Green's functions [36], but this extension will not be treated within the context of this thesis.

2.2.1 Two-body scattering theory

To understand the theoretical approach to the many-body system, it is first relevant to understand the two-body physics. Let us start from the scattering problem of two atoms of mass m that interact via a two-body potential $V(\boldsymbol{x})$. The Schrödinger equation in terms of the relative coordinates and in the center-of-mass frame is given by

$$(\nabla^2 + \boldsymbol{k}^2)\psi_{\boldsymbol{k}}(\boldsymbol{x}) = v(\boldsymbol{x})\psi_{\boldsymbol{k}}(\boldsymbol{x}) \tag{2.41}$$

where we defined

$$\begin{aligned} v(\boldsymbol{x}) &\equiv 2m_{\text{red}}V(\boldsymbol{x}), \\ \boldsymbol{k}^2 &\equiv 2m_{\text{red}}E, \end{aligned} \tag{2.42}$$

and where $m_{\text{red}} = m/2$ is the reduced mass and E is the energy eigenvalue. We can now define the outgoing-wave Green's function $G^{(+)}$ as the solution of the differential equation[2]

$$(\nabla^2_{\boldsymbol{x}} + \boldsymbol{k}^2)\, G^{(+)}(\boldsymbol{x} - \boldsymbol{y}) = -\delta(\boldsymbol{x} - \boldsymbol{y}) \tag{2.43}$$

that is given by

$$G^{(+)}(\boldsymbol{x} - \boldsymbol{y}) = \frac{1}{4\pi}\frac{e^{ik|\boldsymbol{x}-\boldsymbol{y}|}}{|\boldsymbol{x} - \boldsymbol{y}|}, \tag{2.44}$$

where $k = |\boldsymbol{k}|$. This allows us to express the equation (2.41) in the integral form

$$\psi^{(+)}_{\boldsymbol{k}}(\boldsymbol{x}) = e^{i\boldsymbol{k}\cdot\boldsymbol{x}} - \int d\boldsymbol{y}\, G^{(+)}(\boldsymbol{x} - \boldsymbol{y})v(\boldsymbol{y})\psi^{(+)}_{\boldsymbol{k}}(\boldsymbol{y}), \tag{2.45}$$

where the scattering wave function is expressed in terms of an incident plane wave and an outgoing scattered wave. By using the explicit expression (2.44) for $G^{(+)}$ and taking the limit for $|\boldsymbol{x}| \to \infty$ one obtains the asymptotic form of $\psi^{(+)}$:

$$\psi^{(+)}_{\boldsymbol{k}}(\boldsymbol{x}) \sim e^{i\boldsymbol{k}\cdot\boldsymbol{x}} + f(\boldsymbol{k'}, \boldsymbol{k})\frac{e^{ikx}}{x} \quad \text{for} \quad x \to \infty, \tag{2.46}$$

[2]Note that this Green's function $G^{(+)}$ has nothing to do with the many-body Green's functions defined in (2.3) and (2.29). It is simply the solution of the differential equation (2.43).

where $x = |\boldsymbol{x}|$ and $f(\boldsymbol{k'}, \boldsymbol{k})$ is the *scattering amplitude* for the transition from an incident wave vector $\boldsymbol{k}$ to a final wave vector $\boldsymbol{k'}$ and is given by

$$f(\boldsymbol{k'}, \boldsymbol{k}) = \frac{1}{4\pi} \int d\boldsymbol{y}\, e^{-i\boldsymbol{k'}\cdot\boldsymbol{y}} v(\boldsymbol{y}) \psi_{\boldsymbol{k}}^{(+)}(\boldsymbol{y}). \tag{2.47}$$

For future purposes, it is also useful to cast the previous two-body problem in momentum space. With the Fourier transforms:

$$\begin{aligned} \psi_{\boldsymbol{k}}(\boldsymbol{p}) &= \int d\boldsymbol{x}\, e^{-i\boldsymbol{p}\cdot\boldsymbol{x}} \psi_{\boldsymbol{k}}^{(+)}(\boldsymbol{x}), \\ v(\boldsymbol{p}) &= \int d\boldsymbol{x}\, e^{-i\boldsymbol{p}\cdot\boldsymbol{x}} v(\boldsymbol{x}), \\ G^{(+)}(\boldsymbol{p}) &= \int d\boldsymbol{x}\, e^{-i\boldsymbol{p}\cdot\boldsymbol{x}} G^{(+)}(\boldsymbol{x}) = \frac{1}{\boldsymbol{p}^2 - \boldsymbol{k}^2 - i\eta}, \end{aligned} \tag{2.48}$$

the integral Schrödinger equation (2.45) becomes

$$\psi_{\boldsymbol{k}}(\boldsymbol{p}) = (2\pi)^3 \delta(\boldsymbol{p} - \boldsymbol{k}) - \frac{\tilde{f}(\boldsymbol{p}, \boldsymbol{k})}{\boldsymbol{p}^2 - \boldsymbol{k}^2 - i\eta} \tag{2.49}$$

where we have defined the modified scattering amplitude in momentum space

$$\tilde{f}(\boldsymbol{k'}, \boldsymbol{k}) = -4\pi\, f(\boldsymbol{k'}, \boldsymbol{k}) = \int \frac{d\boldsymbol{q}}{(2\pi)^3} v(\boldsymbol{q}) \psi_{\boldsymbol{k}}(\boldsymbol{k'} - \boldsymbol{q}). \tag{2.50}$$

If one multiplies the equation (2.49) by $v(\boldsymbol{p} - \boldsymbol{k'})$ and integrates $(2\pi)^{-3} \int d\boldsymbol{p}$, one obtains the following equation for the momentum scattering amplitude

$$\tilde{f}(\boldsymbol{k'}, \boldsymbol{k}) = v(\boldsymbol{k} - \boldsymbol{k'}) - \int \frac{d\boldsymbol{p}}{(2\pi)^3} v(\boldsymbol{p} - \boldsymbol{k'})\, G^{(+)}(\boldsymbol{p}) \tilde{f}(\boldsymbol{p}, \boldsymbol{k}). \tag{2.51}$$

This equation is still exact: no approximation has been made. If the scattering potential v is weak, it is possible to expand the previous equation and truncate it at a certain order in v. This is, however, not our case: in the Fermi gas across the BCS-BEC crossover the potential v can be really strong, and we are obliged to solve the integral equation (2.51) exactly at all orders to correctly take into account the effects of the interaction potential on the scattering wavefunction. As it will be shown in the next section, this is still possible if we limit ourselves to the low-energy s-wave scattering, that is usually the only relevant scattering process in ultracold gases.

To conclude this section, let us consider the expansion of the self-consistent equation (2.51) by repeatedly substituting it into itself:

$$\begin{aligned} \tilde{f}(\boldsymbol{k}, \boldsymbol{k'}) &= v(\boldsymbol{k} - \boldsymbol{k'}) - \int \frac{d\boldsymbol{p}}{(2\pi)^3}\, v(\boldsymbol{p} - \boldsymbol{k'})\, G^{(+)}(\boldsymbol{p})\, v(\boldsymbol{k} - \boldsymbol{p}) \\ &+ \int \frac{d\boldsymbol{p}}{(2\pi)^3} \int \frac{d\boldsymbol{p'}}{(2\pi)^3}\, v(\boldsymbol{p} - \boldsymbol{k'})\, G^{(+)}(\boldsymbol{p})\, v(\boldsymbol{p'} - \boldsymbol{p})\, G^{(+)}(\boldsymbol{p'}) v(\boldsymbol{k} - \boldsymbol{p'}) + \dots \end{aligned} \tag{2.52}$$

We see that any term of the perturbation series of the scattering amplitude is a repetition of interactions v and propagations $G^{(+)}$ of the pair of interacting particles. This is exactly the structure of the ladder diagrams that will be introduced in the many-body approach. Indeed, it will be shown that the ladder diagrams are the many-body generalization of the perturbation terms of the scattering amplitude of the two-body problem.

2.2.2 S-wave scattering

Let us focus now on the specific interaction potential of an attractive Fermi gas. In general, the physical origin of two-body interactions is the molecular potential $V_{\mathrm{mol}}(x)$, which is strongly repulsive at short range and attractive at long range, going to zero as $1/x^6$. Its behavior is qualitatively represented in Figure 2.2.

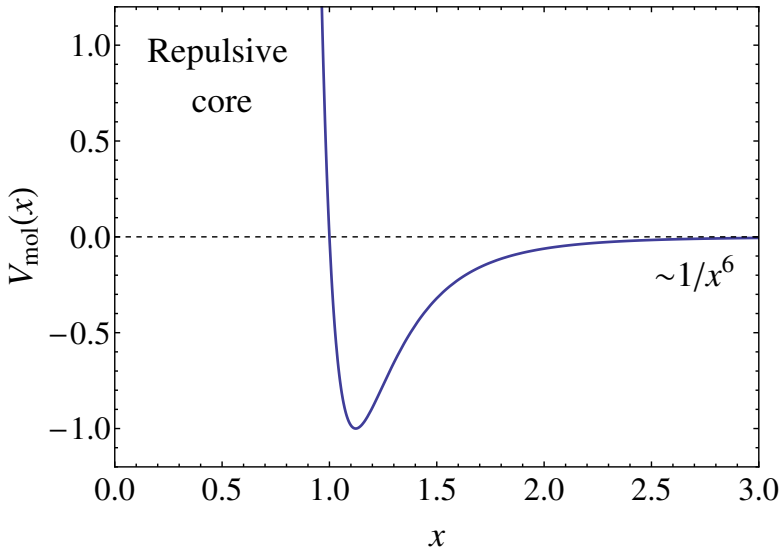

Figure 2.2: Typical molecular potential $V_{\mathrm{mol}}(x)$ between two atoms.

For most atoms, this potential is not know with precision. However, its exact knowledge is not necessary in the limit of low-energy scattering, which is a very well verified condition for ultracold atoms. To understand this, let us consider again the scattering Schrödinger equation (2.41) with the same notation $v(x) = 2m_{\mathrm{red}}V_{\mathrm{mol}}(x)$:

$$(\nabla^2 + \boldsymbol{k}^2)\psi_{\boldsymbol{k}}(\boldsymbol{x}) = v(x)\psi_{\boldsymbol{k}}(\boldsymbol{x}). \tag{2.53}$$

As the potential is spherically symmetric, we can expand the scattering wavefunction into partial waves with angular momentum ℓ

$$\psi_{\boldsymbol{k}}(\boldsymbol{x}) = \sum_{\ell=0}^{\infty} \frac{u_{\boldsymbol{k}\ell}(x)}{x} Y_{\ell 0}(\theta). \tag{2.54}$$

where $Y_{\ell m}$ are the spherical harmonics of angular momentum ℓ and $x = |\boldsymbol{x}|$. Note that in the expansion we have omitted terms with $m \neq 0$ because of the cylindrical symmetry of

the problem. By substituting this expansion in the Schrödinger equation (2.53) we find a 1D equation along the direction of $\boldsymbol{k}$ for each radial wave $u_{\boldsymbol{k}\ell}(x)$

$$(\partial_x^2 + k^2)\, u_{\boldsymbol{k}\ell}(x) = \left[v(x) + \frac{\ell(\ell+1)}{x^2}\right] u_{\boldsymbol{k}\ell}(x). \tag{2.55}$$

In this equation, we can consider the sum of the potential $v(x)$ and the angular momentum contribution as an effective potential, given by

$$v_{\text{eff}}^{(\ell)}(x) = v(x) + \frac{\ell(\ell+1)}{x^2}. \tag{2.56}$$

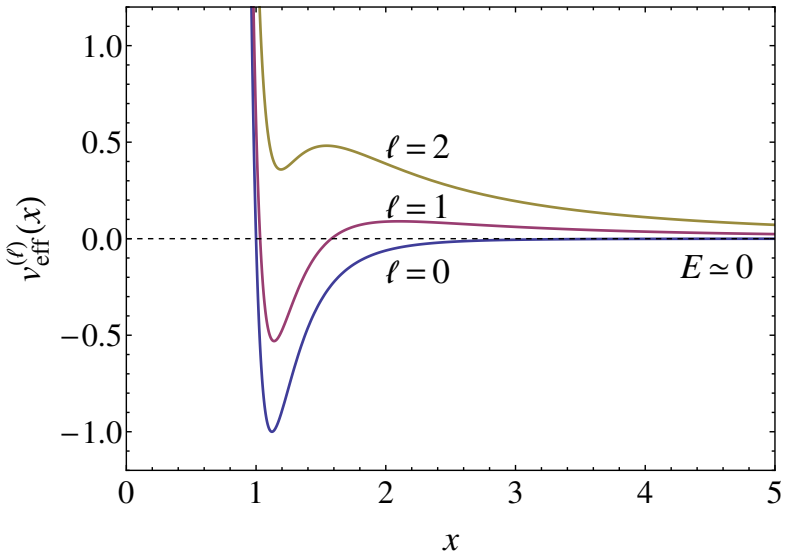

Figure 2.3: Effective potential $v_{\text{eff}}^{(\ell)}(x)$ of Eq. (2.56) for different partial waves ℓ.

This effective potential is plotted in Fig. 2.3 for different partial waves. For the partial wave $\ell = 0$, it is equal to the molecular potential $v(x)$. For the other partial waves ($\ell > 0$), the centrifugal barrier $\ell(\ell+1)/x^2$ is also present. If the relative energy $E = \boldsymbol{k}^2/(2m_{\text{red}})$ of the two particles is much lower of the height of this barrier, they will not experience the short-range potential $v(x)$ and will be simply reflected by the centrifugal barrier. We then qualitatively expect that in the limit of low energy the only relevant contribution to the scattering will be given by the $\ell = 0$ partial wave. As the latter is known also as the s-wave, this process is usually called *s-wave scattering*. It can be shown that, in this low-energy limit, the momentum scattering amplitude assumes the simple form [109]

$$\tilde{f}(\boldsymbol{k}, \boldsymbol{k'}) = \frac{4\pi}{a^{-1} + i|\boldsymbol{k}|} \tag{2.57}$$

and all the scattering properties are described in terms of the *scattering length* a, that is defined as

$$a = \lim_{|\boldsymbol{k}|\to 0} \frac{\tan\delta_0(\boldsymbol{k})}{|\boldsymbol{k}|} \tag{2.58}$$

where δ_0 is the phase-shift between the incident and the scattered asymptotic wavefunctions for the partial wave $\ell = 0$.

Let us conclude this section with a consideration on the indistinguishability of the scattering particles. Up to here, we have supposed that the two particles are in some way distinguishable. For identical fermions, however, we have to take into account also the anti-symmetrization principle of the wavefunction, which states that $\psi_{\boldsymbol{k}}(\boldsymbol{x}) = -\psi_{\boldsymbol{k}}(-\boldsymbol{x})$, i.e. that the wavefunction in relative coordinates is odd under parity transformation. Knowing that the parity of spherical harmonic functions $Y_{l,0}(\theta)$ is $(-1)^l$, we see that in the partial wave expansion (2.54) only the odd l partial waves survive for fermions, so these are the only partial waves that contribute to the scattering. As $l = 0$ is an even partial wave, this means that s-wave scattering is suppressed for identical fermions, due to the anti-symmetrization principle. As a consequence, in our system we will have interactions between two fermions only when they are distinguishable, i.e. only when they are in different spin states.

2.2.3 Contact pseudo-potential

The idea is now to replace the complicated molecular potential $V_{\text{mol}}(x)$ with a simpler "contact" (zero-range) potential $V(\boldsymbol{x}) = v_0\delta(\boldsymbol{x})$, with the constant v_0 chosen in a way that it can reproduce the s-wave scattering with the correct scattering length. Note also that the contact potential automatically makes the interaction possible only for fermions in different spin states, because for identical fermions $\delta(\boldsymbol{x})\psi_{\boldsymbol{k}}(\boldsymbol{x}) = 0$ due to the anti-symmetrization imposed on the wavefunction by the fermionic statistics.

The choice of a contact potential however brings a problem when we deal with homogeneous systems: its Fourier transform is a constant $V(\boldsymbol{k}) = v_0$, and this can make integrals in $\boldsymbol{k}$-space diverge for large k. This problem can be overcome by introducing an ultraviolet cutoff k_0, and defining an effective scattering potential directly in momentum space as

$$V(\boldsymbol{k} - \boldsymbol{k}') = v_0\,\theta(|\boldsymbol{k}| - k_0)\,\theta(|\boldsymbol{k}'| - k_0) \tag{2.59}$$

where $\theta(k)$ is the step function. Note that the choice of a potential that is separable in $\boldsymbol{k}$ and $\boldsymbol{k}'$ is just an useful theoretical trick that becomes irrelevant in the $k_0 \to \infty$ limit to recover the contact potential. If we insert this separable potential in the equation (2.51) and we use the s-wave form of the scattering amplitude (2.57), we obtain the relation that connects the scattering length to the parameters v_0 and k_0:

$$\frac{m}{4\pi a_F} = \frac{1}{v_0} + \int_{|\boldsymbol{k}|<k_0} \frac{d\boldsymbol{k}}{(2\pi)^3}\frac{m}{\boldsymbol{k}^2}. \tag{2.60}$$

In the view of the BCS-BEC crossover where we deal also with composite bosons, the subscript F is put here to highlight that a_F is the scattering length between two fermionic atoms. This expression allows us to take the limits $k_0 \to \infty$ and $v_0 \to 0^-$ at the same time so that the scattering length a_F is kept at the desired value without incurring in any ultraviolet divergence, thus giving us a rigorous *regularization procedure* for the contact potential (2.59). This relation also allows us to replace the scattering potential v with

the scattering length a_F in all the expressions of our theory, so that the interaction is described only in terms of a_F, instead of both v_0 and k_0. This is useful not only on the theoretical side, but also for the comparison with the experiments, as the scattering length a_F is the easiest parameter to access experimentally.

Other than the scattering properties, it is important to show that for $a_F > 0$ the contact potential (2.59) presents a single bound molecular state with binding energy $\varepsilon_0 = (m a_F)^{-1}$. This can be seen by looking for a solution of the Schrödinger equation (2.41) without the incident plane wave boundary condition and with negative energy $E = -\boldsymbol{\kappa}^2/(2m_{\rm red}) = -\boldsymbol{\kappa}^2/m$. This translates, in momentum space, to the following equation

$$\psi_{\boldsymbol{\kappa}}(\boldsymbol{p}) = -\frac{m\, v_0}{\boldsymbol{p}^2 + \boldsymbol{\kappa}^2} \int_{|\boldsymbol{q}|<k_0} \frac{d\boldsymbol{q}}{(2\pi)^3} \psi_{\boldsymbol{\kappa}}(\boldsymbol{q}). \tag{2.61}$$

If we integrate $\int_{|\boldsymbol{p}|<k_0} d\boldsymbol{p}/(2\pi)^3$ and simplify the integrals of the wavefunctions we have

$$\frac{1}{m\, v_0} = -\int_{|\boldsymbol{p}|<k_0} \frac{d\boldsymbol{p}}{(2\pi)^3} \frac{1}{\boldsymbol{p}^2 + \boldsymbol{\kappa}^2}. \tag{2.62}$$

If now we express $1/v_0$ in terms the scattering length a_F by means of the regularization procedure (2.60) and we perform the (regularized) integral on $\boldsymbol{p}$, we finally obtain

$$|\boldsymbol{\kappa}| = \frac{1}{a_F}, \tag{2.63}$$

that for $a_F > 0$ corresponds to the energy eigenvalue

$$E = -\varepsilon_0 = -\frac{1}{m a_F^2} \tag{2.64}$$

for the bound state. Replacing the $\boldsymbol{\kappa}$ obtained in (2.63) in the integral equation (2.61), one obtains the (normalized) wavefunction for the bound state

$$\phi_b(\boldsymbol{p}) = \sqrt{\frac{8\pi}{a_F}} \frac{1}{\boldsymbol{p}^2 + a_F^{-2}}, \tag{2.65}$$

which, transformed to the real space, becomes

$$\phi_b(\boldsymbol{\rho}) = \frac{1}{\sqrt{2\pi a_F}} \frac{e^{-\rho/a_F}}{\rho}, \tag{2.66}$$

where $\rho = |\boldsymbol{\rho}|$ and we used $\boldsymbol{\rho}$ for the relative variable to match the expressions in Chapters 5 and 6.

2.2.4 Bethe-Salpeter equation

Let us now turn to the many-body problem, and start from the basic ingredient of our theory: the ladder diagrams. These diagrams are represented in Fig. 2.4 and represent

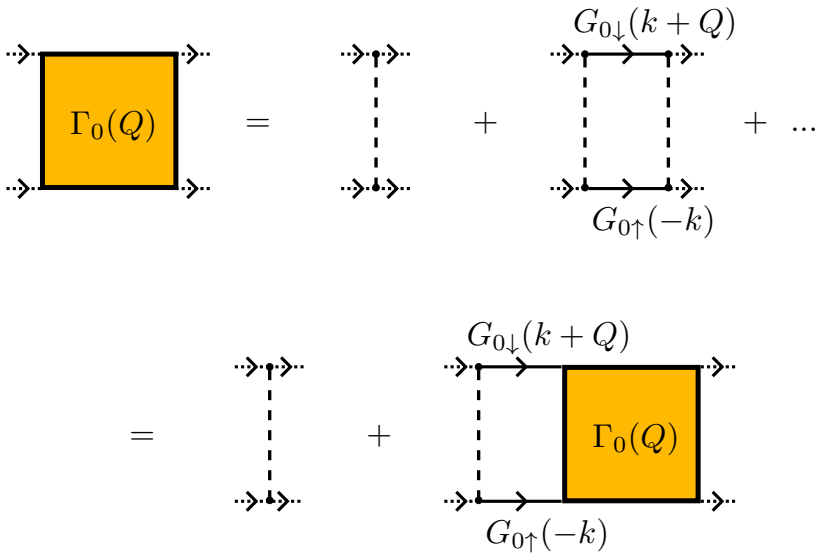

Figure 2.4: Diagrammatic representation of the particle-particle propagator Γ_0, defined as the sum of all the ladder diagrams.

the sum of all the particle-particle scattering processes. The sum of all these ladder diagrams Γ_0 is called *particle-particle propagator* (or sometimes also t-matrix or vertex of the ladder diagrams). The equation that defines Γ_0 can be more conveniently expressed in a self-consistent manner, as it is shown on the lower part of Fig. 2.4, with the n-th order ladder built by the $(n-1)$-th order ladder plus an additional rung of two particle lines and an interaction line. By applying the rules of the Feynman diagrams of Section 2.1.3, we obtain:

$$\begin{aligned}\Gamma_0(\boldsymbol{p},\boldsymbol{p}',Q) &= -V(\boldsymbol{p}-\boldsymbol{p}') \\ &- \int \frac{d\boldsymbol{k}}{(2\pi)^3}\frac{1}{\beta}\sum_n V(\boldsymbol{p}-\boldsymbol{k})G_{0\downarrow}(k+Q)G_{0\uparrow}(-k)\Gamma_0(\boldsymbol{p},\boldsymbol{p}',Q)\end{aligned} \tag{2.67}$$

Here, we used the shorthand notation $k=(\boldsymbol{k},\omega_n)$ and $Q=(\boldsymbol{Q},\Omega_\nu)$, where ω_n and Ω_ν are, respectively, the fermionic and bosonic Matsubara frequencies as defined in (2.11). $G_{0\sigma}\equiv G^0_{\sigma\sigma}$ is the spin-σ ($\sigma=\uparrow,\downarrow$) bare propagator, and it is defined as in (2.26)

$$G_{0\sigma}(k)=\frac{1}{i\omega_n-\xi_{\boldsymbol{k},\sigma}} \tag{2.68}$$

where $\xi_{\boldsymbol{k},\sigma}=\boldsymbol{k}^2/(2m)-\mu_\sigma$. Note that here we have allowed for different chemical potentials $\mu_\uparrow$ and $\mu_\downarrow$ for the spin-up and spin-down components, which are equal only for a Fermi gas with balanced spin populations ($N_\uparrow=N_\downarrow$).

To write the expression (2.67), we used the fact that the interaction potential is

non-zero only between atoms of different spin, so the only possible choice for the two propagators connected by an interaction line is $G_{0\uparrow}G_{0\downarrow}$.

We can now directly compare this equation with the self-consistent equation for the scattering amplitude (2.51) of the two-body problem. Indeed, the structure is very similar, with Γ_0 taking the role of the scattering amplitude $\tilde{f}$ and $\beta^{-1}\sum_n G_{0\downarrow}G_{0\uparrow}$ taking the role of $G^{(+)}$. There is, however, an important difference: while $\tilde{f}(\boldsymbol{p},\boldsymbol{p}')$ depends only on the incident and scattered wave-vectors $\boldsymbol{p}$ and $\boldsymbol{p}'$, the particle-particle propagator $\Gamma_0(\boldsymbol{p},\boldsymbol{p}',Q)$ depends also on the four-momentum of the pair $Q=(\boldsymbol{Q},\Omega_\nu)$. In this sense, the particle-particle propagator Γ_0 can be regarded as the many-body generalization of the scattering amplitude of the two-body problem. Indeed, it can be shown [108] that if we take the dilute limit of the many-body problem, the function Γ_0 with the appropriate replacement $i\Omega_\nu - \boldsymbol{Q}^2/4 + 2\mu \to \boldsymbol{p}^2/(2m_{\text{red}})$ reduces to the scattering amplitude $\tilde{f}$ of the two-body problem.

Let us now concentrate specifically on the case of a contact potential of the form (2.59) with the regularization condition (2.60). By replacing it in the equation (2.67), we obtain the expression

$$\Gamma_0(\boldsymbol{p},\boldsymbol{p}',Q) = -v_0 - v_0\int_{|\boldsymbol{k}|<k_0}\frac{d\boldsymbol{k}}{(2\pi)^3}\frac{1}{\beta}\sum_n G_{0\downarrow}(k+Q)G_{0\uparrow}(-k)\Gamma_0(\boldsymbol{k},\boldsymbol{p}',Q) \tag{2.69}$$

where the limit $k_0\to\infty$ is already taken where possible, leaving the dependence on the cutoff k_0 only in the (otherwise diverging) integral on $\boldsymbol{k}$. By direct inspection of the perturbative expansion of Eq. (2.69), one can see that the particle-particle propagator is actually only a function of the pair four-momentum $Q=(\boldsymbol{Q},\Omega_\nu)$ and does not depend on the relative momenta $\boldsymbol{p}$ and $\boldsymbol{p}'$, so $\Gamma_0(\boldsymbol{p},\boldsymbol{p}',Q)\equiv\Gamma_0(Q)$. With this consideration in mind, we can bring $\Gamma_0(Q)$ out of the $\boldsymbol{k}$-integral and rewrite the previous expression in the simple form

$$\Gamma_0(Q) = -\frac{1}{1/v_0 + \chi_{pp}(Q)}, \tag{2.70}$$

where we have defined the *particle-particle bubble*:

$$\chi_{pp}(Q) = \int_{|\boldsymbol{k}|<k_0}\frac{d\boldsymbol{k}}{(2\pi)^3}\frac{1}{\beta}\sum_n G_{0\downarrow}(k+Q)G_{0\uparrow}(-k). \tag{2.71}$$

This expression is still ultraviolet divergent in the limit $k_0\to\infty$. This divergence is eliminated by using Eq. (2.60) to express the $1/v_0$ appearing in (2.70) in terms of the scattering length a_F, obtaining

$$\Gamma_0(Q) = -\frac{1}{m/(4\pi a_F) + R^0_{pp}(Q)} \tag{2.72}$$

where $R^0_{pp}(Q)$ is now the *renormalized particle-particle bubble*

$$R^0_{pp}(Q) = \int\frac{d\boldsymbol{k}}{(2\pi)^3}\left(\frac{1}{\beta}\sum_n G_{0\downarrow}(k+Q)G_{0\uparrow}(-k) - \frac{m}{\boldsymbol{k}^2}\right). \tag{2.73}$$

The sum over fermionic frequencies ω_n in the previous expression can be carried out analytically and the explicit result is

$$R^0_{pp}(Q) = \int \frac{d\boldsymbol{k}}{(2\pi)^3} \left(\frac{1 - f(\xi_{\boldsymbol{k}+\boldsymbol{Q}/2,\uparrow}) - f(\xi_{\boldsymbol{k}-\boldsymbol{Q}/2,\downarrow})}{\xi_{\boldsymbol{k}+\boldsymbol{Q}/2,\uparrow} + \xi_{\boldsymbol{k}-\boldsymbol{Q}/2,\downarrow} - i\Omega_\nu} - \frac{m}{\boldsymbol{k}^2} \right), \tag{2.74}$$

where $f(\xi) = (e^{\beta\xi} + 1)^{-1}$ is the Fermi distribution function, and $\xi_{\boldsymbol{k},\sigma} = k^2/(2m) - \mu_\sigma$. By inspecting the large $\boldsymbol{k}$ behavior of this expression, it is now clear that the ultraviolet divergence of (2.71) is eliminated by the $-m/\boldsymbol{k}^2$ counter-term, so that the $k_0 \to \infty$ limit can be taken without any issue.

2.2.5 Non-self-consistent t-matrix

Now that the particle-particle propagator Γ_0 has been introduced, we can turn to define our (approximate) self-energy as

$$\Sigma_{0\sigma}(k) = -\int \frac{d\boldsymbol{Q}}{(2\pi)^3} \frac{1}{\beta} \sum_\nu \Gamma_0(Q) G_{0\bar{\sigma}}(Q - k) \tag{2.75}$$

where σ and $\bar{\sigma}$ are opposite spin indices. This self-energy is represented in terms of Feynman diagrams in Fig. 2.5. The intuitive interpretation of this self-energy is that, if we treat Γ_0 as an "effective" interaction in the medium, the self-energy corresponds to a Hartree-like term of this effective interaction.[3]

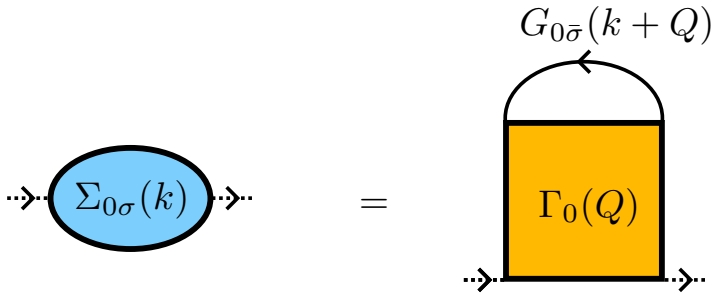

Figure 2.5: Diagrammatic representation of the t-matrix self-energy (2.147). The representation of the particle-particle propagator $\Gamma_0(Q)$ is shown in Fig. 2.4.

[3]See equation (2.27) and Fig. 2.1 for comparison with the Hartree term of the bare interaction. Note that here we are not considering any Fock-like term (as Galitskii did in his original paper [103]) because, for a Fermi gas with contact interaction, this term is exactly zero due to the absence of same-spin interactions. Nonetheless, this Fock-like self-energy is actually needed to consistently define two-particle Green's functions, and for this reason it will be considered in Section 2.6.

We now have all the ingredients to calculate the Green's function of our system. We first calculate the particle-particle bubble R^0_{pp} of Eq. (2.73) from which we obtain the particle-particle propagator Γ_0 with the Bethe-Salpeter equation (2.72), then we calculate the self-energy Σ_0 as in (2.147) and we finally obtain the single-particle Green's function G via the Dyson equation (2.24) (check also Fig. 2.7(a)). The equations are here summarized for later convenience:

$$G_\sigma(k) = \left[G_{0\sigma}(k)^{-1} - \Sigma_{0\sigma}(k)\right]^{-1} \tag{2.76}$$

$$\Sigma_{0\sigma}(k) = -\int \frac{d\boldsymbol{Q}}{(2\pi)^3}\frac{1}{\beta}\sum_\nu \Gamma_0(Q)G_{0\bar{\sigma}}(Q-k) \tag{2.77}$$

$$\Gamma_0(Q) = -\left[\frac{m}{4\pi a_F} + R^0_{pp}(Q)\right]^{-1} \tag{2.78}$$

$$R^0_{pp}(Q) = \int \frac{d\boldsymbol{k}}{(2\pi)^3}\left[\frac{1}{\beta}\sum_n G_{0\downarrow}(k+Q)G_{0\uparrow}(-k) - \frac{m}{\boldsymbol{k}^2}\right]. \tag{2.79}$$

This set of equations is known as the *non-self-consistent t-matrix* approximation. In these equations, the free parameters are four: the temperature T, the scattering length a_F and the chemical potentials μ_σ for the two spin species $\sigma =\uparrow,\downarrow$ (in the balanced case $\mu_\uparrow = \mu_\downarrow = \mu$). The chemical potentials μ_σ can be found in terms of the densities $n_\sigma = N_\sigma/V$ by inverting the density equations (2.17):

$$n_\sigma = \int \frac{d\boldsymbol{k}}{(2\pi)^3}\frac{1}{\beta}\sum_n e^{i\omega_n\eta}G_\sigma(\boldsymbol{k},\omega_n). \tag{2.80}$$

It is however possible to reduce the number of free parameters by rescaling all the quantities in terms of the total density $n = n_\uparrow + n_\downarrow$. This corresponds to express all the wave vectors in units of the Fermi wave vector $k_F = (3\pi n)^{1/3}$, all the lengths in units of its inverse k_F^{-1} and all the energies in units of the Fermi energy $E_F = k_F^2/(2m)$, and leaves us with only three free parameters:

1. The coupling $(k_F a_F)^{-1}$.
2. The temperature T/T_F (where $T_F = E_F/k_B$).
3. The density imbalance (or polarization) $\alpha = (n_\uparrow - n_\downarrow)/(n_\uparrow + n_\downarrow)$ or, equivalently, the minority fraction $x = n_\downarrow/n_\uparrow$.

In the balanced case, the density imbalance α is 0 ($x = 1$) and the free parameters reduce to just the coupling $(k_F a_F)^{-1}$ and the temperature T/T_F.

One of the main virtues of the non-self-consistent t-matrix approach is that it recovers the superfluid critical temperature in the BEC and BCS limits (albeit only with logarithmic accuracy in the latter case) and smoothly interpolates between them [102]. To get the critical temperature we use the *Thouless criterion*, that states that at $T = T_c$ the particle-particle propagator has a pole at $\boldsymbol{Q} = 0$ and $\Omega_\nu = 0$, signaling a macroscopic accumulation of pairs in the state of momentum $\boldsymbol{Q} = 0$ [110]:

$$\left[\Gamma_0(\boldsymbol{Q} = 0, \Omega_\nu = 0)|_{T=T_c}\right]^{-1} = 0. \tag{2.81}$$

As it will be shown in the next sections, this criterion, when solved together with the density equation (2.80), corresponds to the $\Delta = 0$ condition of BCS theory in the weak-coupling limit $(k_F a_F)^{-1} \ll -1$ and to $\mu_B = 0$ in the condition for condensation of bosons in the strong-coupling limit $(k_F a_F)^{-1} \gg 1$. For simplicity, in the next sections the case of a balanced gas with $\mu_\uparrow = \mu_\downarrow = \mu$ will be considered, and the irrelevant spin indices will be dropped.

2.2.6 Strong-coupling (BEC) limit

In the strong-coupling limit $(k_F a_F)^{-1} \gg 1$, the dominant energy scale is the chemical potential of the fermions that becomes big and negative, so that $\beta|\mu| \gg 1$. In fact, suppose to add a pair of spin-up and spin-down fermions to the system (so that it remains spin-balanced). Due to the strong coupling, the pair will form a molecular state of binding energy $\varepsilon_0 = (m a_F^2)^{-1}$ (see Eq. (2.64)), so the variation of energy of the system per fermion will be $\mu \simeq -\varepsilon_0/2$. This shows that μ (being proportional to $\varepsilon_0 \to \infty$) is the dominant energy scale. By taking the $\beta|\mu| \gg 1$ limit, we can neglect the Fermi functions in the renormalized the particle-particle bubble (2.74) and the integral can be carried out analytically, yielding

$$R_{pp,\mathrm{sc}}(Q) = -\frac{m^{3/2}}{4\pi}\sqrt{\frac{\boldsymbol{Q}^2}{4m} - 2\mu - \frac{i\Omega_\nu}{2}}. \tag{2.82}$$

Inserting this expression in equation (2.72) we obtain the particle-particle propagator in the strong-coupling limit

$$\Gamma_{\mathrm{sc}}(Q) = -\frac{1}{\frac{m}{4\pi a_F} - \frac{m^{3/2}}{4\pi}\sqrt{\frac{\boldsymbol{Q}^2}{4m} - 2\mu - \frac{i\Omega_\nu}{2}}}, \tag{2.83}$$

or, by rearranging the previous expression,

$$\Gamma_{\mathrm{sc}}(Q) = -\frac{4\pi}{m^2 a_F}\frac{1 + \sqrt{1 + \left(\frac{\boldsymbol{Q}^2}{4m} - \mu_B - i\Omega_\nu\right)\varepsilon_0^{-1}}}{i\Omega_\nu - \left(\frac{\boldsymbol{Q}^2}{4m} - \mu_B\right)} \tag{2.84}$$

where we defined the bosonic chemical potential as $\mu_B = 2\mu + \varepsilon_0$. Note that, within the square root, the term multiplied by ε_0^{-1} is actually subleading in the strong-coupling limit, so to the lowest order the particle-particle propagator assumes the polar form

$$\Gamma_{\mathrm{sc}}(Q) \simeq -\frac{8\pi}{m^2 a_F}\frac{1}{i\Omega_\nu - \xi^B_{\boldsymbol{Q}}} \tag{2.85}$$

with $\xi^B_{\boldsymbol{Q}} = \boldsymbol{Q}^2/(4m) - \mu_B$. This means that in the strong-coupling limit, apart for a multiplicative factor, the particle-particle propagator reduces to the bare propagator for composite bosons (cf. Eq. (2.18)).

By taking the same strong-coupling limit for the self-energy (2.77), we can neglect the Q-dependence of G_0 as $|\mu|$ is the dominant energy scale in the denominator, and we obtain

$$\Sigma_0(k) \simeq -G_0(-k) \int \frac{d\boldsymbol{Q}}{(2\pi)^3} \frac{1}{\beta} \sum_\nu e^{i\Omega_\nu \eta} \Gamma_{\rm sc}(Q) \tag{2.86}$$

with $\eta \to 0^+$. At the same time, as $G_0 \sim |\mu|^{-1}$, we can expand the Dyson equation (2.76) as

$$G(k) \simeq G_0(k) + G_0(k)\Sigma_0(k)G_0(k). \tag{2.87}$$

If now one integrates this $G(k)$ to obtain the total density of the fermions as in (2.80), one obtains

$$\begin{aligned} n \simeq\ & 2 \int \frac{d\boldsymbol{k}}{(2\pi)^3} \frac{1}{\beta} \sum_n e^{i\omega_n \eta}\, G_0(k) \\ & - 2 \int \frac{d\boldsymbol{k}}{(2\pi)^3} \frac{1}{\beta} \sum_n e^{i\omega_n \eta}\, [G_0(k)]^2 G_0(-k) \int \frac{d\boldsymbol{Q}}{(2\pi)^3} \frac{1}{\beta} \sum_\nu e^{i\Omega_\nu \eta}\, \Gamma_{\rm sc}(Q). \end{aligned} \tag{2.88}$$

The first term simply gives the free fermion density as in (2.19). This contribution is exponentially suppressed in the limit $\beta|\mu| \gg 1$ and can be neglected. In the second term, the sum over the fermionic frequencies ω_n and the integral over $\boldsymbol{k}$ can be carried out analytically and it yields a constant factor

$$\int \frac{d\boldsymbol{k}}{(2\pi)^3} \frac{1}{\beta} \sum_n [G_0(k)]^2 G_0(-k) \simeq -\frac{m^2}{8\pi\sqrt{2m|\mu|}} \simeq -\frac{m^2 a_F}{8\pi}. \tag{2.89}$$

Note that this constant factor exactly compensates the multiplicative factor of $\Gamma_{\rm sc}$ in its polar form (2.85). The sum over the bosonic frequencies Ω_ν can be carried out as in (2.19) and one obtains a Bose-like expression for the density

$$n \simeq 2 \int \frac{d\boldsymbol{Q}}{(2\pi)^3} \frac{1}{e^{\beta \xi^B_{\boldsymbol{Q}}} - 1} \equiv 2 n_B. \tag{2.90}$$

This means that in the BEC limit the non-self-consistent t-matrix theory correctly recovers a system of non-interacting composite bosons with mass $2m$. The critical temperature at a fixed boson density $n_B = n/2$ can be obtained by letting $\mu_B \to 0^-$ in the previous expression (note, as anticipated above, that this is equivalent to the Thouless criterion $[\Gamma_{\rm sc}(Q=0)]^{-1} = 0$). In this way, one finds that the system recovers the critical temperature for non-interacting composite bosons:

$$T_c^{\rm BEC} = \frac{2\pi}{\zeta(3/2)^{2/3}} \frac{n_B^{2/3}}{2m} \simeq 0.218 T_F. \tag{2.91}$$

2.2.7 Weak-coupling (BCS) limit

Let us now consider the weak-coupling limit $(k_F a_F)^{-1} \ll -1$, and let us set ourselves at the critical temperature T_c by imposing the Thouless criterion (2.81), which can be

rewritten in terms of the renormalized particle-particle bubble (2.79) as

$$\frac{m}{4\pi a_F} + R^0_{pp}(Q=0)|_{T=T_c} = 0. \tag{2.92}$$

As the coupling gets weaker, we expect the system to get closer to a non-interacting Fermi gas, so the critical temperature T_c will go to zero and the chemical potential will be $\mu \simeq E_F$. We can then take the limit $T_c/\mu \ll 1$ in the renormalized particle-particle bubble and obtain [111]:

$$R^0_{pp}(Q) \simeq \frac{(2m)^{3/2}\sqrt{\mu}}{4\pi^2}\Big[\ln\Big(\frac{8\mu e^\gamma}{k_B \pi T_c}\Big) - 2\Big]. \tag{2.93}$$

Where γ is the Euler constant. By inserting this expression in (2.92) and solving for T_c we obtain

$$T_c \simeq \frac{8\mu e^\gamma}{k_B \pi e^2} \exp\Big(\frac{\pi}{2k_F a_F}\sqrt{E_F/\mu}\Big). \tag{2.94}$$

Indeed, we found that the temperature is exponentially suppressed for $(k_F a_F)^{-1} \ll -1$ as it was assumed at the beginning. By simply replacing the chemical potential μ with the Fermi energy E_F in the previous expression, one obtains the BCS critical temperature [108]

$$T_c^{\rm BCS} = \frac{8e^\gamma T_F}{\pi e^2} \exp\Big(\frac{\pi}{2k_F a_F}\Big). \tag{2.95}$$

Note however that, if μ has some linear corrections in the coupling $\mu \simeq E_F(1 + A\, k_F a_F)$, the expression (2.94) would present a constant prefactor $\exp(-\pi A/4)$ coming from the exponential. It is then relevant to understand which is the leading correction in the weak-coupling expansion of the chemical potential in powers of $(k_F a_F)$. To do so, let us start by noticing that if one replaces the expression (2.94) for T_c in the particle-particle bubble (2.93) one finds that it is linear in $(k_F a_F)$ (except for a small region around $Q \simeq 0$, where it is $\sim m/(4\pi a_F)$ because of the Thouless criterion (2.92)). This means that, for most Q's, $R^0_{pp}(Q)$ is subleading with respect to $m/(4\pi a_F)$ in the denominator of the particle-particle propagator (2.78), so one can set

$$\Gamma_0(Q) \simeq -\frac{4\pi a_F}{m} \tag{2.96}$$

in the expression for the self-energy (2.77), obtaining

$$\Sigma_0(k) \simeq \frac{4\pi a_F}{m}\int \frac{d\boldsymbol{Q}}{(2\pi)^3}\frac{1}{\beta_c}\sum_\nu \frac{1}{i\Omega_\nu - i\omega_n - \xi_{\boldsymbol{Q}-\boldsymbol{k}}} = \frac{2\pi a_F}{m} n_0, \tag{2.97}$$

where n_0 is the density of the non-interacting fermions, that in the $T_c/\mu \ll 1$ limit is given by

$$n_0 = 2\int \frac{d\boldsymbol{Q}}{(2\pi)^3}\frac{1}{e^{\beta_c \xi_{\boldsymbol{Q}}}+1} \simeq 2\int \frac{d\boldsymbol{Q}}{(2\pi)^3}\,\theta(-\xi_{\boldsymbol{Q}}) = \frac{(2m\mu)^{3/2}}{3\pi^2}. \tag{2.98}$$

From (2.97) we see that at the leading order the self-energy reduces to a constant that is linear in the scattering length a_F. This constant simply corresponds to a mean-field shift of the chemical potential. As $(k_F a_F) \to 0^-$, we can expand the Dyson equation (2.76) to the first order in Σ_0

$$G(k) \simeq G_0(k) + G_0(k)\Sigma_0(k)G_0(k). \tag{2.99}$$

Integrating $G(k)$ as in (2.80) to obtain the total density n, we find a first term that is simply the free contribution n_0 of equation (2.98) and a second term that is given by

$$\begin{aligned} \int \frac{d\boldsymbol{k}}{(2\pi)^3} \frac{1}{\beta_c} \sum_n e^{i\omega_n \eta} [G_0(k)]^2 \Sigma_0(k) \simeq \\ \frac{2\pi a_F}{m} n_0 \int \frac{d\boldsymbol{k}}{(2\pi)^3} \frac{1}{\beta_c} \sum_n \frac{1}{(i\omega_n - \xi_{\boldsymbol{k}})^2} \simeq \frac{\sqrt{2m\mu}}{\pi} n_0 a_F, \end{aligned} \tag{2.100}$$

so the total density in the weak-coupling limit is given by

$$n \simeq n_0 \left(1 - \frac{2\sqrt{2m\mu}}{\pi} a_F \right). \tag{2.101}$$

Inverting the previous equation to isolate μ and expanding at the first order in $(k_F a_F)$ we obtain

$$\mu \simeq E_F \left(1 + \frac{4 k_F a_F}{3\pi} \right) \tag{2.102}$$

where we used the relations $n = k_F^3/(3\pi^2)$ and $E_F = k_F^2/(2m)$. Replacing this expression for the chemical potential in (2.94) we obtain that the critical temperature in the weak-coupling limit for the non-self-consistent t-matrix is given by:

$$T_c \simeq \frac{8 e^\gamma T_F}{\pi e^2} \exp\left(\frac{\pi}{2 k_F a_F} - \frac{1}{3} \right) = e^{-1/3}\, T_c^{\mathrm{BCS}} \tag{2.103}$$

This means that the non-self-consistent t-matrix recovers the BCS critical temperature (2.95) with a spurious $e^{-1/3}$ factor. This spurious factor can be corrected by self-consistently including the mean-field shift $\Sigma_0 = 2\pi a_F n_0/m$ of Eq. (2.97) in the bare Green's functions G_0 within the renormalized particle-particle bubble of Eq. (2.92). This corresponds to the replacement $\mu \to \mu - \Sigma_0$ in (2.93), and with this replacement we can easily see that the mean-field shift Σ_0 exactly compensates the linear term of Eq. (2.102) so that $\mu - \Sigma_0 = E_F(1 + \mathcal{O}(k_F a_F)^2)$. Without linear terms in $(k_F a_F)$, the spurious $-1/3$ term in the exponential of (2.103) is removed and one recovers $T_c \simeq T_c^{\mathrm{BCS}}$ in the weak-coupling limit.

2.3 Inclusion of self-consistency

The non-self consistent approach presented in the last section can be improved with the inclusion of (partial or full) self-consistency in the equations (2.76-2.79). This improvement has been implemented in many different ways in the literature [26–28, 60, 65], but the

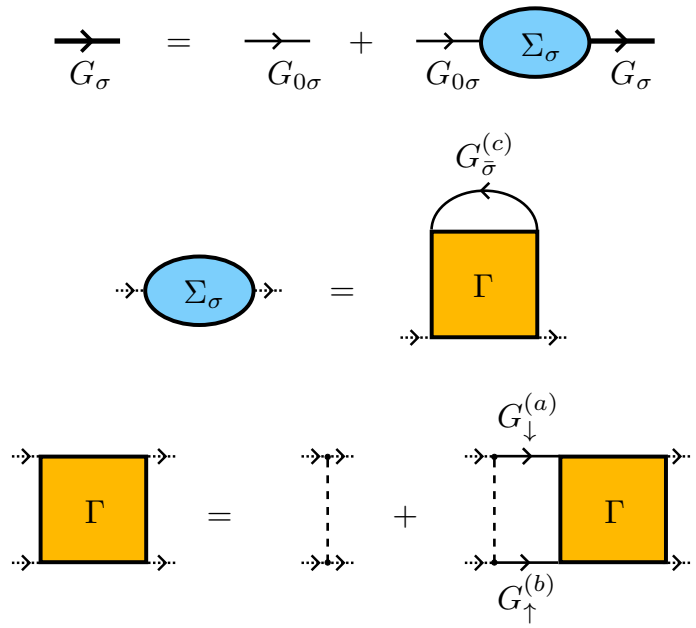

Figure 2.6: Diagrammatic representation of the equations (2.104-2.107) for a generic $(G^{(a)}G^{(b)})G^{(c)}$ t-matrix approach. The propagators $G^{(a)}$, $G^{(b)}$ and $G^{(c)}$ can be either bare (G_0) or dressed (G).

core concept is the same: to include self-consistency by replacing some (or all) bare propagators G_0 with dressed propagators G in the ladder and self-energy diagrams. The generalization of the non-self-consistent t-matrix equations (2.76-2.79) with the inclusion of self-consistency is the following:

$$G_\sigma(k) = \left[G_{0\sigma}(k)^{-1} - \Sigma_\sigma(k)\right]^{-1} \tag{2.104}$$

$$\Sigma_\sigma(k) = -\int \frac{d\boldsymbol{Q}}{(2\pi)^3}\frac{1}{\beta}\sum_\nu \Gamma(Q)G^{(c)}_{\bar\sigma}(Q-k) \tag{2.105}$$

$$\Gamma(Q) = -\left[\frac{m}{4\pi a_F} + R_{pp}(Q)\right]^{-1} \tag{2.106}$$

$$R_{pp}(Q) = \int \frac{d\boldsymbol{k}}{(2\pi)^3}\left[\frac{1}{\beta}\sum_{\omega_n} G^{(a)}_\downarrow(k+Q)G^{(b)}_\uparrow(-k) - \frac{m}{\boldsymbol{k}^2}\right]. \tag{2.107}$$

These equations are represented in diagrammatic form in Figure 2.6. The single-particle propagators $G^{(a)}$, $G^{(b)}$ and $G^{(c)}$ can be either a dressed propagator G or a bare propagator G_0, and every possible combination of G and G_0 gives a different t-matrix approach. In the following, we will use the shorthand notation $(G^{(a)}G^{(b)})G^{(c)}$ to identify a specific t-matrix approach, where the propagators $G^{(a)}$ and $G^{(b)}$ within the parentheses correspond

to the ones entering the particle-particle bubble (2.107), while the external propagator $G^{(c)}$ enters the self-energy (2.105). The five different schemes considered in this thesis are reported in Table 2.1 with the corresponding references in the literature.[4]

$(G^{(a)}G^{(b)})G^{(c)}$	Reference
$(G_0G_0)G_0$	Ref. [31]
$(G_0G_0)G$	Ref. [60]
$(GG_0)G_0$	Ref. [28]
$(GG)G_0$	Ref. [65]
$(GG)G$	Refs. [26, 27]

Table 2.1: Shorthand notations for the t-matrix approaches with various degrees of self-consistency considered within this thesis and corresponding references in the literature.

With the inclusion of (partial or full) self-consistency, all the considerations done for the non-self-consistent t-matrix in Section 2.2.5 still apply: the chemical potentials μ_σ can be found by inverting the density equations (2.80)

$$n_\sigma = \int \frac{d\boldsymbol{k}}{(2\pi)^3} \frac{1}{\beta} \sum_n e^{i\omega_n \eta} G_\sigma(\boldsymbol{k}, \omega_n), \tag{2.108}$$

and the critical temperature for the superfluid transition T_c can be found by generalizing the Thouless criterion of equation (2.81) to the dressed particle-particle propagator Γ:

$$\left[\Gamma(\boldsymbol{Q} = 0, \Omega_\nu = 0)|_{T=T_c}\right]^{-1} = 0. \tag{2.109}$$

In this generalization, note that the $(GG)G_0$ and $(GG)G$ approaches automatically include the mean-field shift Σ_0 in the weak-coupling limit of the particle-particle bubble (2.93), so these approaches correctly recover the BCS critical temperature (2.95) in this limit without any spurious prefactor (cf. Section 3.1.1).

Let us turn now to introduce the numerical methods used to solve the self-consistent equations (2.104-2.107). As soon as we add any degree of self-consistency, the Green's function G of equation (2.104) becomes a functional of itself. In order to calculate it, the simplest method is to solve the equations iteratively and try to converge to a stable solution. In this work, we follow the numerical procedure originally developed by Haussmann in Refs. [27, 47]. This procedure makes use of the Fourier transforms from the $(\boldsymbol{k}, \omega_n)$ and $(\boldsymbol{Q}, \Omega_\nu)$ spaces to the $(\boldsymbol{r}, \tau)$ space, given by the expressions

$$G(\boldsymbol{r}, \tau) = \int \frac{d\boldsymbol{k}}{(2\pi)^3} \frac{1}{\beta} \sum_n e^{i(\boldsymbol{k}\cdot\boldsymbol{r} - \omega_n \tau)} G(\boldsymbol{k}, \omega_n) \tag{2.110}$$

$$\Gamma(\boldsymbol{r}, \tau) = \int \frac{d\boldsymbol{Q}}{(2\pi)^3} \frac{1}{\beta} \sum_\nu e^{i(\boldsymbol{Q}\cdot\boldsymbol{r} - \Omega_\nu \tau)} \Gamma(\boldsymbol{Q}, \Omega_\nu), \tag{2.111}$$

[4] Note that the $(GG_0)G_0$ and $(GG)G_0$ approaches have been often implemented in the literature with an additional "pseudo-gap approximation" on top of the t-matrix approximation [28, 29, 65]. For a comparison of the calculation with and without this additional approximation, see Appendix C.

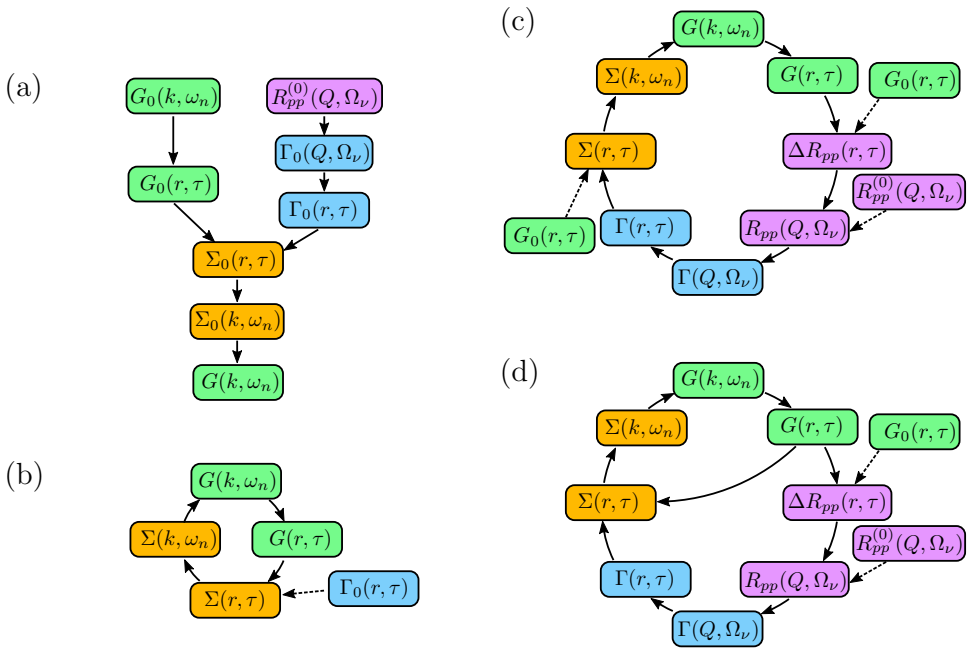

Figure 2.7: Flowchart for the routes toward self-consistency of the various t-matrix approaches: (a) non-self-consistent $(G_0G_0)G_0$; (b) extended t-matrix $(G_0G_0)G$; (c) partially self-consistent $(GG_0)G_0$ and $(GG)G_0$; (d) fully self-consistent $(GG)G$.

and analogous expressions for $\Sigma(\boldsymbol{k},\omega_n)$ and $R_{pp}(\boldsymbol{Q},\Omega_\nu)$. These transformations allow us to simplify the calculation of the convolution products (2.105) and (2.107) by writing them as simple products in the transformed space:

$$\Sigma(\boldsymbol{r},\tau) = -\Gamma(\boldsymbol{r},\tau)G^{(c)}(-\boldsymbol{r},-\tau) \tag{2.112}$$

$$R_{pp}(\boldsymbol{r},\tau) = G^{(a)}(\boldsymbol{r},\tau)G^{(b)}(\boldsymbol{r},\tau) - \Lambda\delta(\boldsymbol{r})\delta(\tau), \tag{2.113}$$

where $\Lambda = \int_{|\boldsymbol{k}|<k_0} d\boldsymbol{k}/(2\pi)^3 m/\boldsymbol{k}^2$ is a constant that diverges together with the cutoff $k_0 \to \infty$ of the separable potential introduced in Section 2.2.3. To avoid dealing directly with this diverging constant, in $(\boldsymbol{r},\tau)$ space we will always work in terms of the difference

$$\Delta R_{pp}(\boldsymbol{r},\tau) = R_{pp}(\boldsymbol{r},\tau) - R^0_{pp}(\boldsymbol{r},\tau) = G^{(a)}(\boldsymbol{r},\tau)G^{(b)}(\boldsymbol{r},\tau) - [G_0(\boldsymbol{r},\tau)]^2, \tag{2.114}$$

where $R^0_{pp}(\boldsymbol{r},\tau)$ is the Fourier transform of the renormalized particle-particle bubble built with G_0's of equation (2.74).

The flowchart shown in Fig. 2.7 summarizes schematically the self-consistent iterative procedures for all the approaches presented in Table 2.1. Although the non-self-consistent $(G_0G_0)G_0$ approach does not require any self-consistent cycling, we have reported its flowchart in Fig. 2.7(a), since its calculation is always used as input for all the other self-consistent approaches. Fig. 2.7(b) shows instead the flowchart for the $(G_0G_0)G$ approach (called "extended t-matrix" in Ref. [60]), for which the self-consistency is performed

only at the level of the self-energy (2.105) and the particle-particle propagator remains the non-self-consistent Γ_0 built with bare G_0. Finally, we show the flowcharts for the partially self-consistent approaches $(GG_0)G_0$ and $(GG)G_0$ (Fig. 2.7(c)) and for the fully self-consistent approach $(GG)G$ (Fig. 2.7(d)), where the self-consistent cycle involves also the particle-particle propagator Γ. Note that in these last two flowcharts the renormalized particle-particle bubble $R_{pp}(\boldsymbol{Q}, \Omega_\nu)$ is obtained by Fourier transforming the difference $\Delta R_{pp}(\boldsymbol{r}, \tau)$ defined in (2.114) and then adding the non-self-consistent $R^0_{pp}(\boldsymbol{Q}, \Omega_\nu)$.

Most of the functions that are Fourier transformed in the self-consistent cycles represented in Fig. 2.7 present a slowly decaying tail in the variables $(\boldsymbol{k}, \omega_n)$ and $(\boldsymbol{Q}, \Omega_\nu)$, to which a singular behavior for $(\boldsymbol{r}, \tau) \to 0^+$ corresponds. For this reason, the Fourier transforms (2.110) and (2.111) should be performed on a logarithmic scale, following the prescription of Refs. [27, 47]. Moreover, it is also necessary to subtract some appropriate semi-analytic expressions from the functions to be Fourier transformed in order to make their slow decay faster or, alternatively, their singular behavior weaker. These expressions must have also a semi-analytic representation in the transformed space, so that they can be added back to the functions after the Fourier transform. A detailed account of the semi-analytic expressions used in our numerical calculations is given in Appendix A. In Appendix B, instead, we discuss the optimization procedures that were found necessary to achieve the convergence toward self-consistency within the $(GG_0)G_0$, $(GG)G_0$ and $(GG)G$ t-matrix approaches, especially in the region close to T_c where the straightforward iterative procedures of Fig. 2.7 do not work properly.

The reason to consider and compare all these different approaches with different degrees of self-consistency is that the inclusion of self-consistency does not necessarily improve the results with respect to the experimental data. Nevertheless, there are some general properties that only the the fully self-consistent $(GG)G$ approach is guaranteed to respect. For this reason, in the next section we will focus only on this approach, showing which are the advantages that it brings with respect to the other partial or non-self-consistent approaches.

2.4 Conserving approximations

When one makes a certain approximation for the self-energy Σ, like the t-matrix approximation, it is important to check if the approximation still respects some general theorems that are valid for the exact theory. In particular, one could wish to check if the approximated theory respects the conservation laws for the number of particles, the momentum and the energy when an external perturbation U is added and the linear response of the system to that perturbation is investigated. If these conservation laws are built into the structure of the approximation used, the theory is said to be *conserving*. In 1961–1962, Baym and Kadanoff developed a general method for generating conserving approximations [112, 113]. Without going into the details of the derivation, we are going to state here their result.

Theorem 1 (Conserving approximations)**.** A *sufficient* condition for an approximated theory to be *conserving* is that its self-energy Σ can be written as the functional derivative

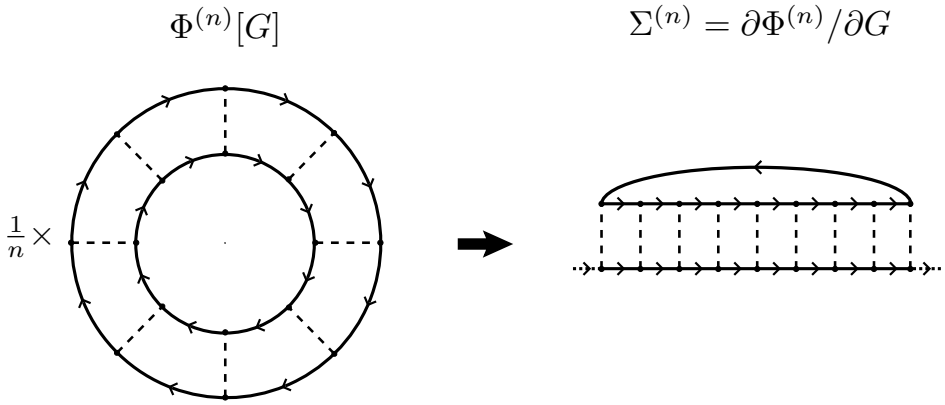

Figure 2.8: Diagrammatic representation of the n-th order diagram for the functional $\Phi[G]$ and the corresponding self-energy within the self-consistent t-matrix approximation.

of a functional Φ with respect to the single-particle Green's function G

$$\Sigma(1,1') = \frac{\delta\Phi}{\delta G(1,1')} \tag{2.115}$$

where Φ is a functional of *only* dressed single-particle Green's functions G and interaction lines V. Here, we used the shorthand notation for the variables $1 = (\boldsymbol{r}_1, \tau_1, \sigma_1)$ and $1' = (\boldsymbol{r}'_1, \tau'_1, \sigma'_1)$.

Among all the approaches considered in Table 2.1, only the fully self-consistent $(GG)G$ approach respects this requirement, as it is the only one that can be derived by a functional Φ that is not built also with bare Green's functions G_0. The n-th order contribution of the functional Φ for this approach is represented on the left side of Fig. 2.8 in terms of Feynman diagrams. The functional derivative (2.115) simply consists in plucking away one of the particle lines in the diagrams, leading to the self-energy diagrams of the self-consistent t-matrix approximation (its n-th order is represented on the right side of Fig. 2.8).

Having a conserving approximation is particularly useful when treating non-equilibrium phenomena like transport, but it has also some important implications on the equilibrium properties of the theory. As in this thesis we are mostly dealing with equilibrium properties, we will give some insight on this aspect.

In the Green's function formalism, the grand potential Ω (or, equivalently, the grand canonical partition function $\mathcal{Z}$) can be calculated in terms of the Green's function G by means of the linked cluster expansion [108]. This calculation consists in replacing the two-body interaction V with λV, where $\lambda \in [0,1]$ is a numerical coupling constant, and integrate the expectation value of the interaction energy on λ

$$\Omega[G] - \Omega_0 = -\frac{1}{\beta}\big[\ln(\mathcal{Z}[G]) - \ln(\mathcal{Z}_0)\big] = \int_0^1 \frac{d\lambda}{\lambda}\,\langle \lambda V\rangle\,, \tag{2.116}$$

where $\Omega_0 = \ln(\mathcal{Z}_0)$ is the grand potential of the free system and $\langle \lambda V \rangle$ can be calculated in terms of the the single-particle Green's function as [108]

$$\langle \lambda V \rangle = \mp \frac{1}{2} \int d\boldsymbol{x} \lim_{\boldsymbol{x}' \to \boldsymbol{x}} \lim_{\tau' \to \tau^+} \sum_\sigma \left[-\frac{\partial}{\partial \tau} + \frac{\nabla^2_{\boldsymbol{x}}}{2m} - \mu \right] G_{\sigma,\lambda}(\boldsymbol{x}, \tau, \boldsymbol{x}', \tau'). \tag{2.117}$$

In a Φ-derivable conserving approximation, the linked cluster expansion (2.116) can written in terms of the functional Φ as

$$\Omega[G] = -\frac{1}{\beta} \ln(\mathcal{Z}[G]) = \mp \frac{1}{\beta} \big(\Phi[G] - \mathrm{Tr}[G\Sigma] + \mathrm{Tr}[\ln(-G)] \big) \tag{2.118}$$

where with the symbol of trace we mean integration over all the $\boldsymbol{r}$ and τ variables and sum over all the spin indices. For example, the second term is:

$$\mathrm{Tr}[G\Sigma] = \int d\boldsymbol{r}\, d\boldsymbol{r}' \int_0^\beta d\tau\, d\tau' \sum_\sigma G_\sigma(\boldsymbol{r}, \tau, \boldsymbol{r}', \tau') \Sigma_\sigma(\boldsymbol{r}, \tau, \boldsymbol{r}', \tau'). \tag{2.119}$$

The good property of conserving approximations is that the thermodynamic quantities derived by the grand canonical potential (2.118) or directly by the Green's function of the system are the same, so that one have a consistent picture of thermodynamic properties. As a concrete example, let us consider the average total number of particles $\langle \hat{N} \rangle$. This can be calculated directly from the single-particle Green's function (see Eq. (2.16))

$$\langle \hat{N} \rangle = \mp \int d\boldsymbol{x} \lim_{\tau' \to \tau^+} \sum_\sigma G_\sigma(\boldsymbol{x}, \tau, \boldsymbol{x}, \tau'). \tag{2.120}$$

but it can also be derived by the grand potential Ω as

$$\langle \hat{N} \rangle = \frac{\partial \Omega}{\partial \mu}. \tag{2.121}$$

Only if the approximation is conserving the two calculations (2.120) and (2.121) are guaranteed to give the same result. The same happens for the expectation values of all the other thermodynamic quantities, like the energy E or the pressure P. On the contrary, we do not expect the other non-self-consistent or partially self-consistent approaches to satisfy these thermodynamic relations, and in those cases we must always specify in which way we are calculating the various thermodynamic quantities.

In addition, it was shown in Ref. [107] that the fully self-consistent t-matrix approximation $(GG)G$ is bound to satisfy an important theorem for an imbalanced interacting Fermi gas at zero temperature in the normal phase: the *Luttinger theorem* [106]. The statement of the theorem in this case is the following:

Theorem 2 (Luttinger Theorem)**.** For an interacting normal Fermi system at $T = 0$, the volume enclosed by the Fermi surface of the species σ is equal to the volume enclosed by the Fermi surface of the same species σ for the non-interacting system at $T = 0$ with the same number of fermions N_σ in that species.

In the isotropic case (where the Fermi surface is a sphere), this theorem means that the discontinuity in the momentum distribution $n_\sigma(\boldsymbol{k})$ of the interacting system happens at $|\boldsymbol{k}| = k_{F,\sigma}$ where $k_{F,\sigma} = (6\pi^2 n_\sigma)^{1/3}$ is the Fermi wave vector for the species σ.

2.5 Tan's contact

An important physical quantity that characterizes a Fermi gas with short-range interaction is the *contact* C [114–117]. Physically, this quantity describes how two-body physics merges with the surrounding many-body problem, and it can be related to many thermodynamic and dynamical properties. A way to define it is to look at the short-distance behavior of the opposite-spin correlation function (check Chapter 5 for details)

$$g_{\uparrow\downarrow}(\boldsymbol{\rho}) = \left\langle \hat{\psi}_\uparrow^\dagger\left(\frac{\boldsymbol{\rho}}{2}\right)\hat{\psi}_\downarrow^\dagger\left(-\frac{\boldsymbol{\rho}}{2}\right)\hat{\psi}_\downarrow\left(-\frac{\boldsymbol{\rho}}{2}\right)\hat{\psi}_\uparrow\left(\frac{\boldsymbol{\rho}}{2}\right)\right\rangle - n_\uparrow n_\downarrow. \tag{2.122}$$

that is given by (cf. Section 5.2)

$$g_{\uparrow\downarrow}(\boldsymbol{\rho}) \xrightarrow[\rho\to 0]{} \frac{C}{(4\pi)^2}\left(\frac{1}{\rho^2} - \frac{2}{a_F\rho} + \cdots\right), \tag{2.123}$$

where $\rho = |\boldsymbol{\rho}|$. In this sense, the contact C is related to the probability of finding two opposite spin fermions at short distances. In fact, if we consider a small sphere of radius $\delta\rho$ centered on a particle, the probability for unit volume to find a particle with opposite spin inside the sphere is given by:

$$P(|\boldsymbol{\rho}| < \delta\rho)/V_{\delta\rho} = \int_{|\boldsymbol{\rho}|<\delta\rho} d\boldsymbol{\rho}\, g_{\uparrow\downarrow}(\boldsymbol{\rho}) \simeq \frac{C}{4\pi}\delta\rho, \tag{2.124}$$

where $V_{\delta\rho} = 4\pi(\delta\rho)^3/3$ is the volume of the sphere and we have assumed that $\delta\rho$ is much smaller than the scattering length a_F and all the other relevant lengths in the system (such as $n^{-1/3}$ and $\lambda_T = \sqrt{2\pi/(mk_BT)}$). Note that, as the probability $P(|\boldsymbol{\rho}| < \delta\rho)$ must be dimensionless, this relation defines the units of the contact as the inverse of a length to the fourth power.

The contact C also appears in the large-$\boldsymbol{k}$ tail of the momentum distributions $n_\sigma(\boldsymbol{k})$ [114]

$$n_\sigma(\boldsymbol{k}) \xrightarrow[|\boldsymbol{k}|\to\infty]{} \frac{C}{\boldsymbol{k}^4}, \tag{2.125}$$

and in the high-frequency tail of the of the radio-frequency (rf) spectrum $I_{\rm rf}(\omega)$ [53]

$$I_{\rm rf}(\omega) \xrightarrow[\omega\to\infty]{} \frac{C}{2^{1/2}\pi^2}\left(\frac{E_F}{\omega}\right)^{3/2}. \tag{2.126}$$

where the normalization $\int_{-\infty}^{+\infty} I_{\rm rf}(\omega)d(\omega/E_F) = 1$ has been used (see Section 3.2.4).

Moreover, the contact C enters several thermodynamic relations. For example, the total internal energy for unit volume E/V and the pressure P can be written in terms of the contact [114, 115]:

$$\frac{E}{V} = \frac{C}{4\pi a_F m} + \int \frac{d\boldsymbol{k}}{(2\pi)^3}\frac{\boldsymbol{k}^2}{2m}\left(n_\sigma(\boldsymbol{k}) - \frac{C}{k^4}\right) \tag{2.127}$$

$$P = \frac{2}{3}\frac{E}{V} + \frac{C}{12\pi a_F m}. \tag{2.128}$$

In addition, one can show that the contact is related to the derivative with respect to the inverse of the scattering length a_F^{-1} of internal energy E (at constant entropy) and of the free energy F (at constant temperature) through the *adiabatic relations* [115]:

$$\left(\frac{\partial E}{\partial a_F^{-1}}\right)_S = -\frac{CV}{4\pi m} \tag{2.129}$$

$$\left(\frac{\partial F}{\partial a_F^{-1}}\right)_T = -\frac{CV}{4\pi m}. \tag{2.130}$$

The thermodynamic relations (2.127) and (2.128) and the adiabatic relations (2.129) and (2.130) are guaranteed to be verified only by conserving approximations (as defined in Section 2.4). In our case, this applies only to the fully self-consistent $(GG)G$ approach.[5] For the other non-conserving t-matrix approaches, one has to specify an operative definition for the contact, because in principle the previous relations can be violated. In these cases, we assumed that the contact is defined by the large-$\boldsymbol{k}$ behavior of the momentum distribution as in (2.125).[6]

The most straightforward way to obtain this contact within the t-matrix formalism is to relate it to the trace Δ_∞^2 of the particle-particle propagator Γ:

$$C = (m\Delta_\infty)^2 = m^2 \int \frac{d\boldsymbol{Q}}{(2\pi)^3} \frac{1}{\beta} \sum_\nu e^{i\Omega_\nu \eta}\, \Gamma(\boldsymbol{Q}, \Omega_\nu). \tag{2.131}$$

The relation (2.131) was first demonstrated for the non-self-consistent $(G_0G_0)G_0$ approach in Ref. [53], and then generalized to the fully self-consistent $(GG)G$ approach in Ref. [93]. A sketch of the proof for the $(G_0G_0)G_0$ approach is the following. For large $\boldsymbol{k}$, the approximation performed in the integrand of Eq. (2.88) holds up for any coupling, and one obtains

$$n_\sigma(\boldsymbol{k}) \xrightarrow[\boldsymbol{k}\to+\infty]{} -\Delta_\infty^2 \frac{1}{\beta} \sum_n G_0(k)^2 G_0(-k). \tag{2.132}$$

If one now performs the sum over the fermionic Matsubara frequencies ω_n of the right hand side, for large $\boldsymbol{k}$ one obtains:

$$\frac{1}{\beta} \sum_n [G_0(k)]^2 G_0(-k) \simeq -\frac{1}{4\xi_{\boldsymbol{k}}^2} \simeq -\frac{m^2}{\boldsymbol{k}^4}. \tag{2.133}$$

Direct comparison of (2.132) with (2.125) yields the relation:

$$C = (m\Delta_\infty)^2 = m^2 \int \frac{d\boldsymbol{Q}}{(2\pi)^3} \frac{1}{\beta} \sum_\nu e^{i\Omega_\nu \eta}\, \Gamma_0(\boldsymbol{Q}, \Omega_\nu), \tag{2.134}$$

which corresponds to (2.131) within the $(G_0G_0)G_0$ approach.

[5] A full numerical verification of the thermodynamic relation (2.127) by the fully self-consistent $(GG)G$ approach across the temperature-coupling phase diagram was reported in Frank's PhD thesis [118].

[6] It is possible to show that, even within non-conserving t-matrix approaches, the contact obtained by the tail of the momentum distribution (2.125) still coincides with the one obtained by the short-range behavior of the pair correlation function (2.123) (cf. Section 5.2).

2.6 Two-particle Green's function formalism

While the single-particle Green's function G contains much information on the system, it does miss two-body observables like the pair correlation function (2.122), that are instead embodied in the *two-particle Green's function* G_2. To introduce its formalism, it is first convenient to adopt the Nambu representation of the fermionic fields operators

$$\hat{\Psi}(\boldsymbol{r},\tau) = \begin{pmatrix} \hat{\psi}_\uparrow(\boldsymbol{r},\tau) \\ \hat{\psi}^\dagger_\downarrow(\boldsymbol{r},\tau) \end{pmatrix}, \tag{2.135}$$

in terms of which the diagrammatic approach for the superfluid phase below T_c is usually formulated [119]. The reason for this choice of representation is that, to develop a consistent picture for the two-particle Green's function within the t-matrix approach, it is important to consider an extra term in the self-energy that is present only in the theory of the superfluid phase, but which contributes (via the functional differentiation discussed below) to the two-particle Green's function even in the normal phase.

In terms of Nambu representation (2.135), the single-particle Green's function (2.3) is

$$G(1,2) = -\langle T_\tau[\hat{\Psi}(1)\hat{\Psi}^\dagger(2)]\rangle \tag{2.136}$$

and the two-particle Green's function is

$$G_2(1,2;1',2') = \langle T_\tau[\hat{\Psi}(1)\hat{\Psi}(2)\hat{\Psi}^\dagger(2')\hat{\Psi}^\dagger(1')]\rangle\,, \tag{2.137}$$

with the shorthand notation $1 = (\boldsymbol{r}_1, \tau_1, \ell_1)$ and so on, where the Nambu index $\ell = (1,2)$ refers to the upper or lower component in the expression (2.135). Often, it is useful to work in terms of the two-particle correlation function, which is defined in terms of G_2 as

$$L(1,2;1',2') = G_2(1,2;1',2') - G(1,1')G(2,2') \tag{2.138}$$

and satisfies the Bethe-Salpeter equation [113, 120, 121]:

$$L(1,2;1',2') = -G(1,2')G(2,1') + \int d3456\, G(1,3)G(6,1')\Xi(3,5;6,4)L(4,2;5,2') \tag{2.139}$$

where the notation $\int d1$ implies an integral over $(\boldsymbol{r}_1, \tau_1)$ and a sum over ℓ_1, and the kernel

$$\Xi(1,2;1',2') = \frac{\delta\Sigma(1,1')}{\delta G(2',2)} \tag{2.140}$$

is obtained by a functional differentiation of the self-energy $\Sigma(1,1')$. Equation (2.139) can be formally solved in terms of the many-particle T-matrix, defined as the solution to the equation [113, 120, 121]

$$T(1,2;1',2') = \Xi(1,2;1',2') + \int d3456\, \Xi(1,4;1',3)G(3,6)G(5,4)T(6,2;5,2'), \tag{2.141}$$

by writing

$$\begin{aligned} L(1,2;1',2') &= -G(1,2')G(2,1') \\ &\quad - \int d3456\, G(1,3)G(6,1')T(3,5;6,4)G(4,2')G(2,5). \end{aligned} \tag{2.142}$$

These equations hold quite generally, regardless of the approximation on the self-energy Σ that specifies the kernel Ξ defined in Eq. (2.140).

At the level of the BCS approximation, the self-energy for a Fermi gas with contact interactions is given by:

$$\begin{aligned} \Sigma^{\rm BCS}(1,1') &= -V(1,1')G(1,1') \\ &= -\sum_{\ell_2,\ell_{2'}} \tau^3_{\ell_1\ell_2} V(x_1 - x_{1'}) \tau^3_{\ell_{1'}\ell_{2'}} G_{\ell_2,\ell_{2'}}(x_1, x_{1'})(1 - \delta_{\ell_1\ell_{1'}}), \end{aligned} \tag{2.143}$$

where we used the notation $x_1 = (\boldsymbol{r}_1, \tau_1)$, the contact interaction potential is $V(x_1 - x_{1'}) = v_0 \delta(\boldsymbol{r}_1 - \boldsymbol{r}'_1)\delta(\tau_1^+ - \tau_{1'})$, and τ^3 is the third Pauli matrix

$$\tau^3 = \begin{pmatrix} 1 & 0 \\ 0 & -1 \end{pmatrix}, \tag{2.144}$$

which, in Nambu formalism, is associated with each vertex that connects an interaction line V to a particle line G [119]. Note also that in expression (2.143) only the off-diagonal $(1 - \delta_{\ell_1\ell_{1'}})$ terms have been retained, as they are the only ones that survive in the regularization (2.60) of the contact potential [36].

Given the BCS approximation of the self-energy (2.143), the corresponding kernel Ξ is

$$\begin{aligned} \Xi^{\rm BCS}(1,2;1',2') &= \frac{\delta \Sigma^{\rm BCS}(1,1')}{\delta G(2',2)} \\ &= -\tau^3_{\ell_1\ell_{2'}} \delta(x_1 - x_2) V(x_1 - x_{1'}) \delta(x_{1'} - x_{2'}) \tau^3_{\ell_{1'}\ell_2} (1 - \delta_{\ell_1\ell_{1'}}). \end{aligned} \tag{2.145}$$

Note that the kernel $\Xi^{\rm BCS}(1,2;1',2')$ is different from zero only for $\ell_1 = \ell_{2'}$, $\ell_{1'} = \ell_2$ and $\ell_1 \neq \ell_{1'}$. When this kernel is inserted in the self-consistent equation (2.141) for the T-matrix, it also imposes a rule on the Nambu indices of $T(1,2;1',2')$. Using the notation $T^{\ell_1\ell_{2'}}_{\ell_{1'}\ell_2}$, one obtains that the four surviving elements of T are $T^{11}_{22} \equiv T_{11}$, $T^{22}_{11} \equiv T_{22}$, $T^{21}_{12} \equiv T_{21}$ and $T^{12}_{21} \equiv T_{12}$.

Let us now consider the specific case of a Fermi gas in the normal phase above T_c. In this case, the calculation is highly simplified because the single-particle Green's functions are diagonal in the Nambu indices:

$$G_{\ell_1\ell_2}(x_1, x_2) = \delta_{\ell_1\ell_2} G_{\ell_1}(x_1, x_2). \tag{2.146}$$

As a consequence, the off-diagonal terms T_{12} and T_{21} of the T-matrix are zero, because at all orders in the expansion of Eq. (2.141) at least one off-diagonal Green's function

G_{12} or G_{21} appears in them. For this reason, above T_c the only non-zero elements of the T-matrix in the BCS approximation are T_{11} and T_{22}.

Let us now consider a fully self-consistent t-matrix self-energy like (2.105) with $G^{(a,b,c)} = G$, that in Nambu representation reads

$$\Sigma^{t\text{-matrix}}(1,1') = -\int d22'\,\Gamma(2,1';1,2)G(2,2') \tag{2.147}$$

with

$$\begin{aligned}\Gamma(1,2;1',2') = &- V(1,1')\delta(1-2')\delta(1'-2)\\ &- V(1,1')\int d34\,G(3,1)G(4,1')\Gamma(3,2;4,2').\end{aligned} \tag{2.148}$$

One can wonder how the T-matrix equation (2.141) changes when this self-energy is added to the BCS self-energy (2.143). The answer is that, for a generic choice of the Nambu indices $(\ell_1, \ell_2, \ell_{1'}, \ell_{2'})$, the self-energy (2.147) can produce some additional terms to the kernel $\Xi(1,2;1',2')$ (namely, the Aslamazov-Larkin and Maki-Thomson contributions [34]). However, the only combination of Nambu indices that we will need in Chapters 5 and 6 for the calculation of the pair correlation function and the pairing fraction in the normal phase is $(\ell_1 = 1, \ell_2 = 2, \ell_{2'} = 2, \ell_{1'} = 1)$, or the equivalent combination with $1 \leftrightarrow 2$. For this specific combination, one can show that the contribution of the t-matrix self-energy (2.147) to the kernel Ξ is zero (see Appendix D for the details of the proof). For this reason, the kernel Ξ derived from the total self-energy

$$\begin{aligned}\Sigma(1,1') &= \Sigma^{\text{t-matrix}}(1,1') + \Sigma^{\text{BCS}}(1,1')\\ &= -\int 22'\,\Gamma(2,1';1,2)G(2,2') - V(1,1')G(1,1')\end{aligned} \tag{2.149}$$

is still given by the kernel in the BCS approximation (2.145).

Moreover, the BCS self-energy Σ^{BCS}, whose functional derivative has served to obtain the kernel Ξ^{BCS} of (2.145), vanishes identically in the normal phase, because it includes an off-diagonal single-particle Green's function G_{12}. For this reason, the calculation of the thermodynamics at the level of the single-particle Green's function $G(1,1')$ for the self-energy (2.149) is completely equivalent to the calculation within the fully self-consistent t-matrix approach described in Section 2.3.

It can be shown that the total self-energy (2.149) can still be derived by a functional Φ as in (2.115), given by the sum of the self-consistent t-matrix functional (see Fig. 2.8) plus a BCS functional Φ^{BCS} [113]. The self-energy (2.149) is then a conserving approximation in the sense of Theorem 1 of Section 2.4.

As a final consideration, in this approximation the kernel (2.145) is essentially an interaction line V. For this reason, the approximated equation (2.141) for the T-matrix strongly resemble the equation (2.148) for the particle-particle propagator Γ. Indeed, apart from a sign (coming from $G_{11}(x_2,x_1) = -G_{22}(x_1,x_2)$), it can be shown that at this level of the approximation the diagonal elements of T can be identified with the particle-particle propagator Γ, so that $T_{11} = T_{22} = -\Gamma$ [121].

Chapter 3

Numerical results for t-matrix approaches with different degrees of self-consistency

In this chapter, we are going to report and compare the numerical results obtained within all five the t-matrix approaches of Table 2.1, for both thermodynamic and dynamical quantities (for details on the numerical procedures, see Appendices A and B). The system considered is a homogeneous Fermi gas with balanced spin populations ($n_\uparrow = n_\downarrow$). Most of the results of this chapter have been presented in Ref. [75].

3.1 Thermodynamics

Several thermodynamic properties can be obtained in terms of the temperature Green's function G and the particle-particle propagator Γ. In the following, we are going to present the results for the critical temperature T_c, the chemical potential μ, the scattering length a_B of the residual interaction between the composite bosons in the strong-coupling limit, and the contact C. For many quantities, a comparison with Quantum Monte Carlo (QMC), Diagrammatic Monte Carlo (DMC) and experimental (exp) data is provided. When possible, our data have been checked against the results obtained within the same t-matrix approaches already in the literature [27, 31, 47, 51, 74], finding excellent agreement and supporting the validity of our numerical calculation.

3.1.1 Critical temperature

One of the most important thermodynamic quantities is the critical temperature for the superfluid transition T_c, which can be obtained from the Thouless criterion (2.109). The results for the critical temperature are shown in Figure 3.1 as a function of the coupling $(k_F a_F)^{-1}$ for all five t-matrix approaches considered, together with data from QMC [80] and DMC [91] calculations, and the experimental value at unitarity of Ref. [122].

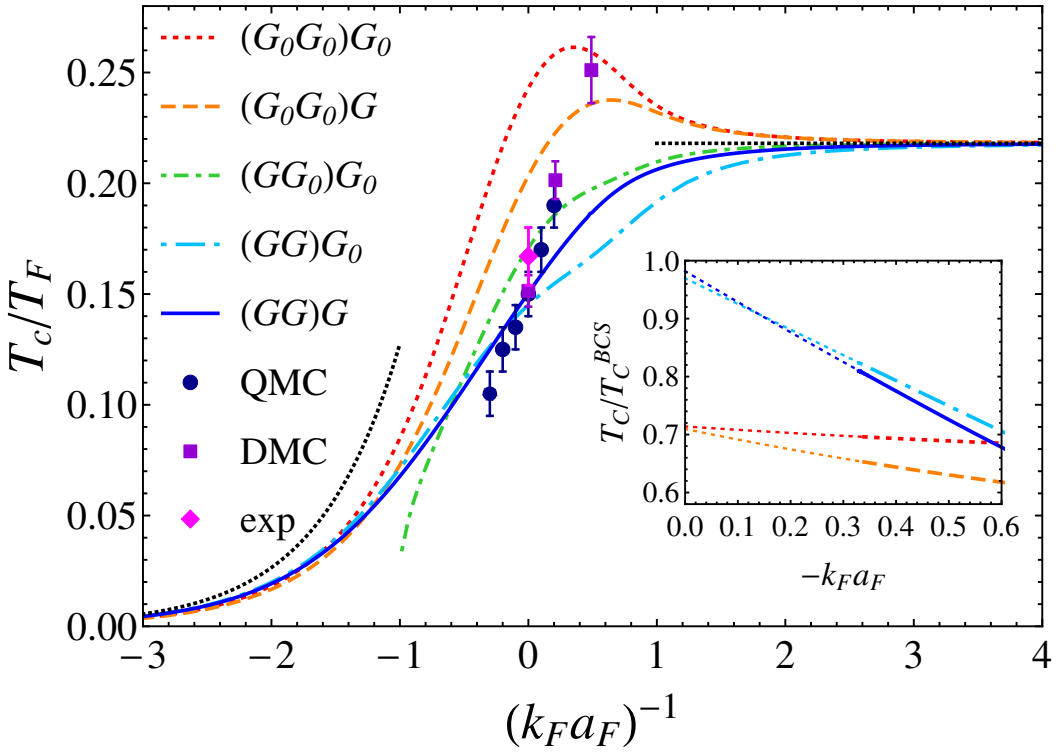

Figure 3.1: Critical temperature T_c (in units of the Fermi temperature T_F) as a function of the coupling $(k_Fa_F)^{-1}$ within alternative t-matrix approaches. The black dotted line corresponds to the BCS critical temperature (3.1) for $(k_Fa_F)^{-1} < -1$ and to the critical temperature for non-interacting composite bosons (3.2) for $(k_Fa_F)^{-1} > 1$. Quantum Monte Carlo (QMC; from Ref. [80] - circles), Diagrammatic Monte Carlo (DMC; from Ref. [91] - squares) and experimental (exp; from Ref. [122] - diamond) data are also shown for comparison. The inset shows the extrapolation of the ratio $T_c/T_c^{\rm BCS}$ in the weak-coupling limit $(k_Fa_F)^{-1} \ll -1$. Here, thick lines correspond to numerical data and thin dotted lines correspond to parabolic fits of the data that extrapolate T_c in the weak-coupling limit.

All the approaches are seen to correctly interpolate between the BCS and BEC critical temperatures (indicated with black dotted lines in Fig. 3.1) with the notable exception of the $(GG_0)G_0$ approach, which fails to reach the BCS limit since its critical temperature drops abruptly to zero at $(k_F a_F)^{-1} \simeq -1$. This failure is to be attributed to the asymmetric treatment of the two Green's function $G^{(a)}$ and $G^{(b)}$ in the particle-particle bubble $R_{pp}(Q)$ of equation (2.107), which generates and artificial imbalance between the two spin components that acts to suppress the critical temperature of the superfluid transition.[1] It is for this reason that, in the following, the results for the $(GG_0)G_0$ approach will not be reported in the BCS limit.

In the crossover region, it is apparent that even a partial dressing of the particle-particle bubble (2.107) acts to suppress the maximum in the T_c curve, that is present instead around $(k_F a_F)^{-1} \simeq 0.5$ for the $(G_0G_0)G_0$ and $(G_0G_0)G$ approaches. The DMC data seems to support the existence of a maximum, however better insight from experiments and QMC calculations would be needed to understand the entity of this maximum.

Regarding the value of T_c at the unitary limit $(k_F a_F)^{-1} = 0$, the $(GG)G$ and $(GG)G_0$ approaches are the ones that are closer to the QMC and DMC values of $T_c/T_F = 0.15(1)$ and $T_c/T_F = 0.151(7)$, and to the experimental value of $T_c/T_F = 0.167(13)$ (in this analysis, the $(GG_0)G_0$ approach has not been considered because of its pathological behavior in the BCS limit).

The T_c curve in the vicinity of $(k_F a_F)^{-1} = 0$, however, appears quite steeper for the QMC and DMC data with respect to the $(GG)G$ and $(GG)G_0$ calculation. In this regard, a recent work by Pisani [70] addresses the questions of the slope and the maximum of the T_c curve by inserting Gorkov-Melik-Barkhudarov (GMB) [126] and Popov corrections on top of the non-self-consistent $(G_0G_0)G_0$ approach. This GMB+Popov approach obtains a better agreement with the critical temperature of the QMC and DMC calculations, at the cost, however, of a worse agreement on the chemical potential μ across the crossover.

The behavior of T_c in the BCS (weak-coupling) limit $(k_F a_F)^{-1} \ll -1$ is shown in the inset of Figure 3.1 for the various approaches. There, one sees that the $(GG)G_0$ and $(GG)G$ approaches, within an error of the order of 1%[2], correctly recover the BCS critical temperature (2.95)

$$T_c^{\mathrm{BCS}} = \frac{8e^{\gamma}T_F}{\pi e^2} \exp\Big(\frac{\pi}{2k_F a_F}\Big), \tag{3.1}$$

while the $(G_0G_0)G$ and $(G_0G_0)G_0$ approaches recover it only with a spurious prefactor

[1] In the weak-coupling limit of the $(GG_0)G_0$ approach, only one of the Green's functions in $R_{pp}(Q)$ self-consistently includes the mean-field shift $\Sigma_0 = 2\pi a_F n_0/m$ of equation (2.97), while the other does not. This can be interpreted as an artificial imbalance $\delta\mu = \Sigma_0$ of the chemical potentials for the spin-up and spin-down species. As in the weak-coupling limit the BCS gap Δ_0 at $T = 0$ becomes exponentially small in $(k_F a_F)$, while $\delta\mu = \Sigma_0$ is linear in $(k_F a_F)$, there must be a coupling where $\delta\mu \gtrsim \Delta_0$, and this condition is enough to suppress superfluidity [123–125]. The reason why this problematic feature has passed unnoticed in the literature is that the $(GG_0)G_0$ approach was often associated with the pseudogap approximation for the self-energy $\Sigma(k) \simeq \Delta_{pg} G_0(-k)$, which improperly removes the mean-field shift Σ_0 in the weak-coupling limit (for more details, see Appendix C).

[2] The error is of the order of 1% only in the extreme BCS regime, where the discontinuity of $G(\boldsymbol{k}, \tau)$ at $|\boldsymbol{k}| \simeq k_F$ generates large oscillations in $\boldsymbol{r}$-space that are difficult to integrate. In the crossover and BEC regimes, the error is much smaller (of the order of 10^{-4}).

$e^{-1/3} \simeq 0.717$ because they do not self-consistently include the mean-field shift Σ_0 in the Green's functions within the particle-particle bubble (2.107) (cf. Section 2.2.7).

In the BEC (strong-coupling) limit $(k_F a_F)^{-1} \gg 1$, at the leading order all the approaches recover the condensation temperature for non-interacting composite bosons (2.91):

$$T_c^{\mathrm{BEC}} = \frac{2\pi}{\zeta(3/2)^{2/3}} \frac{n_B^{2/3}}{2m} \simeq 0.218 T_F. \tag{3.2}$$

However, the various t-matrix approaches differ in the way this value is reached. Specifically, at the subleading order T_c^{BEC} is approached with the expression

$$\frac{T_c - T_c^{\mathrm{BEC}}}{T_c^{\mathrm{BEC}}} = \frac{\alpha}{3\pi} (k_F a_F)^3, \tag{3.3}$$

where the coefficient α differs among the various approaches. In Table 3.1, the extrapolated values for α are reported together with their theoretical expected value. The theoretical values for the $(GG_0)G_0$ and $(GG)G$ approaches are taken from Refs. [26, 40], while the theoretical values for $(G_0G_0)G_0$ and $(G_0G_0)G$ approaches have been calculated independently (the corresponding analytic calculations are not reported here owing to their complexity). Note that even a partial dressing of the particle-particle bubble (2.107) is sufficient to change the sign of α from positive to negative.

$(G^{(a)}G^{(b)})G^{(c)}$	α(th)	α(extr)
$(G_0G_0)G_0$	1	1.02
$(G_0G_0)G$	1.07	1.12
$(GG_0)G_0$	-0.5	-0.48
$(GG)G_0$	na	-2.00
$(GG)G$	-1	-1.02

Table 3.1: Values of the coefficient α of Eq. (3.3) obtained within the various t-matrix approaches, both from analytic calculations (th) and extrapolation of numerical results (extr). One analytic value is not available (na).

As a final note, it is evident that all the approaches fail to recover the correct strong-coupling correction to T_c due to the repulsive interaction between the composite bosons, which should be linear in $(k_F a_F)$ and positive [127]. To include a linear correction, vertex corrections at the level of the particle-particle propagator Γ would be needed [30].

3.1.2 Chemical potential

Let us now consider the chemical potential μ, which is obtained by inverting the density equation (2.108). In Fig. 3.2 the chemical potential μ_c calculated at the critical temperature T_c is shown as a function of the coupling $(k_F a_F)^{-1}$ for all the t-matrix approaches, together with QMC data from Ref. [80] and experimental data from Ref. [122].

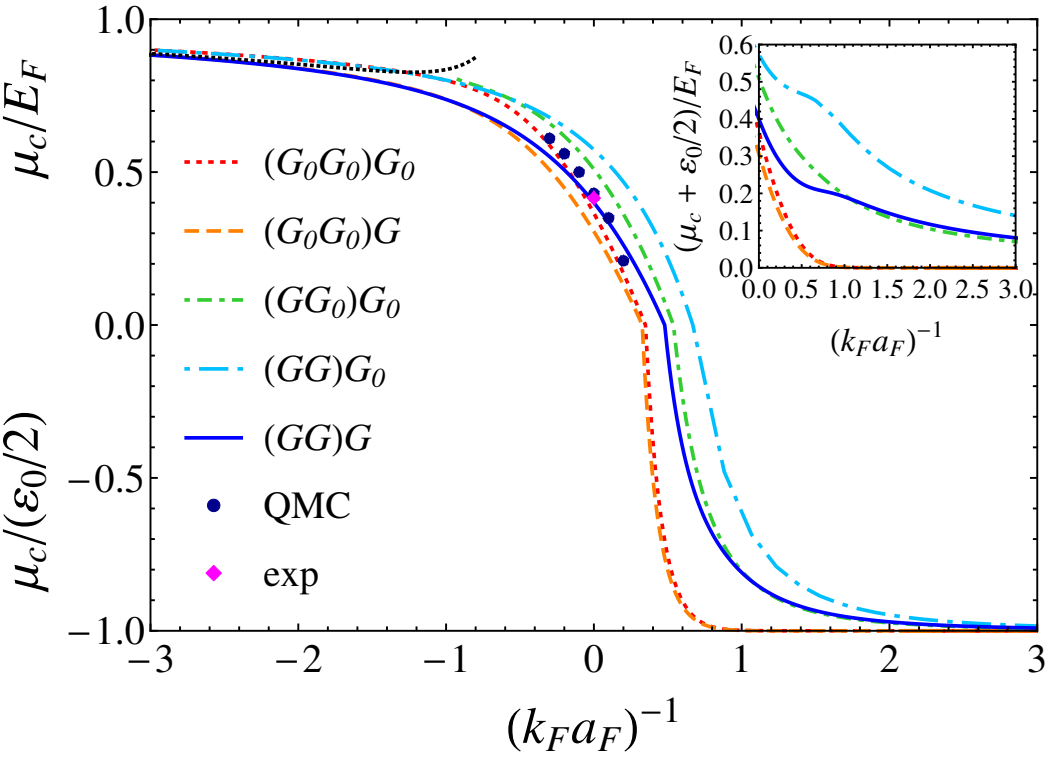

Figure 3.2: Chemical potential μ_c at T_c (in units of the Fermi energy E_F when $\mu_c > 0$ and of half the binding energy $\varepsilon_0 = (ma_F^2)^{-1}$ of composite bosons when $\mu_c < 0$) as a function of $(k_F a_F)^{-1}$ within alternative t-matrix approaches. The black dotted line in weak-coupling corresponds to the Galitskii's result (3.4). Quantum Monte Carlo (QMC; from Ref. [80]- circles) and experimental (exp; from Ref. [122] - diamond) data are also shown for comparison. In the inset, $\mu_c + \varepsilon_0/2$ (in units of the Fermi energy E_F) is reported in order to amplify the subleading behavior of the chemical potential in the strong-coupling limit $(k_F a_F)^{-1} \gg 1$.

At the unitary limit $(k_F a_F)^{-1} = 0$, the fully self-consistent $(GG)G$ approach, with $\mu_c/E_F = 0.400$, is the one that better agrees with the QMC value $\mu_c/E_F = 0.43(1)$ and the experimental value $\mu_c/E_F = 0.415$.

In the weak-coupling limit $(k_F a_F)^{-1} \ll -1$, all the approaches (except for the pathological $(GG_0)G_0$) recover the linear correction in $(k_F a_F)$ to μ_c of equation (2.102). However, only the $(G_0G_0)G$ and $(GG)G$ approaches (which dress the external Green's function $G^{(c)}$) recover also the quadratic correction in $(k_F a_F)$ obtained analytically by Galitskii in Ref. [103]:

$$\frac{\mu^{\text{Gal}}}{E_F} = 1 + \frac{4}{3\pi}(k_F a_F) + \frac{4}{15\pi^2}\big[11 - 2\ln 2\big](k_F a_F)^2. \tag{3.4}$$

In the strong-coupling limit $(k_F a_F)^{-1} \gg 1$, instead, all the approaches recover the leading order $\mu_c \simeq -\varepsilon_0/2 = -(2ma_F^2)^{-1}$ (cf. Section 2.2.6). However, the subleading behavior varies significantly among the approaches. This is shown in the inset of Fig. 3.2, where the leading behavior $-\varepsilon_0/2$ has been subtracted to μ_c, so that the subleading term $\delta\mu = \mu_B/2 = \mu_c + \varepsilon_0/2$ can be directly observed (μ_B being the chemical potential of the composite bosons). This correction vanishes linearly in $(k_F a_F)$ for the $(GG_0)G_0$, $(GG)G_0$ and $(GG)G$ approaches which (partially or fully) dress the particle-particle propagator Γ, while it vanishes exponentially for the $(G_0G_0)G_0$ and $(G_0G_0)G$ approaches which use a bare particle-particle propagator Γ_0. This happens because the residual repulsive interaction between the composite bosons is included in the theory only by dressing the particle-particle propagator Γ. This residual interaction will be treated more in detail in Section 3.1.3.

In Fig. 3.3 the chemical potential μ is reported as a function of the temperature T for the three characteristic couplings $(k_F a_F)^{-1} = (-0.5, 0.0, 0.5)$ and for all the t-matrix approaches. At low temperature, all the curves terminate at the respective critical temperature T_c. Note that the curves of $\mu(T)$ for the $(G_0G_0)G_0$ and $(G_0G_0)G$ approaches shows a maximum at a temperature $T > T_c$ for the couplings $(k_F a_F)^{-1} = 0$ and 0.5, while the other approaches do not.

In panel (b) of Fig. 3.3 (corresponding to the coupling $(k_F a_F)^{-1} = 0$), QMC data from Ref. [85] and experimental data from Ref. [122] are also shown for comparison. Here, we see that the agreement of the fully self-consistent $(GG)G$ approach with these data remains valid also for temperatures $T > T_c$.

3.1.3 Scattering length of composite bosons

The scattering length a_B of the repulsive interaction between the composite bosons can be determined from the chemical potential μ_c at the critical temperature T_c in the strong-coupling limit $(k_F a_F)^{-1} \gg 1$. This is done by comparing the chemical potential of the composite bosons $\mu_B = 2\mu_c + \varepsilon_0$ (cf. Section 2.2.6) with the chemical potential $\mu_B^0 = 8\pi a_B n_B/m_B$ of a dilute gas of bosons of mass m_B and density n_B at T_c. Knowing that for the composite bosons $m_B = 2m$ and $n_B = n/2$, the comparison yields

$$\frac{a_B}{a_F} = \lim_{k_F a_F \to 0^+} \frac{3\pi}{4(k_F a_F)} \frac{\mu_B}{E_F}. \tag{3.5}$$

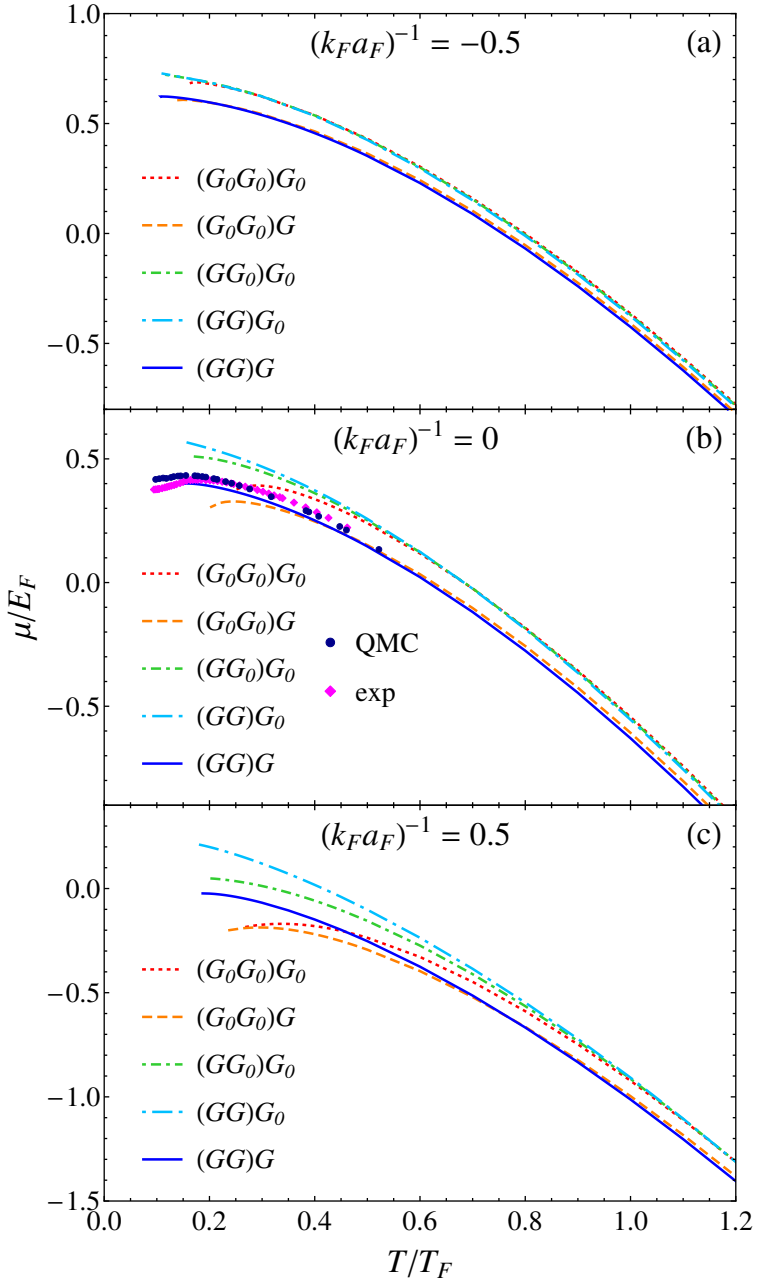

Figure 3.3: Chemical potential μ (in units of the Fermi energy E_F) as a function of the temperature T (in units of the Fermi temperature T_F) for the couplings $(k_F a_F)^{-1} = (-0.5, 0.0, 0.5)$ within alternative t-matrix approaches. Comparison with QMC data from Ref. [85] (circles) and experimental data from Ref. [122] (diamonds) is also shown for the coupling $(k_F a_F)^{-1} = 0$ in panel (b).

This limit is actually non-zero only for the approaches $(GG_0)G_0$, $(GG)G_0$ and $(GG)G$ that (partially or fully) dress the particle-particle propagator Γ.

In Fig. 3.4(a) we show the extrapolation of the expression (3.5) in the $(k_F a_F) \to 0^+$ limit for these three approaches. Note that the fully self-consistent $(GG)G$ approach recovers the value $a_B/a_F = 1.16$, in contrast with the value $a_B/a_F = 2$ predicted in Ref. [26]. We argue that it is our value $a_B/a_F = 1.16$ to be correct. In fact, the numerical values for a_B can be compared with the analytical calculation of a_B in the various approaches, performed by expressing the dressed particle-particle propagator Γ as a series of diagrams in terms of the bare Γ_0 and G_0, and retaining only the leading contributions in the strong-coupling limit $\beta|\mu| \gg 1$ [30].

For the $(GG_0)G_0$ and $(GG)G_0$ approaches, the only diagram that contributes to a_B is the one on the left of Fig. 3.4(b) (for the $(GG)G_0$ approach also its symmetric version that dress the lower propagator contributes). Comparison of the analytical evaluation of this diagram in the strong-coupling limit [27, 30] with the leading self-energy correction for a dilute Bose gas $\Sigma_B = 8\pi a_B n_B/m_B$ yields the value $a_B/a_F = 1$ for the $(GG_0)G_0$ approach and the value $a_B/a_F = 2$ for the$(GG)G_0$ approach, in agreement with the extrapolated values of Fig. 3.4(a).

For the $(GG)G$ approach, instead, the right diagram of Fig. 3.4(b) also contributes to a_B at the leading order (together with its symmetrized version). This diagram, which had apparently escaped the analysis of Ref. [27], yields a correction of $-2\times 0.421 a_F = -0.842 a_F$ to the scattering length a_B, so that the final value for the bosonic scattering length is $a_B/a_F = 2 - 0.842 = 1.158$, in excellent agreement with what was obtained from the extrapolation of the numerical data. The analytical estimate of the right diagram of Fig. 3.4 can be performed by noticing that in the strong-coupling limit the calculation coincides with the one of the GMB diagram analyzed in Ref. [70]. However, it should be remarked that the correspondence of these two diagrams holds in the BEC limit only. In fact, in the BCS limit the self-consistent t-matrix approximation fails to recover the $e^{-1/4}$ reduction factor to T_c due to the GMB correction [70].

As a final note, the values of a_B/a_F obtained with the extrapolation of Figure 3.4 should be compared with the exact result $a_B/a_F \simeq 0.60$ obtained either by a numerical solution of the four-body Schrödinger equation in Ref. [128] or by a full diagrammatic treatment in the zero-density limit in Ref. [42]. In this regard, the $(GG)G$ and $(GG_0)G_0$ approaches are the ones that get closer to this result with $a_B/a_F = 1.16$ and $a_B/a_F = 1$, respectively. Note, however, that the result for the $(GG_0)G_0$ is somewhat artificial, as it is due to an incomplete symmetrization of the bosonic interaction vertex.

3.1.4 Tan's contact

The contact C, introduced in Section 2.5, can be obtained directly from the particle-particle propagator Γ using equation (2.131). For internal consistency, we verified that the contact calculated in this way coincides with the coefficient of the $\boldsymbol{k}^{-4}$ tail of the momentum distribution per spin component $n_\sigma(\boldsymbol{k})$ (see equation 2.125). In Figure 3.5, the contact C_c calculated at the critical temperature T_c is shown as a function of the coupling $(k_F a_F)^{-1}$ for all the t-matrix approaches.

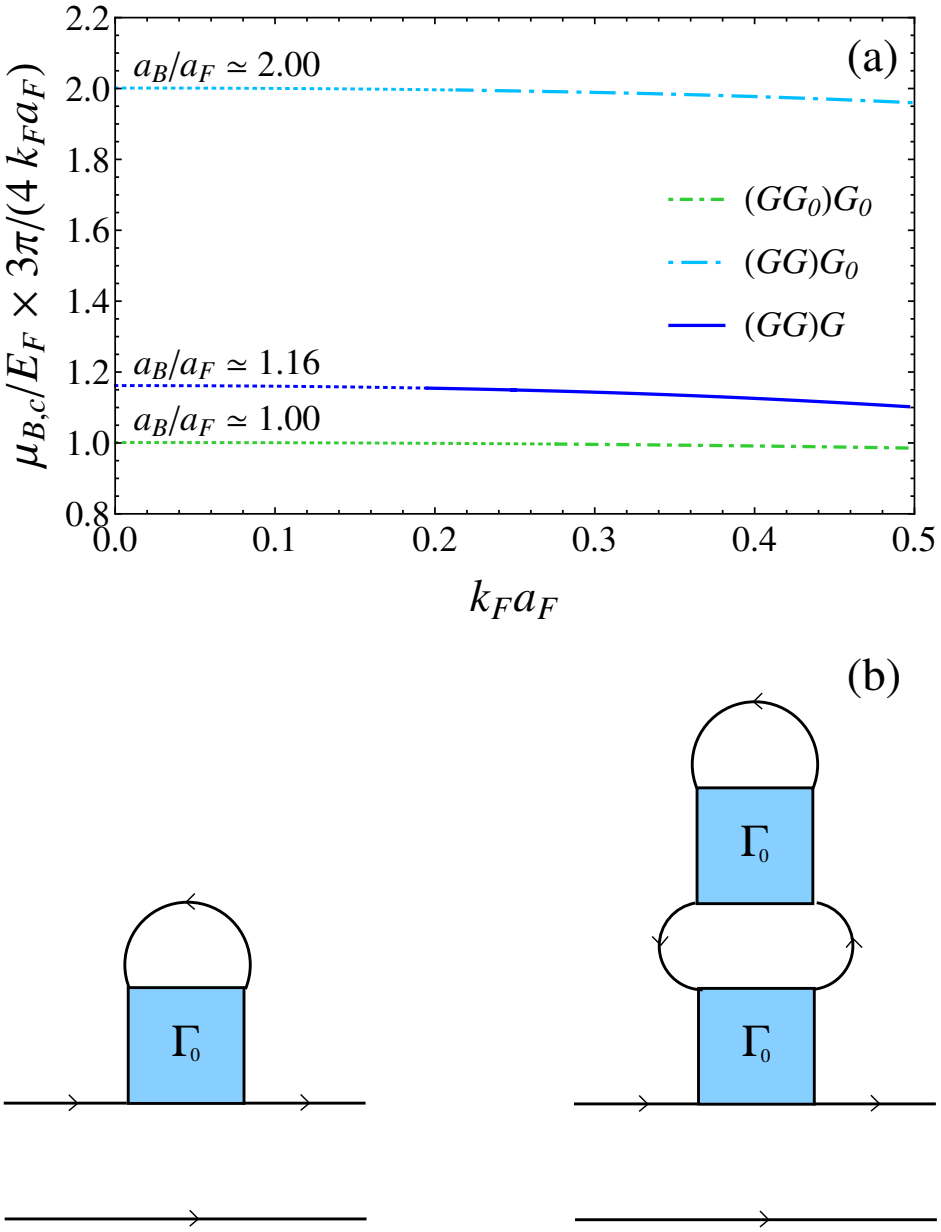

Figure 3.4: (a) Extrapolation of the ratio a_B/a_F defined in (3.5) for the $(GG_0)G_0$, $(GG)G_0$ and $(GG)G$ approaches. The thick lines are the actual numerical data, the thin dotted lines are parabolic extrapolations to the $(k_F a_F) \to 0^+$ limit. (b) Diagrams that contribute to the bosonic scattering length a_B within the $(GG)G$ approach. Thin lines in the diagrams correspond to the bare propagator G_0.

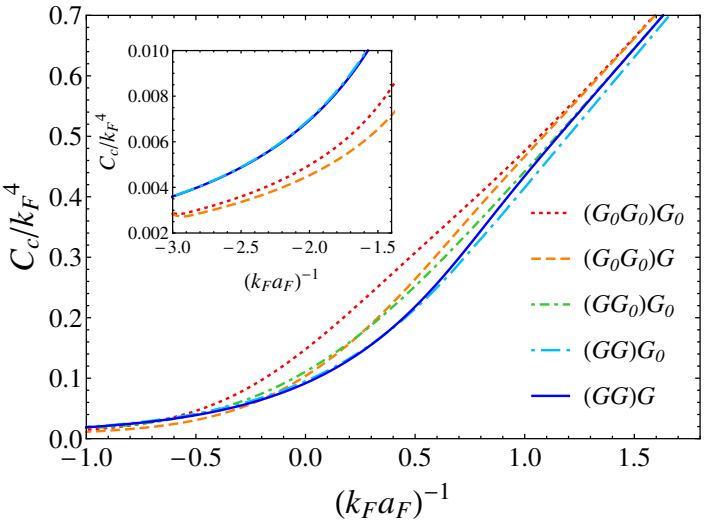

Figure 3.5: Contact C_c (in units of k_F^4) at the critical temperature T_c as a function of the coupling $(k_F a_F)^{-1}$ within alternative t-matrix approaches. The black dotted line represents the leading order of the contact in the strong-coupling limit (3.9). In the inset, a zoom on the weak-coupling region is shown. Here, the black dotted line corresponds to the Galitskii result (3.7).

In the weak-coupling limit $(k_F a_F)^{-1} \ll -1$, the contact C_c at $T_c \to 0$ can be obtained analytically by considering Galitskii's expansion in powers of $(k_F a_F)$ of the energy density at $T = 0$ [103]

$$\frac{E^{\mathrm{Gal}}}{V} = nE_F\left[\frac{3}{5} + \frac{2}{3\pi}(k_F a_F) + \frac{4}{35\pi^2}(11 - 2\ln 2)(k_F a_F)^2\right], \tag{3.6}$$

and use the adiabatic relation (2.129) to obtain

$$\frac{C_c^{\mathrm{Gal}}}{k_F^4} = \frac{4(k_F a_F)^2}{9\pi^2}\left[1 + \frac{12}{35\pi}(11 - 2\ln 2)(k_F a_F)\right]. \tag{3.7}$$

This expression is recovered at the leading order by the $(G_0G_0)G_0$, $(G_0G_0)G$ and $(GG_0)G_0$ approaches, and up to the subleading order by the $(GG)G_0$ and $(GG)G$ approaches.

In the strong-coupling limit $(k_F a_F)^{-1} \gg 1$, instead, the energy density of the system is given at the leading order by the total binding energy of the composite pairs:

$$\frac{E^{\mathrm{BEC}}}{V} = -n\frac{\varepsilon_0}{2} = -\frac{1}{3\pi^2}\frac{k_F}{a_F^2}E_F. \tag{3.8}$$

By using the adiabatic relation (2.129), one obtains the leading order expression for the contact in the strong-coupling limit

$$\frac{C_c^{\mathrm{BEC}}}{k_F^4} = \frac{4}{3\pi(k_F a_F)} \tag{3.9}$$

which is recovered by all the approaches.

3.1.5 Summary of the thermodynamic results

While the results for the thermodynamic properties can be extracted directly from the figures of previous section, it might be useful to summarize in a table the numerical values of the critical temperature T_c, the chemical potential μ_c and the contact C_c at T_c obtained within the various t-matrix approaches, so that the differences among the results can be most readily appreciated. Accordingly, in Table 3.2 the values for these quantities are reported for five couplings in the interval $-1 \leq (k_F a_F)^{-1} \leq 1$ and for all the t-matrix approaches considered.

$(k_F a_F)^{-1}$	T_c/T_F	μ_c/E_F	C_c/k_F^4
	0.08495	0.7997	0.01462
	0.07294	0.7381	0.01139
-1.0	na	na	na
	0.07132	0.8006	0.01930
	0.06776	0.7375	0.01874
	0.1649	0.6846	0.04595
	0.1358	0.6018	0.03076
-0.5	0.1132	0.7230	0.03999
	0.1112	0.7269	0.04099
	0.1077	0.6226	0.03892
	0.2429	0.3655	0.1479
	0.2034	0.3059	0.1036
0.0	0.1709	0.5096	0.1108
	0.1451	0.5734	0.09513
	0.1505	0.4000	0.09170
	0.2588	-0.1890	0.3075
	0.2361	-0.2005	0.2638
0.5	0.1975	0.04935	0.2522
	0.1674	0.2176	0.2148
	0.1870	-0.02339	0.2182
	0.2351	-0.9986	0.4759
	0.2320	-0.9987	0.4666
1.0	0.2097	-0.8042	0.4418
	0.1918	-0.6250	0.4150
	0.2062	-0.8092	0.4342

Table 3.2: Numerical values of the critical temperature T_c, chemical potential μ_c, and contact C_c at T_c are reported for five characteristic couplings and for all the t-matrix approaches. A few numerical values are not available (na) for the reasons discussed in the text. For each coupling, reference to different t-matrix approaches follows the conventions (from top to bottom) of Table 2.1.

As far as which approach gives better results for thermodynamic properties, it is evident that the fully self-consistent $G(GG)$ approach has some clear advantages, as:

1. It reproduces quite well the QMC, DMC and experimental values for the critical temperature T_c and for the chemical potential μ at the unitary limit $(k_F a_F)^{-1} = 0$.

2. In the weak-coupling limit $(k_F a_F)^{-1} \ll -1$, it correctly recovers the BCS critical temperature and Galitskii's expansions of the chemical potential μ_c and the contact C_c up to the subleading order.

3. In the strong-coupling limit $(k_F a_F)^{-1} \gg 1$, like the other t-matrix approaches, it recovers the leading order value for the critical temperature T_c, the chemical potential μ_c and the contact C_c. Moreover, it at least includes a repulsive interaction between the composite bosons, albeit with scattering length $a_B/a_F \simeq 1.16$ instead of the exact value $a_B/a_F \simeq 0.60$.

3.2 Dynamics

From the Green's function G, it is possible to extract also spectral quantities, in addition to the thermodynamic properties of the last section. As explained in Section 2.1.4, however, one has to perform an analytical continuation to the function $\bar{G}(\boldsymbol{k}, z)$, starting from its knowledge at the discrete points on the imaginary axis $z = i\omega_n$ where it assumes the values of the temperature Green's function $\bar{G}(\boldsymbol{k}, z = i\omega_n) = G(\boldsymbol{k}, \omega_n)$. To do so, we employed the method of *Padé approximants* [129, 130], that consists in approximating the function $\bar{G}(\boldsymbol{k}, z)$ for any given $\boldsymbol{k}$ as the ratio of two polynomials:

$$\bar{G}(\boldsymbol{k}, z) = \frac{p_1 + p_2 z + \cdots + p_r z^{r-1}}{q_1 + q_2 z + \cdots q_r z^{r-1} + z^r}, \tag{3.10}$$

where the $2r$ real coefficients $\{p_i, q_i; i = 1, \ldots, r\}$ are uniquely determined by the values of $\bar{G}(\boldsymbol{k}, z)$ at $2r$ points on the imaginary axis. This is done by means of a simple recursion algorithm developed by Serene in Ref. [129]. Once the approximate analytical continuation (3.10) has been performed, it is possible to evaluate it just above the real axis to obtain the single-particle spectral function $A(\boldsymbol{k}, \omega)$ as in (2.40):

$$A(\boldsymbol{k}, \omega) = -\frac{1}{\pi} \mathrm{Im}[\bar{G}(\boldsymbol{k}, \omega + i\eta)]. \tag{3.11}$$

In principle, this procedure gives a positive-definite $A(\boldsymbol{k}, \omega)$ that respects the sum rule (2.34). In practice, however, the procedure is quite sensitive to the numerical errors in the input values on the imaginary axis $\bar{G}(\boldsymbol{k}, z = i\omega_n)$, to the extent that sometimes defects appear in the spectral function $A(\boldsymbol{k}, \omega)$, distorting it and even making it acquire negative values. To mitigate this issue, we followed the prescriptions of Ref. [131] and we averaged over multiple analytic continuations (typically 12) performed with different sets of $2r$ (typically 50) points on the imaginary axis, discarding the analytic continuations that yielded $A(\boldsymbol{k}, \omega) < 0$ for some ω's. In addition, even if the analytic continuation is

performed in the Im$z > 0$ plane, we often found it useful to include in the sets of $2r$ points the first few frequencies (from one up to three) on the negative imaginary axis, as also proposed in Ref. [131]. In fact, this allowed us to remove some defects without substantially change the shape of the spectral function.

3.2.1 Single-particle spectral function

In Figure 3.6, the results for the single-particle spectral function $A(\boldsymbol{k}, \omega)$ at the unitary limit $(k_F a_F)^{-1} = 0$ and at the critical temperature T_c are shown for some values of $k = |\boldsymbol{k}|$ and for all the t-matrix approaches considered.

Note that the shape of the spectral function $A(\boldsymbol{k}, \omega)$ appears quite different among the various approaches. The most notable difference is between the approaches that dress the external Green's function $G^{(c)}$ in the self-energy (2.105) and those that do not. In fact, for the $(G_0G_0)G_0$, $(GG_0)G_0$ and $(GG)G_0$ approaches the single-particle spectral function presents a persistent double-peak structure up to at least $k \simeq k_F$, with the two peaks exchanging weight by varying k, while for the $(G_0G_0)G$ and $(GG)G$ approaches a clear evidence of two peaks is present only at small wave-vectors. Note, however, that even for these last two approaches the shape of $A(\boldsymbol{k}, \omega)$ is not consistent with what one would expect from a Fermi liquid [132, 133] (as sometimes claimed instead in the literature [134]) because the single peak broadens around $k \simeq k_F$ with a width of the order of E_F (instead of becoming more narrow).

Concerning the single-vs-double peak debate for the single-particle spectral function at unitarity, the only other evidence that can be found in the literature is a QMC calculation performed by Magierski in Ref. [83, 84]. While the QMC spectral functions reported are quite noisy, they seem to present a double peak structure at least up to $T/T_F \simeq 0.20$ (even if this feature is somewhat dependent on the analytical continuation method used). It seems then that the partial self-consistent approaches that do not dress the external Green's function $G^{(c)}$ work better in reproducing this qualitative feature than the others. Still, a cross-check with other QMC calculations or with momentum resolved experimental spectra would be important to have a clearer picture.

3.2.2 Density of states and pseudogap temperature

To avoid the reference to a specific wave vector $\boldsymbol{k}$, one can integrate the spectral function $A(\boldsymbol{k}, \omega)$ over $\boldsymbol{k}$ to obtain the density of states $N(\omega)$ as shown in equation (2.35).

In Figure 3.7, the density of states at T_c is shown for the three characteristic couplings $(k_F a_F)^{-1} = (-0.5, 0, 0.5)$ and for all the t-matrix approaches. In all cases, a depletion in the density of states appears around $\omega = 0$. This depletion is associated with the existence of a *pseudogap*, i.e. a precursor of the pairing gap Δ of the superfluid phase that develops in the normal phase due to pairing fluctuations (for a review of the pseudo-gap physics within various theoretical approaches, see Ref. [135]). While all the schemes present this pseudogap feature, the details of its structure are still strongly dependent on the specific t-matrix approach.

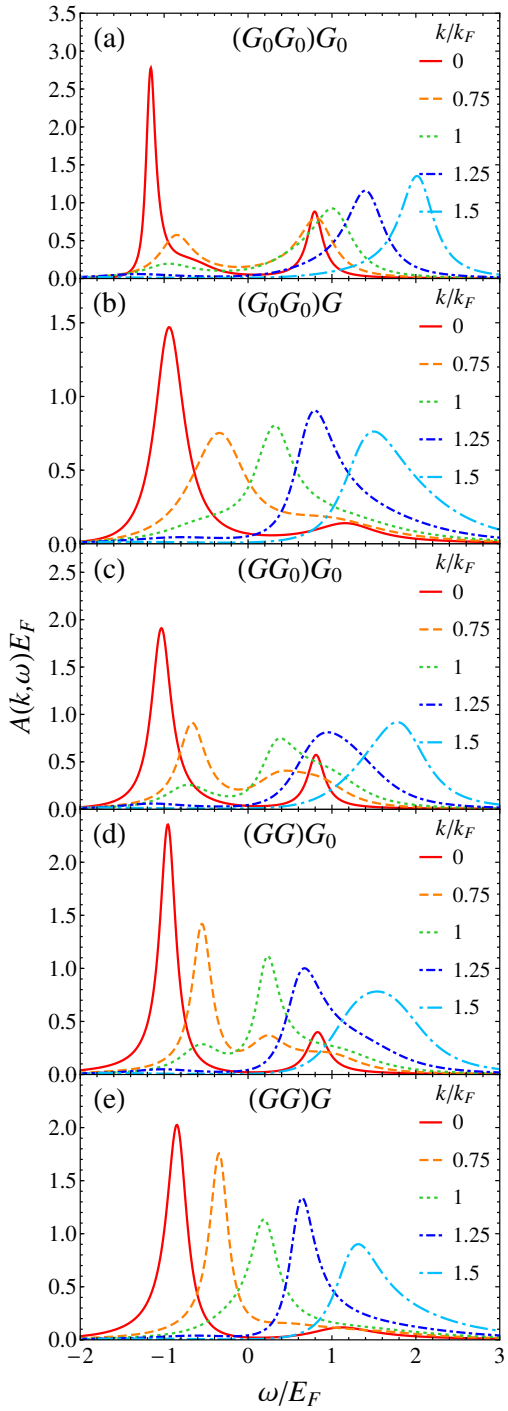

Figure 3.6: Single-particle spectral function $A(\boldsymbol{k},\omega)$ (in units of E_F^{-1}) at $(k_F a_F)^{-1} = 0$ and $T = T_c$ for different values of $k = |\boldsymbol{k}|$ (in units of k_F) within alternative t-matrix approaches.

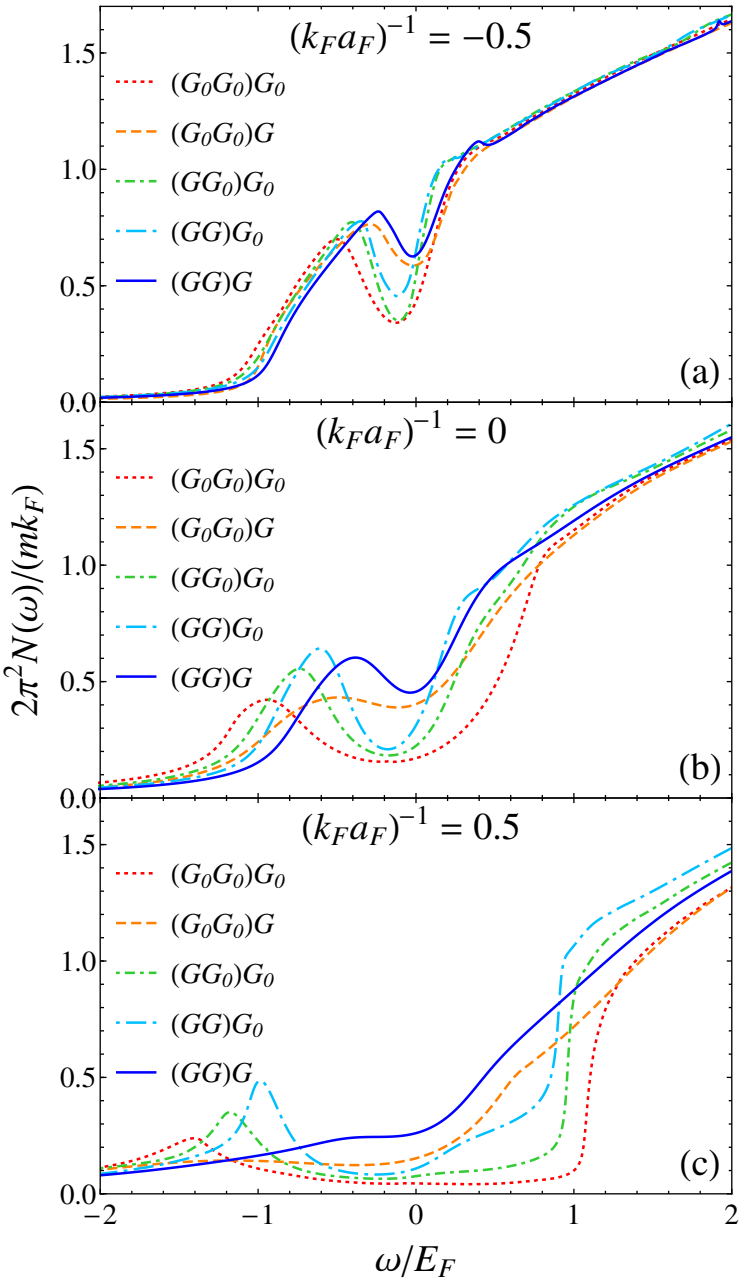

Figure 3.7: Density of states $N(\omega)$ at $T = T_c$ for the coupling values $(k_F a_F)^{-1} = (-0.5, 0.0, 0.5)$ within alternative t-matrix approaches. The non-interacting density of states $N_0 = mk_F/(2\pi^2)$ per spin component at the Fermi level is used to normalize $N(\omega)$.

Let us start by considering the unitary case $(k_F a_F)^{-1} = 0$ represented in Fig. 3.7(b). Analogously to what was observed for the spectral function $A(\boldsymbol{k}, \omega)$, the t-matrix approaches can be divided in two classes: those that dress the external $G^{(c)}$ in the self-energy (2.105), and those that do not. In fact, the $(G_0G_0)G$ and $(GG)G$ approaches overall present a reduced pseudogap feature with respect to the $(G_0G_0)G_0$, $(GG_0)G_0$, and $(GG)G_0$ ones. This is strictly related to the single-peak structure of the $A(\boldsymbol{k}, \omega)$ within the $(G_0G_0)G$ and $(GG)G$ approaches, that partially fills the $\omega \simeq 0$ region in the integration over $\boldsymbol{k}$, as opposed to the double-peak structure of the $(G_0G_0)G_0$, $(GG_0)G_0$, and $(GG)G_0$ approaches that leaves the $\omega \simeq 0$ region less filled.

For the coupling $(k_F a_F)^{-1} = -0.5$ (Fig. 3.7(a)), the depletion around $\omega = 0$ appears only as a small dip in the density of states of the non-interacting system $N_0(\omega) = m^{3/2}\sqrt{2(\omega + \mu)}/(2\pi^2)$. Here, the differences among the schemes are somewhat smaller, even if the $(G_0G_0)G$ and $(GG)G$ approaches still present a reduced pseudogap with respect to the others.

For the coupling $(k_F a_F)^{-1} = 0.5$ (Fig. 3.7(c)), instead, the differences become really important, to the point that the $(G_0G_0)G$ and $(GG)G$ approaches shows almost no evidence of a pseudogap, while the $(G_0G_0)G_0$, $(GG_0)G_0$ and $(GG)G_0$ present a very deep depletion around $\omega = 0$.

For a given fixed coupling, it is also possible to follow the evolution of the density of states $N(\omega)$ with the temperature T above T_c. In Fig. 3.8 this evolution is shown at $(k_F a_F)^{-1} = 0$ for all the t-matrix approaches considered. By increasing the temperature, the depletion in the pseudogap region gets more and more shallow, until the local minimum of $N(\omega)$ around $\omega = 0$ disappears. We define then the pseudogap temperature T^* as the temperature at which this local minimum disappears.[3]

Figure 3.9 shows T^* as a function of the coupling $(k_F a_F)^{-1}$ calculated within all the t-matrix approaches. Similarly to what was observed for the density of states, also the values of T^* differ considerably among the various approaches. In particular, one notices that for the $(G_0G_0)G$ and $(GG)G$ approaches the T^* is strongly suppressed with respect to the other approaches as a consequence of the reduced depletion of the density of states. In addition, for these two approaches there is a coupling region where the temperature T^* cannot be defined above T_c, as the density of states does not present a local minimum around $\omega = 0$ even at $T = T_c$. This occurs around $(k_F a_F)^{-1} \simeq 0.3$ for the $(G_0G_0)G$ approach and around $(k_F a_F)^{-1} \simeq 0.6$ for the $(GG)G$ approach, and the boundaries of these regions are reported as non-connected points of their respective T^* curves in Fig. 3.9. Finally, for all the approaches we observe that T^* begins to increase rapidly at coupling $(k_F a_F)^{-1} \simeq 0.5 - 0.7$. This happens because at this coupling there is a crossover from a pseudogap phase, where the depletion in the density of states is rather shallow and a truly many-body effect, to a normal-Bose-gas phase, where the depletion in the density of states is deep and is just an evidence of the two-body pairing of the composite bosons [67].

[3]Note that the temperature T^* has also been defined in different ways in the literature. For example, in Refs. [83, 84] it was determined by looking directly at the non-integrated spectral function $A(\boldsymbol{k}, \omega)$.

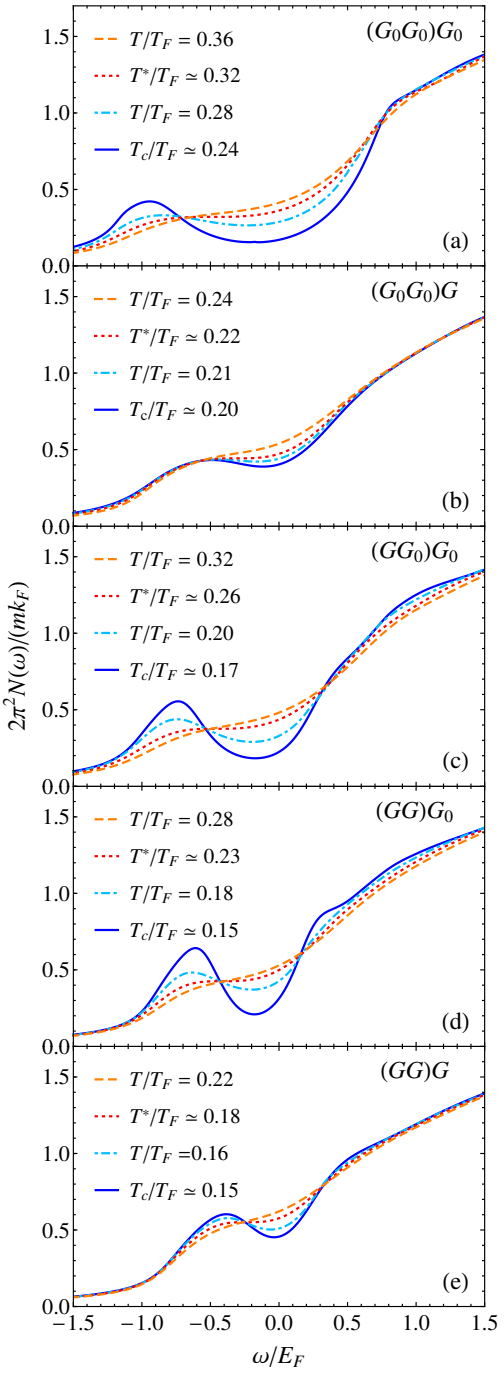

Figure 3.8: Evolution of the density of states $N(\omega)$ at $(k_F a_F)^{-1} = 0$ for temperatures $T \geq T_c$ within alternative t-matrix approaches.

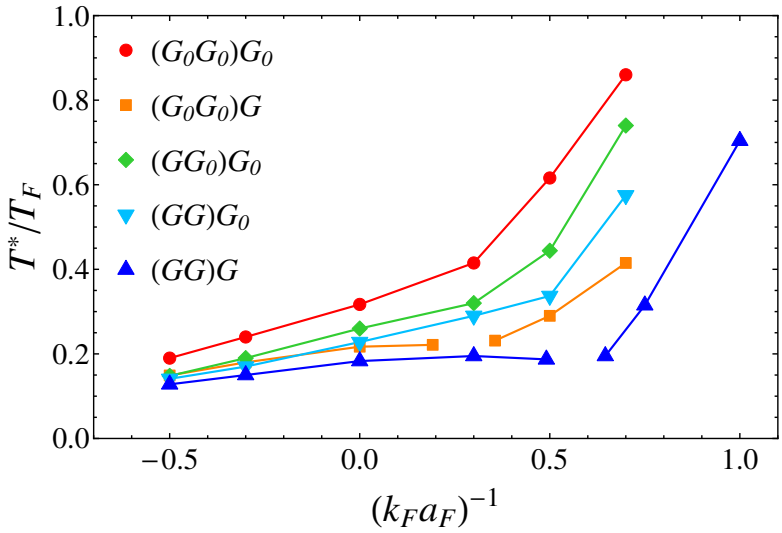

Figure 3.9: Crossover temperature T^* (in units of T_F) for the appearance of a pseudo-gap in the density of states, as a function of $(k_F a_F)^{-1}$ within alternative t-matrix approaches. The non-connected regions that appear for the $(G_0G_0)G$ and $(GG)G$ approaches signal that there a $T^* \geq T_c$ cannot be identified, to the extent that a local minimum near $\omega = 0$ cannot be found in $N(\omega)$ even at $T = T_c$.

3.2.3 Luttinger wave vector

The crossover between the pseudogap and normal-Bose-gas phase can be characterized in terms of the Luttinger wave vector k_L. This wave vector was originally introduced in Ref. [58] within the non-self-consistent $(G_0G_0)G_0$ approach as the wave vector at which the back-bending of the lower branch of the single-particle dispersion $\epsilon(k)$ occurs. In Ref. [58], this dispersion was obtained by following the position of the low-energy peak of the single-particle spectral function $A(\boldsymbol{k}, \omega)$ as a function of $|\boldsymbol{k}| = k$ (cf. panel (a) of Fig. 3.6). The Luttinger wave vector k_L was then obtained by fitting this dispersion with the BCS-like form

$$\frac{\epsilon(k)}{E_F} = \mu' - \sqrt{\left[(k/k_F)^2 - (k_L/k_F)^2\right]^2 + \Delta'^2}, \tag{3.12}$$

where μ' and Δ' and k_L are fitting parameters (the energy shift μ' was needed to account for the dispersion away from the weak-coupling regime).

Physically, a non-vanishing k_L signals the presence of an underlying Fermi surface, which endows the system with a persistent fermionic character even in the presence of strong attractive inter-particle interactions. In these terms, the crossover between the fermionic pseudogap phase and the normal-Bose-gas phase is complete when the Luttinger wave vector k_L becomes zero at some critical coupling, signaling the disappearance of the underlying Fermi surface.

The definition of k_L introduced in Ref. [58] cannot however be applied to the $(G_0G_0)G$

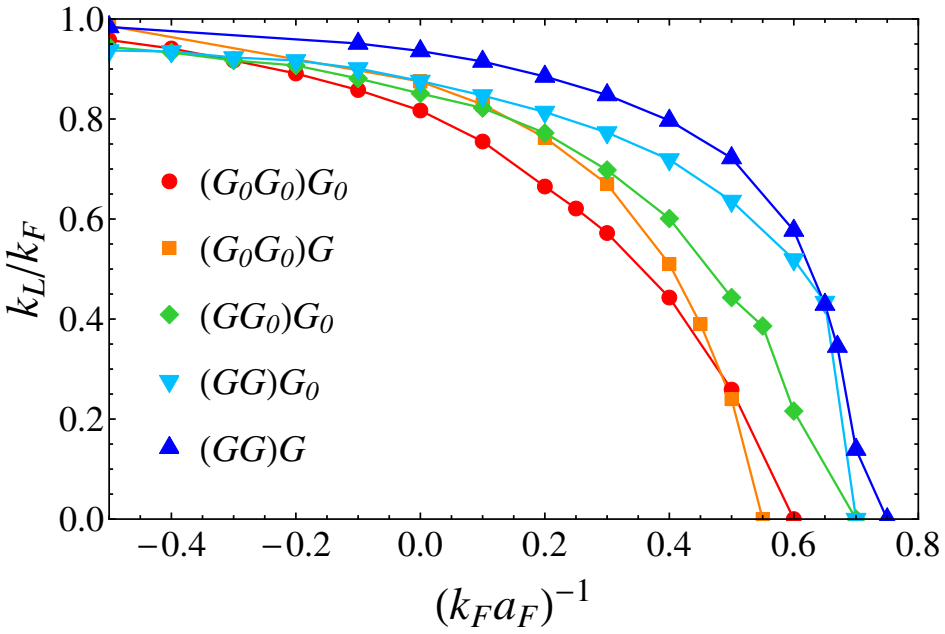

Figure 3.10: Luttinger wave vector k_L (in units of k_F) vs $(k_Fa_F)^{-1}$ obtained at $T = T_c$ within alternative t-matrix approaches (the definition of k_L for the different approaches is given in the text).

and $(GG)G$ approaches, where a lower branch of the dispersion cannot be identified due to the single-peak shape of the spectral functions $A(\boldsymbol{k}, \omega)$ (cf. Fig. 3.6(b) and Fig. 3.6(e)) and the absence of a back-bending in the dispersion for most couplings. As a consequence, for most wave vectors of these approaches we adopted an alternative operative definition of k_L that is closer in spirit to the one that is used for a Fermi liquid, identifying k_L as the wave vector for which the single peak in $A(\boldsymbol{k}, \omega)$ passes through $\omega = 0$. Nevertheless, this definition works only for couplings $(k_Fa_F)^{-1} \lesssim 0.4$ for the $(G_0G_0)G$ approach and $(k_Fa_F)^{-1} \lesssim 0.6$ for the $(GG)G$ approach, because for stronger couplings a double-peak structure in $A(\boldsymbol{k}, \omega)$ starts to appear also for these approaches. To be able to extend the k_L-vs-coupling curve up to $k_L \to 0$, for the coupling regime where the double peak occurs we thus found more appropriate to identify k_L as the wave vector at which the peaks in $A(\boldsymbol{k}, \omega)$ at negative and positive frequencies mutually exchange the height of their maxima.

Figure 3.10 shows the values of the Luttinger wave vector k_L (following the definitions given above) as a function of the coupling $(k_Fa_F)^{-1}$ for all the t-matrix approaches. Here, depending on the approach, k_L appears to vanish for coupling in the range between 0.55 and 0.7, with the largest critical coupling reached by the fully self-consistent $(GG)G$ approach.

3.2.4 Radio-frequency spectroscopy

In a recent experimental work [136], the radio-frequency (rf) spectra of the balanced unitary Fermi gas in a uniform box potential were investigated for an extended range of temperatures. Knowledge of the Rabi frequency of the transition induced by the radio signal, and the number of atoms trapped in the box, allowed for the definition of a normalized dimensionless rf spectrum depending only on ω/E_F and T/T_F. These spectra provide quite a compelling test for theory.

More specifically, the experiment in Ref. [136] involved the three lowest hyperfine levels $|1\rangle$, $|2\rangle$, $|3\rangle$ of the fermionic atom ^{6}Li. A balanced mixture of two hyperfine states $|\downarrow\rangle = |1\rangle$ and $|\uparrow\rangle = |3\rangle$ of the ^{6}Li atoms was initially prepared at the unitary resonance of the inter-spin interaction. Then a square rf pulse transferred atoms from state $|\downarrow\rangle$ into the final state $|f\rangle = |2\rangle$. The final state $|f\rangle$ was chosen so that the interactions between atoms in state $|f\rangle$ and atoms in states $|\uparrow\rangle$ and $|\downarrow\rangle$ were small ($k_F a_f \lesssim 0.2$, where a_f is the scattering length of the interaction between atoms in the final and initial states).

After the rf pulse, the atom number in the initial state $N_\downarrow$ (before the rf pulse) and in the final state N_f (after the rf pulse) were measured. From this measurement, the experimental dimensionless rf spectrum is defined as

$$\tilde{I}_{\rm rf}(\omega) = \left[\frac{N_f(\omega)}{N_\downarrow}\right]\left(\frac{E_F}{\Omega_R^2 T_{\rm Pulse}}\right) \tag{3.13}$$

where Ω_R is the Rabi frequency of the $|\downarrow\rangle \to |f\rangle$ transition, $T_{\rm Pulse}$ is the pulse duration and $\omega = \omega_{\rm rf} - \omega_{\downarrow f}$ is the detuning of the rf pulse frequency $\omega_{\rm rf}$ from the bare atomic transition frequency $\omega_{\downarrow f}$. Under the assumption that the final state $|f\rangle$ is empty before the transition, this rf spectrum satisfies the sum rule [48]

$$\int \tilde{I}_{\rm rf}(\omega)\, d(\omega/E_F) = \frac{\pi}{2}. \tag{3.14}$$

One can then define

$$I_{\rm rf}(\omega) = \frac{2}{\pi}\tilde{I}_{\rm rf}(\omega) \tag{3.15}$$

so that the sum rule becomes

$$\int I_{\rm rf}(\omega)\, d(\omega/E_F) = 1. \tag{3.16}$$

Within linear response theory and neglecting final-state interactions, the rf spectrum $I_{\rm rf}(\omega)$ can be calculated in terms of the single-particle spectral function $A(\boldsymbol{k},\omega)$ of Section 3.2.1 as [58]

$$I_{\rm rf}(\omega) = \frac{E_F}{n_\downarrow}\int \frac{d\boldsymbol{k}}{(2\pi)^3} A(\boldsymbol{k}, \xi_{\boldsymbol{k}} - \omega) f(\xi_{\boldsymbol{k}} - \omega) \tag{3.17}$$

where $f(\xi) = 1/(e^{\beta\xi}+1)$ is the Fermi distribution.

Figure 3.11 shows the comparison of the rf spectra calculated within the various t-matrix approaches, together with the experimental data from Ref. [136], for the coupling

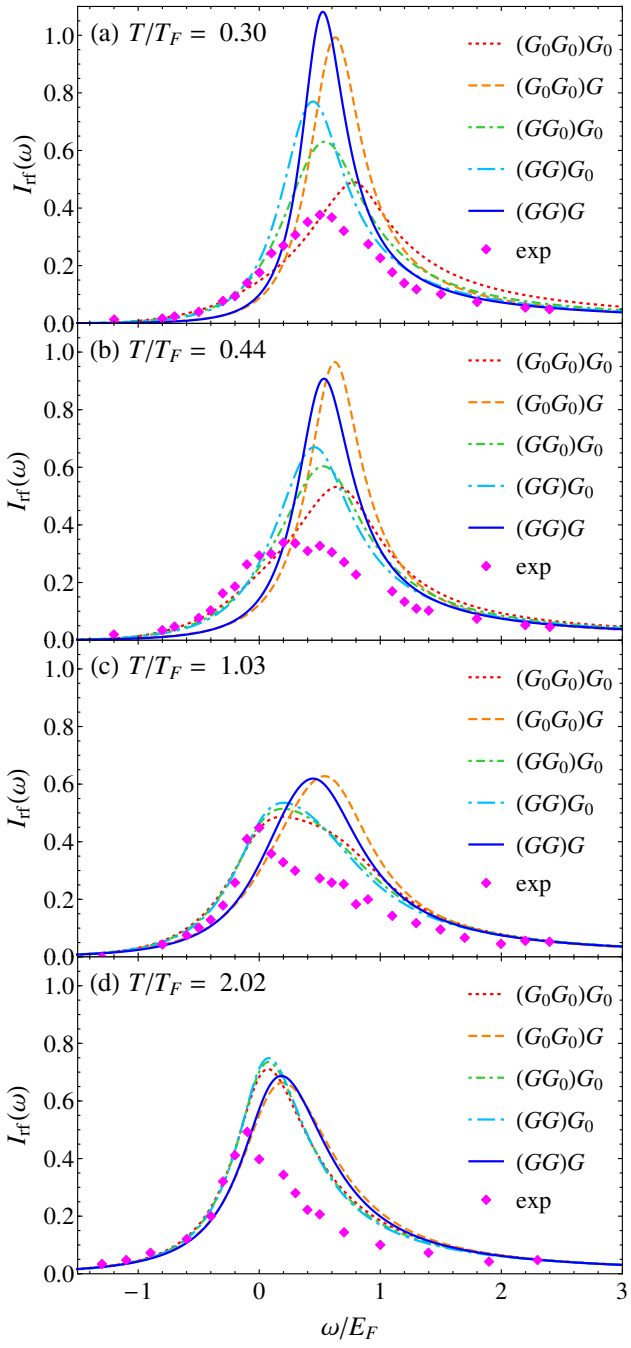

Figure 3.11: Radio-frequency spectra $I_{\rm rf}(\omega)$ at coupling $(k_F a_F)^{-1} = 0$ for the temperatures (a) $T/T_F = 0.44$, (b) $T/T_F = 1.03$, (c) $T/T_F = 2.02$ within alternative t-matrix approaches. Experimental data from Ref. [136] (diamonds) are added for comparison.

$(k_F a_F)^{-1} = 0$ and for four different temperatures above T_c. The values of the temperature have been chosen so that they correspond to the experimental ones.

While the single-peak shape of the rf spectrum is always recovered, the spectra are quite different for the various approaches, especially at low temperature. Like for the other spectral properties of the previous sections, larger differences are seen between the $(G_0G_0)G$ and $(GG)G$ approaches that dress the external Green's function $G^{(c)}$ and the $(G_0G_0)G_0$, $(GG_0)G_0$ and $(GG)G_0$ approaches that do not.

None of the theoretical approaches is able to recover the whole experimental spectrum. Still, one can see that the approaches which do not dress the external $G^{(c)}$ are at least able to recover the initial part of the spectrum (namely $\omega \leq 0$). Note, however, that all the experimental spectra seem to present a reduced area under the peak, as if they would not satisfy the sum rule (3.16). The depletion of the experimental spectra could be related to final state effects [48], but a quantitative investigation of these effects is still needed.

It is finally interesting to note that at the highest temperature $T/T_F = 2$ the differences between the various approaches get smaller. This is expected, since all t-matrix approaches converge to the second order virial expansion in the high-temperature limit [43, 99]. It is somewhat surprising that even at this relatively high temperature significant differences with respect to the experimental result still persist.

Figs. 3.12 and 3.13 show instead the position of the maximum ($E_p = -\omega_{\max}$) and the full width at half maximum (FWHM) of the peak in the rf spectra as a function of the temperature for all the t-matrix approaches and the experimental data of Ref. [136].[4]

For the position of the maximum, the only approach that seems to recover the qualitative behavior of the experimental data is the non-self-consistent $(G_0G_0)G_0$ approach. Still, the $(G_0G_0)G_0$ result is consistently shifted to higher temperatures, as we could expect since this approach does not recover the correct thermodynamics at unitarity (cf. Section 3.1).

As far as the width of the peak, all the schemes present a maximum at a certain temperature, which is $T/T_F \simeq 0.9$ for the $(G_0G_0)G_0$, $(GG_0)G_0$ and $(GG)G_0$ approaches and $T/T_F \simeq 1.3$ for the $(G_0G_0)G$ and $(GG)G$ approaches. Note also that the self-consistently dressing of the particle-particle propagator Γ tends to reduce the width of the spectra. However, none of the approaches recover the experimental width, that shows a maximum at the lower temperature $T/T_F \simeq 0.5$.

3.2.5 Summary of the results for spectral quantities

We have seen that the main differences in the spectral functions obtained within the various approaches originate by the dressing of the external $G^{(c)}$ in the self-energy (2.105). In particular, at unitarity, the inclusion of this self-consistency removes the double-peak structure from the single-particle spectral function $A(\boldsymbol{k}, \omega)$, and this in turn reduces the pseudo-gap feature in the density of states $N(\omega)$. At the same time, however, QMC

[4] The minus sign in the definition of the position of the peak maximum is introduced to be consistent with the notation of Ref. [136].

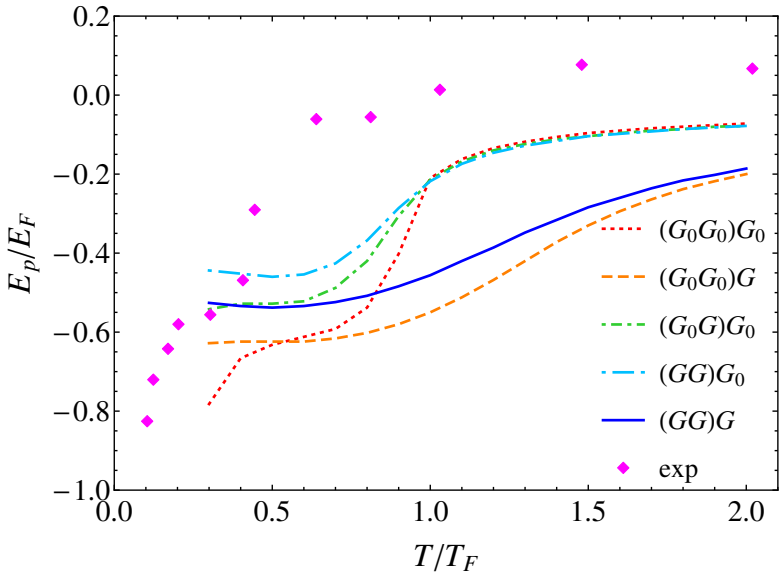

Figure 3.12: Frequency of the maximum $E_p = -\omega_{\max}$ (in units of E_F) of the peak in the radio-frequency spectra as a function of the temperature (in units of T_F) for the coupling $(k_F a_F)^{-1} = 0$ within alternative t-matrix approaches. Experimental data from Ref. [136] (diamonds) are added for comparison.

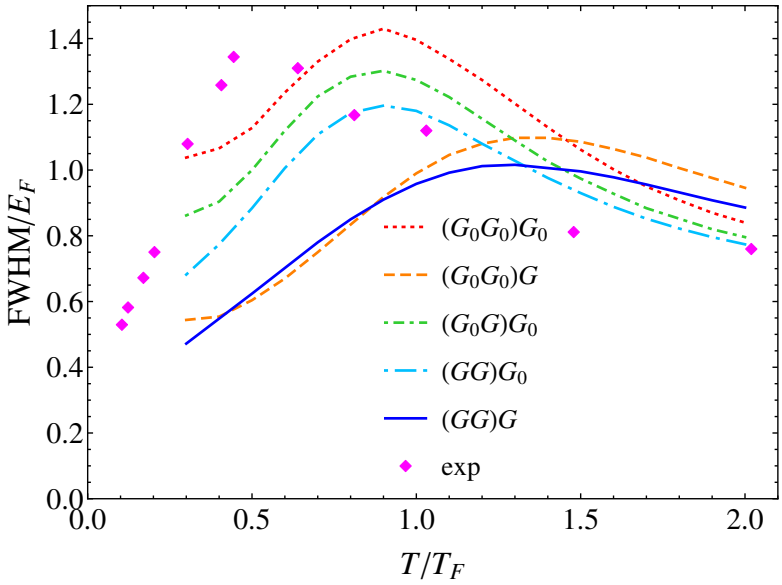

Figure 3.13: Full width at half maximum (in units of E_F) of the peak in the radio-frequency spectra as a function of the temperature (in units of T_F) for the coupling $(k_F a_F)^{-1} = 0$ within alternative t-matrix approaches. Experimental data from Ref. [136](diamonds) are added for comparison.

data from Refs. [83, 84] seem to point out that this double-peak structure is indeed present, at least at $T = T_c \simeq 0.15 T_F$. Moreover, the $(G_0G_0)G$ and $(GG)G$ approaches are those which compare worst with the rf spectra of Ref. [136]. From these evidences, it appears that the fully self-consistent scheme $(GG)G$, which gives really good results for the thermodynamics, fails to catch even the qualitative features of the spectral functions, while the non-self-consistent $(G_0G_0)G_0$ approach can at least recover some qualitative properties.

That a fully self-consistent diagrammatic approximation may end up degrading the description of spectral features with respect to its non-self-consistent version(s) has also been evidenced in other physical contexts. For example, this is consistently seen in GW diagrammatic calculations of the excitation spectra of semiconductors and insulators [137], as well as of complex molecules [138]. Similar conclusions have further been drawn in the context of a simpler model [139]. In these cases, attempts have recently been made to mitigate the effects of self-consistency by introducing vertex corrections on the GW calculations [140, 141].

In the present context of the t-matrix approximation for an attractive Fermi gas, too, vertex corrections have recently been included on top of a partially self-consistent version of this approximation in Ref. [70, 71]. It could therefore be interesting to assess whether including a similar kind of vertex correction on top of the fully self-consistent t-matrix approximation may result in a better description for spectral properties.

Chapter 4

Trapped system

All the results that were shown in the previous chapter refer to the homogeneous Fermi gas. While some recent experiments have been performed in a homogenous box potential [136, 142, 143], most of the experimental data so far available have been obtained within a harmonic trapping potential. It is then important to extend the t-matrix approach also to harmonic trapping potentials in order to have a meaningful comparison with these experimental data.

In this chapter, the details of this extension will be presented, together with the results for the density profiles and the critical temperature in the trap calculated within the fully self-consistent t-matrix approach. A comparison with experimental data for the same quantities is also provided.

4.1 Local density approximation

Let us consider a spin-balanced Fermi gas trapped composed by $N = N_\uparrow + N_\downarrow$ particles in an anisotropic harmonic potential of the form

$$V(\boldsymbol{r}) = \frac{1}{2} m \left(\omega_x^2 x^2 + \omega_y^2 y^2 + \omega_z^2 z^2 \right), \tag{4.1}$$

where ω_x, ω_y and ω_z are the harmonic frequencies along the x, y and z directions.

To describe a system in this kind of potential, one can adopt a *local density approximation* (LDA) approach. This approach consists in keeping the same equations (2.104-2.107) of the homogeneous system, but replacing the chemical potential μ in all the expressions with a position-dependent chemical potential $\mu(\boldsymbol{r}) = \mu_0 - V(\boldsymbol{r})$, thereby obtaining a local Green's function $G(\boldsymbol{k}, \omega_n; \mu(\boldsymbol{r}))$. One can then repeat the homogeneous calculation on a grid of $\boldsymbol{r}$-points to obtain the density profile

$$n(\boldsymbol{r}) = 2 \int \frac{d\boldsymbol{k}}{(2\pi)^3} \frac{1}{\beta} \sum_n G(\boldsymbol{k}, \omega_n; \mu(\boldsymbol{r})), \tag{4.2}$$

and then fix the chemical potential $\mu(\boldsymbol{r} = 0) = \mu_0$ at the center of the trap by inverting

the number equation

$$N = 2 \int d\boldsymbol{r}\, n(\boldsymbol{r}). \tag{4.3}$$

To simplify the calculation, it is however useful to map the anisotropic potential $V(\boldsymbol{r})$ to its equivalent isotropic potential, so that $\boldsymbol{r}$ needs to be evaluated only on a one-dimensional radial grid. For simplicity, let us consider the typical experimental situation where the trapping frequencies are taken to be $\omega_x = \omega_y$ and $\omega_z = \lambda\omega_x$, so that the anisotropy is only along the z-axis. One can then rescale the variables as

$$(x, y, z) \to (x' = \lambda^{-1/3}x,\, y' = \lambda^{-1/3}y,\, z' = \lambda^{2/3}z), \tag{4.4}$$

such that the trapping potential becomes

$$V(x', y', z') = \frac{1}{2}\bar{\omega}^2 r'^2, \tag{4.5}$$

where $r' = \sqrt{x'^2 + y'^2 + z'^2}$ and $\bar{\omega} = (\omega_x\omega_y\omega_z)^{1/3} = \lambda^{1/3}\omega_x$ is the average trap frequency. Accordingly, the original density distribution $n(x, y, z)$ is mapped to an isotropic distribution $n'(x', y', z') = n'(r')$. As the number of particles N is kept to be the same in the rescaling, we have

$$N = \int dx\, dy\, dz\, n(x, y, z) = \int dx' dy' dz'\, n'(x', y', z'), \tag{4.6}$$

thus, the mapping between the density distributions in the rescaling is simply given by

$$n(x, y, z) = n'(\lambda^{-1/3}x, \lambda^{-1/3}y, \lambda^{2/3}z). \tag{4.7}$$

Once the calculation is performed in the isotropic system, the previous rescaling relation can be applied to recover the results for any anisotropic system.

In Fig. 4.1 the isotropic density profiles calculated within the fully self-consistent t-matrix approach are shown for the couplings $(k_F a_F)^{-1} = (-0.5, 0.0, 0.5)$ and for different temperatures in the normal phase. Here, the coupling $(k_F a_F)^{-1}$ is expressed in terms of $k_F = \sqrt{2mE_F}$, where $E_F = \bar{\omega}(3N)^{1/3}$ is the Fermi energy of the trap. The position in the trap r', instead, is expressed in units of the Thomas-Fermi radius R_{TF}, that corresponds to the radius of the density profile of a non-interacting Fermi gas at zero temperature and is given by the relation

$$\frac{1}{2}m\bar{\omega}^2 R_{\mathrm{TF}}^2 = E_F \quad \Rightarrow \quad R_{\mathrm{TF}} = \sqrt{\frac{2E_F}{m\bar{\omega}^2}}. \tag{4.8}$$

Note that both E_F and R_{TF} are invariant in the isotropic mapping, because both N and $\bar{\omega}$ do not change in the transformation.

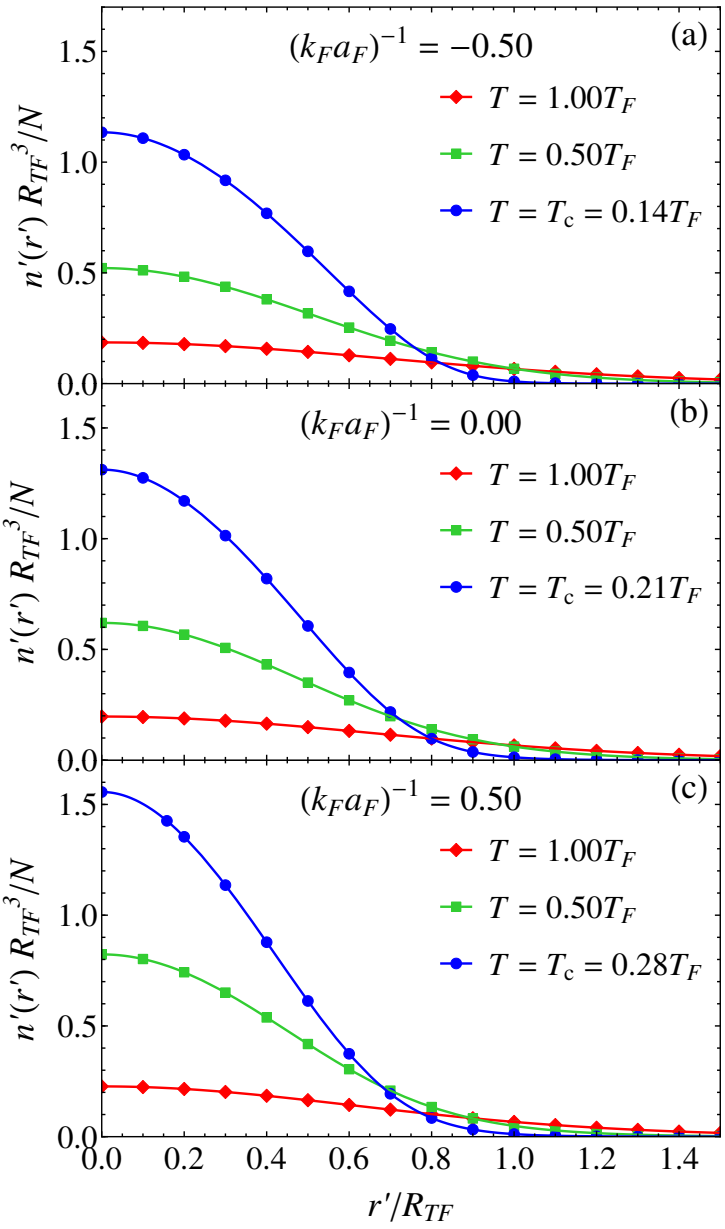

Figure 4.1: Isotropic radial density $n'(r')$ calculated within the fully self-consistent $(GG)G$ t-matrix approach for the couplings: (a) $(k_F a_F)^{-1} = -0.5$; (b) $(k_F a_F)^{-1} = 0.0$; (c) $(k_F a_F)^{-1} = 0.5$. In each panel, the results for $T = T_c$ (dots), $T = 0.5T_F$ (squares), $T = T_F$ (diamonds) are shown. Lengths are in units of the Thomas-Fermi radius $R_{\rm TF}$ given by the expression (4.8), such that $8N/(\pi^2 R_{\rm TF}^3)$ is the value of $n'(r' = 0)$ for the non-interacting gas at $T = 0$ within the local-density approximation.

4.2 Comparison with experimental axial densities

A quantity that can be compared with the experimental data in a harmonic potential is the so-called *axial* density $n_{\rm a}(z)$, where z runs along the main axis of the trap. This quantity is obtained by integrating the full density $n(x,y,z)$ over the transversal directions x and y

$$n_{\rm a}(z) = \int dx\, dy\, n(x,y,z) \tag{4.9}$$

Specifically, the experimental profiles $n_{\rm a}(z)$ can be compared with their theoretical counterparts $n'_{\rm a}(z')$, obtained by integrating over x' and y' the isotropic profiles $n'(r') = n'(x',y',z')$ (like those shown in Fig. 4.1) and then performing the rescaling

$$n_{\rm a}(z) \,=\, \lambda^{2/3}\, n'_{\rm a}(\lambda^{2/3} z)\,. \tag{4.10}$$

Figure 4.2 shows this comparison for three sets of values of temperature, coupling, and anisotropy λ. The experimental data were obtained by the group of J. Hecker Denschlag in Ulm [77]. In all cases, excellent agreement results between the experiment and the self-consistent t-matrix approach with no adjustable parameter.

4.3 Critical temperature in the trap

The values of the critical temperature T_c in the trapped case, reported in Fig. 4.1 for three specific couplings, can be obtained throughout the whole BCS-BEC crossover. To calculate this critical temperature, it is useful to think in terms of a local Fermi temperature $T_F(\boldsymbol{r}) = [3\pi^2 n(\boldsymbol{r})]^{2/3}/(2mk_B)$, corresponding to the Fermi temperature of the homogeneous system with density equal to the local density $n(\boldsymbol{r})$. This implies that the local Fermi temperature $T_F(\boldsymbol{r})$, like the density $n(\boldsymbol{r})$, has its maximum value at $\boldsymbol{r} = 0$, to which there corresponds a minimum value for the ratio $T/T_F(\boldsymbol{r})$ for a given temperature T. Accordingly, the central portion of the trap is where superfluidity is first established upon lowering the temperature from the normal phase.

The critical temperature T_c for the trapped system is then obtained by applying the Thouless criterion (2.109) to the center of the trap:

$$\left[\Gamma\left(\boldsymbol{Q}=0, \Omega_\nu = 0; \mu(\boldsymbol{r}=0)\right)^{-1}\right]_{T=T_c} = 0. \tag{4.11}$$

Figure 4.3 shows the result for T_c in the trap across the BCS-BEC crossover, calculated for both the fully self-consistent $(GG)G$ and the non-self-consistent $(G_0G_0)G_0$ t-matrix approaches.

Note that in the BCS limit $(k_F a_F)^{-1} \ll -1$ the critical temperatures for the two approaches are really close. Still, there is a difference in the pre-exponential factor, similarly to what happens in the homogeneous case (cf. inset of Fig. 3.1). To understand this, we can write the expression of the critical temperature in the weak-coupling limit (2.94) by replacing μ with the chemical potential μ_0 at the center of the trap:

$$T_c \simeq \frac{8\mu_0 e^\gamma}{k_B \pi e^2} \exp\left(\frac{\pi}{2k_F a_F}\sqrt{E_F/\mu_0}\right). \tag{4.12}$$

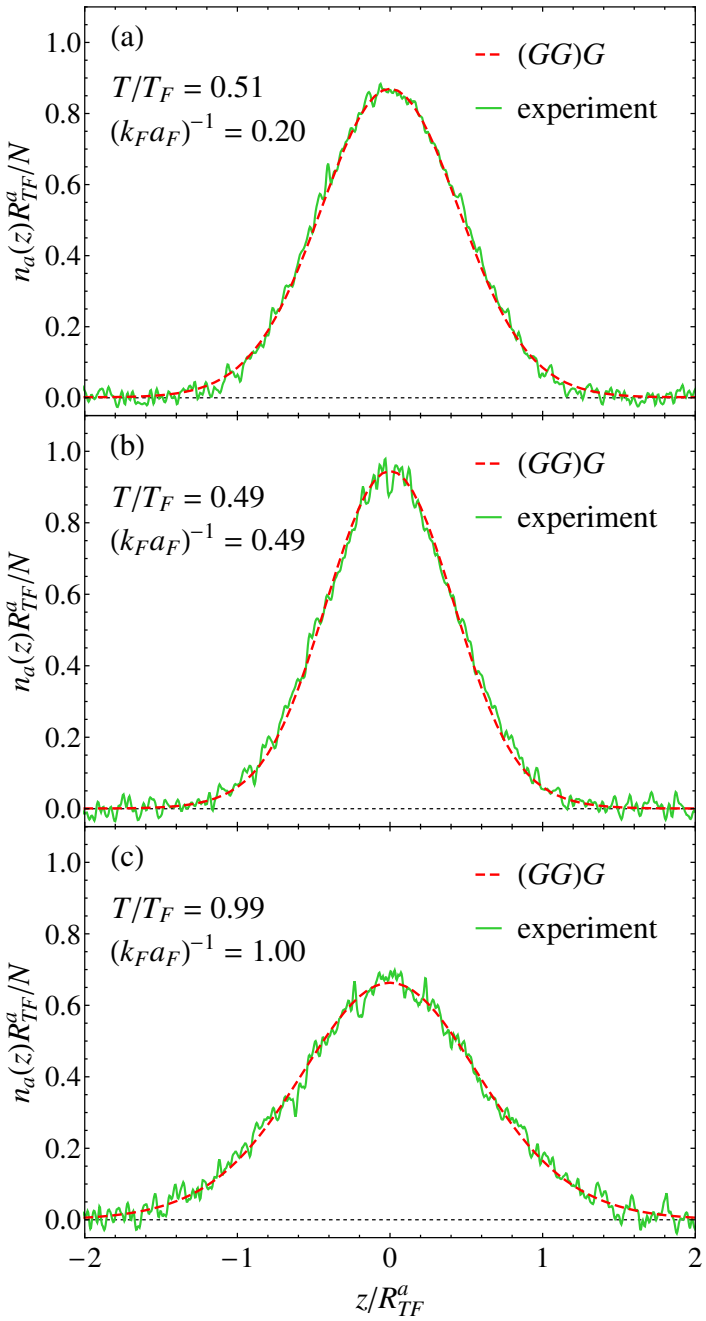

Figure 4.2: Comparison between the axial densities along the main axis of the trap, as observed experimentally in Ref. [77] (full lines) and calculated within the self-consistent t-matrix approach (dashed lines) for (a) $T/T_F = 0.51(4)$ and $(k_F a_F)^{-1} = 0.20(3)$ (b) $T/T_F = 0.49(4)$ and $(k_F a_F)^{-1} = 0.49(3)$ (c) $T/T_F = 0.99(6)$ and $(k_F a_F)^{-1} = 1.00(5)$. The ratio λ between the axial and radial trap frequencies equals 0.0435(8) in (a), 0.0424(7) in (b), and 0.0272(4) in (c). The axial Thomas Fermi radius $R^a_{TF} = \lambda^{-2/3} R_{TF}$ is used for normalization.

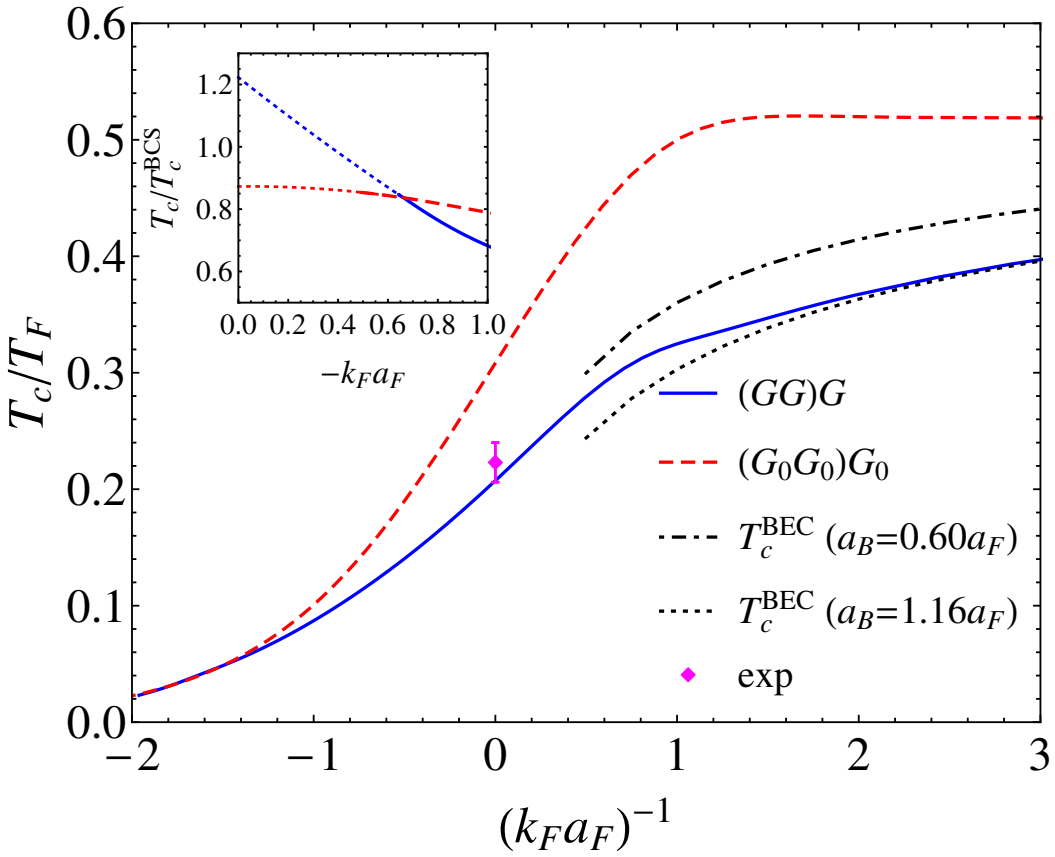

Figure 4.3: Critical temperature T_c (in units of T_F) vs $(k_F a_F)^{-1}$ for the trapped system. Results are shown for the fully self-consistent $(GG)G$ (full line) and for the non-self-consistent $(G_0G_0)G_0$ (dashed line) t-matrix approaches. At unitarity, the experimental value $T_c/T_F = 0.223(17)$ (diamond) obtained in Ref. [144] is shown for comparison. In the BEC regime, the results of a calculation for trapped bosons with a mean-field-type interaction (cf. Appendix E) are also shown with the values $a_B = 1.16a_F$ (dotted line) and $a_B = 0.60a_F$ (dash-dotted line) for the bosonic scattering length. In addition, the inset shows the extrapolation of the ratio $T_c/T_c^{\rm BCS}$ in the weak-coupling limit $(k_F a_F)^{-1} \ll -1$. Here, thick lines correspond to numerical data and thin dotted lines correspond to parabolic fits of the data that extrapolate T_c in the weak-coupling limit.

At the leading order in $(k_F a_F)$, $\mu_0 \simeq E_F$ and one recovers the same expression of the BCS critical temperature as for the homogeneous system

$$T_c^{\mathrm{BCS}} = \frac{8e^{\gamma} T_F}{\pi e^2} \exp\Big(\frac{\pi}{2k_F a_F}\Big), \tag{4.13}$$

with the only difference that now $T_F = \bar{\omega}(3N)^{1/3}/k_B$ is the Fermi energy in the trap. However, like for the homogeneous system (cf. Section 2.2.7), one has to take into account also the subleading order in $(k_F a_F)$ of μ_0 (in both approaches) and the effects of the dressing of the particle-particle bubble (in the $(GG)G$ approach), which give rise to different pre-exponential factors to the expression of the critical temperature (4.13). In particular, with a procedure similar to the one of Section 2.2.7, one can show that, in the BCS limit,

$$T_c \simeq A\, T_c^{\mathrm{BCS}}, \tag{4.14}$$

where the pre-exponential factor is $A = \exp(-128/(315\pi)) \simeq 0.879$ for the $(G_0G_0)G_0$ approach and $A = \exp(-128/(315\pi) + 1/3) \simeq 1.226$ for the $(GG)G$ approach[1]. From numerical extrapolation in the $(k_F a_F)^{-1} \to 0^-$ limit (see inset of Fig. 4.3), we found $A^{\mathrm{extr}} \simeq 0.87$ for the $(G_0G_0)G_0$ approach and $A^{\mathrm{extr}} \simeq 1.22$ for the $(GG)G$ approach, in good agreement (within an error of the order of 1%) with the values estimated analytically. In this regard, it is important to say that, in this case, it is the fully self-consistent approach $(GG)G$ that produces a better result with respect to the BCS and $(G_0G_0)G_0$ approaches, because it keeps into account the effects of the interactions (through the mean-field shift Σ_0) on both the density equation and the Thouless criterion (4.11).

On the BEC side of unitarity, instead, the $(G_0G_0)G_0$ and $(GG)G$ approaches differ considerably. In fact, the $(G_0G_0)G_0$ approach quickly recovers the critical temperature of a trapped gas of non-interacting composite bosons $T_c^{\mathrm{BEC}}/T_F = (6\zeta(3))^{-1/3} \simeq 0.5176$, while the $(GG)G$ approach presents a considerably lower T_c and recovers the asymptotic BEC value much more slowly.[2]

This substantial difference is to be attributed to the occurrence of a residual repulsive interaction between the composite bosons in the BEC regime, which is present within the fully self-consistent $(GG)G$ approach but is absent within the non-self-consistent $(G_0G_0)G_0$ approach (cf. Section 3.1.3). In fact, the repulsion between the composite bosons generates a depletion of the density $n(\boldsymbol{r} = 0)$ at the center of the trap. This, in turn, increases the local temperature $T/T_F(\boldsymbol{r} = 0)$, such that the global temperature T must be lower to reach superfluidity at the center of the trap. This effect can be described within bosonic mean-field theory, whereby the decrease of the critical temperature at the leading order in the dilute limit is linear in the bosonic scattering length a_B [145].

To make a check on the results of the $(GG)G$ numerical calculation in the BEC limit, we performed a mean-field self-consistent calculation of T_c for a low-density Bose gas with scattering length a_B (see Appendix E). The scattering length between the bosons was

[1] Similarly to the homogeneous case, the difference in the prefactor between the $(GG)G$ and $(G_0G_0)G_0$ approaches originates from the inclusion of the mean-field shift Σ_0 in the Green's functions of the particle-particle propagator (cf. Section 2.2.7).

[2] $\zeta(z)$ appearing in the expression of T_c^{BEC} is the Riemann zeta function of argument z.

first set to the approximate value $a_B = 1.16a_F$ (dotted line) obtained within the $(GG)G$ approach (cf. Section 3.1.3). The agreement of the bosonic mean-field calculation with the $(GG)G$ result in the $(k_F a_F)^{-1} \gg 1$ limit provides a numerical check on the accuracy of our calculations and evidences the important effect of the boson-boson repulsion on T_c for the trapped system in the BEC regime.

The same mean-field bosonic calculation was then performed for the exact value $a_B = 0.60a_F$ [42, 128](dash-dotted line). Comparing the $(GG)G$ result with this calculation in the BEC limit, we see that it quite underestimates the correct value of T_c, because of its overestimation of the scattering length between composite bosons. Still, the prediction is much improved with respect to the non-self-consistent $(G_0G_0)G_0$ approach, where the interaction between composite boson is completely neglected.

At the unitary limit $(k_F a_F)^{-1} = 0$, the experimental value $T_c/T_F = 0.223(13)$ is shown for comparison. This value was obtained in Ref. [144] from the value for the homogeneous system of Ref. [122] by using a local density approximation and the experimental equation of state. Similarly to the homogeneous case (cf. Fig. 3.1), the value $T_c/T_F = 0.2074$ obtained at unitarity within the fully self-consistent $(GG)G$ approach is the one that better agrees with the experimental data.

Finally, it should be mentioned that the $(GG)G$ value of T_c at unitarity coincides with that obtained in Ref. [50] by the same approach. However, our calculation for T_c in the trapped system is extended to the whole BCS-BEC crossover, while that of Ref. [50] was limited only to unitarity.

Chapter 5

Pair correlations

In this chapter, we investigate pair correlations in the normal phase of a spin-balanced attractive Fermi gas. To study these pair correlations, the pair correlation function $g_{\uparrow\downarrow}(\boldsymbol{\rho})$ and the pair coherence length ξ_{pair} are introduced and calculated within the fully self-consistent t-matrix approach.

5.1 Theoretical approach for the pair correlation function and the pair coherence length

In an homogeneous system, the *pair correlation function* for fermions with opposite spin is defined in terms of fermionic field operators as[1]

$$g_{\uparrow\downarrow}(\boldsymbol{\rho}) = \left\langle \hat{\psi}_{\uparrow}^{\dagger}\left(\frac{\boldsymbol{\rho}}{2}\right) \hat{\psi}_{\downarrow}^{\dagger}\left(-\frac{\boldsymbol{\rho}}{2}\right) \hat{\psi}_{\downarrow}\left(-\frac{\boldsymbol{\rho}}{2}\right) \hat{\psi}_{\uparrow}\left(\frac{\boldsymbol{\rho}}{2}\right) \right\rangle - n_{\uparrow} n_{\downarrow}. \tag{5.1}$$

This function contains information about the correlations of pairs of fermions with opposite spin at a distance $\rho = |\boldsymbol{\rho}|$. The uncorrelated value $n_{\uparrow} n_{\downarrow}$ is subtracted in the definition to emphasize only the correlations due to interaction.

From the function (5.1), one can extract the *pair coherence length* ξ_{pair}

$$\xi_{\mathrm{pair}}^2 = \frac{\int d\boldsymbol{\rho}\, \boldsymbol{\rho}^2 g_{\uparrow\downarrow}(\boldsymbol{\rho})}{\int d\boldsymbol{\rho}\, g_{\uparrow\downarrow}(\boldsymbol{\rho})}, \tag{5.2}$$

which represents in general the range of pairing correlations and generalizes the definition of BCS pairing length (see Ref. [10]) in a such a way that it can be extended also to the normal phase.

Let us now introduce the theoretical approach to calculate the pair correlation function (5.1) and the pair coherence length (5.2) within the self-consistent t-matrix approach. As these are two-body observables, to describe them one needs the two-particle Green's function formalism (see Section 2.6).

[1] Note that the τ-dependence in the field operators $\hat{\psi}_{\sigma}(\boldsymbol{r}, \tau)$ has been dropped as they are all calculated at the same imaginary time τ.

Restoring the τ-dependence in the definition (5.1), together with the use of the Nambu representation (2.135), one can identify the pair correlation (5.1) with the two-particle Green's function (2.137)

$$g_{\uparrow\downarrow}(\boldsymbol{\rho}) + n_\uparrow n_\downarrow = \langle T_\tau[\hat{\Psi}(1)\hat{\Psi}(2)\hat{\Psi}^\dagger(2')\hat{\Psi}^\dagger(1')]\rangle = G_2(1,2;1',2') \tag{5.3}$$

with the following choice for the variables

$$\begin{aligned} 1 &= (\boldsymbol{\rho}/2, \tau, \ell_1 = 1), \\ 2 &= (-\boldsymbol{\rho}/2, \tau^{++}, \ell_2 = 2), \\ 1' &= (-\boldsymbol{\rho}/2, \tau^{+}, \ell_{1'} = 2), \\ 2' &= (\boldsymbol{\rho}/2, \tau^{+++}, \ell_{2'} = 1), \end{aligned} \tag{5.4}$$

where $\tau^+ = \tau + \eta$ with $\eta \to 0^+$. For a Fermi gas in the normal phase, and with the variables (5.4), the $G(1,1')G(2,2')$ term in the definition (2.138) of the two-particle correlation function L is zero because it is formed by off-diagonal single-particle Green's function, which are zero above T_c (cf. Eq. (2.146)). So, in this case one has $L(1,2;1',2') = G_2(1,2;1',2')$, and the formal solution (2.142) for L is valid also for G_2:

$$\begin{aligned} G_2(1,2;1',2') = &-G(1,2')G(2,1') \\ &- \int d3456\, G(1,3)G(6,1')T(3,5;6,4)G(4,2')G(2,5). \end{aligned} \tag{5.5}$$

With the external variables (5.4), the first term on the right hand side of (5.5) is $-G(1,2')G(2,1') = n_\uparrow n_\downarrow$, and thus exactly cancels the uncorrelated value $n_\uparrow n_\downarrow$ on the left hand side of Eq. (5.3). In the second term, instead, only the element $T_{22}^{11} = T_{11} = -\Gamma$ of the T-matrix survives above T_c (cf. Section 2.6). Fourier transforming Eq. (5.5) to the frequency-momentum space, one finally obtains the expression for the pair correlation function in the normal phase in terms of the single-particle Green's function G and the particle-particle propagator Γ [66]:

$$g_{\uparrow\downarrow}(\boldsymbol{\rho}) = \int \frac{d\boldsymbol{Q}}{(2\pi)^3} \frac{1}{\beta} \sum_\nu e^{i\Omega_\nu \eta}\, \Gamma(\boldsymbol{Q}, \Omega_\nu)\, [\Pi(\boldsymbol{\rho}; \boldsymbol{Q}, \Omega_\nu)]^2 \tag{5.6}$$

where

$$\Pi(\boldsymbol{\rho}; \boldsymbol{Q}, \Omega_\nu) = \int \frac{d\boldsymbol{k}}{(2\pi)^3}\, e^{i\boldsymbol{k}\cdot\boldsymbol{\rho}}\, \Pi(\boldsymbol{k}; \boldsymbol{Q}, \Omega_\nu) \tag{5.7}$$

is the Fourier transform of the particle-particle bubble

$$\Pi(\boldsymbol{k}; \boldsymbol{Q}, \Omega_\nu) = \frac{1}{\beta} \sum_n G_\uparrow(\boldsymbol{k} + \boldsymbol{Q}/2, \omega_n + \Omega_\nu) G_\downarrow(\boldsymbol{k} - \boldsymbol{Q}/2, -\omega_n). \tag{5.8}$$

Once that $g_{\uparrow\downarrow}(\boldsymbol{\rho})$ has been calculated, in principle one can directly apply the definition (5.2) and obtain the pair coherence length ξ_{pair}. In practice, however, we found that this procedure is not the best to apply numerically, because especially when $g_{\uparrow\downarrow}(\boldsymbol{\rho})$ present

long and oscillating tails in $\boldsymbol{\rho}$ (for example, in weak-coupling at low temperature) the integration over $\boldsymbol{\rho}$ of the numerator of (5.2) is quite sensible to numerical noise.

Accordingly, for the calculation of $\xi_{\rm pair}$, we avoid the $\boldsymbol{\rho}$-space completely and work directly in momentum space. In fact, if one replaces the expression (5.6) for $g_{\uparrow\downarrow}(\boldsymbol{\rho})$ into the denominator and numerator of the definition (5.2) for $\xi_{\rm pair}$, one obtains [66]:

$$\int d\boldsymbol{\rho}\, g_{\uparrow\downarrow}(\boldsymbol{\rho}) = \int \frac{d\boldsymbol{Q}}{(2\pi)^3}\frac{1}{\beta}\sum_{\nu} e^{i\Omega_\nu \eta}\,\Gamma(\boldsymbol{Q},\Omega_\nu)\int \frac{d\boldsymbol{k}}{(2\pi)^3}\Pi[(\boldsymbol{k};\boldsymbol{Q},\Omega_\nu)]^2, \tag{5.9}$$

$$\int d\boldsymbol{\rho}\,\boldsymbol{\rho}^2\, g_{\uparrow\downarrow}(\boldsymbol{\rho}) = \int \frac{d\boldsymbol{Q}}{(2\pi)^3}\frac{1}{\beta}\sum_{\nu} e^{i\Omega_\nu \eta}\,\Gamma(\boldsymbol{Q},\Omega_\nu)\int \frac{d\boldsymbol{k}}{(2\pi)^3}[\nabla_{\boldsymbol{k}}\,\Pi(\boldsymbol{k};\boldsymbol{Q},\Omega_\nu)]^2, \tag{5.10}$$

where the particle-particle bubble Π is defined in (5.8).

A detailed account of the calculation of the expressions (5.6), (5.9) and (5.10) within the fully self-consistent t-matrix approach is given in Appendix F.

5.2 Short-range behavior of $g_{\uparrow\downarrow}(\boldsymbol{\rho})$

The small-$\boldsymbol{\rho}$ behavior of the pair correlation function $g_{\uparrow\downarrow}(\boldsymbol{\rho})$ can be obtained analytically. Let us start by considering the $\boldsymbol{\rho}\to 0$ limit of the particle-particle bubble (5.7)

$$\begin{aligned}
\Pi(\boldsymbol{\rho};\boldsymbol{Q},\Omega_\nu) &= \int \frac{d\boldsymbol{k}}{(2\pi)^3}\, e^{i\boldsymbol{k}\cdot\boldsymbol{\rho}}\,\Pi(\boldsymbol{k},\boldsymbol{Q},\Omega_\nu) \\
&= \int \frac{d\boldsymbol{k}}{(2\pi)^3} e^{i\boldsymbol{k}\cdot\boldsymbol{\rho}}\,\frac{m}{\boldsymbol{k}^2} - \int \frac{d\boldsymbol{k}}{(2\pi)^3} e^{i\boldsymbol{k}\cdot\boldsymbol{\rho}}\,\left[\Pi(\boldsymbol{k},\boldsymbol{Q},\Omega_\nu) - \frac{m}{\boldsymbol{k}^2}\right] \\
&\xrightarrow[\boldsymbol{\rho}\to 0]{} \frac{m}{4\pi\rho} + R_{pp}(\boldsymbol{Q},\Omega_\nu),
\end{aligned} \tag{5.11}$$

where, by setting $\boldsymbol{\rho}=0$ in the second term, we identified the renormalized particle-particle bubble $R_{pp}(\boldsymbol{Q},\Omega_\nu)$ as defined in (2.107) with $G^{(a)}_{\uparrow} = G_{\uparrow}$ and $G^{(b)}_{\downarrow} = G_{\downarrow}$. Replacing this expression in (5.6) and using the relation

$$\Gamma(\boldsymbol{Q},\Omega_\nu)R_{pp}(\boldsymbol{Q},\Omega_\nu) = -\frac{R_{pp}(\boldsymbol{Q},\Omega_\nu)}{\frac{m}{4\pi a_F} + R_{pp}(\boldsymbol{Q},\Omega_\nu)} = -1 + \frac{m}{4\pi a_F}\Gamma(\boldsymbol{Q},\Omega_\nu) \tag{5.12}$$

we obtain

$$\begin{aligned}
g_{\uparrow\downarrow}(\boldsymbol{\rho}) &\xrightarrow[\boldsymbol{\rho}\to 0]{} \int \frac{d\boldsymbol{Q}}{(2\pi)^3}\frac{1}{\beta}\sum_{\nu} e^{i\Omega_\nu\eta}\,\Gamma(\boldsymbol{Q},\Omega_\nu)\left[\left(\frac{m}{4\pi\rho}\right)^2 + 2\frac{m}{4\pi\rho}R_{pp}(\boldsymbol{Q},\Omega_\nu)\right] \\
&= \left(\frac{m}{4\pi}\right)^2 \int \frac{d\boldsymbol{Q}}{(2\pi)^3}\frac{1}{\beta}\sum_{\nu} e^{i\Omega_\nu\eta}\,\Gamma(\boldsymbol{Q},\Omega_\nu)\left(\frac{1}{\rho^2} - \frac{2}{a_F\rho}\right).
\end{aligned} \tag{5.13}$$

By identifying the trace of the particle-particle propagator Γ (times m^2) with Tan's contact C as in (2.131) one finally obtains

$$g_{\uparrow\downarrow}(\boldsymbol{\rho}) \xrightarrow[\boldsymbol{\rho}\to 0]{} \frac{C}{(4\pi)^2}\left(\frac{1}{\rho^2} - \frac{2}{a_F\rho} + \cdots\right). \tag{5.14}$$

5.3 BEC limit of $g_{\uparrow\downarrow}(\boldsymbol{\rho})$

Let us now consider the BEC limit of the pair correlation function (5.6).As in the BEC limit the chemical potential $\mu \simeq -\varepsilon_0/2$ is the dominant energy scale (cf. Section 2.2.6), we can approximate the Green's function within the particle-particle bubble (5.8) as bare G_0 and perform the sum on the fermionic frequency as in (2.74):

$$\Pi(\boldsymbol{k};\boldsymbol{Q},\Omega_\nu) \simeq \frac{1-f(\xi_{\boldsymbol{k}+\boldsymbol{Q}/2})-f(\xi_{\boldsymbol{k}-\boldsymbol{Q}/2})}{\xi_{\boldsymbol{k}+\boldsymbol{Q}/2}+\xi_{\boldsymbol{k}-\boldsymbol{Q}/2}-i\Omega_\nu} \simeq \frac{1}{\xi_{\boldsymbol{k}+\boldsymbol{Q}/2}+\xi_{\boldsymbol{k}-\boldsymbol{Q}/2}-i\Omega_\nu}, \tag{5.15}$$

where $\xi_{\boldsymbol{k}} = \boldsymbol{k}^2/(2m)-\mu$ and the Fermi distributions $f(\xi) = 1/(e^{\beta\xi}+1)$ in the numerator have been neglected in the strong-coupling $\beta|\mu| \gg 1$ limit.

Taking the Fourier transform on $\boldsymbol{k}$ of expression (5.15), one obtains the analytical expression:

$$\Pi(\boldsymbol{\rho};\boldsymbol{Q},\Omega_\nu) \simeq \Pi_{\rm sc}(\boldsymbol{\rho};\boldsymbol{Q},\Omega_\nu) = \frac{m}{4\pi\rho} e^{-m^{1/2}\rho\sqrt{\boldsymbol{Q}^2/(4m)-2\mu-i\Omega_\nu}}. \tag{5.16}$$

One then finds for the pair correlation function (5.6)

$$g_{\uparrow\downarrow}(\boldsymbol{\rho}) \simeq \int \frac{d\boldsymbol{Q}}{(2\pi)^3}\frac{1}{\beta}\sum_\nu e^{i\Omega_\nu\eta}\,\Gamma_{\rm sc}(\boldsymbol{Q},\Omega_\nu)\,[\Pi_{\rm sc}(\boldsymbol{\rho};\boldsymbol{Q},\Omega_\nu)]^2, \tag{5.17}$$

where $\Gamma_{\rm sc}$ is the particle-particle propagator in the strong-coupling limit (2.84). At the lowest order in the $\beta|\mu| \gg 1$ limit, one can express $\Gamma_{\rm sc}$ in its polar form (2.85) and neglect the $\boldsymbol{Q}$ and Ω_ν dependence in (5.16), obtaining:

$$g_{\uparrow\downarrow}(\boldsymbol{\rho}) \simeq \frac{8\pi(n/2)}{a_F}\frac{e^{-2\rho/a_F}}{(4\pi\rho)^2} = \frac{C^{\rm BEC}}{(4\pi)^2}\frac{e^{-2\rho/a_F}}{\rho^2} \tag{5.18}$$

where $C^{\rm BEC}/k_F^4 = 4/(3\pi k_F a_F)$ is the strong coupling limit of the contact. Note that, apart from a multiplicative constant, the pair correlation function correspond in this limit to the square of the two-body bound state (2.66):

$$g_{\uparrow\downarrow}(\boldsymbol{\rho}) \simeq \frac{n}{2}\,|\phi_b(\boldsymbol{\rho})|^2. \tag{5.19}$$

Replacing the expression (5.18) in the $\xi_{\rm pair}$ definition (5.2), one can easily carry out the integrals over $\boldsymbol{\rho}$ and obtain $\xi_{\rm pair} \simeq \sqrt{2}a_F$ in the BEC limit.

5.4 Results for the spin-balanced system

In this section we report the results for the pair correlation function $g_{\uparrow\downarrow}(\boldsymbol{\rho})$ and the pair coherence length $\xi_{\rm pair}$ for a spin-balanced Fermi gas in the normal phase across the BCS-BEC crossover. The main results are obtained within the fully self-consistent $(GG)G$ t-matrix approach. For the pair coherence length, a comparison with the results of the non-self-consistent $(G_0G_0)G_0$ approach is also shown.

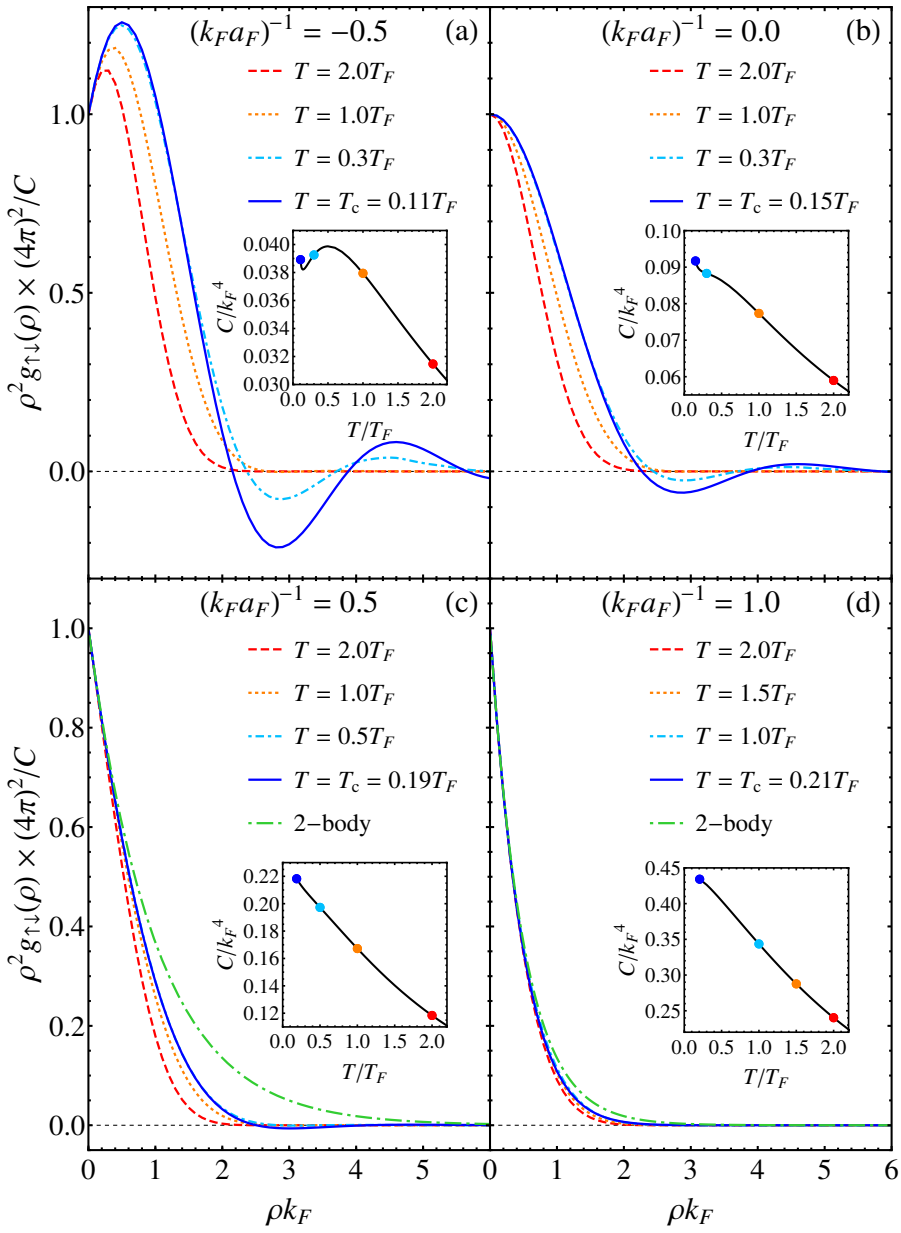

Figure 5.1: Spatial profiles of $\rho^2\, g_{\uparrow\downarrow}(\rho)$ vs ρ (in units of k_F^{-1}) within the fully self-consistent t-matrix approach, for several couplings and temperatures above T_c. The profiles are normalized with respect to their value at $\rho = 0$. In each panel, the inset gives the dependence of the contact C over an extended range of temperature (in units of the Fermi temperature T_F), where the dots correspond to the temperatures reported in the same panel. In panels (c) and (d), the expression $(2\pi a_F)\rho^2|\phi_b(\rho)|^2 = e^{-2\rho/a_F}$ corresponding to the two-body bound state (2.66) is reported for comparison (long dash-dotted lines).

In Figure 5.1, spatial profiles of the pair correlation function $g_{\uparrow\downarrow}(\boldsymbol{\rho})$ calculated within the fully self-consistent t-matrix approach are shown for several couplings and temperatures above T_c. The profiles are multiplied by ρ^2 and renormalized with respect to their value at $\rho = 0$ to facilitate the comparison. Reported in each inset are also the respective values of the contact C, from which the numerical values of $g_{\uparrow\downarrow}(\boldsymbol{\rho})$ can be explicitly reconstructed.

Note the oscillatory behavior of $g_{\uparrow\downarrow}(\boldsymbol{\rho})$, which is present on the BCS side at low temperatures but quickly fades away either by moving towards the BEC side or by increasing temperature. This behavior is strictly related to the existence of an underlying Fermi surface at a finite momentum, which is translated in oscillations in real space [146]. In fact, one can show that in the BCS limit these oscillations have a period determined by the wave vector k_F [66].

In the BEC limit, instead, the pair correlation function is seen to correctly recover the expression (5.18) (long dash-dotted lines) proportional to the square of the two-body bound state (2.66).

In Figure 5.2, instead, is shown the temperature dependence of the pair coherence length ξ_{pair} calculated within the fully self-consistent $(GG)G$ (full line) and non-self-consistent $(G_0G_0)G_0$ (dashed line) approaches for three characteristic couplings. In general, one observes a consistent reduction of ξ_{pair} at low temperature when self-consistency is added in the calculation. For $T/T_F > 2$, instead, both approaches have basically the same behavior and they slowly recover the high-temperature value $\lambda_T/\sqrt{4\pi}$, where $\lambda_T = \sqrt{2\pi/(mk_BT)}$ [66].

Finally, Figure 5.3 reports the pair coherence length ξ_{pair} at the critical temperature T_c as a function of the coupling, for both the self-consistent $(GG)G$ (full line) and the non-self-consistent $(G_0G_0)G_0$ (dashed line) approaches. Also here, it appears that the self-consistent value of ξ_{pair} is reduced with respect to the non-self-consistent one across the whole crossover. On the BEC side, one can see that the self-consistent approach recovers the limiting value $\xi_{\text{pair}}^{\text{BEC}} = \sqrt{2}a_F$ much more slowly with respect to the non-self-consistent one. This is due the residual repulsion between the composite bosons, included in the $(GG)G$ approach, that tends to shrink the pair correlation function with respect to the $(G_0G_0)G_0$ approach, which completely neglects this residual interaction (for an analysis of the size shrinking of pairs due to the interaction between composite bosons, see Ref. [147]).

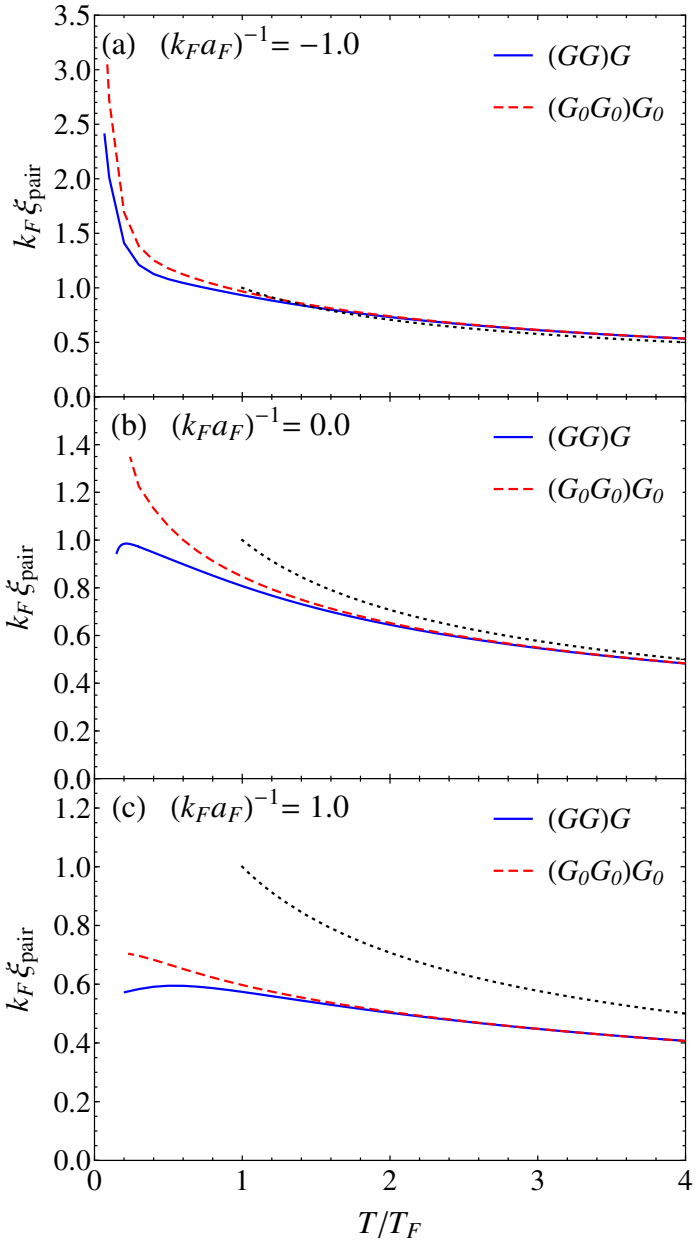

Figure 5.2: Temperature dependence of the pair coherence length $\xi_{\rm pair}$ for the couplings (a) $(k_F a_F)^{-1} = -1.0$, (b) $(k_F a_F)^{-1} = 0.0$, and (c) $(k_F a_F)^{-1} = 1.0$. The results are shown for the fully self-consistent (full line) and non-self-consistent (dashed line) t-matrix approaches, and at low temperature the curves terminate at their respective critical temperature T_c. The dotted line represents the high-temperature limit $\lambda_T/\sqrt{4\pi}$, with $\lambda_T = \sqrt{2\pi/(mk_BT)}$.

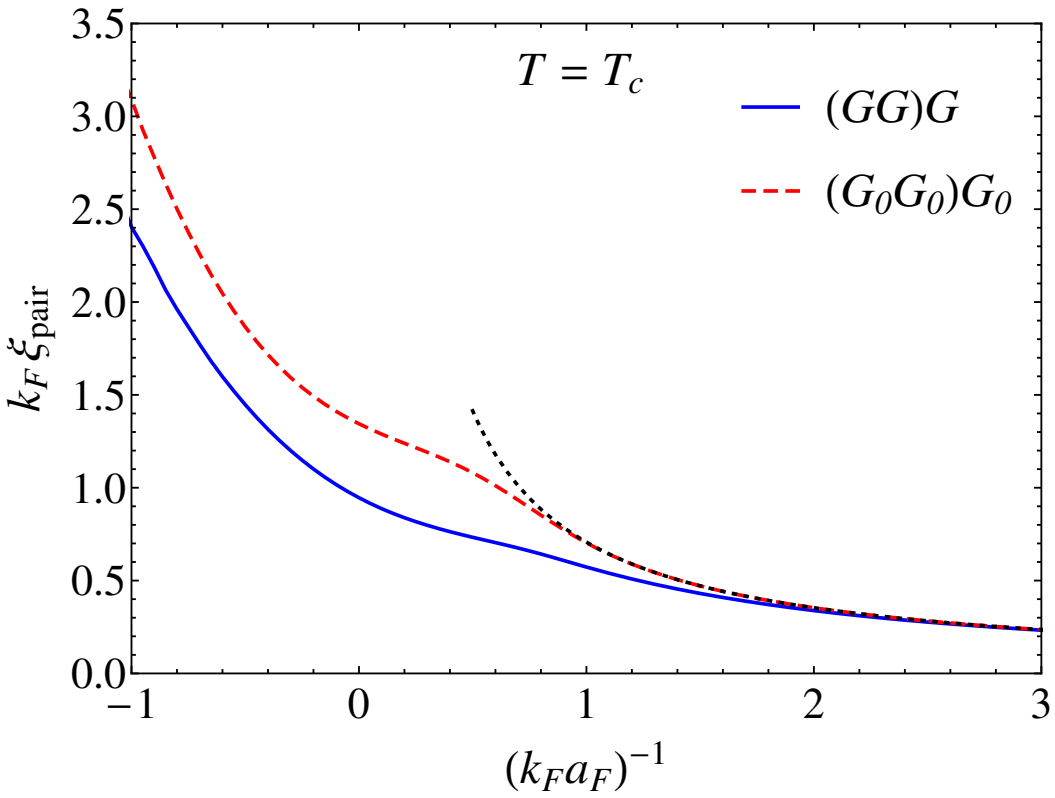

Figure 5.3: Pair coherence length $\xi_{\rm pair}$ calculated at the critical temperature T_c as a function of the coupling $(k_Fa_F)^{-1}$. The results are shown for the fully self-consistent (full line) and non-self-consistent (dashed line) t-matrix approaches. The dotted line represents the BEC limit value for the pair coherence length $\xi_{\rm pair}^{\rm BEC} = a_F/\sqrt{2}$.

Chapter 6

Pairing fraction

In this chapter, we address the problem of pair formation in the normal phase of an attractive Fermi gas. These preformed pairs are usually associated with the occurrence of a pseudo-gap in the density of states, which can be viewed as a carry-over of the pairing gap in the superfluid phase to the normal phase [28, 135, 148] (see Section 3.2.2).

Pairing in the normal phase was recently investigated in an experiment with a spin-balanced two-component Fermi gas of ^{6}Li [105], where the number of fermion pairs N_p was determined by converting all atom pairs to tightly-bound diatomic molecules which afterwards were detected. A brief description of the experimental procedure to measure the pairing fraction N_p/N_σ (where N_σ is the number of fermions per spin-state) is presented in the first section of this chapter. At first, the experimental results are compared to a simple statistical model of non-interacting atoms and molecules at equilibrium [4, 153]. Then, a preliminary many-body account of the experimental pairing fraction, based on the self-consistent t-matrix approach, is presented. This preliminary many-body approach is able to describe the experimental data in the BEC region ($(k_F a_F)^{-1} \gtrsim 0.5$) of the crossover. Finally, the many-body approach is improved and extended to the whole BCS-BEC crossover, obtaining good agreement with experimental data also for more intermediate couplings. Most of the results in this chapter have been presented in Refs. [77, 105].

6.1 Experimental approach to the pairing fraction

Let us start with a brief description of the experimental approach used in Ref. [105] to measure the pairing fraction N_p/N_σ on the BEC side of the crossover. The experimental system is a spin-balanced two-component Fermi gas of ^{6}Li atoms, where the two components are the states with $m_F = +1/2$ ($|\uparrow\rangle$) and $m_F = -1/2$ ($|\downarrow\rangle$) of the $F = 1/2$ hyperfine level of the ground state of ^{6}Li. These atoms are confined in a three-dimensional cigar-shaped trapping potential, generated by a focused dipole trap laser along the radial directions and by a magnetic field gradient along the axial direction.

In order to determine the pairing fraction N_p/N_σ, the particle numbers N_p and N_σ are measured separately. N_σ is obtained by means of spin-selective absorption imaging

of the $|\uparrow\rangle$ component using a σ^--polarized laser beam resonant with the D_2 transition of ^{6}Li ($\lambda = 671$ nm) [149]. All $|\uparrow\rangle$ atoms are counted regardless of whether they are free or bound in pairs. In order to determine the number of pairs N_p, all the pairs are transferred to states that are invisible in the previous detection scheme and the number of the remaining $|\uparrow\rangle$ atoms is measured via absorption imaging. The transfer of the pairs to an invisible state is performed with different methods, which produce consistent results. They are briefly described in the following.

6.1.1 Optical Transfer (OT) method

This transfer method is based on the resonant excitation of fermion pairs to a more strongly bound molecular state ($A^1\Sigma_u^+$, $v' = 68$) with a laser ($\lambda = 673$ nm) which is detuned by 2 nm from the atomic transition. Subsequently, the excited molecules quickly decay to undetected atomic or molecular states; see Fig. 6.1(a). This optical excitation of the fermion pairs occurs via an admixture of the molecular bound state $X^1\Sigma_g^+$, $v = 38$ to the fermion pair wave function [150].

If one ignores other loss processes, the number of fermion pairs decays exponentially as a function of the laser pulse length Δt, such that the measured total number $N_\sigma(\Delta t)$ of the $|\uparrow\rangle$ atoms as a function of time is given by

$$N_\sigma(\Delta t) = N_\sigma(0) - N_\mathrm{p}(1 - e^{-k_1 \Delta t}), \tag{6.1}$$

where $1/k_1$ is the time constant for the optical excitation. Figure 6.1(b) shows this decay for five different initial temperatures T/T_F at a magnetic field of 726 G. By fitting Eq. (6.1) to the measured data one is able to extract the pair number N_p. Besides the photoexcitation of pairs, a loss in N_σ could in principle also be induced by photoassociation of two free atoms. However, it was made sure its rate is negligible with respect to the photoexcitation rate k_1. For example, in figure 6.1(b) the photoassociation time scale is at least of the order of 33 ms. Closer to the Feshbach resonance, where the rates for photoassociation and pair excitation become more comparable, a short (0.3 ms) expansion of the cloud is performed before applying the laser pulse, in order to reduce the density of the gas. This, in turn, reduces the photoassotiation rate. It was checked that during the expansion the fermion pairs did not break up.

In general the OT method works very well up to magnetic fields of about $B = 820$ G, close to the Feshbach resonance ($B_\mathrm{res} = 832$ G [151, 152]). There, one start to observe marked deviations from the exponential decay in Eq. (6.1), so the experimental data were acquired only for magnetic fields below 820 G, where the analysis is unequivocal.

6.1.2 Magnetic Transfer (MT) method

This method, instead, consists in quickly increasing the binding energy of the pairs by ramping the magnetic field at 20 G/ms down to 550 G; see Fig. 6.1(c). At 550 G the fermion pairs cannot be resonantly excited anymore by the imaging laser and become invisible to the detection scheme. N_p is determined as the difference between the number of spin-up fermions (N_σ) measured before the ramp and the number of unbound atoms

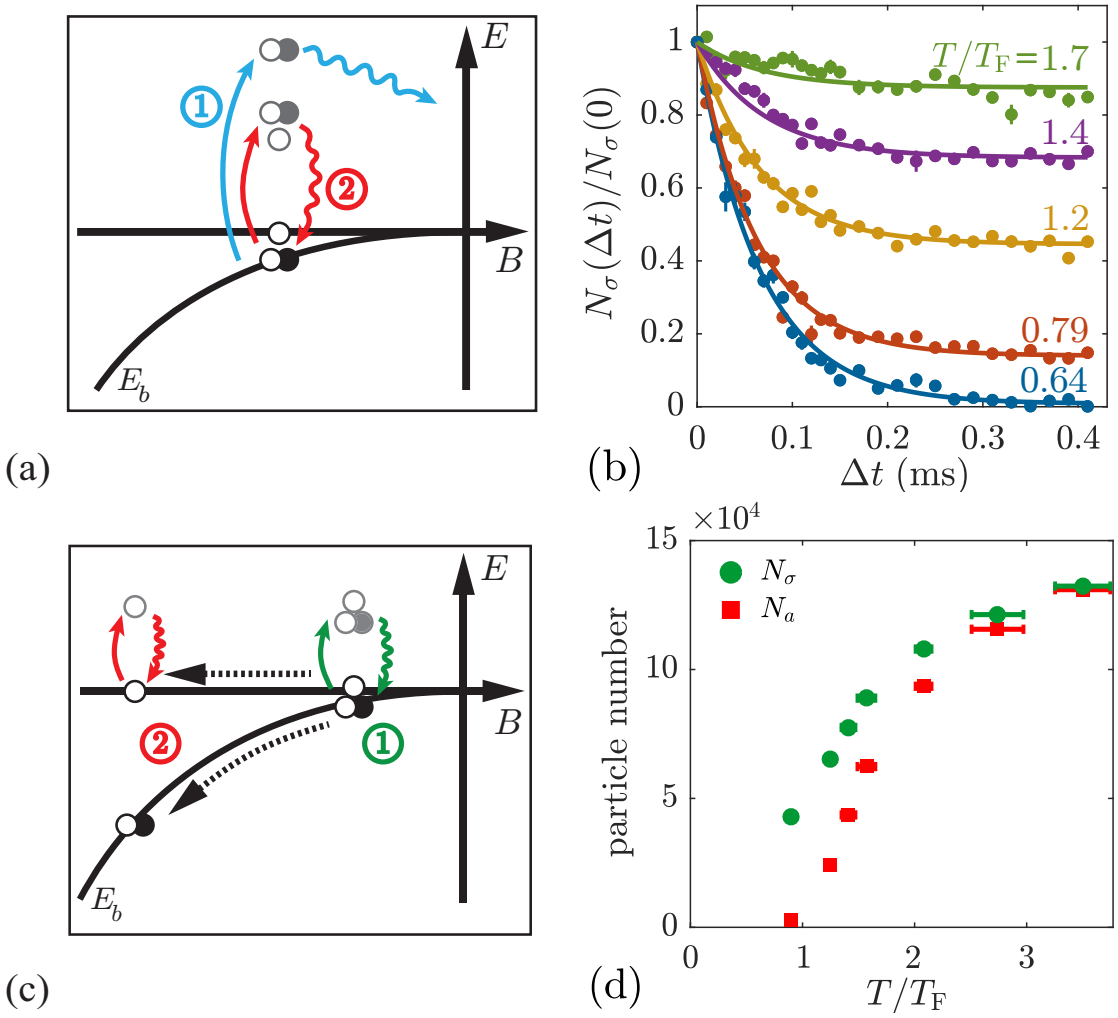

Figure 6.1: Measurement of the number of fermion pairs. (a, b) Optical transfer method. A resonant laser pulse transfers pairs to states which are invisible to the detection scheme [blue arrows (1)]. The total number $N_\sigma(\Delta t)$ of atoms in the $|\uparrow\rangle$ state is measured by absorption imaging [red arrows (2)]. (b) shows $N_\sigma(\Delta t)/N_\sigma(0)$ as a function of the pulse length Δt at a magnetic field of 726 G for various temperatures $T/T_F = (0.64, 0.79, 1.2, 1.4, 1.7)$. The solid lines are fit curves using Eq. (6.1). (c, d) Magnetic transfer method. Using absorption imaging, the particle number $N_\sigma = N_a + N_p$ is measured at the magnetic field (1) and the number of unbound atoms N_a is measured after a fast ramp to (2). (d) shows the measured particle numbers at (1) ($B = 726$ G, green solid circles) and at (2) ($B = 550$ G, red solid squares) for various temperatures T/T_F.

(N_a) obtained after the ramp. Figure 6.1(d) shows these particle numbers for different temperatures at a magnetic field of 726 G.

Measurements with the MT method were not performed for magnetic fields higher than 750 G because of technical limitations for the ramping speed. In fact, if the field ramp duration ($\sim$ 10 ms for the case of 750 G) becomes comparable to the equilibration time for the atom-molecule mixture (a few milliseconds at 750 G) the measurement does not yield the correct pair number anymore. This restriction of the magnetic field ramp implies that one cannot use the MT method in the crossover regime, but only in the far BEC regime. There, however, the MT method was quite useful to check for consistency with the OT method.

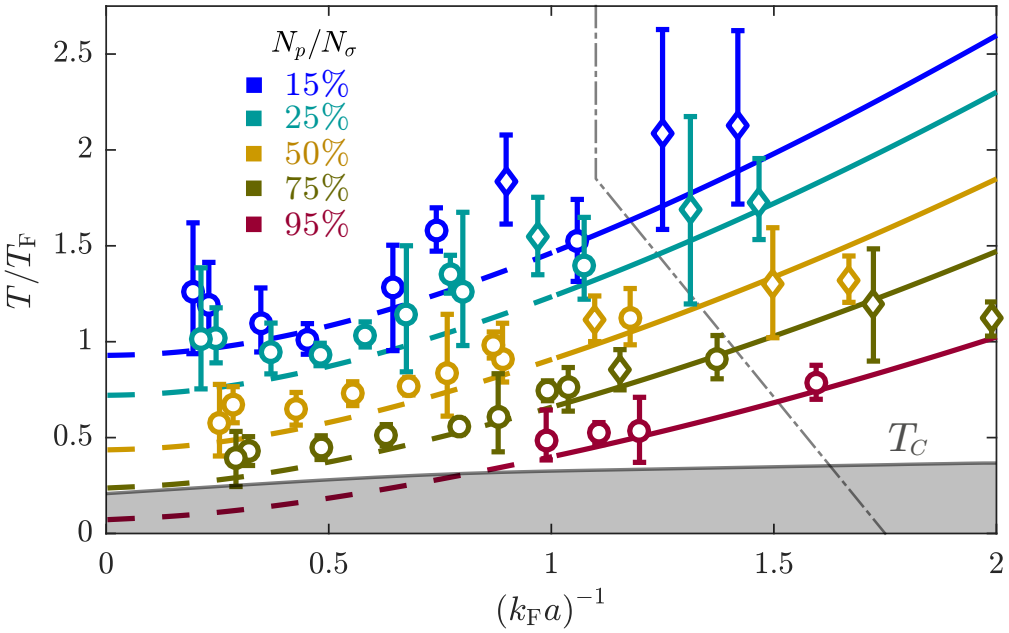

Figure 6.2: Experimental contour plots of the pairing fraction N_p/N_σ in the temperature-coupling phase diagram of the trapped system on the BEC-side of the Feshbach resonance. The circles (diamonds) are measurements obtained with the OT (MT) method. The thick solid and dashed lines are calculations based on a classical model of non-interacting atoms and molecules (cf. Refs. [4, 153] and Appendix H). They are dashed in the crossover region where the classical model is expected to be no longer valid. The error bars include both a statistical and a systematic part, i.e. the standard deviation of the mean of 10 temperature measurements and the uncertainty in determining the molecule fraction from the fit, respectively. The upper-right area bounded by the gray dash-dotted line exhibits $> 5\,\%$ particle loss due to inelastic collisions on the timescale of a measurement. The gray shaded area indicates the superfluid phase below T_c, where T_c is calculated within the self-consistent t-matrix approach (cf. Fig. 4.3).

6.1.3 Experimental results

The experimental results for the pairing fraction $N_{\rm p}/N_\sigma$ obtained with both methods are shown in Figure 6.2 (circles, OT method; diamonds, MT method). The data are shown as contour plots fo fixed pairing fraction $N_{\rm p}/N_\sigma$ on the BEC side of the temperature-vs-coupling phase diagram.

The area on the right-hand side of Fig. 6.2, as bounded by the thin dash-dotted line, marks a region where a non-negligible loss of particles is observed (>5%) due to inelastic collisions of bound pairs. In order to simplify the discussion, only data points outside this area are considered.

The solid and dashed lines in Fig. 6.2 correspond to a classical statistical mechanics approach treating the particles as a canonical ensemble of non-interacting molecules and atoms in chemical equilibrium (cf. Refs. [4, 153] and Appendix H). Surprisingly, one finds that the model remains in good agreement with the measured data even in the crossover regime. However, this classical model can be considered valid only in the deep BEC regime. For this reason, it is necessary to develop a true many-body theory to describe the pairing fraction throughout the whole BCS-BEC crossover.

6.2 Many-body theoretical approach to the pairing fraction

Let us consider now the many-body approach to calculate the pairing fraction. We begin by introducing the composite pair propagator

$$\mathcal{G}_B(x,x') = -\langle T_\tau[\hat{\Psi}_B(x)\hat{\Psi}_B^\dagger(x')]\rangle\,, \tag{6.2}$$

where $x=(\boldsymbol{r},\tau)$ groups the spatial position $\boldsymbol{r}$ and imaginary time τ and $\hat{\Psi}_B(\boldsymbol{r})$ is a bosonic field operator. In terms of this propagator, the total number of pairs is given by

$$N_{\rm p} = -\int d\boldsymbol{r}\,\mathcal{G}_B(x,x^+) = -\int d\boldsymbol{r}\int\frac{d\boldsymbol{Q}}{(2\pi)^3}\frac{1}{\beta}\sum_\nu e^{i\Omega_\nu\eta}\,\mathcal{G}_B(\boldsymbol{Q},\Omega_\nu). \tag{6.3}$$

In the last line of Eq. (6.3) a homogeneous system has been assumed, for which one may simply write $N_{\rm p}=\mathcal{V}\,n_{\rm p}$ where $\mathcal{V}$ is the volume occupied by the system and $n_{\rm p}$ the pair density (for the extension to the trapped system, see the end of this section).

To the extent that these bosonic entities are made up of fermion pairs, the bosonic operator $\hat{\Psi}_B(\boldsymbol{r})$ has to be related to its fermionic counterparts $\hat{\psi}_\sigma(\boldsymbol{r})$, where $\sigma=(\uparrow,\downarrow)$ is the spin projection. This can be achieved by setting

$$\hat{\Psi}_B(\boldsymbol{r}) = \int d\boldsymbol{\rho}\,\phi(\boldsymbol{\rho})\,\hat{\psi}_\downarrow(\boldsymbol{r}-\boldsymbol{\rho}/2)\,\hat{\psi}_\uparrow(\boldsymbol{r}+\boldsymbol{\rho}/2) \tag{6.4}$$

where $\phi(\boldsymbol{\rho})$ is a suitable function that should itself embody the correlations within a fermion pair. We postpone the discussion on this function to Sections 6.3 and 6.4.[1]

[1]The definitions (6.2) and (6.4), together with the two-body bound state expression (2.66) for $\phi(\boldsymbol{\rho})$, were originally used in Ref. [121] to describe condensed composite bosons well below the superfluid transition temperature T_c with fermions treated within the mean-field approximation [2].

With the definition (6.4) for the bosonic field, and using the Nambu representation of the fermionic operators (2.135), the composite pair propagator $\mathcal{G}_B$ of Eq. (6.2) can be written in terms of the two-particle correlation function L of Eq. (2.138):

$$\mathcal{G}_B(\boldsymbol{r}\tau, \boldsymbol{r}'\tau') = -\int d\boldsymbol{\rho}\int d\boldsymbol{\rho}'\phi(\boldsymbol{\rho})\phi^*(\boldsymbol{\rho}')\, L(1,2;1',2') \tag{6.5}$$

with the following identification of the variables

$$\begin{aligned} 1 &= (\boldsymbol{r}+\boldsymbol{\rho}/2, \tau, \ell_1 = 1),\\ 2 &= (\boldsymbol{r}'-\boldsymbol{\rho}'/2, \tau', \ell_2 = 2),\\ 1' &= (\boldsymbol{r}-\boldsymbol{\rho}/2, \tau^+, \ell_{1'} = 2),\\ 2' &= (\boldsymbol{r}'+\boldsymbol{\rho}'/2, \tau'^+, \ell_{2'} = 1), \end{aligned} \tag{6.6}$$

where $\tau^+ = \tau + \eta$ with $\eta \to 0^+$.[2]

Hereafter, it will be understood that only the terms that survive once carried over from below to above T_c will be retained in the expression (6.5), as discussed in Section 2.6.

For a homogeneous system, one can further make use of the Fourier representation and rewrite Eq.(6.5) as

$$\begin{aligned} \mathcal{G}_B(\boldsymbol{Q}, \Omega_\nu) = -\int \frac{d\boldsymbol{p}}{(2\pi)^3}\frac{1}{\beta}\sum_n \int \frac{d\boldsymbol{p}'}{(2\pi)^3}\frac{1}{\beta}\sum_{n'} \\ \times \phi(\boldsymbol{p}+\boldsymbol{Q}/2)\phi(\boldsymbol{p}'+\boldsymbol{Q}/2)\, L_{22}^{11}(\boldsymbol{p}\,\omega_n, \boldsymbol{p}'\omega_{n'}; \boldsymbol{Q}\,\Omega_\nu). \end{aligned} \tag{6.7}$$

This expression will be used in Eq. (6.3) to obtain the number of pairs N_p. If one then solves for the many-particle T-matrix of Eq. (2.141), enters the result in Eq. (2.142) for L, and uses the relation $T_{11}^{22} = T_{11} = -\Gamma$ (cf. discussion at the end of of Section 2.6), Eq. (6.7) reduces eventually to the form [121]:

$$\mathcal{G}_B(\boldsymbol{Q}, \Omega_\nu) = -\mathcal{F}_2(\boldsymbol{Q}, \Omega_\nu) - \mathcal{F}_1(\boldsymbol{Q}, \Omega_\nu)^2\, \Gamma(\boldsymbol{Q}, \Omega_\nu)\,. \tag{6.8}$$

Here,

$$\mathcal{F}_j(\boldsymbol{Q}, \Omega_\nu) = \int \frac{d\boldsymbol{p}}{(2\pi)^3}\, \phi(\boldsymbol{p}+\boldsymbol{Q}/2)^j\, \frac{1}{\beta}\sum_n G(\boldsymbol{p}+\boldsymbol{Q}, \omega_n + \Omega_\nu) G(-\boldsymbol{p}, -\omega_n) \tag{6.9}$$

are "form factors" associated with the particle-particle bubble where $j = (1, 2)$, and Γ is the particle-particle propagator (2.106) for the fully self-consistent t-matrix approach. For a detailed account of the numerical procedures to calculate the form factors (6.9) and the number of pairs (6.3), see Appendix G.

In the preliminary theoretical account aimed to the describe only the BEC side of the crossover (see Section 6.3), the first term on the right-hand side of Eq. (6.8) was not

[2]Note that, for this choice of the Nambu indices in L, a self-consistent t-matrix self-energy of the form (2.149), and a gas in the normal phase above T_c, one can take the kernel Ξ of the T-matrix equation (2.141) in the BCS form (2.145). For more details, see Appendix D.

retained, as it becomes negligible in the BEC limit (cf. Appendix H). This term will be referred to as the "unbound" term, as opposed to the "bound" term discussed below.

In the more complete theoretical account presented in Section 6.4, instead, we are going to keep this "unbound" term and show that it gives a non-negligible contribution to $N_{\rm p}$, through the pairing correlations contained both in the fermionic single-particle Green's function G and in the function $\phi(\boldsymbol{p})$ that enter the expression (6.9) with $j = 2$. Accordingly, through this term spin-↑ and spin-↓ fermions correlate with each other indirectly via their separate interaction with the environment.

In contrast, the second term on the right-hand side of Eq. (6.8) is referred to as the "bound" term, because in this case spin-↑ and spin-↓ fermions correlate with each other directly through their inter-particle attractive interaction. In Appendix H, it will be shown that the result for $N_{\rm p}$ obtained from this "bound" term reduces, in the BEC limit, to that of the statistical model of atom-molecule equilibrium introduced in Refs. [4, 153] and shown in Fig. 6.2.

Finally, in order to compare with the experimental data of Fig. 6.2, the theoretical approach must also take into account the harmonic trapping potential $V(\boldsymbol{r})$ that contains the Fermi gas. As in Section 4.1, one can adopt a local density approach and replace $\mu \to \mu(\boldsymbol{r}) = \mu_0 - V(\boldsymbol{r})$ in the expression (6.8) for the bosonic propagator $\mathcal{G}_B(\boldsymbol{Q}, \Omega_\nu)$. Through Eq. (6.17), one thus obtains the local density of the pairs $n_{\rm p}(\boldsymbol{r})$ as a function of the position $\boldsymbol{r}$ within the trap. One can then integrate over $\boldsymbol{r}$ and obtain the number of pairs:

$$N_{\rm p} = \int d\boldsymbol{r}\, n_{\rm p}(\boldsymbol{r}) = \int d\boldsymbol{r} \int \frac{d\boldsymbol{Q}}{(2\pi)^3} \frac{1}{\beta} \sum_\nu \mathcal{G}_B(\boldsymbol{Q}, \Omega_\nu; \mu(\boldsymbol{r})). \tag{6.10}$$

The number of atoms in a spin component N_σ is instead obtained by integrating the density profile $n_\sigma(\boldsymbol{r}) = n(\boldsymbol{r})/2$ over $\boldsymbol{r}$ (see Eqs. (4.2) and (4.3)).

6.3 Preliminary approach to the pairing fraction on the BEC side of the crossover

On physical grounds, at sufficiently low temperature in the BEC regime it is reasonable to take $\phi(\boldsymbol{\rho})$ in the expression (6.4) as the (normalized) bound-state wave function of the fermionic two-body problem *in vacuum* (2.66)

$$\phi_b(\boldsymbol{\rho}) = \frac{1}{\sqrt{2\pi a_F}} \frac{e^{-\rho/a_F}}{\rho} \tag{6.11}$$

where $\rho = |\boldsymbol{\rho}|$, whose Fourier transform is (2.65)

$$\phi_b(\boldsymbol{p}) = \sqrt{\frac{8\pi}{a_F}} \frac{1}{\boldsymbol{p}^2 + a_F^{-2}}\,. \tag{6.12}$$

Using this expression for $\phi(\boldsymbol{\rho})$, and retaining only the "bound" term on the right side of Eq. (6.8), we can obtain a preliminary account for the pairing fraction that is valid in the BEC regime.

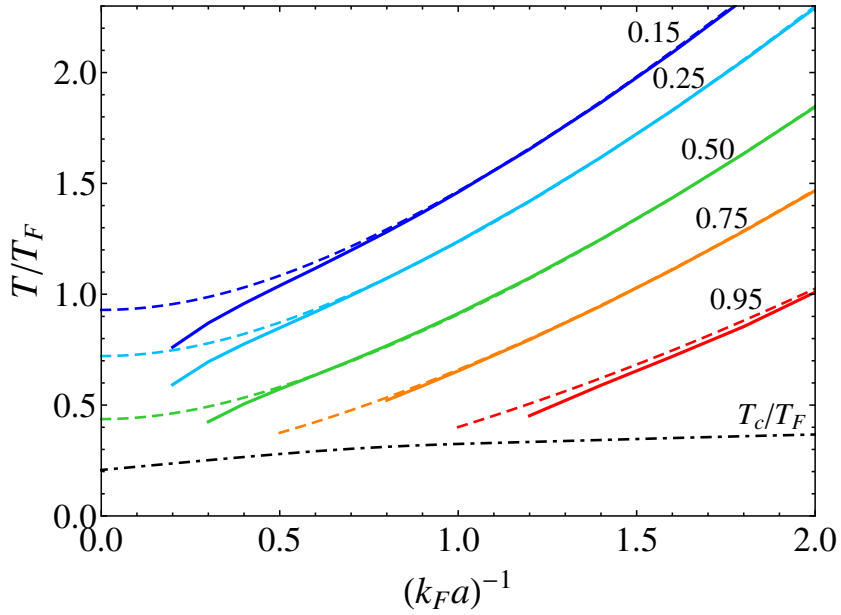

Figure 6.3: Theoretical contour plots of the pairing fraction $N_{\rm p}/N_\sigma$ on the BEC side of the temperature-coupling phase diagram of the trapped system for both the many-body preliminary approach of this section (full lines) and the classical equilibrium model (dashed lines). The value of the pairing fraction $N_{\rm p}/N_\sigma$ is reported above each line. The dash-dotted line corresponds to T_c calculated within the self-consistent t-matrix approach (cf. Fig. 4.3).

In Figure 6.3, the results for the pairing fraction for the trapped system within this preliminary approach are compared to the classical atom-molecule equilibrium model, which was already shown in Fig. 6.2 together with the experimental data. From the comparison, we see that the results for two models essentially coincide up to coupling $(k_F a_F)^{-1} \simeq 0.5$, notwithstanding the fact that the many-body theory includes a much more complete description of the system with respect to the classical model. This explains the surprising agreement between the classical model and the experimental data of Fig. 6.2.

For more intermediate couplings ($(k_F a_F)^{-1} \lesssim 0.5$), however, also the many-body theory appears to fail, predicting a downturn of the contour plots at fixed pairing fraction. This is directly related to the fact that the expression (6.11) for $\phi(\boldsymbol{\rho})$ loses any physical meaning close to unitarity. A more general expression for $\phi(\boldsymbol{\rho})$ is then needed if one wants to describe the pairing fraction in the crossover region. In the next Section, we show how this generalization can be performed.

6.4 Extension to the whole crossover: definition of $\phi(\boldsymbol{\rho})$ in terms of pair correlations

To account for the experimental data of Fig. 6.2 in a comprehensive way, the function $\phi(\boldsymbol{\rho})$ with which the projection is performed in Eq. (6.4) should acquire a more general form than the expression (6.11), which is expected to be valid only in the BEC regime at low temperature. Accordingly, in what follows we replace the expression (6.11) by a more general form obtained from the pair correlation function $g_{\uparrow\downarrow}(\boldsymbol{\rho})$ studied in Chapter 5, a form which can thus be utilized even past unitarity towards the BCS regime and up to a temperature of even several times T_F.

In Section 5.3 we verified that, in the BEC limit and at sufficiently low temperatures, $g_{\uparrow\downarrow}(\boldsymbol{\rho})$ reduces to the product of the density $n_\sigma = n/2$ of a single fermionic species times the square of the wave function (6.11) corresponding to the fermionic two-body problem. This suggests that the function $\phi(\boldsymbol{p})$, to be utilized in the form factors (6.9), can be extracted from the pair correlation function $g_{\uparrow\downarrow}(\boldsymbol{\rho})$ also away from the BEC limit and at high temperatures. To this end, we adopt the following strategy.

We begin by fitting the spatial profiles of the function $\frac{(4\pi)^2}{C}\rho^2 g_{\uparrow\downarrow}(\rho)$ of Fig. 5.1 with the expression

$$\rho^2\phi(\rho)^2 = \exp(-2\rho/a_F)\,\exp(-2b\rho^2)\,, \tag{6.13}$$

where $\rho = |\boldsymbol{\rho}|$ and b is a parameter that depends on coupling and temperature (note that the function (6.13), too, has unit value at $\rho = 0$). This fit is meant to extract the relevant features of the short-range behavior of $g_{\uparrow\downarrow}(\rho)$ and average out its oscillations about zero (whenever present).

In Fig. 6.4 some examples of these fits are shown for $T/T_F = 0.5$ and three different couplings across the crossover, together with the corresponding value of the parameter b.

One can then take the square root of the expression (6.13) to extract $\phi(\rho)$, and multiply the result by a suitable normalization factor $\mathcal{N}$, thus writing:

$$\phi(\rho) = \mathcal{N}(a_F, b)\,\frac{e^{-\rho/a_F}}{\rho}\,\exp(-b\rho^2) \tag{6.14}$$

with

$$\mathcal{N}(a_F, b) = \frac{1}{\pi^{3/4}}\Big(\frac{b}{2}\Big)^{1/4}\frac{\exp[-\frac{1}{4ba_F^2}]}{\sqrt{\mathrm{erfc}[\frac{1}{\sqrt{2b}a_F}]}} \tag{6.15}$$

where $\mathrm{erfc}(z)$ is the complementary error function of (complex) argument z [174]. Note that the two-body wave function (6.11) is recovered for $b \to 0$. Finally, one can take the Fourier transform of the expression (6.14) and obtain the desired result:

$$\phi(\boldsymbol{p}) = \frac{2\pi^{3/2}\mathcal{N}(a_F, b)}{\sqrt{b}\,p}\,\mathrm{Im}\Bigg\{\exp\left[\frac{\big(a_F^{-1} - ip\big)^2}{4b}\right]\mathrm{erfc}\left(\frac{a_F^{-1} - ip}{2\sqrt{b}}\right)\Bigg\} \tag{6.16}$$

where $p = |\boldsymbol{p}|$. This expression recovers Eq. (6.12) in the limit $b \to 0$.

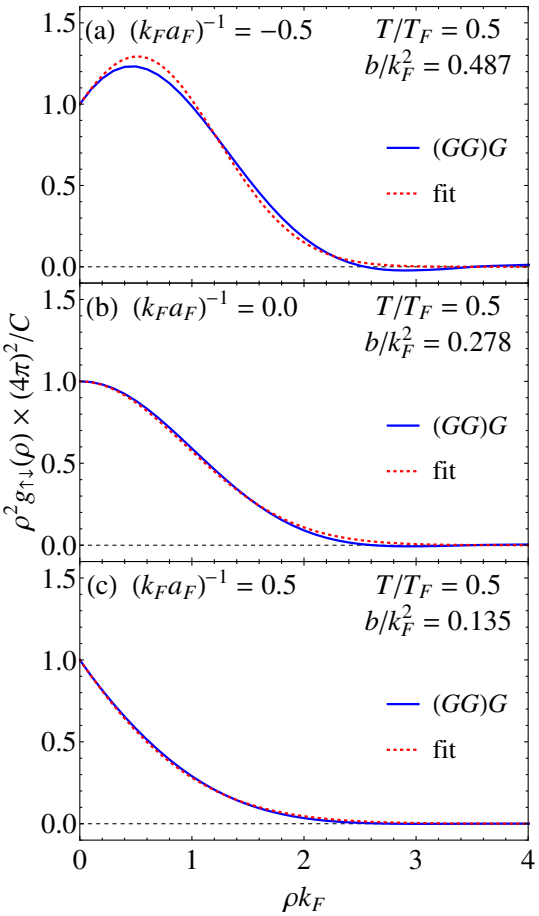

Figure 6.4: Spatial profiles of $\frac{(4\pi)^2}{C}\rho^2\, g_{\uparrow\downarrow}(\rho)$ calculated within the self-consistent t-matrix approach (full lines) and their corresponding fit with their expression (6.13) (dotted lines) for the temperature $T/T_F = 0.5$ and couplings $(k_F a_F)^{-1} = (-0.5, 0.0, 0.5)$. The corresponding value of the fit parameter b is reported in each panel.

Figure 6.5 shows the behavior of the parameter b obtained in this way, over a wide range of coupling and temperature. In particular, for sufficiently high temperature and irrespective of coupling, b is expected to become proportional to λ_T^{-2} where $\lambda_T = \sqrt{\frac{2\pi}{mk_BT}}$ is the thermal wavelength. To evidence this linear behavior of b vs T at high temperature, the inset of Fig. 6.5 plots the derivative of b with respect to T for the same temperature range and couplings of the main panel. In all cases, we have found that, at high temperature, this derivative is well reproduced by the expression $\frac{k_B}{2m}\frac{\partial b}{\partial T} = 0.25 - 0.175(k_F a_F)^{-1}\sqrt{T_F/T}$.

As a final note, the fitting function $\phi(\rho)$ given by Eq. (6.14) focuses on the short-range (exponentially decaying) part of the pair-correlation function $g_{\uparrow\downarrow}(\boldsymbol{\rho})$, which is dominated by the intra-pair correlations of relevance here. It thus disregards a possible long-range (power-law decaying) part of $g_{\uparrow\downarrow}(\boldsymbol{\rho})$, which may include correlations between spin-$\uparrow$ and

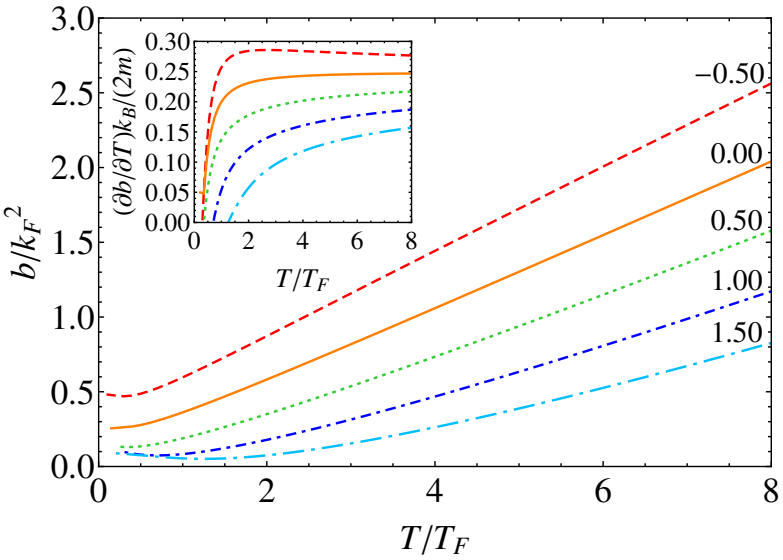

Figure 6.5: Temperature dependence of the parameter b of the expressions (6.14-6.16) for several values (reported above each line) of the coupling $(k_F a_F)^{-1}$ across the BCS-BEC crossover. The inset shows the derivative of b with respect to T for the same couplings of the main panel to better evidence the high-temperature behavior.

spin-$\downarrow$ fermions belonging to different pairs (although this long-range part does not occur within the self-consistent t-matrix approach adopted here).

6.5 Results for a homogeneous gas

We can now calculate the pair density n_p for the homogeneous system, given by

$$n_\mathrm{p} = -\int \frac{d\boldsymbol{Q}}{(2\pi)^3} \frac{1}{\beta} \sum_\nu e^{i\Omega_\nu \eta} \mathcal{G}_B(\boldsymbol{Q}, \Omega_\nu) \tag{6.17}$$

together with the fermionic density n_σ given by Eq. (2.108), to obtain the pairing fraction n_p/n_σ as a function of coupling and temperature (see Appendix G for the details of the calculation).

To begin with, Fig. 6.6 compares the pairing fraction n_p/n_σ at T_c over a wide range of the coupling $(k_F a_F)^{-1}$, as obtained by the fully self-consistent and non-self-consistent t-matrix approaches. As for other thermodynamic quantities (cf. Section 3.1), also in this case the fully self-consistent approach proves superior to the non-self-consistent one, to the extent that the ratio n_p/n_σ should never exceed unity. Accordingly, from now on results obtained by the fully self-consistent approach will only be presented. In addition, the use of the two-body form (6.12) for $\phi(\boldsymbol{p})$ in the form factors (6.9) is seen to lead to unstable results upon entering the unitary regime with $(k_F a_F)^{-1} \lesssim +1$, as expected from the preliminary analysis of Section 6.3.

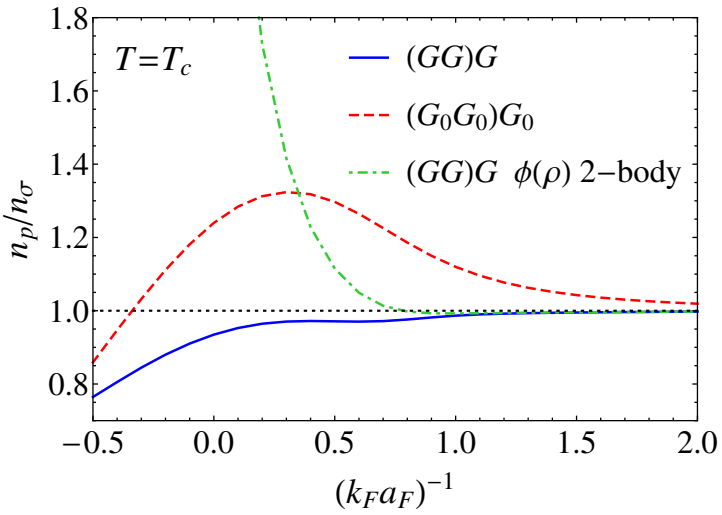

Figure 6.6: Pair fraction $n_{\rm p}/n_\sigma$ at T_c vs $(k_Fa_F)^{-1}$, obtained by the fully self- consistent (full line) and non-self-consistent (dashed line) t-matrix approaches. In both cases, $\phi(\boldsymbol{p})$ in the form factors (6.9) is obtained from the expression (6.16) within the respective approximations for the pair correlation function. Also shown is the result obtained by the fully self-consistent calculation, with $\phi(\boldsymbol{p})$ approximated instead by the two-body form (6.12) (dashed-dotted line).

In Fig. 6.7 the pair fraction $n_{\rm p}/n_\sigma$ is shown as a function of temperature for a selected number of couplings across unitarity. In particular, this figure compares the results obtained by including (full lines) or neglecting (dashed lines) the "unbound" term represented by the term $-\mathcal{F}_2$ on the right-hand side of Eq. (6.8). One sees that inclusion of this unbound term over and above the "bound" term (represented by the second term on the right-hand side of Eq. (6.8)) leads to substantial differences, especially in the unitary regime at low temperature.

Fig. 6.8 shows instead three contour plots where a given value of the pair fraction $n_{\rm p}/n_\sigma$ is seen to evolve in the temperature-vs-coupling phase diagram. Similarly to what was done in Fig. 6.7, for each of the three values of $n_{\rm p}/n_\sigma$ here reported the numerical results have been obtained by including (full lines) or neglecting (dashed lines) the unbound term in Eq. (6.8). In all cases, the difference between these two sets of results turns out to be substantial as soon as entering the unitary regime with $(k_Fa_F)^{-1} \lesssim +1$. This implies that, in this regime of most physical interest, the fermionic character of the constituent particles (included in the "unbound" term) reveals itself. As a consequence, this counting has to rely on filtering the occurrence of fermionic correlations, and not merely on signaling the presence of bound pairs which would instead apply to the molecular regime with $(k_Fa_F)^{-1} \gtrsim +1$.

To confirm this point of view, Fig. 6.8 also shows for comparison the contour plots of $n_{\rm p}/n_\sigma$ corresponding to the statistical model (dotted lines) for the homogeneous system,

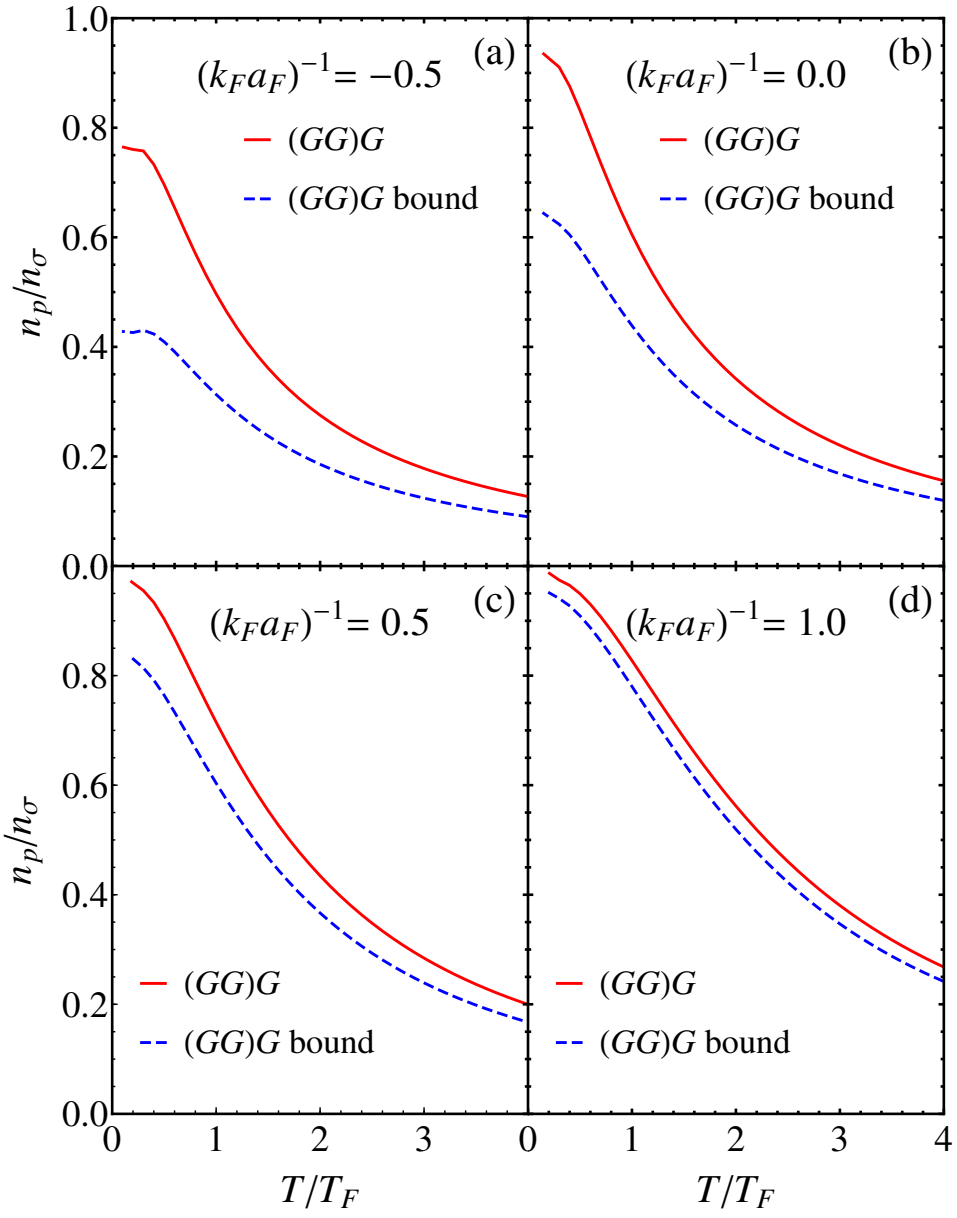

Figure 6.7: Pair fraction $n_{\rm p}/n_\sigma$ vs T/T_F for four couplings, obtained by the fully self-consistent t-matrix approach including (full lines) or neglecting (dashed lines) the "unbound" term in Eq. (6.8). In the second case, only the "bound" term is retained in Eq. (6.8), as specified in the panels.

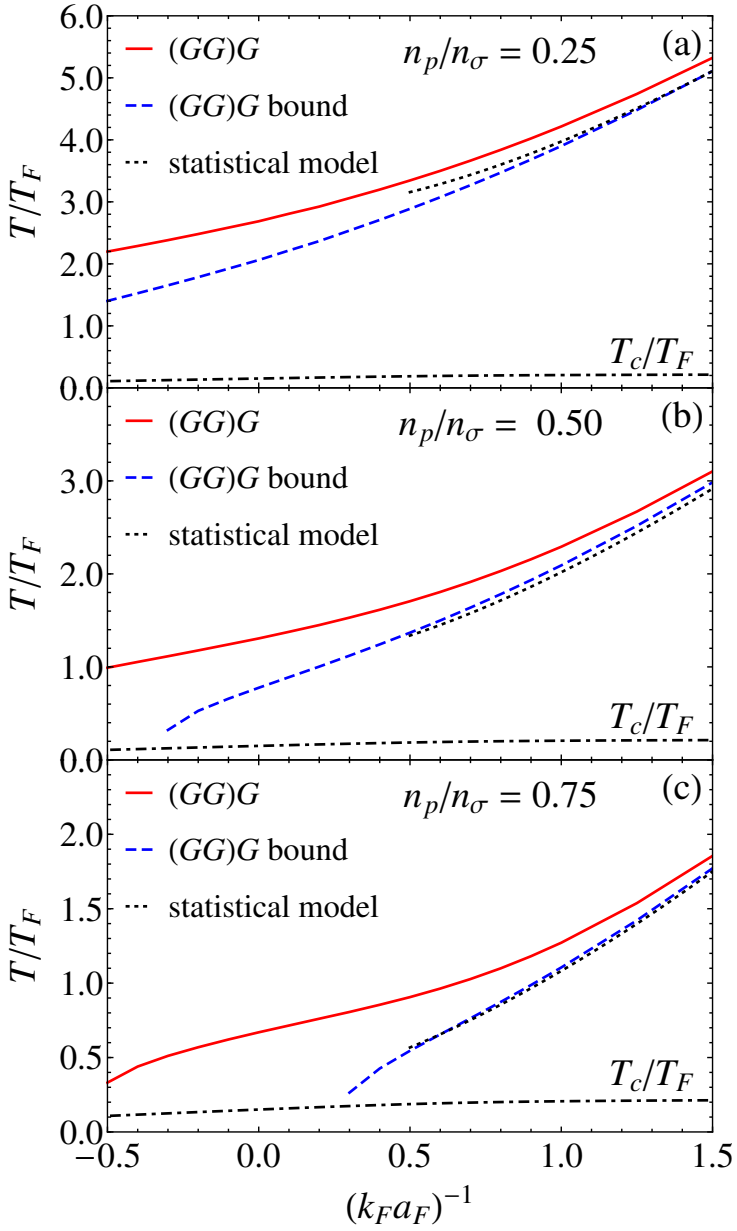

Figure 6.8: Contour plots of the pair fraction $n_{\rm p}/n_\sigma$ in the temperature-coupling phase diagram of the homogeneous system, obtained by the fully self-consistent t-matrix approach by including (full lines) or neglecting (dashed lines) the "unbound" term in Eq. (6.8). Also shown are the results of the statistical model obtained from Eq. (6.18) (dotted lines). In each panel, the coupling dependence of the critical temperature T_c (in units of T_F) is reported (dashed-dotted line), which sets the boundary of the normal phase for the homogeneous system.

as obtained from the law of mass action

$$\frac{n_{\rm f}^2}{n_{\rm p}} = \frac{1}{8}\left(\frac{mk_BT}{\pi}\right)^{3/2} e^{-\varepsilon_0/k_BT} \tag{6.18}$$

where $\varepsilon_0 = (ma_F^2)^{-1}$ is the two-body binding energy, which results from the integrals in Eq. (H.11) of Appendix H by neglecting ± 1 in the denominators therein. It turns out that the results of the statistical model coincides with those of the quantum many-body approach that includes only the bound term, but only at most up to $(k_F a_F)^{-1} \approx 0.6$ after which the molecular regime with the two-body wave function (6.11) loses its meaning.

6.6 Results for the trapped system and comparison with experimental data

Figure 6.9 presents the comparison of the pairing fraction $N_{\rm p}/N_\sigma$ obtained by our quantum many-body calculation with the experimental data of Fig. 6.2 over the temperature-coupling phase diagram (where k_F and T_F now refer to the trapped system, as defined in Chapter 4). The comparison is made for three characteristic values of $N_{\rm p}/N_\sigma$. In all cases, good agreement is obtained between theory and experiment.

In particular, this comparison shows that the contribution of the unbound term significantly improves the agreement of our calculations with the experimental data, despite the presence of the trap which acts to suppress the entity of this contribution (which is evident by comparing Figs. 6.8 and 6.9). This suggests that the experimental data probe indeed the pairing correlations between spin-up and spin-down fermions as defined in our formalism.

Finally, from this comparison one can argue that the crossover, between the pseudo-gap regime (where the fermionic character of the constituent particles matters) and the molecular regime (where only the presence of bosonic pairs is relevant), sets in about where the theoretical results for $N_{\rm p}/N_\sigma$, obtained with and without the unbound term, start departing from each other. This argument cannot be made in terms of the statistical atom-molecule model, that misses the contribution of the unbound term.

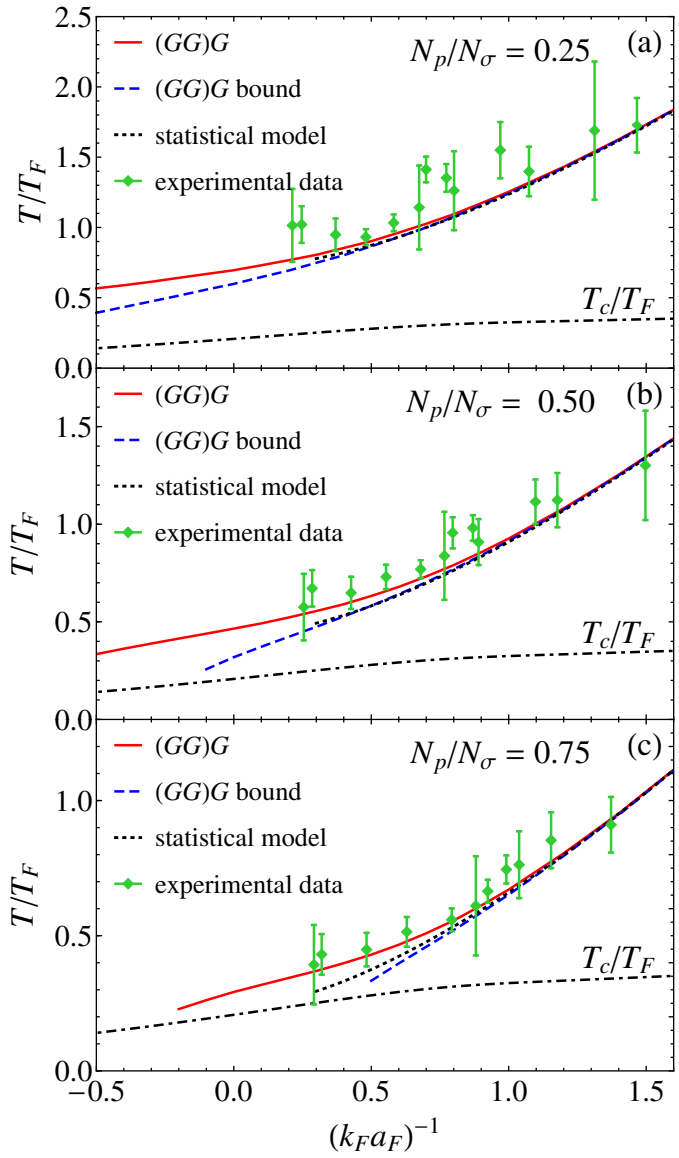

Figure 6.9: Contour plots of the pair fraction $N_{\rm p}/N_\sigma$ in the temperature-coupling phase diagram of the trapped system, obtained by the fully self-consistent t-matrix approach by including (full lines) or neglecting (dashed lines) the "unbound" term in Eq. (6.8). The theoretical curves are compared with the experimental data of Ref. [105] (diamonds with vertical error bars). For $(k_F a_F)^{-1} \gtrsim 0.3$ the results of the statistical model obtained from Eq. (H.15) of Appendix H are also shown (dotted lines). In each panel, the coupling dependence of the critical temperature T_c (in units of T_F) is reported (dashed-dotted line), which sets the boundary of the normal phase for the trapped system.

Chapter 7

Preliminary results for the spin-imbalanced system

The effects of an imbalance of the spin populations in an attractive Fermi gas were studied shortly after the development of the BCS theory. Within the BCS approach, Clogston, Chandraseckhar and Sarma were the first to address the problem [123–125], finding that a spin-population imbalance introduces a phase transition between the superfluid and the normal phase, with a complete suppression of superfluidity when the semi-difference of the chemical potentials of the two species $h = (\mu_\uparrow - \mu_\downarrow)/2$ exceeds $\Delta/\sqrt{2}$, where Δ is the pairing gap. In Ref. [125], it was found that the normal-superfluid phase transition, that is of second order for the balanced Fermi gas, becomes of first order at low temperatures.

An alternative solution for the superfluid phase of a spin-imbalanced Fermi gases at low temperature was given independently by Fulde and Ferrel (FF) [154] and Larkin and Ovchinnikov (LO) [155]. The idea is that the mismatch of the Fermi surfaces of the two spin components favors the existence of a spatially inhomogeneous superfluid phase, usually referred to as the FFLO phase, where pairing between fermions with opposite spins happens at a finite momentum $\boldsymbol{Q}$ instead than at $\boldsymbol{Q} = 0$ as in BCS theory. More recently, the FFLO instability was analyzed thoroughly in the weak-coupling limit in Ref. [156], where it was found in particular that the transition from the normal phase to the FFLO phase is weakly first order.

Away from the weak-coupling limit, the nature of the phases of the imbalanced system is less clearly assessed. Experimentally, ultracold Fermi gases offer a perfect environment to study this rich phase diagram across the BCS-BEC crossover. In fact, while in superconductors an imbalance of spin populations is obtained by applying a magnetic field which couples also to the orbital degrees of freedom of the electrons, in ultracold Fermi gases this complication is not present, as the spin and orbital degrees of freedom can be controlled independently. In this context, some key experiments have been performed to describe the nature of the phase diagram across the BCS-BEC crossover [157–163]. In particular, at unitarity the transition line from normal to superfluid has been found to evolve from second order to first order (phase separation) as the temperature is lowered [159], without however a clear indication on the nature of the superfluid phase.

In the BEC limit, instead, the gas remains a superfluid mixture of bosons and excess fermions even for strong imbalances [161, 163]. Still, no evidence of the elusive FFLO phase has been found in ultracold gases.[1] These experiments have been followed by a big theoretical effort to describe the observations either by mean-field [167], quantum Monte Carlo (QMC) [78, 79, 81, 82, 89], renormalization group [95] or diagrammatic [32, 41, 44, 60, 61, 72] methods (for a review on the t-matrix approaches to the phase diagram of the imbalanced system, see Section 3.7 of Ref. [102]).

An interesting regime, accessible with ultracold Fermi gases, is the strongly imbalanced limit. In this case, the system is in the normal phase and the minority (e.g. spin-down) fermions act as dressed impurities, called *polarons*, immersed in a bath of majority (e.g. spin-up) fermions. In this regime, the system can be described as a Fermi liquid of weakly-interacting quasiparticles, coherently dressed by particle-hole excitations of the majority component Fermi sea (for a review see Ref. [168]).

In ultracold Fermi gas experiments, the energy E_p, the quasiparticle residue $\mathcal{Z}$ and the effective mass m^*/m of the Fermi polaron have been characterized by studying the radio-frequency spectra [143, 169] and the low-lying excitation modes [170] of the strongly imbalanced system. On the theory side, the polaron problem has been approached by means of variational [171–173], QMC [79, 82], diagrammatic Monte Carlo (DMC) [90, 92], and diagrammatic methods [46, 49, 52, 55, 69, 73, 76]. Quite surprisingly, it turned out that a simple theory that considered only single particle-hole excitations [46, 171] (equivalent to the non-self-consistent t-matrix approach in the fully imbalanced case at $T = 0$) is able to grasp the main features of the polaron system in the unitarity region and agrees with more advanced QMC and DMC calculations, as well as with the experimental data. The reason for this agreement was explained in Ref. [49], where it was shown that higher-order particle-hole contributions almost exactly cancel each other.

In the context of t-matrix approaches, the generalization to the imbalanced case is quite straightforward (see Sections 2.2.5 and 2.3): it is sufficient to introduce two different chemical potentials $\mu_\uparrow$ and $\mu_\downarrow$ and Green's functions $G_\uparrow$ and $G_\downarrow$ for the two spin species. Indeed, Eqs. (2.105-2.107) were already written in this more general form. The chemical potentials of the two species are obtained by the density equations (2.108) by fixing the total density $n = n_\uparrow + n_\downarrow$ and the spin polarization $\alpha = (n_\uparrow - n_\downarrow)/n$ (or, equivalently, the minority fraction $x = n_\downarrow/n_\uparrow = (1-\alpha)/(1+\alpha)$).[2]

However, the NSR and $(G_0G_0)G_0$ approaches present a problem: the spin susceptibility $\chi_s = dm/dh$, where $m = n_\uparrow - n_\downarrow$ is the magnetization and $h = (\mu_\uparrow - \mu_\downarrow)/2$ is the imbalancing field, is negative for the balanced system near unitarity slightly above T_c [41, 44, 60]. This means that, for these approaches, there is a region where a small imbalance of the chemical potentials $\mu_\uparrow > \mu_\downarrow$ produces the unphysical result of an opposite imbalance of the densities $n_\uparrow < n_\downarrow$. To avoid this issue, it is necessary to include (at least) some degree of self-consistency, either by introducing a quasi-particle

[1] In superconductors, evidence of an FFLO phase has been reported in heavy-fermion systems [164, 165]. For ultracold Fermi gases, indirect evidence for the occurrence of FFLO ordering has been reported so far only for a one-dimensional spin-imbalanced Fermi gas [166].

[2] Throughout this Chapter, we assume $n_\uparrow > n_\downarrow$ without loss of generality.

energy shift in all particle lines [61], by dressing the external Green's function $G_{\bar{\sigma}}^{(c)}$ in the self-energies (2.105) ($(G_0G_0)G$ approach) [60], or by implementing full self-consistency ($(GG)G$ approach) [72].

In the following sections, we show some preliminary results for thermodynamic properties of the imbalanced Fermi gas obtained within the fully self-consistent $(GG)G$ approach, with some comparisons with the $(G_0G_0)G_0$ and $(G_0G_0)G$ approaches. We first present the phase diagram, and then we focus on thermodynamic properties of the system in the normal phase, i.e. the chemical potentials and the energy at $T = 0$, the contact as a function of the temperature, and the pair correlation function.

7.1 Critical temperature

One of the most important aspects to characterize of a spin-imbalanced attractive Fermi gas is the temperature-coupling-polarization phase diagram. In this preliminary study, we focus on the standard normal-superfluid transition (with pairing at $\boldsymbol{Q} = 0$), which can be obtained by the Thouless criterion (2.109):

$$\left[\Gamma(\boldsymbol{Q} = 0, \Omega_\nu = 0)|_{T=T_c}\right]^{-1} = 0. \tag{7.1}$$

The region where FFLO correlations build up, instead, proved particularly difficult to be reached due to instabilities in the convergence of the self-consistent t-matrix approach. While these instabilities can be overcome by finely tuning the iterative algorithm, as it was done in Refs. [72, 118], it is still not clear how the normal-FFLO transition boundary can be reached.[3] In fact, an FFLO transition would mean a divergence in the particle-particle propagator Γ at a finite $\boldsymbol{Q}_0$:

$$\left[\Gamma(\boldsymbol{Q} = \boldsymbol{Q}_0, \Omega_\nu = 0)|_{T=T_c^{\mathrm{FFLO}}}\right]^{-1} = 0. \tag{7.2}$$

In the limit $\boldsymbol{Q} \to \boldsymbol{Q}_0$, however, $\Gamma(\boldsymbol{Q})$ would diverge as $(|\boldsymbol{Q}| - |\boldsymbol{Q}_0|)^{-2}$. As it was pointed out in Ref. [32], this divergence is non-integrable in the expression of the self-energy (2.105), in contrast to the standard $\boldsymbol{Q} \to 0$ case where the $|\boldsymbol{Q}|^{-2}$ divergence is compensated by the factor $|\boldsymbol{Q}|^2$ of the spherical integration over $\boldsymbol{Q}$. This problem was circumvented in Refs. [72, 118] by choosing a small number ϵ, and setting the critical temperature T_c^{FFLO} when $[\Gamma(\boldsymbol{Q} = \boldsymbol{Q}_0, \Omega_\nu = 0)]^{-1} = \epsilon$. Still, this does not solve the intrinsic problem of the divergence when the limit $\epsilon \to 0$ is taken.[4]

In Figure 7.1 the curves of T_c obtained by the Thouless criterion (7.1) within the fully self-consistent $(GG)G$ approach are shown as a function of the spin polarization $\alpha = (n_\uparrow - n_\downarrow)/n$ for six characteristic couplings across the BCS-BEC crossover. Here, the units used for the temperature and the coupling are related to the average Fermi energy

[3] In this context, we are treating the normal-FFLO transition as second-order, as the study of a first-order transition would require an approach working also in the broken-symmetry phase.

[4] Of course, this problem would be solved if the normal-FFLO phase transition was indeed first-order, like in the weak coupling regime. In this case, the transition would happen in a region where the divergence of Γ is still not reached.

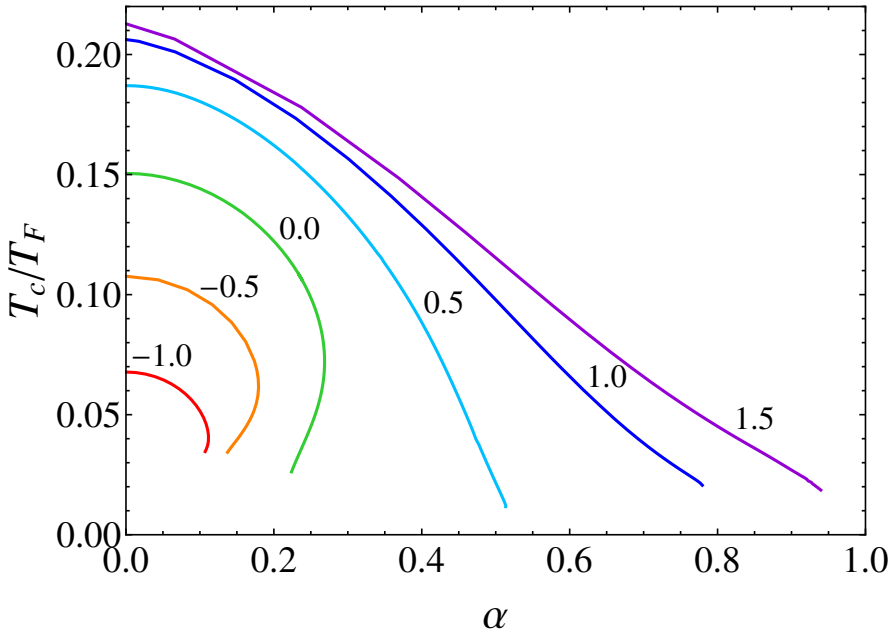

Figure 7.1: Critical temperature T_c (in units of $T_F = (3\pi^2 n)^{2/3}/(2mk_B)$) as a function of the polarization $\alpha = (n_\uparrow - n_\downarrow)/n$ calculated within the fully self-consistent t-matrix approach for various couplings $(k_F a_F)^{-1}$ across the crossover (reported above each line).

$E_F = (3\pi^2 n)^{2/3}/(2m)$ as in the balanced case, so that $T_F = E_F/k_B$ and $k_F = (3\pi^2 n)^{1/3}$. The curves are not terminated at $T \simeq 0$ due to convergence issues of the iterative algorithm for $T = T_c$ that still need to be addressed.

Note that the T_c-vs-α curves for coupling $(k_F a_F)^{-1} \lesssim 0$ show a reentrance at a finite critical imbalance α_c ($\alpha_c \simeq 0.27$ at unitarity). We expect this reentrant behavior to be related to an underlying first-order transition, as it happens in mean-field theory. In strong-coupling, instead, we observe the T_c curve approaching the point $(T_c, \alpha) = (0, 1)$. Indeed, there is a critical coupling $(k_F a_F)_c^{-1}$ for which, even at full imbalance ($\alpha \simeq 1$), the attractive interaction is so strong that the minority fermions form a tightly bound molecular state with a single majority fermion, instead of behaving as dressed impurities. This critical coupling was calculated within the self-consistent t-matrix approach in Refs. [73, 118] and corresponds to $(k_F a_F)_c^{-1} = 1.13(3)$, in excellent agreement with the value $(k_F a_F)_c^{-1} = 1.15(3)$ predicted by the DMC calculation of Ref. [92] and the value $(k_F a_F)_c^{-1} = 1.11$ obtained within the diagrammatic approach of Ref. [55].

7.2 Chemical potentials and energy

We pass now to characterize the normal phase of a strongly imbalanced Fermi gas. In this section, we focus on the chemical potentials and the energy of the system at the unitary limit $(k_F a_F)^{-1} = 0$ and low temperature, and we compare the results for the $(G_0 G_0)G_0$,

$(G_0G_0)G$ and $(GG)G$ approaches. The chemical potentials are given in units of the Fermi energy of the majority component $E_{F\uparrow} = (6\pi^2 n_\uparrow)^{2/3}/(2m)$ and the imbalance is specified in terms of the minority fraction $x = n_\downarrow/n_\uparrow$, following the usual conventions for the polaron regime.

Let us start with some general considerations on the energy and the chemical potentials of a strongly imbalanced ($x \to 0$) Fermi gas at $T = 0$. In the limit $x \to 0$, the dressed minority impurities act as free fermionic quasiparticles with effective mass m^* and binding energy $E_p = -\frac{3}{5}AE_{F\uparrow}$ (E_p is proportional to the Fermi energy of the majority component $E_{F\uparrow}$ because it is the only energy scale of the system at $x = 0$). The energy of the system in the normal phase as a function of the minority fraction x for $x \to 0$ can then be written as [79, 82]

$$E(x) = \frac{3}{5}E_{F\uparrow}N_\uparrow\left(1 - Ax + \frac{m}{m^*}x^{5/3} + Fx^2\right), \tag{7.3}$$

where the coefficients A, m^*/m and F depend on the coupling $(k_F a_F)^{-1}$, and the term Fx^2 accounts for the interaction energy between the quasiparticles. Differentating the expression (7.3) with respect to $N_\uparrow$ and $N_\downarrow$, one obtains the chemical potentials for the two spin species in the $x \to 0$ limit:

$$\mu_\uparrow(x) = E_{F\uparrow}\left(1 - \frac{2}{5}Ax - \frac{1}{5}Fx^2\right), \tag{7.4}$$

$$\mu_\downarrow(x) = E_{F\uparrow}\left(-\frac{3}{5}A - \frac{m}{m^*}x^{2/3} + \frac{6}{5}Fx\right). \tag{7.5}$$

In Figure 7.2 we report the temperature dependence of the chemical potentials for the minority ($\mu_\downarrow$) and majority ($\mu_\uparrow$) spin-components at fixed minority fraction $x = n_\uparrow/n_\downarrow = 0.1$ within the three alternative t-matrix approaches. Note that, at the lowest reachable temperature ($T/T_F \simeq 0.005 - 0.010$), the chemical potential curves are essentially flat, so we can assume that the low T results are essentially the ones for $T = 0$ (within an error of the order of 10^{-3}). Setting $T/T_F = 0.01$, we calculated the chemical potentials for the two spin components as a function of the minority fraction $x = n_\uparrow/n_\downarrow$, which are shown in Figure 7.3. The data are calculated up to the largest minority fraction x where convergence could be reached. In particular, the $(GG)G$ approach shows a strong FFLO instability, so that the standard iterative algorithm (that does not carefully treat the forming divergence in $\Gamma(\boldsymbol{Q}, \Omega_\nu = 0)$ at $\boldsymbol{Q} = \boldsymbol{Q_0}$) could be used only up to $x \simeq 0.35$.

For the minority chemical potential $\mu_\downarrow(x)$, one observes that the $(G_0G_0)G_0$ and $(G_0G_0)G$ approaches recover nearly the same result. The reason is that in the self-energy for the minority component $\Sigma_\downarrow$, the particle-particle propagator is closed by the Green's function for the majority component $G_\uparrow$, which in turn is becoming non-interacting in the fully imbalanced $x \to 0$ limit. In this limit, then, the two approaches are essentially the same as far as the minority chemical potential $\mu_\downarrow$. On the other hand, the $(GG)G$ dresses also the Green's function $G_\downarrow$ within the particle-particle propagator Γ, and this has a significant effect on the self-energy and chemical potential of the minority species.

Taking the $x \to 0$ limit of $\mu_\downarrow(x)$, one can also obtain the energy of the polaron $E_p/E_{F\uparrow} = -3A/5$. From the extrapolation, we obtained $E_p/E_{F\uparrow} = -0.606$ ($A = 1.01$)

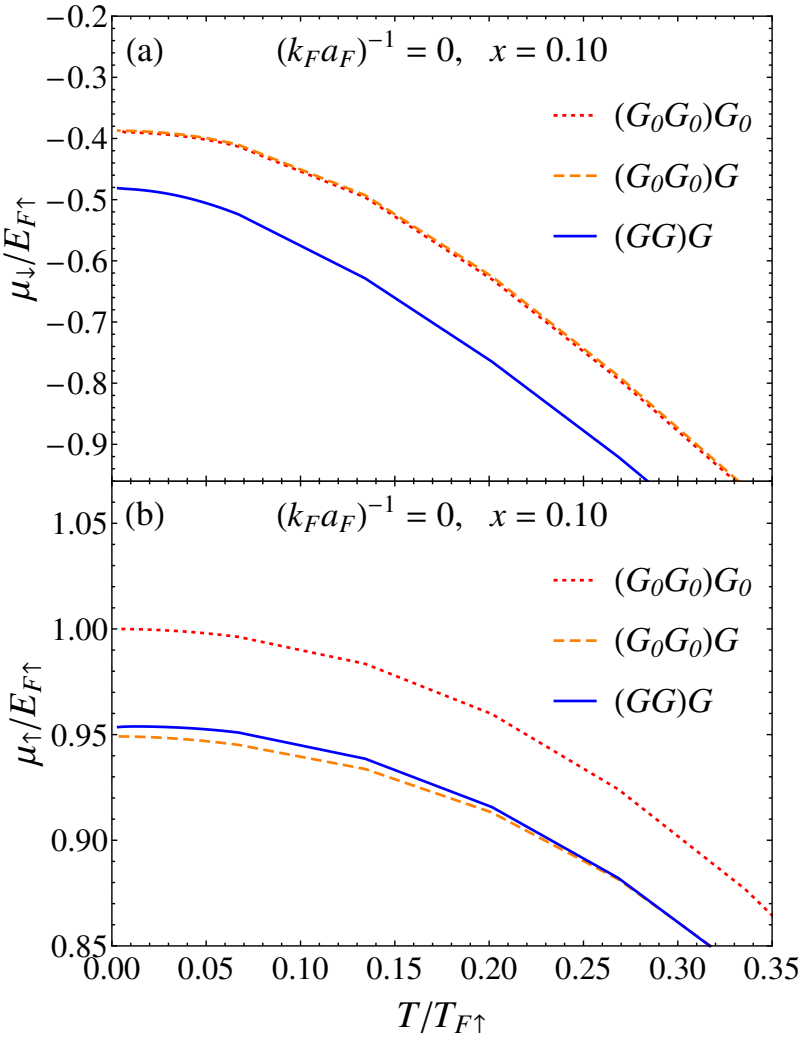

Figure 7.2: Chemical potential for the minority (a) and majority (b) spin-components (in units of $E_{F\uparrow} = (6\pi^2 n_\uparrow)^{2/3}/(2m)$) at $(k_F a_F)^{-1} = 0$ and $x = n_\uparrow/n_\downarrow = 0.10$ as a function of the temperature T (in units of $T_{F\uparrow} = E_{F\uparrow}/k_B$) calculated within alternative t-matrix approaches.

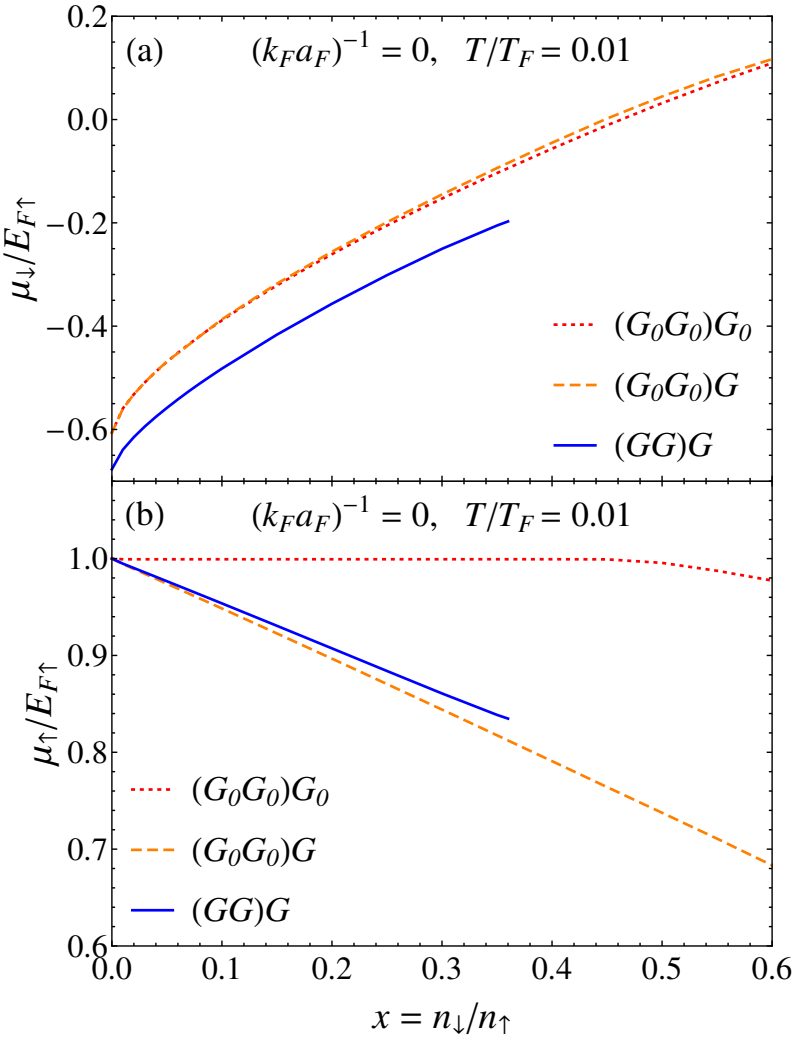

Figure 7.3: Chemical potential for the minority (a) and majority (b) spin-components at $(k_F a_F)^{-1} = 0$ and $T \simeq 0$ $(T/T_F = 0.01)$ as a function of the minority fraction $x = n_\downarrow/n_\uparrow$ calculated within alternative t-matrix approaches.

for the $(G_0G_0)G_0$ and $(G_0G_0)G$ approaches, and $E_p/E_{F\uparrow} = -0.677$ ($A = 1.13$) for the $(GG)G$ approach, in good agreement with the $T = 0$ results obtained within the same approaches reported in Refs. [46, 49, 171]. These results can be compared with the experimental $E_p/E_{F\uparrow} = -0.58(5)$ [160] and $E_p/E_{F\uparrow} = -0.60(5)$ [143], the QMC $E_p/E_{F\uparrow} = -0.58(1)$ [79, 82], the DMC $E_p/E_{F\uparrow} = -0.615(1)$ [90, 92] and the diagrammatic $E_p/E_{F\uparrow} = -0.616$ obtained within a theory that takes into account double particle-hole excitations [49]. One sees that the $(G_0G_0)G_0$ and $(G_0G_0)G$ approaches recover a value that is in really good agreement with the QMC/DMC/experimental data, while the $(GG)G$ result presents a deviation of $\sim 10 - 15\%$. This was explained in Ref. [49] by observing that self-consistency breaks the almost complete cancellation of higher-order diagrams by retaining only some of them, and in Ref. [92] it was shown that this disagreement could indeed be corrected by considering higher-order diagrams. By fitting the expression (7.5) to $\mu_\downarrow(x)$ up to $x = 0.25$, we also found $m^*/m = 1.00$ and $F = 0.01$ for $(G_0G_0)G_0$ approach, $m^*/m = 1.00$ and $F = 0.04$ for the $(G_0G_0)G$ approach, and $m^*/m = 1.25$ and $F = 0.20$ for the $(GG)G$ approach.[5] The values for the effective mass m^*/m can be compared with the experimental result $m^*/m = 1.17(10)$ [170], the QMC result $m^*/m = 1.09(2)$ [79, 82], the DMC result $m^*/m = 1.23(4)$ [90, 92] and the diagrammatic result $m^*/m = 1.20(2)$ [49, 55].

As far as the majority chemical potential $\mu_\uparrow(x)$, instead, the behavior is quite different among the three approaches. For the non-self-consistent $(G_0G_0)G_0$ approach, the chemical potential remains $\mu_\uparrow \simeq E_{F,\uparrow}$ up to $x \simeq 0.5$, completely missing the linear behavior with x of Eq. (7.4) (i.e. $A \simeq 0$). For the $(G_0G_0)G$ and $(GG)G$ approaches, instead, the subleading linear behavior is recovered. By fitting the expression (7.4) to $\mu_\downarrow(x)$ up to $x = 0.25$, we obtain $A = 1.26$ and $F = 0.23$ for the $(G_0G_0)G$ approach, and $A = 1.13$ and $F = 0.19$ for the $(GG)G$ approach. Note that for both the $(G_0G_0)G_0$ and $(G_0G_0)G$ approaches the coefficients A extracted by the chemical potential $\mu_\uparrow$ does not coincide with that extracted from $\mu_\downarrow$, while they correctly coincide for the $(GG)G$ approach. The reason is that the $(GG)G$ approach respects the thermodynamic relations $\mu_\sigma = \partial E/\partial N_\sigma$ (see Section 2.4), while the $(G_0G_0)G_0$ and $(G_0G_0)G$ approaches, being not-conserving approximations, can violate these thermodynamic relations, as they indeed do.

Finally, we calculated the energy of the system in the normal phase as a function of the imbalance by integrating the thermodynamic relation $\mu_\downarrow = \partial E/\partial N_\downarrow$ for the minority chemical potential:

$$E(x) = E_{F\uparrow}N_\uparrow \left(\frac{3}{5} + \int_0^x dx' \mu_\downarrow(x') \right), \tag{7.6}$$

where we used the boundary condition $E(x = 0) = 3E_{F\uparrow}N_\uparrow/5$. Note that, for non-conserving approximations like the $(G_0G_0)G_0$ and $(G_0G_0)G$ approaches, the energy could also be calculated in different ways (for example, with the linked cluster expansion of Eq. (2.116)). The expression (7.6) then specifies the way we are calculating the energy in this context. For the conserving $(GG)G$ approach, instead, all the possible ways to obtain the energy must give the same result.

[5] For the $(GG)G$ approach the fit is somewhat unstable due to the comparable contributions of the $\sim x^{2/3}$ and $\sim x$ terms. The estimates for the errors of the fit are $\sim 3\%$ for m^*/m and $\sim 20\%$ for F.

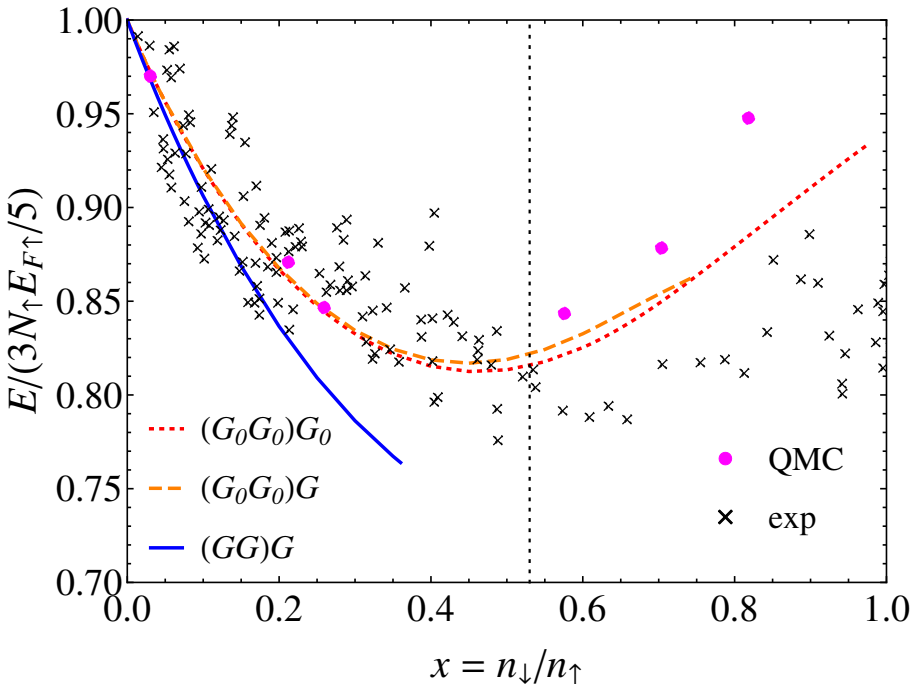

Figure 7.4: Internal energy (in units of $E(x = 0) = 3n_\uparrow E_{F\uparrow}/5$) of the normal phase at $T \simeq 0$ and $(k_F a_F)^{-1} = 0$ as a function of the minority fraction $x = n_\downarrow/n_\uparrow$ within alternative t-matrix approaches, compared with the QMC data from from Refs. [79, 82] (circles) and the experimental data from Ref. [160] (small crosses). The thin dotted vertical line represent the experimental value $x_c = 0.53(5)$ for the normal-superfluid phase separation [160].

The results for the energy of the normal phase calculated within the three t-matrix approaches are shown in Fig. 7.4, together with the QMC data from Refs. [79, 82] (circles) and the experimental data from Ref. [160] (small crosses).

We notice that the $(G_0G_0)G_0$ and $(G_0G_0)G$ approaches reproduce quite well the experimental and QMC data up to $x \simeq 0.5$, while the $(GG)G$ predicts a much lower energy, especially in the intermediate region. Indeed, this is partially related to the incorrect result for the polaron energy $E_p = -3A/5$ of the $(GG)G$ approach, obtained by the limit $x \to 0$ of $\mu_\downarrow(x)$ (see Fig. 7.3(a)), which determines the linear coefficient A of the expression (7.3) for $E(x)$. On the other hand, we remark that the QMC results are obtained within a variational ansatz, so they represent only an upper bound for the real energy of the system. In fact, in this regard the QMC approach of Refs. [79, 82] predicts also an energy for the balanced superfluid gas at $T = 0$ and unitarity of $E_{\rm SF}/(3NE_F/5) = \xi = 0.42(1)$, to be compared with the experimental value $\xi = 0.37(1)$ [122] and the $(GG)G$ value of $\xi = 0.36$ [47]. Moreover, it must be recalled that for the $(G_0G_0)G_0$ and $(G_0G_0)G$ approaches, it is the choice of the expression (7.6) for the calculation of the energy which makes this comparison particularly favorable.

7.3 Luttinger theorem

Another important property to consider for the imbalanced system is the Luttinger theorem [106], which states that in an interacting Fermi gas in the normal phase at $T = 0$ the Fermi surface for the spin-σ component ($\sigma = \uparrow, \downarrow$) must remain at the same wave vector $|\boldsymbol{k}| = k_{F\sigma} = (6\pi n_\sigma)^{1/3}$ of the non-interacting system. (see Section 2.4). In Ref. [107], it was proved that the fully self-consistent $(GG)G$ approach satisfies this theorem. We then calculated the momentum distributions $n_\sigma(\boldsymbol{k}) = G_\sigma(\boldsymbol{k}, \tau = \beta^-)$ at the low temperature $T/T_F = 0.005$ within the $(G_0G_0)G_0$, $(G_0G_0)G$ and $(GG)G$ approaches, and we compared the position of the discontinuity with the Fermi wave vectors $k_{F\sigma}$. Figure 7.5 shows the results for coupling $(k_F a_F)^{-1} = 0$ and minority fraction $x = n_\uparrow/n_\downarrow = 0.20$.

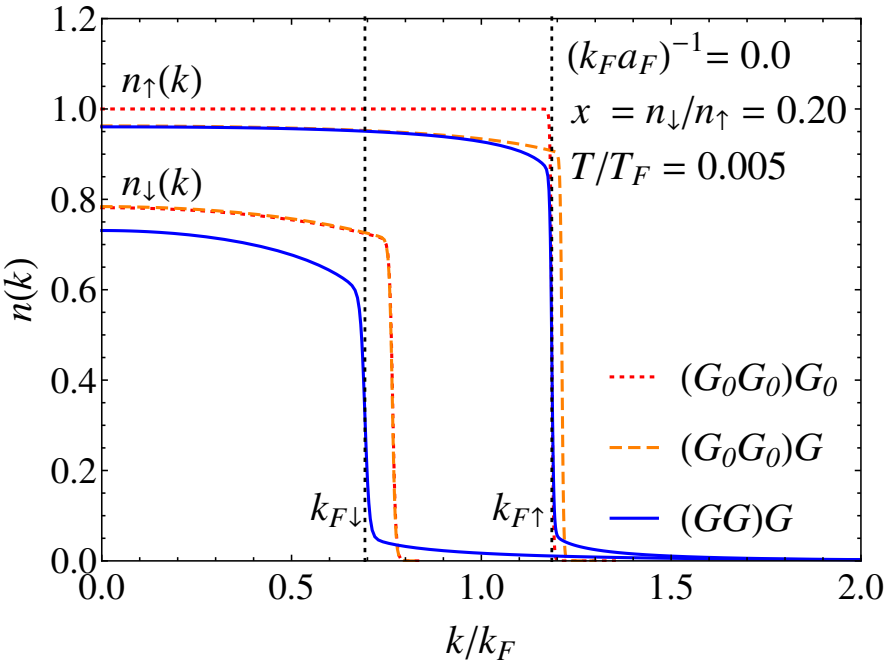

Figure 7.5: Momentum distributions for the majority ($n_\uparrow(\boldsymbol{k})$) and minority ($n_\downarrow(\boldsymbol{k})$) spin-components calculated within alternative t-matrix approaches for coupling $(k_F a_F)^{-1} = 0$, minority fraction $x = n_\uparrow/n_\downarrow = 0.20$ and $T/T_F = 0.005$. The vertical dotted lines correspond to the Fermi wave vectors $k_{F\sigma} = (6\pi^2 n_\sigma)^{1/3}$ for the two spin-components and identify the Fermi surfaces of the non-interacting system.

First of all, we notice that the fully self-consistent $(GG)G$ approach correctly recovers the Fermi surfaces of the non-interacting system, consistently with the analytic proof of Ref. [107]. As far as the $(G_0G_0)G_0$ and $(G_0G_0)G$ approaches, they both present a similar violation of the Luttinger theorem for the minority component. For the majority component, the violation is present only in the $(G_0G_0)G$ approach, however the reason of this apparent virtue of the non-self-consistent $(G_0G_0)G_0$ approach is that the majority component is incorrectly treated as almost non-interacting (see also Fig. 7.3(a)). This can

also understood by noting that the $(G_0G_0)G_0$ approach does not present any depletion of the momentum distribution of the majority component for $|\boldsymbol{k}| \simeq 0$, which is instead present in the other two approaches.

7.4 Tan's contact

In the experiment of Ref. [143], the contact C (see Section 2.5) was extracted by the high-frequency tail of radio-frequency spectra of a strongly imbalanced ($x = n_\downarrow/n_\uparrow = 0.10(3)$) attractive Fermi gas at unitarity for various temperatures. In Figure 7.6, we compare the contact calculated within the three t-matrix approaches with the experimental data (diamonds with error bars). We also show the result from the virial expansion at third order (thin dash-dotted line) from Ref. [143]. The contact is expressed in units of $2n_\downarrow k_{F\uparrow}$, so that it assumes a finite value also in the limit of small minority fraction $x = n_\downarrow/n_\uparrow$.

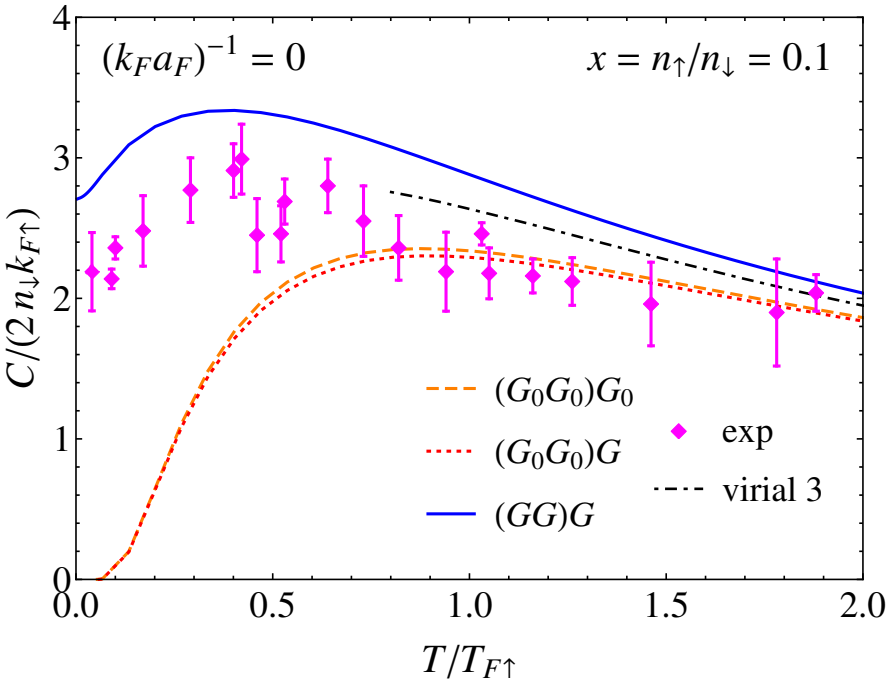

Figure 7.6: Temperature dependence of the contact C (in units of $2n_\downarrow k_{F\uparrow}$) at $(k_F a_F)^{-1} = 0$ for $x = n_\downarrow/n_\uparrow = 0.10$ within alternative t-matrix approaches. Also shown are the experimental data (diamonds with error bars) and the third order virial expansion (dash-dotted line) of the contact from Ref. [143].

Quite noticeably, only the $(GG)G$ approach is able to reproduce a finite value of the contact at $T = 0$. In fact, it can be proved analytically that the approaches that use the bare particle-particle propagator Γ_0, like the $(G_0G_0)G_0$ and $(G_0G_0)G$ approaches, present a vanishing contact at $T = 0$ if $\mu_\downarrow < 0$ (as it is in the present case, see Fig. 7.3(a)). On the other hand, dressing the particle-particle propagator Γ as in the $(GG)G$ approach

solves this problem. For this reason, the $(GG)G$ approach compares better with the experimental data, reproducing the maximum of the contact for $T/T_{F\uparrow} \simeq 0.4$ of the experimental data (albeit predicting slightly larger values for the contact).

7.5 Pair correlations

The last quantity that we present for the imbalanced system is the pair correlation function $g_{\uparrow\downarrow}(\boldsymbol{\rho})$ calculated within the self-consistent t-matrix approach (see Chapter 5). In particular, we show its evolution by varying the minority fraction $x = n_\downarrow/n_\uparrow$ from the balanced case ($x = 1$) to the strongly imbalanced case ($x = 0.01$) at fixed temperature and for various couplings. The results are shown in Figure 7.7 for the temperature $T/T_F = 0.3$, at which the system is in the normal phase also in the balanced case for any coupling.

The common feature that can be seen at all couplings is the formation of a maximum at a finite ρ in the $\rho^2 g_{\uparrow\downarrow}(\rho)$ profile. Although the pair correlation function $g_{\uparrow\downarrow}(\rho)$ (not multiplied by ρ^2) is always monotonically decreasing, so that the maximum probability for unit volume to find a majority fermion is still on top of a minority fermion, the maximum in the $\rho^2 g_{\uparrow\downarrow}(\rho)$ profile can be interpreted as an accumulation of majority fermions around the minority ones at a finite distance ρ (with respect to the balanced case). In the strongly imbalanced limit, this could give an insight on the real-space shape of the Fermi polaron. It is interesting to note that, while for the couplings $(k_F a_F)^{-1} = -0.5$ and 0.0 the maximum is formed immediately when the system is imbalanced, for the couplings $(k_F a_F)^{-1} = 0.5$ and 1.0 instead there is a competition between a peak at $\rho = 0$, related to the molecular two-body bound state (see Section 5.3), and the accumulation of majority fermions at a finite ρ, so that the maximum at $\rho \neq 0$ is formed only for a substantial imbalance of the spin-populations.

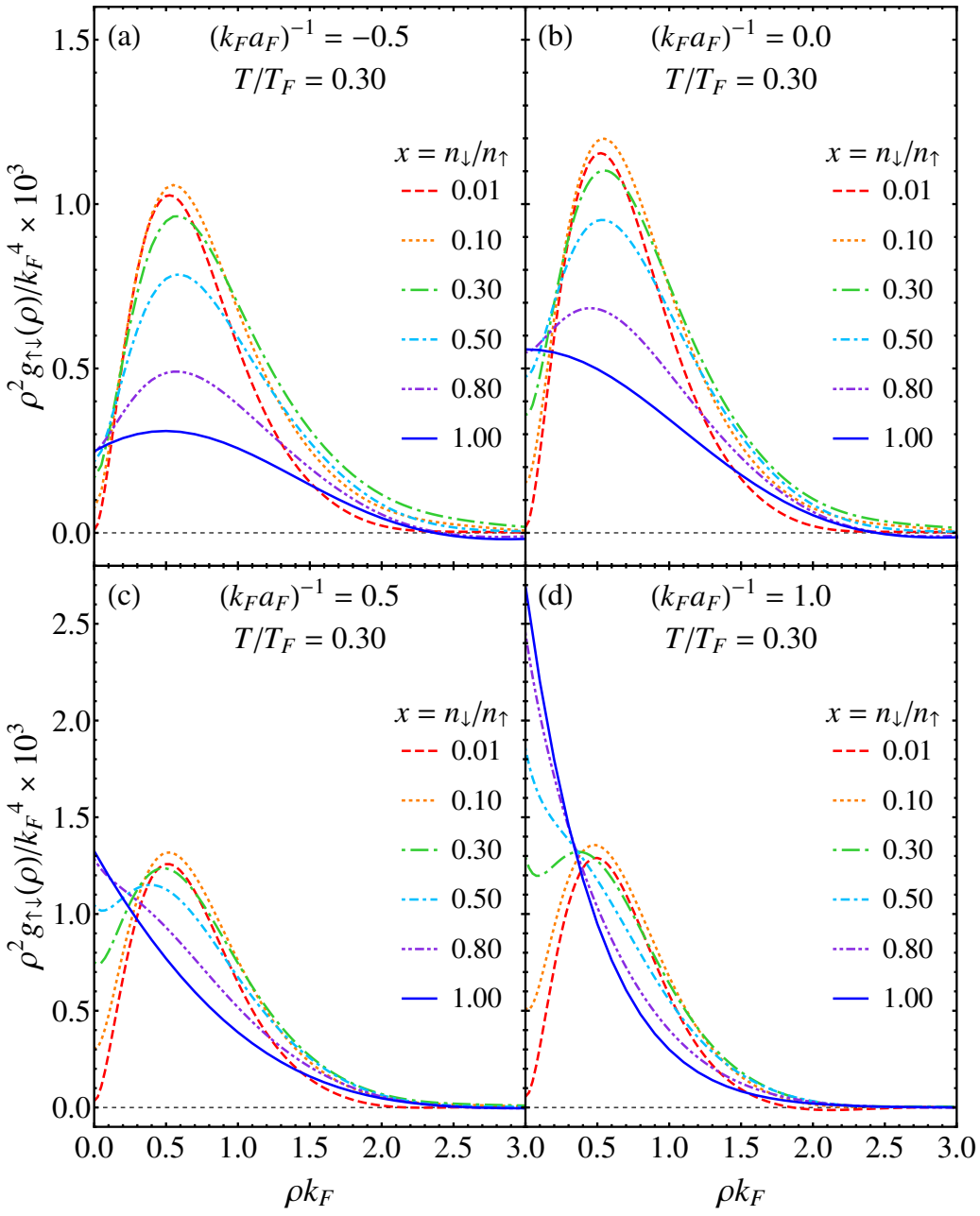

Figure 7.7: Evolution of the spatial profiles $\rho^2 g_{\uparrow\downarrow}(\rho)$ (in units of k_F^4, with $k_F = (3\pi^2 n)^{1/3}$) with the minority fraction $x = n_\uparrow/n_\downarrow$ at $T/T_F = 0.3$ for several couplings $(k_F a_F)^{-1}$ in the crossover.

Chapter 8

Conclusions and Perspectives

In this thesis, we have presented a theoretical study of the properties of an attractive Fermi gas in the normal phase throughout the BCS-BEC crossover for both balanced and imbalanced spin populations. The study has been performed by means of a diagrammatic approach based on the t-matrix approximation, where only ladder diagrams with repeated particle-particle interactions are retained.

First of all, we have implemented the calculation for t-matrix approaches with different degrees of self-consistency, obtained by replacing some or all the bare propagators G_0 with dressed propagators G in the t-matrix self-energy diagrams. We have performed a detailed and unbiased comparative study of the effects of the inclusion of partial or full self-consistency on both thermodynamic and dynamical quantities for the spin-balanced Fermi gas, and when possible these quantities have also been compared with available QMC, DMC and experimental data. In this comparative study, we have found that the fully self-consistent $(GG)G$ approach works better for thermodynamic properties, both for its behavior in the the BCS and BEC limits and for its good agreement with QMC, DMC and experimental data at unitarity. On the other hand, a direct comparison with recent experimental radio-frequency spectra for a homogeneous Fermi gas, has shown that full self-consistency actually deteriorates the results for dynamical quantities, so that for these quantities partially or non-self-consistent approaches appear to work better. In addition, we have found that the $(GG_0)G_0$ approach breaks down in the BCS limit when it is considered without the additional approximations that usually accompanies its implementation in the literature, and that the fully self-consistent $(GG)G$ approach recovers the value $a_B = 1.16a_F$ for the scattering length of the repulsive interaction between the composite bosons in the BEC limit, instead of the value $a_B = 2a_F$ which was believed so far in the literature.

In the second part of the thesis, we have focused on pair correlations in the normal phase. We have first calculated the pair correlation function $g_{\uparrow\downarrow}(\boldsymbol{\rho})$ and the pair coherence length ξ_{pair} within the fully self-consistent t-matrix approach for various couplings and temperatures. We have then developed a new approach, based on the two-body Green's function formalism, to calculate the number of preformed pairs in the normal phase in order to describe the experimental data on this quantity by the group of Prof. Denschlag

in Ulm. The method has first been implemented only in the BEC limit, by using a two-body description for the shape $\phi(\boldsymbol{\rho})$ of the pairs, and then has been extended across the whole crossover by including many-body pair correlations in the function $\phi(\boldsymbol{\rho})$ by means of the pair correlation function $g_{\uparrow\downarrow}(\boldsymbol{\rho})$. In order to compare our calculation with the experimental data, we have also extended the fully self-consistent calculation for a system in a harmonic trapping potential, presenting its T_c curve across the crossover and comparing our calculated axial density profiles with experimental profiles. In general, very good agreement is found with the experimental data.

In the final part of the thesis, we have presented some preliminary results on thermodynamic properties of the spin-imbalanced Fermi gas. We have shown the phase diagram of the normal-BCS superfluid phase transition obtained within the self-consistent t-matrix approach, and some $T \simeq 0$ and finite T thermodynamic quantities (i.e. the chemical potentials, the energy and the contact) calculated within three t-matrix approaches with different degrees of self-consistency. We have numerically verified that the fully self-consistent t-matrix approach is the only approach that satisfies the Luttinger theorem at $T = 0$ among the ones considered, and we have shown some results for the pair correlation function $g_{\uparrow\downarrow}(\boldsymbol{\rho})$ as a function of the spin-imbalance.

As a perspective, it would be interesting to explore in more detail the properties of the spin-imbalanced Fermi gas within the fully self-consistent t-matrix approach. Specifically, the description of the phase diagram could be enriched by studying the regions of FFLO instability and of phase separation, and by characterizing in detail the pair correlation function $g_{\uparrow\downarrow}(\boldsymbol{\rho})$, especially in the strongly imbalanced limit where it gives an insight on the real-space shape of the Fermi polaron.

Appendix A

Details of the numerical procedures to achieve self-consistency

In this Appendix, we present in detail the numerical procedures that are needed to implement the cycles of self-consistency depicted schematically in Fig. 2.7. Specifically, we consider the fully self-consistent $(GG)G$ approach whose cycle is shown in Fig. 2.7(d), since all procedures discussed for this approach can as well be applied to the partially self-consistent approaches. We remark that the procedures here presented for the $(GG)G$ approach are in line with those previously suggested in Ref. [27] and partially with those reported in Refs. [94, 118].

All expressions reported in this Appendix are given in dimensionless units, such that energies are in units of the Fermi energy $E_F = k_F^2/(2m)$ and wave vectors in units of the Fermi wave vector k_F. Accordingly, the single-particle fermionic propagator $G(\boldsymbol{k}, \omega_n)$ is in units of E_F^{-1}, the fermionic self-energy $\Sigma(\boldsymbol{k}, \omega_n)$ in units of E_F, and the particle-particle propagator $\Gamma(\boldsymbol{Q}, \Omega_\nu)$ in units of $(mk_F)^{-1}$. In addition, to further shorten the notation, here we use the symbol $v = (k_F a_F)^{-1}$ for the coupling and we take $k_B = 1$.

A.1 Transforming from $G(\boldsymbol{k}, \omega_n)$ to $G(\boldsymbol{r}, \tau)$

The first function to be Fourier transformed in the self-consistent cycle of Fig. 2.7(d) is the single-particle fermionic propagator G. For this function the Fourier transform can be done in two steps, namely,

$$G(\boldsymbol{k}, \omega_n) \rightarrow G(\boldsymbol{k}, \tau) \rightarrow G(\boldsymbol{r}, \tau) \tag{A.1}$$

with the Fourier transform over the wave vector $\boldsymbol{k}$ following that over the frequency ω_n.

In the first step, to get the Fourier transform over the frequency ω_n, we note that the dressed fermionic propagator $G(\boldsymbol{k}, \omega_n)$ for large frequencies behaves like the free propagator $G_0(\boldsymbol{k}, \omega_n)$:

$$G(\boldsymbol{k}, \omega_n) \underset{\omega_n \rightarrow \infty}{\simeq} G_0(\boldsymbol{k}, \omega_n) = \frac{1}{i\omega_n - \xi_{\boldsymbol{k}}} \tag{A.2}$$

where $\xi_{\boldsymbol{k}} = \boldsymbol{k}^2 - \mu$. One can thus calculate numerically the Fourier transform from ω_n to τ of the difference

$$\Delta G(\boldsymbol{k}, \omega_n) = G(\boldsymbol{k}, \omega_n) - G_0(\boldsymbol{k}, \omega_n), \tag{A.3}$$

which is easier to obtain than the Fourier transform of $G(\boldsymbol{k}, \omega_n)$ since the function (A.3) converges like $\sim \omega_n^{-5/2}$ for large frequencies. One then adds to this result the Fourier transform of $G_0(\boldsymbol{k}, \omega_n)$, which is known analytically in the form [108]

$$G_0(\boldsymbol{k}, \tau) = e^{-\xi_{\boldsymbol{k}}\tau}\big(f(\xi_{\boldsymbol{k}}) - 1\big), \tag{A.4}$$

where $f(\xi_{\boldsymbol{k}}) = (e^{\beta\xi_{\boldsymbol{k}}} + 1)^{-1}$ is the Fermi distribution function.

In the second step, to get the Fourier transform over the wave vector $\boldsymbol{k}$, it is further convenient to split the expression (A.4) in two parts:

$$G_0(\boldsymbol{k}, \tau) = G_0^{(\mathrm{n})}(\boldsymbol{k}, \tau) + G_0^{(\mathrm{a})}(\boldsymbol{k}, \tau) \tag{A.5}$$

where

$$G_0^{(\mathrm{n})}(\boldsymbol{k}, \tau) = e^{-\xi_{\boldsymbol{k}}\tau} f(\xi_{\boldsymbol{k}}), \tag{A.6}$$

$$G_0^{(\mathrm{a})}(\boldsymbol{k}, \tau) = -e^{-\xi_{\boldsymbol{k}}\tau}. \tag{A.7}$$

Here, the labels (n) and (a) signify that the term (A.6) has to be numerically Fourier transformed over $\boldsymbol{k}$, whereas the term (A.7) admits an analytic Fourier transform of the form

$$G_0^{(\mathrm{a})}(\boldsymbol{r}, \tau) = -\frac{e^{\mu\tau} e^{-\frac{r^2}{4\tau}}}{8\pi^{3/2}\tau^{3/2}}, \tag{A.8}$$

which in the limit $\tau \to 0^+$ is a representation of the Dirac delta function $\delta^3(\boldsymbol{r})$. This property is related to the anticommutator between fermionic field operators that appears in the fermionic propagator when passing from $\tau = 0^-$ to $\tau = 0^+$. The term (A.8) thus describes the singular behavior when $(\boldsymbol{r}, \tau) \to 0^+$, not only for the free propagator G_0 but also for the dressed propagator G. It is then convenient to define a new function

$$\tilde{\Delta} G(\boldsymbol{k}, \tau) = G(\boldsymbol{k}, \tau) - G_0^{(\mathrm{a})}(\boldsymbol{k}, \tau), \tag{A.9}$$

which can be readily Fourier transformed over $\boldsymbol{k}$ numerically. The desired Fourier transform $G(\boldsymbol{r}, \tau)$ is eventually obtained by adding $G_0^{(a)}(\boldsymbol{r}, \tau)$ of Eq. (A.8) to the Fourier transform of $\tilde{\Delta} G(\boldsymbol{k}, \tau)$.[1]

[1] Additional care is required in weak coupling, where the expressions that include the factor $e^{\mu\tau}$ become large when $\tau \simeq \beta$ and may then lead to numerical errors. In this case, for the $\boldsymbol{k} \to \boldsymbol{r}$ Fourier transform it is useful to replace the factor $e^{\mu\tau}$ in Eqs. (A.7) and (A.8) for $G_0^{(\mathrm{a})}$ by its expansion $(1 + \mu\tau + \cdots)$ for $\tau \to 0^+$.

A.2 Transforming from $\Gamma(\boldsymbol{Q},\Omega_\nu)$ to $\Gamma(\boldsymbol{r},\tau)$

The next function to be Fourier transformed in the self-consistent cycle of Fig. 2.7(d) is the particle-particle propagator Γ. Also in this case, the Fourier transform can be done in two steps, namely,

$$\Gamma(\boldsymbol{Q},\Omega_\nu) \to \Gamma(\boldsymbol{Q},\tau) \to \Gamma(\boldsymbol{r},\tau), \tag{A.10}$$

with the Fourier transform over the wave vector $\boldsymbol{Q}$ following again that over the frequency Ω_ν.

To perform the first Fourier transform over Ω_ν, we begin by noting that the large-frequency behavior of the particle-particle propagator $\Gamma(\boldsymbol{Q},\Omega_\nu)$ coincides with that of its non-self-consistent counterpart taken in the strong-coupling limit $\beta|\mu| \gg 1$. This is given by the expression (2.83), that in dimensionless units reads:

$$\Gamma(\boldsymbol{Q},\Omega_\nu) \underset{\Omega_\nu\to\infty}{\simeq} \Gamma_{\rm sc}(\boldsymbol{Q},\Omega_\nu) = -\frac{4\pi}{v-\sqrt{\frac{Q^2}{4}-\mu-i\frac{\Omega_\nu}{2}}}. \tag{A.11}$$

However, using $\Gamma_{\rm sc}(\boldsymbol{Q},\Omega_\nu)$ as the reference function to be subtracted in the Fourier transform may lead to problems, because for $\Omega_\nu = 0$ the function (A.11) has a pole at $|\boldsymbol{Q}| = 2\sqrt{v^2+\mu}$ when $v > 0$. To the extent that we are interested only in taking care of the large-frequency behavior of $\Gamma(\boldsymbol{Q},\Omega_\nu)$, we are led to introduce the new reference function

$$\Gamma'_{\rm sc}(\boldsymbol{Q},\Omega_\nu) = \Gamma_{\rm sc}(\boldsymbol{Q},\Omega_\nu) - \Gamma_{\rm sc}(\boldsymbol{Q},\Omega_\nu=0) \tag{A.12}$$

with the zero-frequency term removed from the expression (A.11). Although the Fourier transform of the function (A.12) cannot be calculated analytically, it can be computed with limited effort by writing it as an integral over the complex z-plane as follows:

$$\Gamma'_{\rm sc}(\boldsymbol{Q},\tau) = T\sum_\nu e^{-i\Omega_\nu\tau}\Gamma'_{\rm sc}(\boldsymbol{Q},\Omega_\nu) = \frac{1}{2\pi i}\oint_{\mathcal{C}} dz \frac{e^{z\tau}}{(e^{\beta z}-1)}\Gamma'_{\rm sc}(\boldsymbol{Q},z) \tag{A.13}$$

where the contour $\mathcal{C}$ surrounds the poles of the Bose function $b(z) = 1/(e^{\beta z}-1)$ on the imaginary axis. Here, the function $\Gamma'_{\rm sc}(\boldsymbol{Q},z)$ has a branch cut along the negative real axis starting at $z_{\rm c} = 2(\mu - \boldsymbol{Q}^2/4)$ as well as a pole at $z_{\rm p} = 2v^2 + z_c$ when $v > 0$. The integral in Eq. (A.13) then reduces to the calculation of an integral along the branch cut and of the residue of the pole, and can accordingly be split in the following way:

$$\begin{aligned}\Gamma'_{\rm sc}(\boldsymbol{Q},\tau) &= \Gamma^{\rm (n)}_{\rm sc}(\boldsymbol{Q},\tau) + \Gamma^{\rm (a)}_{\rm sc}(\boldsymbol{Q},\tau) \\ &+ \Gamma_{\rm res}(\boldsymbol{Q},\tau) - T\,{\rm Re}[\Gamma_{\rm sc}(\boldsymbol{Q},\Omega_\nu=0)]\end{aligned} \tag{A.14}$$

where the first two terms are contributed by the branch cut and the third term by the pole. Like in Eq. (A.5), the labels (n) and (a) in the first line of Eq. (A.14) signify that these contributions are calculated numerically or analytically, respectively.

The first term in Eq. (A.14) can be cast in the form

$$\Gamma^{\rm (n)}_{\rm sc}(\boldsymbol{Q},\tau) = \frac{8\sqrt{2}e^{z_{\rm c}\tau}}{\sqrt{\tau}}\int_0^{+\infty} dx \frac{e^{-x^2}\,x^2}{(e^{-\beta(z_{\rm c}-x^2/\tau)}-1)(x^2+2\tau v^2)} \tag{A.15}$$

for $z_{\rm c} < 0$ (that is, for $\mu < \boldsymbol{Q}^2/4$), and in the form

$$\begin{aligned}\Gamma^{(\rm n)}_{\rm sc}(\boldsymbol{Q},\tau) &= \frac{8\sqrt{2}e^{z_{\rm c}\tau}}{\sqrt{\tau}}\int_{\sqrt{\tau(z_{\rm c}-z_0)}}^{+\infty} dx \frac{e^{-x^2}\,x^2}{(e^{-\beta(z_{\rm c}-x^2/\tau)}-1)(x^2+2\tau v^2)} \\ &+ 8\sqrt{\frac{2}{\tau}}\int_0^{\sqrt{\tau(z_{\rm c}-z_0)}} dx \frac{1}{e^{-\beta(z_{\rm c}-x^2/\tau)}-1}\left(\frac{e^{z_{\rm c}\tau-x^2}x^2}{x^2+2\tau v^2} - \frac{x\sqrt{z_{\rm c}}}{z_{\rm p}\sqrt{\tau}}\right) \\ &+ \frac{4\sqrt{2z_{\rm c}}}{z_{\rm p}}\left(z_0 - z_{\rm c} - T\,\ln\left|\frac{e^{-\beta z_{\rm c}}-1}{e^{-\beta z_0}-1}\right|\right)\end{aligned} \tag{A.16}$$

for $z_{\rm c} \geq 0$ (that is, for $\mu \geq \boldsymbol{Q}^2/4$), where z_0 is a negative real number (typically, we have taken $z_0 = -2T$). The second term in Eq. (A.14) has instead the semi-analytic form:

$$\Gamma^{(\rm a)}_{\rm sc}(\boldsymbol{Q},\tau) = 4\sqrt{2\pi}\; c(\tau,v)\,\frac{e^{2\mu\tau}e^{-\boldsymbol{Q}^2\tau/2}}{\sqrt{\tau}} \tag{A.17}$$

with the coefficient $c(\tau, v)$ given by

$$c(\tau,v) = \frac{2}{\sqrt{\pi}}\int_0^{+\infty} dx\,\frac{x^2\,e^{-x^2}}{x^2+2\tau v^2}\,. \tag{A.18}$$

Note that this coefficient is unity for $\tau \to 0^+$ or $v = 0$.

The term (A.17) admits also an analytic Fourier transform from $(\boldsymbol{Q},\tau)$ to $(\boldsymbol{r},\tau)$, which is given by:

$$\Gamma^{(\rm a)}_{\rm sc}(\boldsymbol{r},\tau) = \frac{2\,c(\tau,v)\,e^{2\mu\tau}e^{-\frac{\boldsymbol{r}^2}{2\tau}}}{\pi\tau^2}\,. \tag{A.19}$$

One can show that this is the leading term of the singular behavior of the full $\Gamma(\boldsymbol{r},\tau)$ for $(\boldsymbol{r},\tau) \to 0^+$, not only in the strong-coupling regime but also throughout the BCS-BEC crossover. Finally, the third term in Eq. (A.14) is the residue of the pole at $z = z_{\rm p}$, given by:

$$\Gamma_{\rm res}(\boldsymbol{Q},\tau) = -\theta(v)\frac{16\pi v\,e^{z_{\rm p}\tau}}{e^{\beta z_{\rm p}}-1}\,. \tag{A.20}$$

One can also show that the divergence of this term for $z_{\rm p} = 0$ (that is, for $|\boldsymbol{Q}| = 2\sqrt{v^2+\mu}$) is exactly compensated by the fourth term of (A.14), in such a way that $\Gamma'_{\rm sc}(\boldsymbol{Q},\tau)$ is always a smooth function of $\boldsymbol{Q}$.

At this point, we calculate numerically the Fourier transform from $(\boldsymbol{Q},\Omega_\nu)$ to $(\boldsymbol{Q},\tau)$ of the difference

$$\Delta\Gamma(\boldsymbol{Q},\Omega_\nu) = \Gamma(\boldsymbol{Q},\Omega_\nu) - \Gamma'_{\rm sc}(\boldsymbol{Q},\Omega_\nu) \tag{A.21}$$

to obtain $\Delta\Gamma(\boldsymbol{Q},\tau)$, and then add to it $\Gamma'_{\rm sc}(\boldsymbol{Q},\tau)$ given by Eq. (A.14) to obtain $\Gamma(\boldsymbol{Q},\tau)$.

Finally, for the remaining Fourier transform from $(\boldsymbol{Q},\tau)$ to $(\boldsymbol{r},\tau)$, we can make use of $\Gamma^{(\rm a)}_{\rm sc}(\boldsymbol{Q},\tau)$ defined by Eqs. (A.17) and (A.18) to subtract the leading term of the singular behavior when $(\boldsymbol{r},\tau) \to 0^+$, similarly to what we did in Eq. (A.9). Accordingly, we define the difference function:

$$\tilde{\Delta}\Gamma(\boldsymbol{Q},\tau) = \Gamma(\boldsymbol{Q},\tau) - \Gamma^{(\rm a)}_{\rm sc}(\boldsymbol{Q},\tau) \tag{A.22}$$

and Fourier transform it from $\boldsymbol{Q}$ to $\boldsymbol{r}$ to obtain $\tilde{\Delta}\Gamma(\boldsymbol{r},\tau)$. The desired function $\Gamma(\boldsymbol{r},\tau)$ eventually results by adding to $\tilde{\Delta}\Gamma(\boldsymbol{r},\tau)$ the semi-analytic expression (A.19) for $\Gamma_{\rm sc}^{\rm (a)}(\boldsymbol{r},\tau)$.[2]

A.3 Transforming from $\Sigma(\boldsymbol{r},\tau)$ to $\Sigma(\boldsymbol{k},\omega_n)$

The last function to be Fourier transformed in the self-consistent cycle of Fig. 2.7(d) is the self-energy Σ. Also in this case, the Fourier transform is done in two steps, namely,

$$\Sigma(\boldsymbol{r},\tau) \to \Sigma(\boldsymbol{k},\tau) \to \Sigma(\boldsymbol{k},\omega_n) \tag{A.23}$$

where now one first transforms from $\boldsymbol{r}$ to $\boldsymbol{k}$ and then from τ to ω_n, in the reversed direction to what was done for G (cf. Eq. (A.1)) and for Γ (cf. Eq. (A.10)). This is because from Eq. (2.112), once $G(\boldsymbol{r},\tau)$ and $\Gamma(\boldsymbol{r},\tau)$ are know, $\Sigma(\boldsymbol{r},\tau)$ is also known.

From Eq. (2.112) one can also determine the singular behavior of $\Sigma(\boldsymbol{r},\tau)$ for $(\boldsymbol{r},\tau)\to 0^+$ in terms of those of $G(\boldsymbol{r},\tau)$ [cf. the discussion after Eq. (A.8)] and of $\Gamma(\boldsymbol{r},\tau)$ [cf. the discussion after Eq. (A.19)]. To this end, we rewrite Eq. (2.112) in the alternative forms:

$$\Sigma(\boldsymbol{r},\tau) = -2\,\Gamma(\boldsymbol{r},\tau)\,G(-\boldsymbol{r},-\tau) \tag{A.24}$$

$$= 2\,\Gamma(\boldsymbol{r},\tau)\,G(\boldsymbol{r},\beta-\tau) \tag{A.25}$$

(where the factor of two originates by having expressed the particle-particle propagator Γ in terms of dimensionless quantities). In the second line we have used the spatial isotropy and the anti-periodicity in τ of the fermionic propagator, to write $G(-\boldsymbol{r},-\tau) = -G(\boldsymbol{r},\beta-\tau)$. As discussed previously, both $G(\boldsymbol{r},\tau)$ and $\Gamma(\boldsymbol{r},\tau)$ are strongly peaked for $(\boldsymbol{r},\tau)\to 0^+$. We then expect the singular behavior of $\Sigma(\boldsymbol{r},\tau)$ to be captured by the following alternative expressions:

$$\Sigma^{(+)}(\boldsymbol{r},\tau) \simeq 2\,\Gamma(\boldsymbol{r},\tau)\,G(\boldsymbol{r}=0,\beta^-) \tag{A.26}$$

in the limit $(\boldsymbol{r},\tau)\to(0,0^+)$ and

$$\Sigma^{(-)}(\boldsymbol{r},\tau) \simeq 2\,\Gamma(\boldsymbol{r}=0,\beta^-)\,G(\boldsymbol{r},\beta-\tau) \tag{A.27}$$

in the limit $(\boldsymbol{r},\tau)\to(0,\beta^-)$. Out of the above terms, (A.26) is the dominant one because $\Gamma(\boldsymbol{r},\tau)$ [cf. Eq. (A.19)] is more strongly peaked than $G(\boldsymbol{r},\tau)$ [cf. Eq. (A.8)] in the limit $\tau\to 0^+$.

Accordingly, in order to perform the Fourier transform of $\Sigma(\boldsymbol{r},\tau)$ from $\boldsymbol{r}$ to $\boldsymbol{k}$, we consider the difference

$$\Delta\Sigma(\boldsymbol{r},\tau) = \Sigma(\boldsymbol{r},\tau) - \Sigma^{(+)}(\boldsymbol{r},\tau) \tag{A.28}$$

[2] Also in this case, additional care is required to handle in weak coupling the expressions containing the factor $e^{2\mu\tau}$. In this case, the separation of $\Gamma_{\rm sc}(\boldsymbol{Q},\tau)$ in numeric and analytic parts like in Eq. (A.14) has to be performed only for $\tau\simeq 0$, while $\Gamma_{\rm sc}(\boldsymbol{Q},\tau)$ has to be calculated as a whole for larger values of τ. Moreover, when performing the $\boldsymbol{Q}\to\boldsymbol{r}$ Fourier transform, it is again useful to replace the factor $e^{2\mu\tau}$ in Eqs. (A.17) and (A.19) for $\Gamma_{\rm sc}^{\rm (a)}$ with its expansion $(1+2\mu\tau+\cdots)$ for $\tau\to 0^+$.

with the term (A.26) only. In addition, to the extent that in Eq. (A.28) we are interested in the leading behavior of $\Sigma^{(+)}$ for $(\boldsymbol{r},\tau)\to(0,0^+)$, we can approximate the particle-particle propagator $\Gamma(\boldsymbol{r},\tau)$ in Eq. (A.26) by the analytic result (A.19) and write

$$\Sigma^{(+)}(\boldsymbol{r},\tau) = -2n\,\frac{e^{-\frac{r^2}{2\tau}}}{\pi\tau^2}\,, \tag{A.29}$$

where we have consistently set $c(\tau,v)\to 1$ and $e^{\mu\tau}\to 1$ and used the expression $n = -2\,G(\boldsymbol{r}=0,\beta^-)$ in terms of the fermionic density n (in dimensionless units).[3]

The expression (A.29) has the further advantage that its Fourier transform from τ to ω_n can be obtained analytically in terms of the error function [174], in the form:

$$\Sigma^{(+)}(\boldsymbol{k},\omega_n) = -8\pi n\,\frac{\mathrm{erf}\big(\sqrt{\beta(\boldsymbol{k}^2-2i\omega_n)/2}\,\big)}{\sqrt{\boldsymbol{k}^2-2i\omega_n}}\,. \tag{A.30}$$

This expression correctly reproduces the leading $\omega_n^{-1/2}$ behavior of $\Sigma(\boldsymbol{k},\omega_n)$ for large frequencies.[4]

Once the difference (A.28) has been Fourier transformed numerically (first from $\boldsymbol{r}$ to $\boldsymbol{k}$ and then from τ to ω_n) according to the above prescriptions to obtain $\Delta\Sigma(\boldsymbol{k},\omega_n)$, one can eventually add to it the analytic expression (A.30) and obtain the desired function $\Sigma(\boldsymbol{k},\omega_n)$.

[3]For the t-matrix approaches that use an external G_0 in the place of G, the expression (A.29) needs to be modified by replacing n by the free-fermion density $n_0 = -2\,G_0(\boldsymbol{r}=0,\beta^-)$.

[4]Similarly, $\Sigma^{(-)}$ of Eq. (A.27) can be shown to behave like $\sim\omega_n^{-1}$ for large frequencies [94], thereby confirming that this is a sub-leading contribution also in the frequency domain.

Appendix B

Optimizing the convergence towards self-consistency

In this Appendix, we discuss the procedures that we have adopted to achieve optimal convergence toward self-consistency within the t-matrix approaches considered in this thesis. A judicious optimization in achieving convergence is, in fact, especially required for those approaches that implement partial or total self-consistency in the particle-particle propagator Γ, to the extent that these approaches become intrinsically unstable when the temperature approaches T_c when one uses the straightforward iterative procedure sketched in Section 2.3 (cf. Fig. 2.7 therein). The origin of this problem can be highlighted through the following analytic considerations.

B.1 General considerations on the iterative procedure

For definiteness, we shall consider in detail the fully self-consistent $(GG)G$ approach. The equations (2.104)-(2.107), that need to be self-consistently solved, can be written in a compact way as a functional equation for the self-energy Σ, in the form:

$$\Sigma(k) = \mathcal{F}\big[\Sigma(p)\big](k)\,. \tag{B.1}$$

This is because, once Σ is know, G and Γ in Eqs. (2.104)-(2.107) can also be readily obtained. Let us then see what happens when trying to solve Eq. (B.1) iteratively.

Suppose that $\Sigma^{\rm SC}(k) = \mathcal{F}\big[\Sigma^{\rm SC}(p)\big](k)$ is the self-consistent (SC) solution to Eq. (B.1) which the iterative method is expected to reach. At a generic iteration step (i) toward self-consistency, the self-energy $\Sigma^{(\rm i)}(k)$ deviates from $\Sigma^{\rm SC}(k)$ by some amount $\delta\Sigma^{(\rm i)}(k)$:

$$\Sigma^{(\rm i)}(k) = \Sigma^{\rm SC}(k) + \delta\Sigma^{(\rm i)}(k). \tag{B.2}$$

Provided one is close enough to the self-consistent solution, Eq. (B.1) can be linearized

about Σ^{SC}, to write:

$$\begin{aligned} \Sigma^{\mathrm{SC}}(k) + \delta\Sigma^{(\mathrm{i})}(k) &= \mathcal{F}\big[\Sigma^{(\mathrm{i\text{-}1})}(p)\big](k) \\ \simeq \;\; \Sigma^{\mathrm{SC}}(k) &+ \int dp \left[\frac{\delta\mathcal{F}[\Sigma(p)](k)}{\delta\Sigma(p)}\right]_{\mathrm{SC}} \delta\Sigma^{(\mathrm{i\text{-}1})}(p)\,. \end{aligned} \tag{B.3}$$

Here, the subscript SC indicates that the functional derivative is taken at self-consistency, and the integral over p contains both an integral over the wave vector $\boldsymbol{p}$ and a sum over the Matsubara frequency ω_n. This provides a relation for the distance $\delta\Sigma$ from the self-consistent solution between the steps (i-1) and (i):

$$\delta\Sigma^{(\mathrm{i})}(k) = \int dp \left[\frac{\delta\mathcal{F}[\Sigma(p)](k)}{\delta\Sigma(p)}\right]_{\mathrm{SC}} \delta\Sigma^{(\mathrm{i\text{-}1})}(p). \tag{B.4}$$

When $\Sigma(k)$ is calculated on a k-grid of points, like in our numerical calculations, $\delta\Sigma$ can be regarded as a vector which is acted upon by the functional derivative matrix $[\delta\mathcal{F}/\delta\Sigma]_{\mathrm{SC}}$. The convergence of the iterative procedure, from (i-1) to (i) and so on, is then governed by the behavior of this functional derivative matrix.

To find an explicit expression for $[\delta\mathcal{F}/\delta\Sigma]_{\mathrm{SC}}$, we rewrite it in the form:

$$\frac{\delta\mathcal{F}[\Sigma(p)](k)}{\delta\Sigma(p)} = \frac{\delta\mathcal{F}[\Sigma(p)](k)}{\delta G(p)}\,\frac{\delta G(p)}{\delta\Sigma(p)}\,. \tag{B.5}$$

Here, the factor on the right is given by

$$\frac{\delta G(p)}{\delta\Sigma(p)} = G(p)^2 \tag{B.6}$$

with the use of Eq. (2.104), while the factor on the left can be calculated by recalling that (cf. Eqs. (2.105) and (B.1))

$$\mathcal{F}\big[\Sigma(p)\big](k) = \Sigma(k) = -\int dQ\,\Gamma(Q)G(Q-k)\,, \tag{B.7}$$

yielding

$$\frac{\delta\mathcal{F}[\Sigma(p)](k)}{\delta G(p)} = -\Gamma(p+k) - \int dQ\,\frac{\delta\Gamma(Q)}{\delta G(p)}G(Q-k). \tag{B.8}$$

In this expression, the functional derivative of the particle-particle propagator $\Gamma(Q)$ can be obtained from Eq. (2.106)

$$\frac{\delta\Gamma(Q)}{\delta G(p)} = -\Gamma(Q)^2\,\frac{\delta R_{\mathrm{pp}}(Q)}{\delta G(p)}, \tag{B.9}$$

where the functional derivative of the regularized particle-particle bubble $R_{\mathrm{pp}}(Q)$ is obtained from Eq. (2.107)

$$\frac{\delta R_{\mathrm{pp}}(Q)}{\delta G(p)} = 2\,G(Q-p). \tag{B.10}$$

Grouping all the above results together, Eq. (B.5) becomes eventually:

$$\frac{\delta\mathcal{F}[\Sigma(p)](k)}{\delta\Sigma(p)} = -G(p)^2\left[\Gamma(p+k) - 2\int dQ\,\Gamma(Q)^2 G(Q-k)G(Q-p)\right]. \tag{B.11}$$

When this result is used in Eq. (B.4), $\delta\Sigma^{(i)}$ therein can be conveniently split in two terms

$$\delta\Sigma^{(\mathrm{i})}(k) = \delta\Sigma_1^{(\mathrm{i})}(k) + \delta\Sigma_2^{(\mathrm{i})}(k), \tag{B.12}$$

where we have defined

$$\delta\Sigma_1^{(\mathrm{i})}(k) = -\int dp\,G(p)^2\Gamma(p+k)\,\delta\Sigma^{(\mathrm{i\text{-}1})}(p) \tag{B.13}$$

$$\delta\Sigma_2^{(\mathrm{i})}(k) = 2\int dp\,G(p)^2\int dQ\,\Gamma(Q)^2\,G(Q-k)G(Q-p)\,\delta\Sigma^{(\mathrm{i\text{-}1})}(p). \tag{B.14}$$

Suppose now that $T = T_c$. The Thouless criterion (2.109) then implies that the particle-particle propagator $\Gamma(Q)$ has a pole for $Q = 0$, such that one expects $\Gamma(Q)$ to be strongly peaked in the vicinity of $Q = 0$. The expressions (B.13) and (B.14) can be simplified accordingly, by setting to zero the arguments of the particle-particle propagators in the smooth functions that multiply them. For the term (B.13) we thus have:

$$\begin{aligned}\delta\Sigma_1^{(\mathrm{i})}(k) &\simeq -G(-k)^2\delta\Sigma^{(\mathrm{i\text{-}1})}(-k)\int dp\,\Gamma(p+k)\\ &= -C\;G(-k)^2\,\delta\Sigma^{(\mathrm{i\text{-}1})}(-k)\end{aligned} \tag{B.15}$$

where C is the contact according to Eq. (2.131). This term poses no problem to the convergence, since the quantity that multiplies $\delta\Sigma^{(\mathrm{i\text{-}1})}(-k)$ is finite. For the term (B.14) we instead obtain:

$$\delta\Sigma_2^{(\mathrm{i})}(k) \simeq 2G(-k)\int dQ\,\Gamma(Q)^2\int dp\,G(p)^2G(-p)\,\delta\Sigma^{(\mathrm{i\text{-}1})}(p) \tag{B.16}$$

where the factor

$$\int dQ\,\Gamma(Q)^2 = \int\frac{d\boldsymbol{Q}}{(2\pi)^3}\frac{1}{\beta}\sum_\nu\Gamma(\boldsymbol{Q},\Omega_\nu)^2 \tag{B.17}$$

is infrared divergent at $T = T_c$ even in three dimensions. This is because, for the term with $\Omega_\nu = 0$ therein, $\Gamma(\boldsymbol{Q},\Omega_\nu = 0) \sim \boldsymbol{Q}^{-2}$ when $\boldsymbol{Q} \to 0$ at $T = T_c$ [31].

This divergence represents a problem for the convergence of the iterative algorithm, because it implies that, no matter how close the step (i-1) might be to the self-consistent solution, the step (i) is bound to run infinitely away from it. This problem can affect the convergence of the iterative algorithm also for temperatures $T \gtrsim T_c$, depending on how much $\Gamma(Q)$ is peaked about $Q = 0$.

The only partially self-consistent t-matrix approach not affected by this problem is the $(G_0G_0)G$ approach. This is because in this approach, by construction, the particle-particle propagator Γ coincides with the bare Γ_0, whereby $\delta\Gamma_0/\delta G = 0$. As a consequence, the second term on the right-hand side of Eq. (B.8) identically vanishes and with it the divergent factor in Eq. (B.16).

We pass now to show how this problem can be overcome in practice, both for $T > T_c$ and $T = T_c$.

B.2 Improved method for $T > T_c$

Although the iterative approach (B.4) to solve Eq. (B.1) cannot converge at exactly $T = T_c$, there exists a simple method to make it converge for $T \gtrsim T_c$, with the factor (B.17) keeping a finite (albeit large) value. This method, which has already been used for the self-consistent calculations of electronic structures in atoms and molecules [175], consists in redefining the iterative steps in terms of the weighted sum:

$$\Sigma^{(\mathrm{i})}(k) = \alpha\, \mathcal{F}\big[\Sigma^{(\mathrm{i\text{-}1})}(p)\big](k) + (1-\alpha)\Sigma^{(\mathrm{i\text{-}1})}(k) \tag{B.18}$$

where the weight factor α ranges between 0 and 1. This method is found to reduce the effects of the divergence due to the term (B.16), thereby making the iterative process to converge even sufficiently close to T_c. Nevertheless, the method fails upon approaching T_c, because smaller and smaller values of α are needed for attaining convergence. A smaller value of α, in turn, implies that more iterative steps are required for convergence, since the contribution of a single step, too, becomes smaller and smaller. In practice, we have found that this method can conveniently been used down to temperatures for which $(T - T_c)/T_c$ is of order 1%, before it becomes numerically too demanding.

B.3 Improved method for $T = T_c$

Alternatively, exactly at $T = T_c$ one can rely on a different method that avoids the convergence problem discussed above. This method can be summarized as follows:

1. One begins by fixing the value n of the density, in terms of which one obtains the Fermi wave vector $k_F = (3\pi^2 n)^{1/3}$ and the Fermi energy $E_F = k_F^2/(2m)$. One also fixes a guess value T_{g}/T_F for the temperature in units of the Fermi temperature, as well as the ratio μ/T_{g} between the chemical potential and the guess temperature T_{g}.

2. Next, one replaces the particle-particle propagator of Eq. (2.106) with the following expression
$$\tilde{\Gamma}(Q)^{-1} = R_{\mathrm{pp}}(Q) - R_{\mathrm{pp}}(Q=0)\,, \tag{B.19}$$
in such a way that $\tilde{\Gamma}(Q=0)^{-1} = 0$ by construction. This implies that the Thouless criterion (2.109) is always satisfied by the modified particle-particle propagator (B.19), *no matter* what was the initial guess for T_{g}/T_F.

3. At this point one can proceed and perform the iterative procedure toward self-consistency on the set of equations (2.104)-(2.107), with $\Gamma(Q)$ therein replaced by $\tilde{\Gamma}(Q)$. It will be shown below that this replacement avoids the occurrence of the infrared divergence that plagues instead the expression (B.16) obtained in terms of the original $\Gamma(Q)$.

4. Once self-consistency has been achieved with this modified set of equations, one can obtain the modified density as $\tilde{n} = -2\,\tilde{G}(\boldsymbol{r}=0, \beta^-)$, and the modified scattering

length $\tilde{a}_F$ from the expression

$$\frac{1}{\tilde{a}_F} = -\frac{4\pi}{m}\,\tilde{R}_{\rm pp}(Q=0) \tag{B.20}$$

where $\tilde{R}_{\rm pp}$ is obtained from Eq. (2.107) with $\tilde{G}$ replacing G. The result (B.20) follows directly from the Thouless criterion corresponding to the modified density $\tilde{n}$.

5. Finally, in terms of $\tilde{n}$ one obtains the modified Fermi wave vector $\tilde{k}_F = (3\pi^2\tilde{n})^{1/3}$ and the modified Fermi energy $\tilde{E}_F = \tilde{k}_F^2/(2m)$. The desired value of the critical temperature is then obtained by

$$\frac{T_c}{T_F} = \frac{T_{\rm g}}{T_F}\,\frac{E_F}{\tilde{E}_F} \tag{B.21}$$

in terms of the initial guess $T_{\rm g}/T_F$. From Eq. (B.20) the corresponding coupling value is given by:

$$\frac{1}{k_F a_F} = \frac{1}{\tilde{k}_F\tilde{a}_F} = \frac{1}{k_F\tilde{a}_F}\,\frac{k_F}{\tilde{k}_F} = -\frac{4\pi\tilde{R}_{\rm pp}(Q=0)}{mk_F}\,\frac{k_F}{\tilde{k}_F}\,. \tag{B.22}$$

There remains to explain the reason why this method is not plagued by the convergence problem discussed above for the iterative procedure. The point is that, using the modified particle-particle propagator (B.19) in the place of the original one, one also modifies the structure of the functional derivative in Eq. (B.4). Specifically, for the functional derivative of $\tilde{\Gamma}(Q)$ with respect to $\tilde{G}(p)$ one obtains (cf. Eq. (B.9)):

$$\frac{\delta\tilde{\Gamma}(Q)}{\delta\tilde{G}(p)} = -\tilde{\Gamma}(Q)^2\,\frac{\delta\big(\tilde{R}_{\rm pp}(Q) - \tilde{R}_{\rm pp}(Q=0)\big)}{\delta\tilde{G}(p)} = -2\,\tilde{\Gamma}(Q)^2\,\big[\tilde{G}(Q-p) - \tilde{G}(-p)\big]\,. \tag{B.23}$$

The corresponding variation of the self-energy related to this functional derivative then becomes (cf. Eq. (B.14)):

$$\delta\tilde{\Sigma}_2^{(\rm i)}(k) = 2\int\!dp\,\tilde{G}(p)^2\int\!dQ\,\tilde{\Gamma}(Q)^2\tilde{G}(Q-k)\big[\tilde{G}(Q-p) - \tilde{G}(-p)\big]\,\delta\tilde{\Sigma}^{(\rm i\text{-}1)}(p). \tag{B.24}$$

Comparing this result with Eq. (B.14), one notes that the singular behavior of $\tilde{\Gamma}(Q)^2$ for $Q \to 0$ is now suppressed by the presence of the factor $[\tilde{G}(Q-p) - \tilde{G}(-p)]$. This feature makes it possible to reach convergence *exactly at* $T = T_c$ with a limited number of iterations, without the need for the weighted sum of Eq. (B.18).

Appendix C

Comparison with the pseudogap approximation at T_c

The $(GG_0)G_0$ and $(GG)G_0$ t-matrix approaches have almost invariably been implemented in the literature using a set of approximations (sometimes referred to as the "pseudo-gap approximation"), which considerably simplify the numerical calculations. Specifically, close to T_c where the particle-particle propagator $\Gamma(Q)$ is strongly peaked about $Q = 0$, the fermionic self-energy (2.105) has been approximated as follows [29, 40]:

$$\begin{aligned}\Sigma(\boldsymbol{k},\omega_n) &= -\int\frac{d\boldsymbol{Q}}{(2\pi)^3}\frac{1}{\beta}\sum_{\nu}\Gamma(\boldsymbol{Q},\Omega_\nu)\,G_0(\boldsymbol{Q}-\boldsymbol{k},\Omega_\nu-\omega_n)\\ &\approx G_0(-\boldsymbol{k},-\omega_n)\left(-\int\frac{d\boldsymbol{Q}}{(2\pi)^3}\frac{1}{\beta}\sum_{\nu}\Gamma(\boldsymbol{Q},\Omega_\nu)e^{i\Omega_\nu 0^+}\right)\\ &\equiv G_0(-\boldsymbol{k},-\omega_n)\,\Delta_{\rm pg}^2\,.\end{aligned} \tag{C.1}$$

Due to this approximation for the self-energy, the dressed single-particle propagator G (and thus also the equation for the particle number) coincides with that of BCS theory, with the pseudo-gap energy $\Delta_{\rm pg}$ now playing the role in the normal phase of the BCS gap Δ in the superfluid phase. In addition, the Thouless criterion (2.109) for the dressed Γ coincides with the BCS gap equation (again with the replacement $\Delta \to \Delta_{\rm pg}$) for the $(GG_0)G_0$ approach [29, 40], or with the BCS gap equation plus additional corrections (which become anyway negligible both in the BCS and BEC limits) for the $(GG)G_0$ approach [65]. A further approximation, which is usually adopted within the pseudo-gap approximation when calculating $\Delta_{\rm pg}$ by means of Eq. (C.1), is the use of an expansion of $\Gamma(\mathbf{Q},\Omega_\nu)$ for small values of $\mathbf{Q}$ and Ω_ν.

It should, however, be remarked that the pseudo-gap approximation (C.1) appears justified only in the strong-coupling (BEC) regime $(k_F a_F)^{-1} \gtrsim +1$, where the large fermionic energy scale $|\mu|$ (with $\mu < 0$) dominates over the bosonic energy scales and the approximation (C.1) becomes fully correct. This can also be verified numerically as shown in Fig. C.1, where a comparison is presented for the calculation of T_c between the complete $(GG_0)G_0$ and $(GG)G_0$ approaches (full lines) and their corresponding

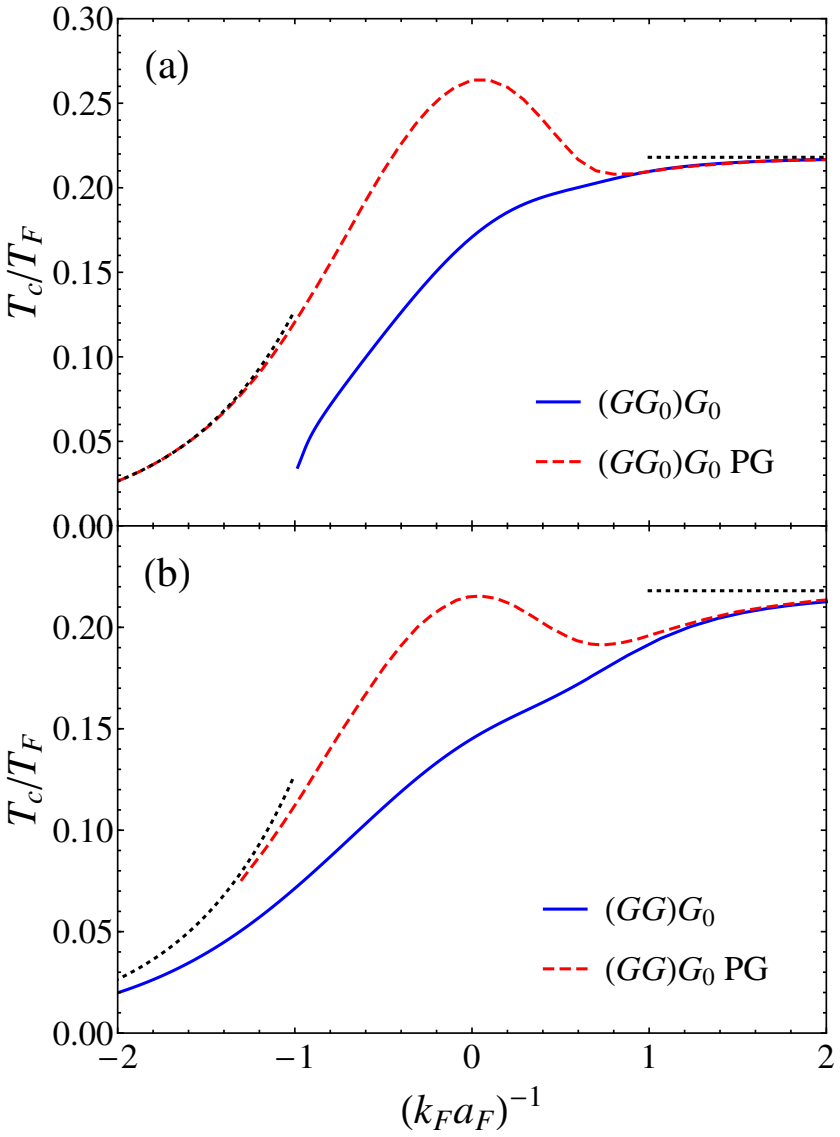

Figure C.1: Critical temperature T_c vs the coupling $(k_F a_F)^{-1}$ for the $(GG_0)G_0$ (panel a) and $(GG)G_0$ (panel b) approaches (full lines), and for their corresponding pseudo-gap (PG) approximation (dashed lines). The BCS and BEC critical temperatures are also reported for comparison (dotted curves on the left and right sides, respectively). The data for the pseudo-gap approximation to the $(GG_0)G_0$ and $(GG)G_0$ approaches are taken from Refs. [56] and [65], respectively.

pseudo-gap approximations (dashed lines). This comparison shows that a good agreement between the complete and approximate calculations occurs only for $(k_F a_F)^{-1} \gtrsim 1$, while significant deviations result both at intermediate and weak couplings.

From Fig. C.1 one also notices that, in the weak-coupling (BCS) regime $(k_F a_F)^{-1} \lesssim -1$, the curves for T_c obtained within the pseudo-gap approximation converge rapidly to the corresponding BCS curve for T_c. This is because $\Delta_{\rm pg}(T)$ is bounded by the value Δ_0 of the BCS gap at $T = 0$ [40], which in turn vanishes exponentially in the weak-coupling limit. This implies that the approximate self-energy (C.1), too, vanishes exponentially, in such a way that the BCS result for T_c is recovered. Without the use of the approximation (C.1), in weak coupling the self-energy would instead approach the value $\Sigma_0 \simeq 2\pi a_F n/m$ associated with a mean-field shift (see Section 2.2.6).

For the complete $(GG_0)G_0$ approach, whereby this shift appears in just one of the two single-particle propagators that enter the particle-particle bubble in Γ, the equation for T_c corresponds to that of a Fermi system in the presence of a chemical potential imbalance $\delta\mu$. This equation is known to have no solution when this imbalance about exceeds the BCS gap Δ_0 of the balanced system at $T = 0$ [123–125]. Given the exponential dependence of Δ_0 on coupling, to be contrasted with the linear dependence $\delta\mu \simeq 2\pi a_F n/m$ associated with the mean-field shift, the condition $\delta\mu > \Delta_0$ is readily met in the weak-coupling regime. This explains why, in the weak-coupling regime, the $(GG_0)G_0$ approach does not admit solution for T_c, as it was already noted in the discussion of Fig. 3.1. For the complete $(GG)G_0$ approach, on the other hand, the differences with respect to its pseudo-gap approximation are overall less pronounced, albeit still significant.

Appendix D

On the self-energy contributions to the kernel Ξ of the T-matrix equation

In Section 2.6, we have argued that only the BSC form (2.145) of the effective two-particle interaction Ξ is of relevance for the calculation of the pair correlation function $g_{\uparrow\downarrow}(\boldsymbol{\rho})$ of Eq. (5.1) and the bosonic propagator $\mathcal{G}_B(\boldsymbol{Q}, \Omega_\nu)$ of Eq. (6.7) (and thus of the quantity $N_{\rm p}$ of Eq. (6.3) of experimental interest). We have also anticipated that the reason for this is to be found in the specific sequence of Nambu indices appearing in the expressions (5.3) and (6.5).

Here, we show specifically how the diagrammatic contributions to Ξ, that would derive from the t-matrix fermionic self-energy $\Sigma^{t\text{-matrix}}$ of Eq. (2.147), cannot modify this result. Under different circumstances, like for the calculation of the density and spin response functions, on the other hand, the diagrams for Ξ corresponding to the Aslamazov-Larkin (AL) and Maki-Thomson (MT) contributions would instead result from the t-matrix self-energy $\Sigma^{t\text{-matrix}}$ (see, e.g., Fig. 3 of Ref. [34]). In our case, the importance of introducing the t-matrix approach for the self-energy arises from the need of obtaining an accurate description of the thermodynamic properties of the Fermi gas in the normal phase (cf. Section 3.1).

Probably the simplest way to convince oneself that the AL-type and MT-type contributions to Ξ, which would result from the t-matrix self-energy taken below T_c, do not contribute to the expressions (5.3) and (6.5) once carried over to the normal phase above T_c, is to draw these contributions in a diagrammatic way. This is done in Fig. D.1. Here, the series of ladder diagrams that approximate the many-particle T-matrix in the broken-symmetry phase is reported in panel (a), while the corresponding t-matrix self-energy is shown in panel (b). For simplicity, in these diagrams only the Nambu indices have been explicitly indicated, while the space and imaginary time variables are not reported since they are not essential to the following argument. The crucial point (already emphasized in Section 2.6) is that for the T-matrix of panel (b) only combinations with Nambu indices $\ell_L \neq \ell'_L$ and $\ell_R \neq \ell'_R$ occur, owing to the inter-particle interaction of the contact form that we have adopted (cf. also Ref. [121]). In addition, only combinations with $\ell_L = \ell_R$ and $\ell'_L = \ell'_R$ will survive when these diagrams are extrapolated to the normal phase. As

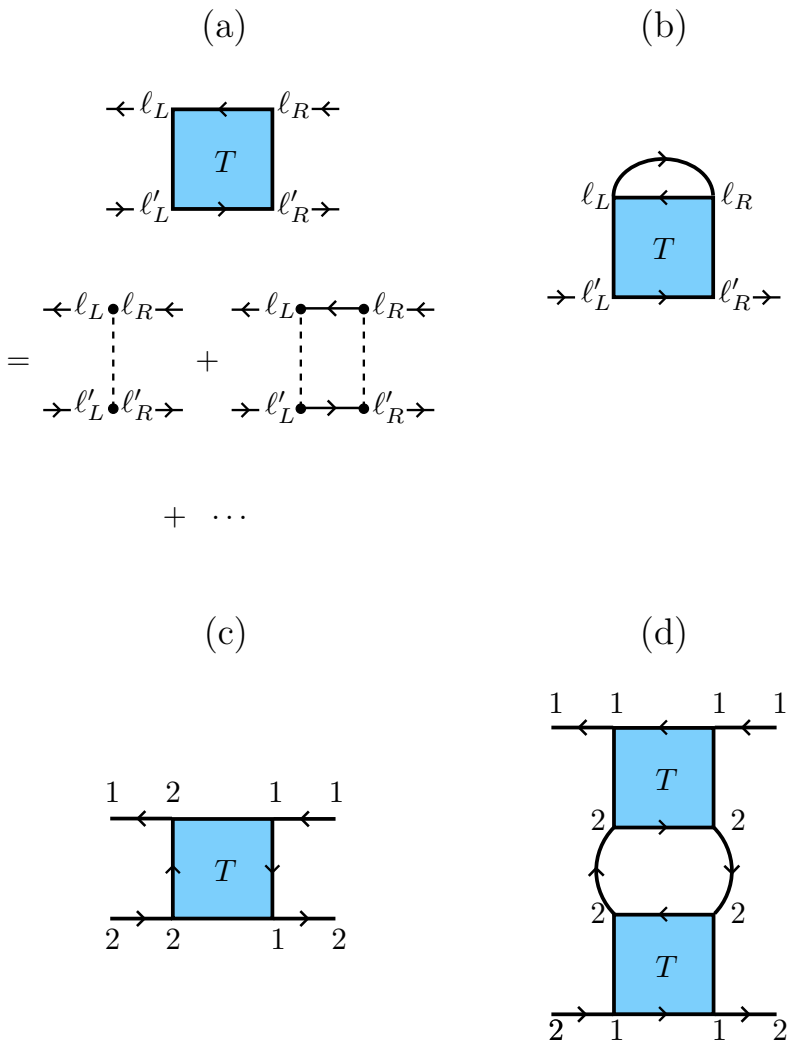

Figure D.1: (a) Ladder diagrams for the T-matrix in the superfluid phase, where dots delimiting potential (dashed) lines represent τ^3 Pauli matrices. (b) Corresponding diagram for the t-matrix fermionic self-energy. Examples of (c) MT and (d) AL diagrammatic contributions to the two-particle Green function G_2 (or, equivalently, to the two-particle correlation function L) with the choice $(\ell_L, \ell'_R, \ell'_L, \ell_R) = (1, 2, 2, 1)$ for the Nambu indices. These contributions are bound to vanish when carried over to the normal phase owing to the presence of two anomalous fermionic single-particle Green's functions which connect $1 \leftrightarrow 2$. For simplicity, only Nambu spin indices have been explicitly indicated in all diagrams.

a consequence, a typical example of MT contribution is shown in Fig. D.1(c), while a typical example of AL contribution is shown in Fig. D.1(d). In all cases, it turns out that at least two single-particle Green's functions with off-diagonal Nambu indices would be required to match these contributions to Ξ with the Nambu indices appearing in the expressions (5.3) and (6.5). Since the off-diagonal (anomalous) single-particle Green's functions vanish in the normal phase above T_c, the MT- and AL-type contributions to Ξ vanish, too, and do not affect the expressions (5.3) and (6.5) which are relevant for the calculation of $g_{\uparrow\downarrow}(\boldsymbol{\rho})$ and N_{p} above T_c. This proves our statement.

Appendix E

Critical temperature for a low-density trapped Bose gas

In this Appendix, we describe the procedure to calculate the superfluid critical temperature of a low-density Bose gas in a trap, where the interaction is treated at the level of the two-body t-matrix specified by the scattering length a_B. Similarly to what we did in Section 4.1, we assume a local density approximation and we write the local bosonic chemical potential as

$$\mu_B(\boldsymbol{r}) = \mu_B^0 - V_B(\boldsymbol{r}) - 2\,t_0\,n_B(\boldsymbol{r}). \tag{E.1}$$

Here, $V_B(r) = m_B\omega r^2/2$ is the harmonic trapping potential for the bosons of mass m_B (we assumed $\omega_x = \omega_y = \omega_z = \omega$ for simplicity), and $2\,t_0\,n_B(r)$ is the leading approximation to the self-energy of a dilute Bose gas in the normal phase with $t_0 = 4\pi a_B/m_B$ [111]. We thus write for the bosonic density

$$n_B(\boldsymbol{r}) = \int \frac{d\boldsymbol{Q}}{(2\pi)^3}\,\frac{1}{e^{\beta[\boldsymbol{Q}^2/(2m_B)-\mu_B(\boldsymbol{r})]}-1}. \tag{E.2}$$

Note that, due to the presence of the local self-energy $2t_0 n_B(r)$, this equation is a self-consistent condition for the local density $n_B(\boldsymbol{r})$. Once $n_B(\boldsymbol{r})$ is known, the number of bosons is obtained as

$$N_B = \int d\boldsymbol{r}\,n_B(\boldsymbol{r}). \tag{E.3}$$

We are now interested in determining the critical temperature T_c for the transition to the superfluid phase. Similarly to what happens for a trapped Fermi gas (cf. Section 4.3), also for a trapped Bose gas the center of the trap is where superfluidity first manifests itself upon lowering the temperature from the normal phase. The superfluid transition is then determined by the Hugenholtz-Pines condition [176] at $\boldsymbol{r} = 0$

$$\mu_B^0 = 2\,t_0\,n_B(\boldsymbol{r}=0). \tag{E.4}$$

At T_c, we can then use the previous condition to write the local chemical potential (E.1) as

$$\mu(\boldsymbol{r}) = -V_B(\boldsymbol{r}) - 2\,t_0\,\delta n_B(\boldsymbol{r}) \tag{E.5}$$

with $\delta n_B(\boldsymbol{r}) = [n_B(\boldsymbol{r}) - n_B(\boldsymbol{r}=0)]$, such that Eq. (E.2) becomes:

$$n_B(\boldsymbol{r}) = \int \frac{d\boldsymbol{Q}}{(2\pi)^3} \frac{1}{e^{\beta_c[\boldsymbol{Q}^2/(2m_B)+V_B(\boldsymbol{r})+2t_0\,\delta n_B(\boldsymbol{r})]} - 1}, \tag{E.6}$$

where $\beta_c = (k_B T_c)^{-1}$. For any given value of $\boldsymbol{r}$, this equation can be solved self-consistently for the variable $n_B(\boldsymbol{r})$. This is conveniently done by fixing an arbitrary value of $n_B(\boldsymbol{r}=0)$ and looking for a solution $n_B(\boldsymbol{r})$ such that it never exceeds the value $n_B(\boldsymbol{r}=0)$.[1] Once the entire density profile $n_B(\boldsymbol{r})$ is obtained in this way, one calculates N_B from Eq. (E.3). The value of $n_B(\boldsymbol{r}=0)$ is then varied to get a new value of N_B and so on, so as to obtain T_c as a function of N_B and a_B. In addition, upon measuring the values of T_c obtained in this way in units of the critical temperature for non-interacting trapped bosons $k_B T_c^{\mathrm{BEC}} = \omega\,[N_B/\zeta(3)]^{1/3}$, one finds that T_c/T_c^{BEC} is a function of the scaling variable $a_B\sqrt{k_B T_c^{\mathrm{BEC}}/m_B}$ only. By translating it back into the language of the BCS-BEC crossover of the main text, one gets eventually that T_c/T_F is a function of the coupling parameter $(k_F a_F)^{-1}$ in the trap since a_B is proportional to a_F (cf. Fig. 4.3).

[1] For example, by means of the bisection root-finding method in the interval $n_B(\boldsymbol{r}) \in [0, n_B(\boldsymbol{r}=0)]$.

Appendix F

Details on the calculation of $g_{\uparrow\downarrow}(\boldsymbol{\rho})$ and ξ_{pair}

In this appendix we give the details of the calculation of the pair correlation function $g_{\uparrow\downarrow}(\boldsymbol{\rho})$ and of the pair coherence length ξ_{pair} introduced in Chapter 5.

F.1 Calculation of $g_{\uparrow\downarrow}(\boldsymbol{\rho})$

The pair correlation function in the self-consistent t-matrix approach is given by the expression (5.6):

$$g_{\uparrow\downarrow}(\boldsymbol{\rho}) = \int \frac{d\boldsymbol{Q}}{(2\pi)^3} \frac{1}{\beta} \sum_{\nu} e^{i\Omega_\nu \eta}\, \Gamma(\boldsymbol{Q}, \Omega_\nu)\, [\Pi(\boldsymbol{\rho}; \boldsymbol{Q}, \Omega_\nu)]^2. \tag{F.1}$$

Let us first focus on the particle-particle bubble in $\boldsymbol{\rho}$-space

$$\Pi(\boldsymbol{\rho}; \boldsymbol{Q}, \Omega_\nu) = \int \frac{d\boldsymbol{k}}{(2\pi)^3}\, e^{i\boldsymbol{k}\cdot\boldsymbol{\rho}}\, \Pi(\boldsymbol{k}; \boldsymbol{Q}, \Omega_\nu) \tag{F.2}$$

which is the Fourier transform of the particle-particle bubble in $\boldsymbol{k}$-space

$$\Pi(\boldsymbol{k}; \boldsymbol{Q}, \Omega_\nu) = \frac{1}{\beta} \sum_{n} G_\uparrow(\boldsymbol{k} + \boldsymbol{Q}/2, \omega_n + \Omega_\nu) G_\downarrow(\boldsymbol{k} - \boldsymbol{Q}/2, -\omega_n). \tag{F.3}$$

The sum over fermionic Matsubara frequencies in (F.3) is a convolution product like the one in the renormalized particle-particle bubble (2.107). It is then more easily computed in τ-space, where it reads:

$$\Pi(\boldsymbol{k}; \boldsymbol{Q}, \tau) = G_\uparrow(\boldsymbol{k} + \boldsymbol{Q}/2, \tau) G_\downarrow(\boldsymbol{k} - \boldsymbol{Q}/2, \tau). \tag{F.4}$$

The $(\boldsymbol{k}, \tau) \to (\infty, 0^+)$ behavior of this expression is given by:

$$\begin{aligned} \Pi(\boldsymbol{k}; \boldsymbol{Q}, \tau) &\simeq \Pi^{(a)}(\boldsymbol{k}; \boldsymbol{Q}, \tau) \\ &= G^{(a)}_{0\uparrow}(\boldsymbol{k} + \boldsymbol{Q}/2, \tau) G^{(a)}_{0\downarrow}(\boldsymbol{k} + \boldsymbol{Q}/2, \tau) = e^{-(\xi_{\boldsymbol{k}+\boldsymbol{Q}/2,\uparrow} + \xi_{\boldsymbol{k}-\boldsymbol{Q}/2,\downarrow})\tau} \end{aligned} \tag{F.5}$$

where $G_0^{(a)}$ was defined in (A.7) and $\xi_{\boldsymbol{k},\sigma} = \boldsymbol{k}^2/(2m) - \mu_\sigma$. The expression (F.5) presents an analytical Fourier transform to the Ω_ν space, that is given by

$$\Pi^{(a)}(\boldsymbol{k};\boldsymbol{Q},\Omega_\nu) = \frac{1 - e^{-\beta(\xi_{\boldsymbol{k}+\boldsymbol{Q}/2,\uparrow}+\xi_{\boldsymbol{k}-\boldsymbol{Q}/2,\downarrow}-i\Omega_\nu)}}{\xi_{\boldsymbol{k}+\boldsymbol{Q}/2,\uparrow}+\xi_{\boldsymbol{k}-\boldsymbol{Q}/2,\downarrow}-i\Omega_\nu}, \tag{F.6}$$

which, in turn, is related to the $(\boldsymbol{k},\Omega_\nu)\to\infty$ behavior of (F.3). It is then convenient to define the difference:

$$\Delta\Pi(\boldsymbol{k};\boldsymbol{Q},\tau) = \Pi(\boldsymbol{k};\boldsymbol{Q},\tau) - \Pi^{(a)}(\boldsymbol{k};\boldsymbol{Q},\tau), \tag{F.7}$$

which can be readily transformed over τ. The expression (F.6) can then be added to the Fourier transform $\Delta\Pi(\boldsymbol{k};\boldsymbol{Q},\Omega_\nu)$ to obtain the desired $\Pi(\boldsymbol{k};\boldsymbol{Q},\Omega_\nu)$.

The next step consists in the Fourier transform of $\Pi(\boldsymbol{k};\boldsymbol{Q},\Omega_\nu)$ to the $\boldsymbol{\rho}$-space (F.2). First of all, one notices that the leading behavior of $\Pi(\boldsymbol{k};\boldsymbol{Q},\Omega_\nu)$ in the $(\boldsymbol{k},\Omega_\nu)\to\infty$ limit is given by:

$$\Pi_{\rm sc}(\boldsymbol{k};\boldsymbol{Q},\Omega_\nu) = \frac{1}{\xi_{\boldsymbol{k}+\boldsymbol{Q}/2,\uparrow}+\xi_{\boldsymbol{k}-\boldsymbol{Q}/2,\downarrow}-i\Omega_\nu}, \tag{F.8}$$

as the exponential in the numerator of (F.6) can be neglected when $\boldsymbol{k}\to\infty$. Note that this expression exactly corresponds to the strong-coupling limit (5.15) of $\Pi(\boldsymbol{k};\boldsymbol{Q},\Omega_\nu)$, which presents the analytical Fourier transform to the $\boldsymbol{\rho}$-space (5.16)

$$\Pi_{\rm sc}(\boldsymbol{\rho};\boldsymbol{Q},\Omega_\nu) = \frac{m}{4\pi\rho}e^{-m^{1/2}\rho\sqrt{\boldsymbol{Q}^2/(4m)-2\mu-i\Omega_\nu}}, \tag{F.9}$$

where $\mu = (\mu_\uparrow+\mu_\downarrow)/2$ and $\rho = |\boldsymbol{\rho}|$.

Also in this case, it is convenient to define a difference function[1]

$$\tilde{\Delta}\Pi(\boldsymbol{k};\boldsymbol{Q},\Omega_\nu) = \Pi(\boldsymbol{k};\boldsymbol{Q},\Omega_\nu) - \Pi_{\rm sc}(\boldsymbol{k};\boldsymbol{Q},\Omega_\nu), \tag{F.10}$$

and perform its Fourier transform on $\boldsymbol{\rho}$:

$$\tilde{\Delta}\Pi(\boldsymbol{\rho};\boldsymbol{Q},\Omega_\nu) = \int \frac{d\boldsymbol{k}}{(2\pi)^3}\, e^{i\boldsymbol{k}\cdot\boldsymbol{\rho}}\, \tilde{\Delta}\Pi(\boldsymbol{k};\boldsymbol{Q},\Omega_\nu). \tag{F.11}$$

Note however that this Fourier transform cannot be performed as the other $\boldsymbol{k}\to\boldsymbol{r}$ transforms, because in the integrand there is a non-trivial dependence on the angles between $\boldsymbol{k}$, $\boldsymbol{Q}$ and $\boldsymbol{\rho}$. The adopted procedure is then the following.

Choose $\boldsymbol{Q}$ as the reference axis, and call γ the angle between $\boldsymbol{Q}$ and $\boldsymbol{\rho}$, θ the angle between $\boldsymbol{k}$ and $\boldsymbol{Q}$ and φ the angle between the components of $\boldsymbol{k}$ and $\boldsymbol{\rho}$ that are perpendicular to $\boldsymbol{Q}$. Note that γ is an external variable, while θ and φ are integration variables. With this choice of variables, the φ dependence appears only in the exponential

[1] Note that the analytical expression (F.8) presents a singularity in $\boldsymbol{k}$ for $\Omega_\nu = 0$ and $\mu > 0$. Accordingly, we set $\mu = 0$ in the subtracted analytical expression (F.8) and in its Fourier transform (F.9) when μ is positive.

$e^{i\boldsymbol{k}\cdot\boldsymbol{\rho}}$, because it is the only term that depends on the direction of $\boldsymbol{\rho}$. The scalar product $\boldsymbol{k}\cdot\boldsymbol{\rho}$ in the exponent is given by:

$$\boldsymbol{k}\cdot\boldsymbol{\rho} = \boldsymbol{k}_\perp\cdot\boldsymbol{\rho}_\perp + \boldsymbol{k}_\parallel\cdot\boldsymbol{\rho}_\parallel = k\rho\sin\theta\sin\gamma\cos\varphi + k\rho\cos\theta\cos\gamma. \tag{F.12}$$

where $k=|\boldsymbol{k}|$, $\rho=|\boldsymbol{\rho}|$, and the expression has been divided in the sum of the components perpendicular and parallel to $\boldsymbol{Q}$. The integral over φ can then be expressed analytically in terms of the Bessel function of first kind and order zero J_0:

$$\int_0^{2\pi} d\varphi\, e^{ik\rho\sin\theta\sin\gamma\cos\varphi} = 2\pi J_0(k\rho\sin\theta\sin\gamma). \tag{F.13}$$

The Fourier transform (F.11) becomes then

$$\begin{aligned}&\tilde{\Delta}\Pi(\boldsymbol{\rho};\boldsymbol{Q},\Omega_\nu) = \\ &\quad\int_0^{+\infty}\frac{dk}{(2\pi)^2}\int_0^{\pi} d\theta\ \sin\theta\, J_0(k\rho\sin\theta\sin\gamma)\, e^{ik\rho\cos\theta\cos\gamma}\,\tilde{\Delta}\Pi(\boldsymbol{k};\boldsymbol{Q},\Omega_\nu).\end{aligned} \tag{F.14}$$

This double integral is performed with the Gauss-Legendre quadrature method using typically 20 points for the θ integral and 40 points for the k integral. Afterwards, the analytical expression (F.9) can be added back to recover the desired $\Pi(\boldsymbol{\rho};\boldsymbol{Q},\Omega_\nu)$.[2]

One can now replace $\Pi(\boldsymbol{\rho};\boldsymbol{Q},\Omega_\nu) = \tilde{\Delta}\Pi(\boldsymbol{\rho};\boldsymbol{Q},\Omega_\nu) + \Pi_{\rm sc}(\boldsymbol{\rho};\boldsymbol{Q},\Omega_\nu)$ into the integral (F.1), obtaining three terms:

$$g_{\uparrow\downarrow}(\boldsymbol{\rho}) = g^{(1)}_{\uparrow\downarrow}(\boldsymbol{\rho}) + g^{(2)}_{\uparrow\downarrow}(\boldsymbol{\rho}) + g^{(3)}_{\uparrow\downarrow}(\boldsymbol{\rho}), \tag{F.15}$$

where

$$g^{(1)}_{\uparrow\downarrow}(\boldsymbol{\rho}) = \int\frac{d\boldsymbol{Q}}{(2\pi)^3}\frac{1}{\beta}\sum_\nu e^{i\Omega_\nu\eta}\,\Gamma(\boldsymbol{Q},\Omega_\nu)\,[\tilde{\Delta}\Pi(\boldsymbol{\rho};\boldsymbol{Q},\Omega_\nu)]^2, \tag{F.16}$$

$$g^{(2)}_{\uparrow\downarrow}(\boldsymbol{\rho}) = 2\int\frac{d\boldsymbol{Q}}{(2\pi)^3}\frac{1}{\beta}\sum_\nu e^{i\Omega_\nu\eta}\,\Gamma(\boldsymbol{Q},\Omega_\nu)\,\Pi_{\rm sc}(\boldsymbol{\rho};\boldsymbol{Q},\Omega_\nu)\tilde{\Delta}\Pi(\boldsymbol{\rho};\boldsymbol{Q},\Omega_\nu), \tag{F.17}$$

$$g^{(3)}_{\uparrow\downarrow}(\boldsymbol{\rho}) = \int\frac{d\boldsymbol{Q}}{(2\pi)^3}\frac{1}{\beta}\sum_\nu e^{i\Omega_\nu\eta}\,\Gamma(\boldsymbol{Q},\Omega_\nu)\,[\Pi_{\rm sc}(\boldsymbol{\rho};\boldsymbol{Q},\Omega_\nu)]^2. \tag{F.18}$$

For these three contributions one has still to perform (i) a sum over the bosonic frequencies Ω_ν (ii) an integral over the angle γ between $\boldsymbol{Q}$ and $\boldsymbol{\rho}$ and (iii) an integral over $Q=|\boldsymbol{Q}|$, in this order.[3]

Let us consider the sums over the bosonic frequencies. As far as the first two contributions, it is possible to show that the high-frequency tail of the integrand is at least $\sim\Omega_\nu^{-5/2}$ for (F.16) and at least $\sim\Omega_\nu^{-3/2}$ for (F.17), so they go to zero fast enough to

[2] In the $\mu>0$ case, when we set $\mu=0$ into (F.8) and (F.9), the large-k tail of the integrand of (F.14) goes like $\sin(k\rho)/k^3$ and must be integrated analytically in terms of the function $\mathrm{Si}(x)=\int_0^x dt\sin(t)/t$ and independently summed afterwards.

[3] The integral over the azimuthal angle φ_γ is trivial and gives a multiplicative 2π factor.

be directly summed over Ω_ν without any further effort. The sum is typically performed by interpolating over a grid of 120 frequencies, of which 30 are fixed to be the first actual frequencies and the remaining 90 are taken on a log scale.

The third contribution (F.18), instead, presents a high-frequency behavior that can be $\sim \Omega_\nu^{-1/2}$ in the proximity of $\rho = 0$ (where $\Pi_{\rm sc}$ is almost a constant). The sum over the bosonic frequencies of this term must then be performed with extra care.

For $\rho \to 0$, the calculation is simply given by the sum over bosonic frequencies of $\Gamma(\boldsymbol{Q}, \Omega_\nu)$, that was already present within the main self-consistent loop and is described in Section A.2. Here, we generalize that scheme to work also for $\rho > 0$. Let us start by defining the difference function:

$$\begin{aligned}\Delta g^{(3)}_{\uparrow\downarrow}(\boldsymbol{\rho}) &= g^{(3)}_{\uparrow\downarrow}(\boldsymbol{\rho}) - g^{(3a)}_{\uparrow\downarrow}(\boldsymbol{\rho}) \\ &= \int \frac{d\boldsymbol{Q}}{(2\pi)^3} \frac{1}{\beta} \sum_\nu e^{i\Omega_\nu \eta} \left[\Gamma(\boldsymbol{Q}, \Omega_\nu) - \Gamma_{\rm sc}(\boldsymbol{Q}, \Omega_\nu)\right] \left[\Pi_{\rm sc}(\boldsymbol{\rho}; \boldsymbol{Q}, \Omega_\nu)\right]^2,'\end{aligned} \tag{F.19}$$

where

$$g^{(3a)}_{\uparrow\downarrow}(\boldsymbol{\rho}) = \int \frac{d\boldsymbol{Q}}{(2\pi)^3} \frac{1}{\beta} \sum_\nu e^{i\Omega_\nu \eta}\, \Gamma_{\rm sc}(\boldsymbol{Q}, \Omega_\nu) \left[\Pi_{\rm sc}(\boldsymbol{\rho}; \boldsymbol{Q}, \Omega_\nu)\right]^2, \tag{F.20}$$

and $\Gamma_{\rm sc}$ is the strong-coupling limit of the particle-particle propagator (2.83).[4] The sum over the bosonic frequencies in (F.19) can now be performed numerically, as the high-frequency tail is at least $\sim \Omega_\nu^{-3/2}$.

What remains to be calculated is the sum over bosonic frequencies within (F.20). For consistency with the Section A.2, the procedure is shown here in the same dimensionless units (cf. introduction of Appendix A). In this units, the particle-particle bubble (F.9) reads

$$\Pi_{\rm sc}(\boldsymbol{\rho}; \boldsymbol{Q}, \Omega_\nu) = \frac{e^{-\frac{\rho}{2}\sqrt{\boldsymbol{Q}^2 - 4\mu - 2i\Omega_\nu}}}{8\pi\rho}, \tag{F.21}$$

while the particle-particle propagator $\Gamma_{\rm sc}$ is given in Eq. (A.11). As in (A.13), one can perform an analytic continuation to the complex z-plane

$$\begin{aligned}\mathcal{I}^{(3a)}(\boldsymbol{\rho}; \boldsymbol{Q}) &= \frac{1}{\beta} \sum_\nu e^{i\Omega_\nu \eta}\, \Gamma_{\rm sc}(\boldsymbol{Q}, \Omega_\nu) \left[\Pi_{\rm sc}(\boldsymbol{\rho}; \boldsymbol{Q}, \Omega_\nu)\right]^2 \\ &= \frac{1}{2\pi i} \oint_{\mathcal{C}} dz \frac{e^{\beta z}}{(e^{\beta z} - 1)} \Gamma_{\rm sc}(\boldsymbol{Q}, z) \left[\Pi_{\rm sc}(\boldsymbol{\rho}; \boldsymbol{Q}, z)\right]^2\end{aligned} \tag{F.22}$$

where the contour $\mathcal{C}$ surrounds the poles of the Bose function $b(z) = 1/(e^{\beta z} - 1)$ on the imaginary axis, and we have used the periodicity in τ to replace $-\eta \to \beta^-$ in the exponential at the numerator. As in (A.13), the integrand presents a branch cut along the negative real axis starting at $z_{\rm c} = 2(\mu - \boldsymbol{Q}^2/4)$ as well as a pole at $z_{\rm p} = 2v^2 + z_c$

[4] As we take $\mu = 0$ in the strong-coupling expressions when $\mu > 0$, the $\Omega_\nu = 0$ term does not have any singularity as it had in Section A.2. The downside of this is that for $\mu > 0$ the high-frequency tail of the difference function in (F.19) is only $\sim \Omega_\nu^{-3/2}$ instead of $\sim \Omega_\nu^{-2}$.

when $v > 0$. The integral in Eq. (A.13) then reduces to the calculation of an integral along the branch cut and of the residue of the pole:

$$\mathcal{I}^{(3a)}(\boldsymbol{\rho};\boldsymbol{Q}) = \mathcal{I}^{(3a)}_{\rm cut}(\boldsymbol{\rho};\boldsymbol{Q}) + \mathcal{I}^{(3a)}_{\rm res}(\boldsymbol{\rho};\boldsymbol{Q}), \tag{F.23}$$

where the first term can be cast in the form[5]

$$\begin{aligned}\mathcal{I}^{(3a)}_{\rm cut}(\boldsymbol{\rho};\boldsymbol{Q}) = \frac{8\sqrt{2/\beta}\, e^{\beta z_{\rm c}}}{(8\pi\rho)^2}\int_0^{+\infty} dx\, \frac{e^{-x^2}\, x}{e^{\beta z_{\rm c}} e^{-x^2} - 1} \\ \times \frac{\sqrt{2\beta} v \sin(\sqrt{2/\beta}\rho x) - x\cos(\sqrt{2/\beta}\rho x)}{x^2 + 2\beta v^2},\end{aligned} \tag{F.24}$$

while the second term assumes the analytical form

$$\mathcal{I}^{(3a)}_{\rm res}(\boldsymbol{\rho};\boldsymbol{Q}) = -\theta(v)\frac{16\pi v}{(8\pi\rho)^2}\frac{e^{\beta z_{\rm p}}\, e^{-2v\rho}}{e^{\beta z_{\rm p}} - 1}. \tag{F.25}$$

Once this calculation is performed, one can integrate (F.23) over $\boldsymbol{Q}$ and γ to obtain $g^{(3a)}_{\uparrow\downarrow}(\boldsymbol{\rho})$ and then sum it to $\Delta g^{(3)}_{\uparrow\downarrow}(\boldsymbol{\rho})$ to finally obtain $g^{(3)}_{\uparrow\downarrow}(\boldsymbol{\rho})$.[6]

Let us conclude with some considerations on the remaining integrations over γ and $Q = |\boldsymbol{Q}|$. In the (F.18) term the integration over γ is trivial, because the integrand does not depend on γ. For the (F.16) and (F.17) terms, instead, the integral must be performed numerically. However, by careful inspection of the expression (F.14) one can see that the integrands of (F.16) and (F.17) are even under the transformation $\gamma \to \pi - \gamma$. This means that the integral can be performed only on the interval $\gamma \in [0, \pi/2]$ and then multiplied by 2. The integrations over γ and $Q = |\boldsymbol{Q}|$ are then performed with the Gauss-Legendre quadrature method with a typical number of points of 15 and 40, respectively.

F.2 Calculation of $\xi_{\rm pair}$

The pair coherence length $\xi_{\rm pair}$ is defined in terms of the pair correlation function $g_{\uparrow\downarrow}(\boldsymbol{\rho})$ as (5.2)

$$\xi^2_{\rm pair} = \frac{\int d\boldsymbol{\rho}\, \boldsymbol{\rho}^2 g_{\uparrow\downarrow}(\boldsymbol{\rho})}{\int d\boldsymbol{\rho}\, g_{\uparrow\downarrow}(\boldsymbol{\rho})}. \tag{F.26}$$

While this calculation can be performed by directly integrating $g_{\uparrow\downarrow}(\boldsymbol{\rho})$ in $\boldsymbol{\rho}$-space, this procedure is somewhat unstable at low temperature and in weak coupling due to the noise in the oscillations at large $\boldsymbol{\rho}$, that is amplified in the numerator of (F.26) because $g_{\uparrow\downarrow}(\boldsymbol{\rho})$ is multiplied by $\boldsymbol{\rho}^2$. It is then more convenient to calculate the denominator and

[5] Note that here we assumed $\mu \leq 0$, so $z_{\rm c}$ is always negative. If one wants to generalize the calculation also to positive z_c, the procedure is similar to what is done in Eq. (A.16).

[6] To convert back in dimensional units, the relation is $g_{\uparrow\downarrow}(\boldsymbol{\rho})/k_F^6 = 2\,\tilde{g}_{\uparrow\downarrow}(\boldsymbol{\rho})$, where the factor of 2 originates by the expression of Γ in dimensionless units.

numerator of (F.26) directly in momentum space as in (5.9) and (5.10)

$$\mathcal{I}_0 = \int d\boldsymbol{\rho}\, g_{\uparrow\downarrow}(\boldsymbol{\rho}) = \int \frac{d\boldsymbol{Q}}{(2\pi)^3}\frac{1}{\beta}\sum_\nu e^{i\Omega_\nu\eta}\,\Gamma(\boldsymbol{Q},\Omega_\nu)\int\frac{d\boldsymbol{k}}{(2\pi)^3}[\Pi(\boldsymbol{k};\boldsymbol{Q},\Omega_\nu)]^2, \tag{F.27}$$

$$\mathcal{I}_2 = \int d\boldsymbol{\rho}\,\boldsymbol{\rho}^2\, g_{\uparrow\downarrow}(\boldsymbol{\rho}) = \int \frac{d\boldsymbol{Q}}{(2\pi)^3}\frac{1}{\beta}\sum_\nu e^{i\Omega_\nu\eta}\,\Gamma(\boldsymbol{Q},\Omega_\nu)\int\frac{d\boldsymbol{k}}{(2\pi)^3}[\nabla_{\boldsymbol{k}}\,\Pi(\boldsymbol{k};\boldsymbol{Q},\Omega_\nu)]^2. \tag{F.28}$$

The procedure to calculate the particle-particle bubble $\Pi(\boldsymbol{k};\boldsymbol{Q},\Omega_\nu)$ has been already described in the first part of the previous section. What remains to be done is (i) an integral over $\boldsymbol{k}$ (which includes an integral over the angle θ between $\boldsymbol{k}$ and $\boldsymbol{Q}$), (ii) a sum over the bosonic frequencies Ω_ν and (iii) an integral over $Q = |\boldsymbol{Q}|$. When it is not stated otherwise, the numerical integrations over $\boldsymbol{Q}$ and $\boldsymbol{k}$ and the sum over Ω_ν are performed with same methods and grids of the previous section. For the numerator (F.28), the derivative $\nabla_{\boldsymbol{k}}\,\Pi(\boldsymbol{k};\boldsymbol{Q},\Omega_\nu)$ is performed numerically. Also here, it is useful to define the difference function (F.10)

$$\tilde{\Delta}\Pi(\boldsymbol{k};\boldsymbol{Q},\Omega_\nu) = \Pi(\boldsymbol{k};\boldsymbol{Q},\Omega_\nu) - \Pi_{\rm sc}(\boldsymbol{k};\boldsymbol{Q},\Omega_\nu), \tag{F.29}$$

where $\Pi_{\rm sc}(\boldsymbol{k};\boldsymbol{Q},\Omega_\nu)$ is given in (F.8).[7]

Let us start with the denominator $\mathcal{I}_0$ of Eq. (F.27). By inserting the difference function (F.29) within it, one obtains

$$\mathcal{I}_0 = \mathcal{I}_0^{(1)} + \mathcal{I}_0^{(2)} + \mathcal{I}_0^{(3)} \tag{F.30}$$

where

$$\mathcal{I}_0^{(1)} = \int \frac{d\boldsymbol{Q}}{(2\pi)^3}\frac{1}{\beta}\sum_\nu e^{i\Omega_\nu\eta}\,\Gamma(\boldsymbol{Q},\Omega_\nu)\int\frac{d\boldsymbol{k}}{(2\pi)^3}[\tilde{\Delta}\Pi(\boldsymbol{k};\boldsymbol{Q},\Omega_\nu)]^2, \tag{F.31}$$

$$\mathcal{I}_0^{(2)} = 2\int \frac{d\boldsymbol{Q}}{(2\pi)^3}\frac{1}{\beta}\sum_\nu e^{i\Omega_\nu\eta}\,\Gamma(\boldsymbol{Q},\Omega_\nu)\int\frac{d\boldsymbol{k}}{(2\pi)^3}\Pi_{\rm sc}(\boldsymbol{k};\boldsymbol{Q},\Omega_\nu)\tilde{\Delta}\Pi(\boldsymbol{k};\boldsymbol{Q},\Omega_\nu), \tag{F.32}$$

$$\mathcal{I}_0^{(3)} = \int \frac{d\boldsymbol{Q}}{(2\pi)^3}\frac{1}{\beta}\sum_\nu e^{i\Omega_\nu\eta}\,\Gamma(\boldsymbol{Q},\Omega_\nu)\int\frac{d\boldsymbol{k}}{(2\pi)^3}[\Pi_{\rm sc}(\boldsymbol{k};\boldsymbol{Q},\Omega_\nu)]^2. \tag{F.33}$$

Out of these expressions, the integrand of the third term (F.33) is the one that has the leading behavior for $(\boldsymbol{k},\Omega_\nu)\to\infty$, and it is the only one that requires extra care in the integration over $\boldsymbol{k}$ and the sum over Ω_ν. The integration over $\boldsymbol{k}$ can be performed analytically, yielding:

$$\int\frac{d\boldsymbol{k}}{(2\pi)^3}[\Pi_{\rm sc}(\boldsymbol{k};\boldsymbol{Q},\Omega_\nu)]^2 = \frac{m^{3/2}}{8\pi\sqrt{\boldsymbol{Q}^2/(4m) - 2\mu - i\Omega_\nu}}. \tag{F.34}$$

[7]Here, similarly to the previous section, we set $\mu/E_F = -0.01$ in the subtracted analytical function $\Pi_{\rm sc}(\boldsymbol{k};\boldsymbol{Q},\Omega_\nu)$ when $\mu/E_F > -0.01$. The choice of the value -0.01 instead of 0 is to facilitate the integration over $\boldsymbol{Q}$.

Note that this term multiplied by $\Gamma(\boldsymbol{Q},\Omega_\nu)$ has an high-frequency tail that goes like $\sim\Omega_\nu^{-1}$. A subtraction is then needed to perform the sum over the bosonic frequencies. Similarly to (F.19), one can define the difference function

$$\Delta\mathcal{I}_0^{(3)} = \mathcal{I}_0^{(3)} - \mathcal{I}_0^{(3a)} = \int \frac{d\boldsymbol{Q}}{(2\pi)^3}\frac{1}{\beta}\sum_\nu e^{i\Omega_\nu\eta}\left[\Gamma(\boldsymbol{Q},\Omega_\nu)-\Gamma_{\rm sc}(\boldsymbol{Q},\Omega_\nu)\right]\int\frac{d\boldsymbol{k}}{(2\pi)^3}[\Pi_{\rm sc}(\boldsymbol{k};\boldsymbol{Q},\Omega_\nu)]^2, \tag{F.35}$$

and perform the sum over the bosonic frequencies of the term

$$\mathcal{I}_0^{(3a)}(\boldsymbol{Q}) = \frac{1}{\beta}\sum_\nu e^{i\Omega_\nu\eta}\left[\Gamma_{\rm sc}(\boldsymbol{Q},\Omega_\nu)\right]\int\frac{d\boldsymbol{k}}{(2\pi)^3}[\Pi_{\rm sc}(\boldsymbol{k};\boldsymbol{Q},\Omega_\nu)]^2, \tag{F.36}$$

on the complex plane. With a procedure analogous to (F.22), and within the same dimensionless units of Section A.2, the expression (F.36) reduces to the calculation of an integral over the branch cut on the negative real axis starting at $z_{\rm c}=2(\mu-\boldsymbol{Q}^2/4)$ and (when $v>0$) of the residue of the pole at $z_{\rm p}=2v^2+z_c$

$$\mathcal{I}_0^{(3a)}(\boldsymbol{Q}) = \mathcal{I}_{0,\rm cut}^{(3a)}(\boldsymbol{Q}) + \mathcal{I}_{0,\rm res}^{(3a)}(\boldsymbol{Q}) \tag{F.37}$$

where the first term can be cast in the form

$$\begin{aligned}\mathcal{I}_{0,\rm cut}^{(3a)}(\boldsymbol{Q}) = \frac{e^{\beta z_{\rm c}}}{e^{\beta z_{\rm c}}-1}\Bigg[&\frac{\sqrt{2\beta}v}{2\pi}\int_0^{x_0}dx\,\frac{1-e^{-x^2}}{(e^{\beta z_{\rm c}}e^{-x^2}-1)(x^2+2\beta v^2)}\\ &-\frac{1}{2\pi}\arctan\left(\frac{\sqrt{2\beta}v}{x_0}\right)+\frac{\mathrm{sgn}(v)}{4}\Bigg]\end{aligned} \tag{F.38}$$

with the cutoff x_0 chosen so that $e^{-x_0^2}\ll 1$, while the second term is given by

$$\mathcal{I}_{0,\rm res}^{(3a)}(\boldsymbol{Q}) = -\frac{\theta(v)}{2}\frac{e^{\beta z_{\rm c}}}{e^{\beta z_{\rm c}}-1}. \tag{F.39}$$

The expression (F.37) can then be integrated over $\boldsymbol{Q}$ and added to (F.35) to finally obtain $\mathcal{I}_0^{(3)}$.

Let us now consider the numerator $\mathcal{I}_2$ of Eq. (F.28). By inserting the difference function (F.29) within (F.28), one obtains

$$\mathcal{I}_2 = \mathcal{I}_2^{(1)} + \mathcal{I}_2^{(2)} + \mathcal{I}_2^{(3)} \tag{F.40}$$

where

$$\mathcal{I}_2^{(1)} = \int\frac{d\boldsymbol{Q}}{(2\pi)^3}\frac{1}{\beta}\sum_\nu e^{i\Omega_\nu\eta}\,\Gamma(\boldsymbol{Q},\Omega_\nu)\int\frac{d\boldsymbol{k}}{(2\pi)^3}[\nabla_{\boldsymbol{k}}\,\tilde\Delta\Pi(\boldsymbol{k};\boldsymbol{Q},\Omega_\nu)]^2, \tag{F.41}$$

$$\mathcal{I}_2^{(2)} = 2\int\frac{d\boldsymbol{Q}}{(2\pi)^3}\frac{1}{\beta}\sum_\nu e^{i\Omega_\nu\eta}\,\Gamma(\boldsymbol{Q},\Omega_\nu)\int\frac{d\boldsymbol{k}}{(2\pi)^3}\nabla_{\boldsymbol{k}}\Pi_{\rm sc}(\boldsymbol{k};\boldsymbol{Q},\Omega_\nu)\cdot\nabla_{\boldsymbol{k}}\,\tilde\Delta\Pi(\boldsymbol{k};\boldsymbol{Q},\Omega_\nu), \tag{F.42}$$

$$\mathcal{I}_2^{(3)} = \int\frac{d\boldsymbol{Q}}{(2\pi)^3}\frac{1}{\beta}\sum_\nu e^{i\Omega_\nu\eta}\,\Gamma(\boldsymbol{Q},\Omega_\nu)\int\frac{d\boldsymbol{k}}{(2\pi)^3}[\nabla_{\boldsymbol{k}}\,\Pi_{\rm sc}(\boldsymbol{k};\boldsymbol{Q},\Omega_\nu)]^2. \tag{F.43}$$

First of all, notice that the derivatives of the kind $\nabla_{\boldsymbol{k}}\,\Pi$ are expressed in spherical coordinates as

$$\nabla_{\boldsymbol{k}}\,\Pi = \frac{\partial\Pi}{\partial k}\hat{k} + \frac{1}{k}\frac{\partial\Pi}{\partial\theta}\hat{\theta} \tag{F.44}$$

where $k = |\boldsymbol{k}|$, θ is the polar angle with respect to $\boldsymbol{Q}$, and the derivative with respect to the azimuthal angle φ is not shown because it is zero. The square of this expression is then given by

$$|\nabla_{\boldsymbol{k}}\,\Pi|^2 = \left(\frac{\partial\Pi}{\partial k}\right)^2 + \frac{1}{k^2}\left(\frac{\partial\Pi}{\partial\theta}\right)^2. \tag{F.45}$$

For the term $\tilde{\Delta}\Pi$, this derivative must be performed numerically. For the analytic term (F.8), instead, the derivative (F.44) is given by

$$\nabla_{\boldsymbol{k}}\,\Pi_{\rm sc}(\boldsymbol{k};\boldsymbol{Q},\Omega_\nu) = \frac{2\boldsymbol{k}/m}{\boldsymbol{k}^2/m + \boldsymbol{Q}^2/(4m) - 2\mu - i\Omega_\nu}, \tag{F.46}$$

and its square is

$$[\nabla_{\boldsymbol{k}}\,\Pi_{\rm sc}(\boldsymbol{k};\boldsymbol{Q},\Omega_\nu)]^2 = \frac{4\boldsymbol{k}^2/m^2}{(\boldsymbol{k}^2/m + \boldsymbol{Q}^2/(4m) - 2\mu - i\Omega_\nu)^2}. \tag{F.47}$$

Like for the denominator $\mathcal{I}_0$, the integrand of the third term (F.43) is the one with the leading behavior for $(\boldsymbol{k},\Omega_\nu) \to \infty$ and the integration over $\boldsymbol{k}$ can be performed analytically, yielding

$$\int \frac{d\boldsymbol{k}}{(2\pi)^3}[\nabla_{\boldsymbol{k}}\,\Pi_{\rm sc}(\boldsymbol{k};\boldsymbol{Q},\Omega_\nu)]^2 = \frac{m^{1/2}}{16\pi[\boldsymbol{Q}^2/(4m) - 2\mu - i\Omega_\nu]^{3/2}}. \tag{F.48}$$

This time, however, the overall high-frequency behavior of this term multiplied by $\Gamma(\boldsymbol{Q},\Omega_\nu)$ is $\sim \Omega_\nu^{-2}$, so it can be directly summed without numerical effort.

Appendix G

Details on the calculation of the pairing fraction

In this appendix we give the details of the calculation of the pairing fraction $n_{\rm p}/n_\sigma$ introduced in Chapter 6.

From Eq. (6.3), the pair density $n_{\rm p}$ is defined as:

$$n_{\rm p} = -\int \frac{d\boldsymbol{Q}}{(2\pi)^3}\frac{1}{\beta}\sum_\nu e^{i\Omega_\nu\eta}\,\mathcal{G}_B(\boldsymbol{Q},\Omega_\nu). \tag{G.1}$$

The bosonic propagator $\mathcal{G}_B(\boldsymbol{Q},\Omega_\nu)$ that appears in this equation is given by Eq. (6.8):

$$\mathcal{G}_B(\boldsymbol{Q},\Omega_\nu) = -\mathcal{F}_2(\boldsymbol{Q},\Omega_\nu) - \mathcal{F}_1(\boldsymbol{Q},\Omega_\nu)^2\,\Gamma(\boldsymbol{Q},\Omega_\nu), \tag{G.2}$$

where

$$\mathcal{F}_j(\boldsymbol{Q},\Omega_\nu) = \int \frac{d\boldsymbol{p}}{(2\pi)^3}\,\phi(\boldsymbol{p}+\boldsymbol{Q}/2)^j\,\frac{1}{\beta}\sum_n G(\boldsymbol{p}+\boldsymbol{Q},\omega_n+\Omega_\nu)G(-\boldsymbol{p},-\omega_n) \tag{G.3}$$

and Γ is the particle-particle propagator (2.106) within the self-consistent t-matrix approach. This means that the pair density $n_{\rm p}$ can be calculated as the sum of the "unbound" and "bound" contributions

$$n_{\rm p} = n_{\rm p}^{(u)} + n_{\rm p}^{(b)}, \tag{G.4}$$

where

$$n_{\rm p}^{(u)} = \int \frac{d\boldsymbol{Q}}{(2\pi)^3}\frac{1}{\beta}\sum_\nu e^{i\Omega_\nu\eta}\,\mathcal{F}_2(\boldsymbol{Q},\Omega_\nu), \tag{G.5}$$

$$n_{\rm p}^{(b)} = \int \frac{d\boldsymbol{Q}}{(2\pi)^3}\frac{1}{\beta}\sum_\nu e^{i\Omega_\nu\eta}\,\mathcal{F}_1(\boldsymbol{Q},\Omega_\nu)^2\,\Gamma(\boldsymbol{Q},\Omega_\nu). \tag{G.6}$$

For the function $\phi(\boldsymbol{p})$ within Eq. (G.3), we assume the form (6.16)

$$\phi(\boldsymbol{p}) = \frac{2\pi^{3/2}\mathcal{N}(a_F,b)}{\sqrt{b}\,p}\,\mathrm{Im}\left\{\exp\left[\frac{\left(a_F^{-1}-ip\right)^2}{4b}\right]\mathrm{erfc}\left(\frac{a_F^{-1}-ip}{2\sqrt{b}}\right)\right\}, \tag{G.7}$$

with

$$\mathcal{N}(a_F, b) = \frac{1}{\pi^{3/4}} \Big(\frac{b}{2}\Big)^{1/4} \frac{\exp[-\frac{1}{4ba_F^2}]}{\sqrt{\mathrm{erfc}[\frac{1}{\sqrt{2}ba_F}]}}, \tag{G.8}$$

where b is the parameter obtained by the fit of the pair correlation function $g_{\uparrow\downarrow}(\boldsymbol{\rho})$ (as explained in Section 6.4), and $\mathrm{erfc}(z)$ is the complementary error function of (complex) argument z [174].

The first thing to do is to calculate the form factors $\mathcal{F}_j(\boldsymbol{Q}, \Omega_\nu)$. By performing the substitution $\boldsymbol{p} \to \boldsymbol{p} - \boldsymbol{Q}/2$ in the momentum integral of Eq. (G.3), one can bring all the $\boldsymbol{Q}$ dependence within the Green's functions G and express $\mathcal{F}_j(\boldsymbol{Q}, \Omega_\nu)$ as

$$\begin{aligned} \mathcal{F}_j(\boldsymbol{Q}, \Omega_\nu) &= \int \frac{d\boldsymbol{p}}{(2\pi)^3}\, \phi(\boldsymbol{p})^j\, \frac{1}{\beta} \sum_n G(\boldsymbol{p} + \boldsymbol{Q}/2, \omega_n + \Omega_\nu) G(\boldsymbol{p} - \boldsymbol{Q}/2, -\omega_n) \\ &= \int \frac{d\boldsymbol{p}}{(2\pi)^3}\, \phi(\boldsymbol{p})^j\, \Pi(\boldsymbol{p}; \boldsymbol{Q}, \Omega_\nu), \end{aligned} \tag{G.9}$$

where we identified the particle-particle bubble $\Pi(\boldsymbol{p}; \boldsymbol{Q}, \Omega_\nu)$ introduced in Eq. (F.3) for the calculation of the pair correlation function. Similarly to Section F.1, it is convenient to work in τ-space where the convolution product within $\Pi(\boldsymbol{p}; \boldsymbol{Q}, \Omega_\nu)$ becomes the simple product (F.4)

$$\Pi(\boldsymbol{p}; \boldsymbol{Q}, \tau) = G(\boldsymbol{p} + \boldsymbol{Q}/2, \tau) G(\boldsymbol{p} - \boldsymbol{Q}/2, \tau). \tag{G.10}$$

One can then can define the transformed form factors as

$$\mathcal{F}_j(\boldsymbol{Q}, \tau) = \int \frac{d\boldsymbol{p}}{(2\pi)^3}\, \phi(\boldsymbol{p})^j\, \Pi(\boldsymbol{p}; \boldsymbol{Q}, \tau). \tag{G.11}$$

For the "unbound" contribution $n_{\mathrm{p}}^{(u)}$, the sum over the bosonic frequencies of Eq. (G.5) simply corresponds to take $\tau = \beta^-$ in the expression (G.11) with $j = 2$, so one has:

$$n_{\mathrm{p}}^{(u)} = \int \frac{d\boldsymbol{Q}}{(2\pi)^3}\, \mathcal{F}_2(\boldsymbol{Q}, \tau = \beta^-) = \int \frac{d\boldsymbol{Q}}{(2\pi)^3} \int \frac{d\boldsymbol{p}}{(2\pi)^3}\, \phi(\boldsymbol{p})^2\, \Pi(\boldsymbol{p}; \boldsymbol{Q}, \tau = \beta^-). \tag{G.12}$$

Here, the integrations over $p = |\boldsymbol{p}|$, $Q = |\boldsymbol{Q}|$ and the angle θ between $\boldsymbol{p}$ and $\boldsymbol{Q}$ can be performed with the Gauss-Legendre quadrature method (with typically 30-40 points for the p and Q integrals, and 20 points for the θ integral) without any additional effort.

As far as the "bound" contribution $n_{\mathrm{p}}^{(b)}$ of Eq. (G.6), instead, the calculation is more complicated because one cannot work directly in τ-space. To transform $\mathcal{F}_1$ back to the Ω_ν-space, it is first convenient to subtract the leading $\tau \to 0^+$ contribution. To determine this leading contribution, one can remember that the leading $(\boldsymbol{p}, \tau) \to (\infty, 0^+)$ contribution of the particle-particle bubble $\Pi(\boldsymbol{p}; \boldsymbol{Q}, \tau)$ is given by Eq. (F.5), so one has

$$\begin{aligned} \mathcal{F}_1(\boldsymbol{Q}, \tau) &\underset{\tau \to 0^+}{\simeq} \int \frac{d\boldsymbol{p}}{(2\pi)^3}\, \phi(\boldsymbol{p})\, e^{-(\xi_{\boldsymbol{p}+\boldsymbol{Q}/2} + \xi_{\boldsymbol{p}-\boldsymbol{Q}/2})\tau} \\ &= e^{\tau\left(\mu - \frac{\boldsymbol{Q}^2}{2m}\right)} \int \frac{d\boldsymbol{p}}{(2\pi)^3}\, \phi(\boldsymbol{p})\, e^{-\tau\, \boldsymbol{p}^2/m} \\ &= \frac{e^{\tau\left(\mu - \frac{\boldsymbol{Q}^2}{2m}\right)}}{\tau^{1/2}} \int \frac{d\boldsymbol{p}'}{(2\pi)^3}\, \frac{\phi(\boldsymbol{p}'/\tau^{1/2})}{\tau}\, e^{-\boldsymbol{p}'^2/m}, \end{aligned} \tag{G.13}$$

where, in the last line, we have performed the substitution $\boldsymbol{p}' = \tau^{1/2}\boldsymbol{p}$. It is evident now that to take the $\tau \to 0^+$ limit of the integrand one has to take the $\boldsymbol{p} \to \infty$ limit of the function $\phi(\boldsymbol{p})$ of Eq. (G.7), which is given by

$$\phi(\boldsymbol{p}) \underset{\boldsymbol{p}\to\infty}{\simeq} \frac{4\pi\mathcal{N}(a_F, b)}{\boldsymbol{p}^2}, \tag{G.14}$$

where the property $\mathrm{erfc}(x) \simeq e^{-x^2}/(\pi^{1/2}x)$ for $x \to \infty$ has been used. Inserting the expression (G.14) in (G.13), performing the integral over $\boldsymbol{p}'$ and taking $\tau = 0$ in the exponential that multiplies the expression, one obtains

$$\mathcal{F}_1(\boldsymbol{Q}, \tau) \underset{\tau\to 0^+}{\simeq} \mathcal{F}_1^{(a)}(\boldsymbol{Q}, \tau) = \frac{m^{1/2}\mathcal{N}(a_F, b)}{4\pi^{3/2}\tau^{1/2}}. \tag{G.15}$$

This expression can be analytically transformed to the frequency space, obtaining

$$\mathcal{F}_1^{(a)}(\boldsymbol{Q}, \Omega_\nu) = \frac{m^{1/2}\mathcal{N}(a_F, b)}{4\pi} \frac{\mathrm{erf}\left[\sqrt{-i\beta\Omega_\nu}\,\right]}{\sqrt{-i\Omega_\nu}} \tag{G.16}$$

where $\mathrm{erf}(z)$ is the error function of (complex) argument z [174].

One can then define the difference function

$$\Delta\mathcal{F}_1(\boldsymbol{Q}, \tau) = \mathcal{F}_1(\boldsymbol{Q}, \tau) - \mathcal{F}_1^{(a)}(\boldsymbol{Q}, \tau), \tag{G.17}$$

Fourier transform it on τ, and then sum (G.16) to its Fourier transform to obtain the desired $\mathcal{F}_1(\boldsymbol{Q}, \Omega_\nu)$. The expression found can be then used in (G.6) to calculate the "bound" contribution to the pair density $n_{\mathrm{p}}^{(b)}$. Note that the expression to be summed over the bosonic frequencies in (G.6) has a large frequency tail $\sim \Omega_\nu^{-3/2}$, so it can be directly summed by interpolating over a grid of (typically 200) frequencies on a log scale. To improve the precision on the sum over the fermionic frequencies, we also analytically summed the large-frequency tail of the integrand (obtainable from Eqs. (G.16) and (A.11)) from the frequency cutoff $(\Omega_\nu)_{\max}$ to $\Omega_\nu \to \infty$. The integral over $\boldsymbol{Q}$ is then performed equivalently to (G.12).

Appendix H

Comparison between the quantum many-body approach and the statistical atom-molecule model for the pairing fraction

It is interesting to determine under what physical circumstances the expressions for the total number of pairs $N_{\rm p}$ and for the total number of spin-σ fermions N_σ of our fully quantum many-body approach reduce to those of a statistical model of a fermion-boson mixture at equilibrium [4, 153].

To this end, we consider a homogeneous system, for which $N_{\rm p} = \mathcal{V}\, n_{\rm p}$ and $N_\sigma = \mathcal{V}\, n_\sigma$ are expressed in terms of the respective densities. By our quantum many-body approach, $n_{\rm p}$ is given by Eq. (6.17) with $\mathcal{G}_B$ given by the expression (6.8), while n_σ is given by the expression (2.108). To recover the physics of a fermion-boson (or atom-molecule) mixture, one requires the fermionic coupling to be sufficiently strong in the BEC regime and the temperature sufficiently low, for the internal structure of the composite bosons (dimers) to become irrelevant.

In this limit, the fermionic chemical potential μ becomes the largest energy scale of the problem and is written in the form $\mu = (\mu_B - \varepsilon_0)/2$, where $\varepsilon_0 = (m a_F^2)^{-1}$ is the dimer binding energy and μ_B the dimer chemical potential (cf. Section 2.2.6). The particle-particle bubble Π within Eq. (G.9) then reduces to

$$\Pi(\boldsymbol{p}; \boldsymbol{Q}, \Omega_\nu) \simeq \frac{1}{2\xi(\boldsymbol{p})}\,, \tag{H.1}$$

which, together with the expression (6.12) for $\phi(\boldsymbol{p})$ appropriate to this limit, yields the the following approximate form for the form factors (6.9) [121]:

$$\mathcal{F}_1(\boldsymbol{Q}, \Omega_\nu) \simeq \sqrt{\frac{m^2 a_F}{8\pi}} \quad , \quad \mathcal{F}_2(\boldsymbol{Q}, \Omega_\nu) \simeq \frac{m a_F^2}{4}\,. \tag{H.2}$$

This implies that, in the BEC limit where $a_F \to 0^+$, the "unbound" term $\mathcal{F}_2$ vanishes faster than $\mathcal{F}_1$ and can be neglected in the expression (6.8). In addition, in the same limit the particle-particle propagator $\Gamma(\boldsymbol{Q}, \Omega_\nu)$ of the "bound" term in the expression (6.8) acquires the polar form (2.85):

$$\Gamma(\boldsymbol{Q}, \Omega_\nu) \simeq -\frac{8\pi}{m^2 a_F} \frac{1}{i\Omega_\nu - \frac{\boldsymbol{Q}^2}{4m} + \mu_B} \,. \tag{H.3}$$

Combining these results together, one gets eventually for the bosonic density:

$$n_{\rm p} \simeq -\int \frac{d\boldsymbol{Q}}{(2\pi)^3} \frac{1}{\beta} \sum_\nu \frac{e^{i\Omega_\nu \eta}}{i\Omega_\nu - \frac{\boldsymbol{Q}^2}{4m} + \mu_B} = \int \frac{d\boldsymbol{Q}}{(2\pi)^3} \frac{1}{e^{\beta \xi_B(\boldsymbol{Q})} - 1} \tag{H.4}$$

in terms of the Bose-Einstein distribution of argument $\xi_B(\boldsymbol{Q}) = \frac{\boldsymbol{Q}^2}{4m} - \mu_B$.

To determine n_σ in the BEC limit at sufficiently low temperature, the procedure is analogous to the one presented in Section 2.2.6. We consider the expression (2.108) where we expand the single-particle Green's function (2.104) in series of the self-energy Σ

$$G(\boldsymbol{p}, \omega_n) \simeq G_0(\boldsymbol{p}, \omega_n) + G_0(\boldsymbol{p}, \omega_n)\, \Sigma(\boldsymbol{p}, \omega_n)\, G_0(\boldsymbol{p}, \omega_n) \, + \cdots \tag{H.5}$$

where $G_0(\boldsymbol{p}, \omega_n) = [i\omega_n - \xi(\boldsymbol{p})]^{-1}$ is the non-interacting single-particle Green's function, by relying on the fact that the fermionic chemical potential μ entering $\xi(\boldsymbol{p}) = \boldsymbol{p}^2/(2m) - \mu$ is the largest energy scale in the problem. We thus obtain:

$$\begin{aligned} n_\sigma &\simeq \int \frac{d\boldsymbol{p}}{(2\pi)^3} \frac{1}{\beta} \sum_n e^{i\omega_n \eta}\, G_0(\boldsymbol{p}, \omega_n) \\ &\quad + \int \frac{d\boldsymbol{p}}{(2\pi)^3} \frac{1}{\beta} \sum_n G_0(\boldsymbol{p}, \omega_n)^2\, \Sigma(\boldsymbol{p}, \omega_n) \, + \cdots \\ &\equiv n_\sigma^{(0)} \, + \, n_\sigma^{(1)} \,. \end{aligned} \tag{H.6}$$

Here,

$$n_\sigma^{(0)} = \int \frac{d\boldsymbol{p}}{(2\pi)^3} \frac{1}{\beta} \sum_n e^{i\omega_n \eta}\, G_0(\boldsymbol{p}, \omega_n) = \int \frac{d\boldsymbol{p}}{(2\pi)^3} \frac{1}{e^{\beta \xi(\boldsymbol{p})} + 1} \tag{H.7}$$

coincides with the density $n_{\rm f}$ of fermions (or atoms) expressed in terms of the Fermi-Dirac distribution of argument $\xi(\boldsymbol{p})$, and

$$\begin{aligned} n_\sigma^{(1)} &= \int \frac{d\boldsymbol{p}}{(2\pi)^3} \frac{1}{\beta} \sum_n G_0(\boldsymbol{p}, \omega_n)^2\, \Sigma(\boldsymbol{p}, \omega_n) \\ &\simeq -\int \frac{d\boldsymbol{p}}{(2\pi)^3} \frac{1}{\beta} \sum_n G_0(\boldsymbol{p}, \omega_n)^2\, G_0(-\boldsymbol{p}, -\omega_n) \int \frac{d\boldsymbol{Q}}{(2\pi)^3} \frac{1}{\beta} \sum_\nu e^{i\Omega_\nu \eta}\, \Gamma(\boldsymbol{Q}, \Omega_\nu) \end{aligned} \tag{H.8}$$

owing to the approximate form for the self-energy (2.105) which is valid in this limit. With the polar approximation (H.3) for $\Gamma(\boldsymbol{Q}, \Omega_\nu)$ and the further approximate result

$$\int \frac{d\boldsymbol{p}}{(2\pi)^3} \frac{1}{\beta} \sum_n G_0(\boldsymbol{p}, \omega_n)^2\, G_0(-\boldsymbol{p}, -\omega_n) \simeq -\frac{m^2\, a_F}{8\pi} \,, \tag{H.9}$$

the expression (H.8) reduces to

$$n_\sigma^{(1)} = \int \frac{d\boldsymbol{Q}}{(2\pi)^3} \frac{1}{e^{\beta\xi_B(\boldsymbol{Q})} - 1} \tag{H.10}$$

which coincides with the density n_p of bosons (or molecules) given by Eq.(H.4). A combination of Eqs. (H.6), (H.7), and (H.10) yields eventually the result:

$$\begin{aligned} n_\sigma = n_\mathrm{f} + n_\mathrm{p} &= \int \frac{d\boldsymbol{p}}{(2\pi)^3} \frac{1}{e^{\beta\xi(\boldsymbol{p})} + 1} \\ &+ \int \frac{d\boldsymbol{Q}}{(2\pi)^3} \frac{1}{e^{\beta\xi_B(\boldsymbol{Q})} - 1} \,. \end{aligned} \tag{H.11}$$

At this point, the fermionic chemical potential μ can be eliminated from Eq. (H.11) by fixing the value of n_σ therein, with the bosonic chemical potential $\mu_B = 2\mu + \varepsilon_0$ following in a consistent way.

There remains to find an explicit connection with the expressions of the fermion-boson (or atom-molecule) model, which were obtained in Refs. [4, 153] in the classical limit and used in Ref. [105] to account for the experimental data in the BEC regime of the phase diagram. To this end, we consider the classical limit of the expressions (H.11) by neglecting ± 1 in the denominators, and perform the trap average by replacing $\mu \to \mu - V_\mathrm{f}(\boldsymbol{r})$ and $\mu_B \to \mu_B - V_\mathrm{p}(\boldsymbol{r})$ and integrating over the space variable $\boldsymbol{r}$, similarly to what was done in Section 4.1. Here,

$$V_{\mathrm{f/p}}(\boldsymbol{r}) = \frac{1}{2} M_{\mathrm{f/p}} \left(\omega_x^2 x^2 + \omega_y^2 y^2 + \omega_z^2 z^2\right) \tag{H.12}$$

is the (anisotropic) harmonic oscillator potential commonly considered for ultracold gases, with $M_\mathrm{f} = m$ for fermions (or atoms) and $M_\mathrm{p} = 2m$ for bosons (or molecules). The results for the total number of fermions N_f and the total number of bosons N_p then become:

$$N_\mathrm{f} \simeq \int d\boldsymbol{r} \int \frac{d\boldsymbol{p}}{(2\pi)^3} e^{-\beta\left[\frac{\boldsymbol{p}^2}{2m} + V_\mathrm{f}(\boldsymbol{r}) - \mu\right]} = \left(\frac{k_B T}{\bar{\omega}}\right)^3 e^{\mu/k_B T} \tag{H.13}$$

and

$$N_\mathrm{p} \simeq \int d\boldsymbol{r} \int \frac{d\boldsymbol{Q}}{(2\pi)^3} e^{-\beta\left[\frac{\boldsymbol{Q}^2}{4m} + V_\mathrm{p}(\boldsymbol{r}) - \mu_B\right]} = \left(\frac{k_B T}{\bar{\omega}}\right)^3 e^{\mu_B/k_B T} \tag{H.14}$$

where $\bar{\omega} = (\omega_x \omega_y \omega_z)^{1/3}$ is the average trap frequency (cf., e.g., Refs.[177, 178]). From these results it follows that

$$\frac{N_\mathrm{f}^2}{N_\mathrm{p}} = \left(\frac{k_B T}{\bar{\omega}}\right)^3 e^{(2\mu - \mu_B)/k_B T} = \left(\frac{k_B T}{\bar{\omega}}\right)^3 e^{-\varepsilon_0/k_B T} \,, \tag{H.15}$$

from which, by replacing $\bar{\omega} = E_F/(6N_\sigma)^{1/3}$ where E_F is the Fermi energy for the trap, one recovers the expression reported in Appendix A of Ref. [105]. More generally, N_p and N_f for the trapped case could be obtained in closed form directly from Eqs. (H.4) and

(H.7), in terms of $\mathrm{Li}_3(e^{\beta\mu_B})$ for bosons and $\mathrm{Li}_3(-e^{\beta\mu_B})$ for fermions (where $\mathrm{Li}_n(z)$ is the poly-logarithmic function of index n and argument z). The expression (H.15) generalizes to a harmonically trapped system the law of mass action valid for a homogeneous system [179].

Finally, it is worth summarizing what is lost when passing from the fully quantum many-body approach to its simplified version obtained above. To get this simplified version, in Eq. (6.8) we have (i) neglected the "unbound" term $-\mathcal{F}_2(\boldsymbol{Q},\Omega_\nu)$, (ii) approximated $\phi(\boldsymbol{p})$ in the expression (6.9) for $\mathcal{F}_1(\boldsymbol{Q},\Omega_\nu)$ by the two-body form (6.12) and taken $\mu=-\varepsilon_0/2$ therein with $\varepsilon_0 \gg k_BT$, and (iii) approximated $\Gamma(\boldsymbol{Q},\Omega_\nu)$ by the polar form (H.3); while in Eq. (2.108) we have performed the expansion (H.5) with the typical approximations that apply to the BEC limit at low temperature when μ is the largest energy scale in the problem. None of these approximations, however, is valid either away from the BEC limit when approaching unitarity at any temperature, or in the BEC limit itself for sufficiently high temperature. In both these cases, the fermionic nature of the "preformed pairs" manifests itself and only fermionic correlations remain physically relevant. On physical grounds, the results of the quantum many-body approach and of the statistical fermion-boson model differ from each other to the extent that the latter bears essentially on the chemical reaction (dimer $\longleftrightarrow$ spin-$\uparrow$ + spin-$\downarrow$) for molecules that break up into atom pairs and vice-versa, with no regard on the way the molecules are formed by the laws of quantum mechanics and on the effects that the surrounding environment might exert on them through the inter-particle collisions.

In this context, it is interesting to explicitly verify to what extent the results of the quantum many-body approach (Q) and of the classical statistical model (C) differ from each other in the BEC limit of the homogeneous system at sufficiently high temperature.

To this end, Fig. H.1 shows the temperature dependence of the relative difference $\delta n_\mathrm{p}/n_\mathrm{p}^{(Q)}$ for the couplings $(k_Fa_F)^{-1}=(0.5,1.0,1.5)$, where $\delta n_\mathrm{p}=n_\mathrm{p}^{(Q)}-n_\mathrm{p}^{(C)}$. One sees that this relative difference can be substantial in all cases. In particular, for $k_BT\lesssim\varepsilon_0$ the relative difference increases with increasing temperature and decreases with increasing coupling, as expected. The following apparent reduction of the relative difference for $k_BT\gtrsim\varepsilon_0$ then turns into a substantial increase (in absolute value) when $k_BT\gg\varepsilon_0$. Again in favor of the results obtained by the quantum many-body (t-matrix) approach, one should recall that in the high-temperature limit this approach correctly recovers the controlled high-temperature (virial) expansion to second order [43]. Specifically, when this high-temperature expansion is made on the self-energy, keeping both the bound-state (pole) and scattering (continuum) contributions to the particle-particle propagator Γ of Eq. (2.106) turns out to be essential to correctly recover the virial expansion. Since the statistical model includes only the bound-state contribution, it unavoidably fails in the high-temperature limit.

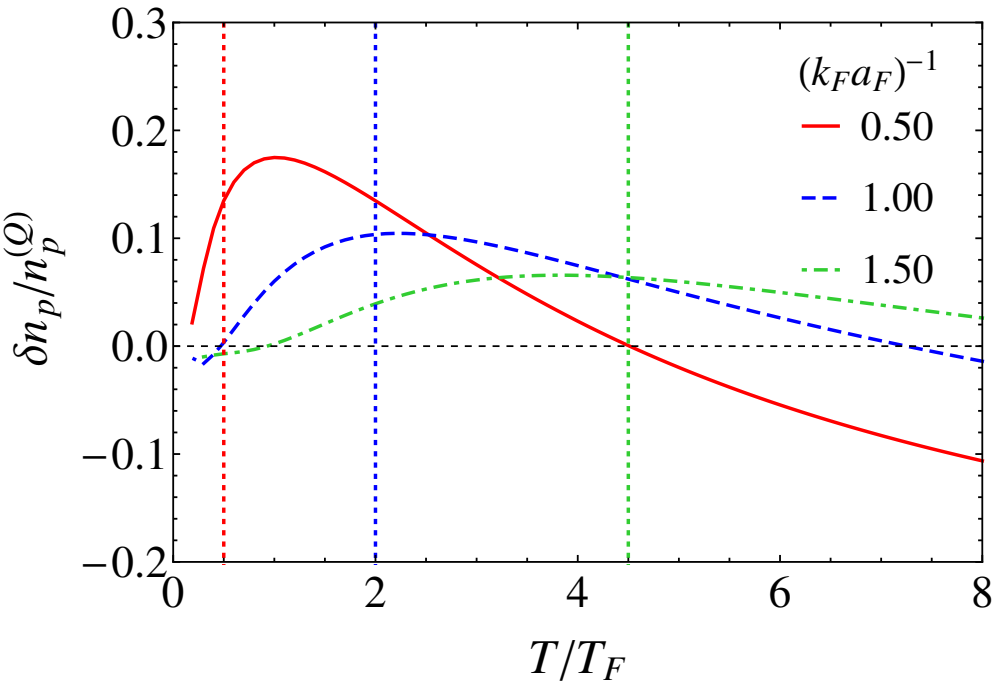

Figure H.1: Temperature dependence of the relative difference $\delta n_{\rm p}/n_{\rm p}^{(Q)}$ with $\delta n_{\rm p} = n_{\rm p}^{(Q)} - n_{\rm p}^{(C)}$ between the quantum many-body (Q) and classical statistical (C) calculations of the pair density $n_{\rm p}$ for the homogeneous system at various couplings. The vertical lines indicate the corresponding binding energies ε_0 (in units of E_F), for increasing coupling from left to right.

Bibliography

[1] H. K. Onnes, *The resistance of pure mercury at helium temperatures*, Commun. Phys. Lab. Univ. Leiden, 12:120 (1911).

[2] J. Bardeen, L. N. Cooper, and J. R. Schrieffer, *Theory of superconductivity*, Phys. Rev. **108**, 1175 (1957).

[3] M. R. Schafroth, S. T. Butler, J. M. Blatt, *Quasi-chemical equilibrium model for superconductivity*, Helv. Phys. Acta **30**, 93–134 (1957).

[4] D. M. Eagles, *Possible pairing without superconductivity at low carrier concentrations in bulk and thin-film superconducting semiconductors*, Phys. Rev. **186**, 456 (1969).

[5] A. J. Leggett, *Diatomic molecules and Cooper pairs*, in: A. Pekalski, R. Przystawa (Eds.), *Modern trends in the theory of condensed matter*, Vol. 115 of Lecture Notes in Physics, Springer-Verlag, Berlin, 1980, p. 13.

[6] M. Randeria, J.-M. Duan, L.-Y. Shieh, *Bound states, Cooper pairing, and Bose condensation in two dimensions*, Phys. Rev. Lett. **62**, 981–984 (1989).

[7] R. Micnas, J. Ranninger, S. Robaszkiewicz, *Superconductivity in narrow-band systems with local nonretarded attractive interactions*, Rev. Mod. Phys. **62**, 113–171 (1990).

[8] M. Randeria, N. Trivedi, A. Moreo, R. T. Scalettar, *Pairing and spin gap in the normal state of short coherence length superconductors*, Phys. Rev. Lett. **69**, 2001–2004 (1992).

[9] M. Drechsler, W. Zwerger, *Crossover from BCS-superconductivity to Bose-condensation*, Annalen der Physik **504**, 15–23 (1992).

[10] F. Pistolesi, G. C. Strinati, *Evolution from BCS superconductivity to Bose condensation: Role of the parameter $k_F\xi$*, Phys. Rev. B **49**, 6356–6359 (1994).

[11] M. Casas, J. M. Getino, M. de Llano, A. Puente, R. M. Quick, H. Rubio, D. M. van der Walt, *BCS-Bose model of exotic superconductors: Generalized coherence length*, Phys. Rev. B **50**, 15945–15952 (1994).

[12] M. Baldo, U. Lombardo, P. Schuck, *Deuteron formation in expanding nuclear matter from a strong coupling BCS approach*, Phys. Rev. C **52**, 975–985 (1995).

[13] M. Greiner, C. A. Regal, D. S. Jin, *Emergence of a molecular Bose-Einstein condensate from a Fermi gas*, Nature **426**, 537–540 (2003).

[14] S. Jochim, M. Bartenstein, A. Altmeyer, G. Hendl, S. Riedl, C. Chin, J. Hecker Denschlag, R. Grimm, *Bose-Einstein condensation of molecules*, Science **302**, 2101–2103 (2003).

[15] S. Jochim, M. Bartenstein, A. Altmeyer, G. Hendl, C. Chin, J. Hecker Denschlag, R. Grimm, *Pure gas of optically trapped molecules created from fermionic atoms*, Phys. Rev. Lett. **91**, 240402 (2003).

[16] M. W. Zwierlein, C. A. Stan, C. H. Schunck, S. M. F. Raupach, S. Gupta, Z. Hadzibabic, W. Ketterle, *Observation of Bose-Einstein condensation of molecules*, Phys. Rev. Lett. **91**, 250401 (2003).

[17] C. A. Regal, M. Greiner, D. S. Jin, *Observation of resonance condensation of fermionic atomic pairs*, Phys. Rev. Lett. **92**, 040403 (2004).

[18] C. Chin, M. Bartenstein, A. Altmeyer, S. Riedl, S. Jochim, J. Hecker Denschlag, R. Grimm, *Observation of the Pairing Gap in a Strongly Interacting Fermi Gas*, Science **305**, 1128–1130 (2004).

[19] M. W. Zwierlein, J. R. Abo-Shaeer, A. Schirotzek, C. H. Schunck, W. Ketterle, *Vortices and superfluidity in a strongly interacting Fermi gas*, Nature **435**, 1047–1051 (2005).

[20] M. Inguscio, W. Ketterle, C. Salomon (Eds.), *Ultracold Fermi Gases*, Vol. CLXIV of Proceedings of the International School of Physics "Enrico Fermi" (IOS Press, Amsterdam, 2007).

[21] C. Chin, R. Grimm, P. Julienne, E. Tiesinga, *Feshbach resonances in ultracold gases*, Rev. Mod. Phys. **82**, 1225–1286 (2010).

[22] S. Simonucci, P. Pieri, G. C. Strinati, *Broad vs. narrow Fano-Feshbach resonances in the BCS-BEC crossover with trapped Fermi atoms*, Europhys. Lett. **69**, 713–718 (2005).

[23] P. Nozières, S. Schmitt-Rink, *Bose condensation in an attractive fermion gas: From weak to strong coupling superconductivity*, J. Low. Temp. Phys. **59**, 195 (1985).

[24] J. W. Serene, *Stability of two-dimensional Fermi liquids against pair fluctuations with large total momentum*, Phys. Rev. B **40**, 10873–10877 (1989).

[25] C. A. R. Sá de Melo, M. Randeria, J. R. Engelbrecht, *Crossover from BCS to Bose superconductivity: Transition temperature and time-dependent Ginzburg-Landau theory*, Phys. Rev. Lett. **71**, 3202–3205 (1993).

[26] R. Haussmann, *Crossover from BCS superconductivity to Bose-Einstein condensation: A self-consistent theory*, Z. Phys. B **91**, 291–308 (1993).

[27] R. Haussmann, *Properties of a Fermi liquid at the superfluid transition in the crossover region between BCS superconductivity and Bose-Einstein condensation*, Phys. Rev. B **49**, 12975 (1994).

[28] B. Jankó, J. Maly, K. Levin, *Pseudogap effects induced by resonant pair scattering*, Phys. Rev. B **56**, R11407 (1997).

[29] J. Maly, B. Jankó, K. Levin, *Numerical studies of the s-wave pseudogap state and related T_c: The "pairing approximation" theory*, Physica C **321**, 113 (1999).

[30] P. Pieri, G. C. Strinati, *Strong-coupling limit in the evolution from BCS superconductivity to Bose-Einstein condensation*, Phys. Rev. B **61**, 15370 (2000).

[31] A. Perali, P. Pieri, G. C. Strinati, C. Castellani, *Pseudogap and spectral function from superconducting fluctuations to the bosonic limit*, Phys. Rev. B **66**, 024510 (2002).

[32] Y. Ohashi, *On the Fulde-Ferrell state in spatially isotropic superconductors*, J. Phys. Soc. Jap. **71** 2625–2628 (2002).

[33] Y. Ohashi, A. Griffin, *BCS-BEC crossover in a gas of Fermi atoms with a Feshbach resonance*, Phys. Rev. Lett. **89**, 130402 (2002).

[34] G. C. Strinati, P. Pieri, C. Lucheroni, *From superconducting fluctuations to the bosonic limit in the response functions above the critical temperature*, Eur. Phys. J. B **30**, 161–173 (2002).

[35] P. Pieri, L. Pisani, G. C. Strinati, *Pairing fluctuation effects on the single-particle spectra for the superconducting state*, Phys. Rev. Lett. **92**, 110401 (2004).

[36] P. Pieri, L. Pisani, G. C. Strinati, *BCS-BEC crossover at finite temperature in the broken-symmetry phase*, Phys. Rev. B **70**, 094508 (2004).

[37] A. Perali, P. Pieri, L. Pisani, G. C. Strinati, *BCS-BEC crossover at finite temperature for superfluid trapped Fermi atoms*, Phys. Rev. Lett. **92**, 220404 (2004).

[38] G. M. Bruun, C. J. Pethick, *Effective theory of Feshbach resonances and many-body properties of Fermi gases*, Phys. Rev. Lett. **92**, 140404 (2004).

[39] G. M. Bruun, H. Smith, *Viscosity and thermal relaxation for a resonantly interacting Fermi gas*, Phys. Rev. A 72, 043605 (2005).

[40] Q. Chen, J. Stajic, S. Tan, and K. Levin, *BCS-BEC crossover: From high temperature superconductors to ultracold superfluids*, Phys. Rep. **412**, 1 (2005).

[41] X.-J. Liu, H. Hu, *BCS-BEC crossover in an asymmetric two-component Fermi gas*, Europhys. Lett. **75**, 364–370 (2006).

[42] I. V. Brodsky, M. Y. Kagan, A. V. Klaptsov, R. Combescot, X. Leyronas, *Exact diagrammatic approach for dimer-dimer scattering and bound states of three and four resonantly interacting particles*, Phys. Rev. A **73**, 032724 (2006).

[43] R. Combescot, X. Leyronas, M. Yu. Kagan, *Self-consistent theory for molecular instabilities in a normal degenerate Fermi gas in the BEC-BCS crossover*, Phys. Rev. A **73**, 023618 (2006).

[44] M. M. Parish, F. M. Marchetti, A. Lamacraft, B. D. Simons, *Finite-temperature phase diagram of a polarized Fermi condensate*, Nat. Phys. **3** 124–128, (2007).

[45] G. M. Falco, H. T. C. Stoof, *Dressed molecules in resonantly interacting ultracold atomic Fermi gases*, Phys. Rev A **75**, 023612 (2007).

[46] R. Combescot, A. Recati, C. Lobo, F. Chevy, *Normal state of highly polarized fermi gases: Simple many-body approaches*, Phys. Rev. Lett. **98**, 180402 (2007).

[47] R. Haussmann, W. Rantner, S. Cerrito, W. Zwerger, *Thermodynamics of the BCS-BEC crossover*, Phys. Rev. A **75**, 023610 (2007).

[48] P. Pieri, A. Perali, G. C. Strinati, *Competition between final-state and pairing-gap effects in the radio-frequency spectra of ultracold Fermi atoms*, Phys. Rev. Lett. **100**, 010402 (2008).

[49] R. Combescot, S. Giraud, *Normal state of highly polarized fermi gases: Full many-body treatment*, Phys. Rev. Lett. **101**, 050404 (2008).

[50] R. Haussmann, W. Zwerger, *Thermodynamics of a trapped unitary Fermi gas*, Phys. Rev. A **78**, 063602 (2008).

[51] H. Hu, X.-J. Liu, and P. D. Drummond, *Comparative study of strong-coupling theories of a trapped Fermi gas at unitarity*, Phys. Rev. A **77**, 061605 (2008).

[52] P. Massignan, G. M. Bruun, H. T. C. Stoof, *Spin polarons and molecules in strongly interacting atomic Fermi gases*, Phys. Rev. A **78**, 031602(R) (2008).

[53] P. Pieri, A. Perali, G. C. Strinati, *Enhanced paraconductivity-like fluctuations in the radiofrequency spectra of ultracold Fermi atoms*, Nat. Phys. **5**, 736–740 (2009).

[54] K. B. Gubbels, J. E. Baarsma, H. T. C. Stoof, *Lifshitz point in the phase diagram of resonantly interacting ^6Li-^{40}K mixtures*, Phys. Rev. Lett. **103**, 195301 (2009).

[55] R. Combescot, S. Giraud, X. Leyronas, *Analytical theory of the dressed bound state in highly polarized Fermi gases*, EPL **88**, 60007 (2009).

[56] K. Levin, Q. Chen, C.-C. Chien, Y. He, *Comparison of different pairing fluctuation approaches to BCS-BEC crossover*, Ann. Phys. **325**, 233 (2010).

[57] T. Enss, R. Haussmann, W. Zwerger, *Viscosity and scale invariance in the unitary Fermi gas*, Ann. Phys. **326** 770 (2011).

[58] A. Perali, F. Palestini, P. Pieri, G. C. Strinati, J. T. Stewart, J. P. Gaebler, T. E. Drake, and D. S. Jin, *Evolution of the normal state of a strongly interacting Fermi gas from a pseudogap phase to a molecular Bose gas*, Phys. Rev. Lett. **106**, 060402 (2011).

[59] F. Palestini, P. Pieri, G. C. Strinati, *Density and spin response of a strongly interacting Fermi gas in the attractive and quasirepulsive regime*, Phys. Rev. Lett. **108**, 080401 (2012).

[60] T. Kashimura, R.Watanabe, Y. Ohashi, *Spin susceptibility and fluctuation corrections in the BCS-BEC crossover regime of an ultracold Fermi gas*, Phys. Rev. A **86**, 043622 (2012).

[61] P.-A. Pantel, D. Davesne, M. Urban, *Polarized Fermi gases at finite temperature in the BCS-BEC crossover*, Phys. Rev. A **90**, 053629 (2014), and Erratum *ibid.* **94**, 019901 (2016).

[62] H. Tajima, R. Hanai, R. Watanabe, Y. Ohashi, *Spin susceptibility and strong coupling effects in an ultracold Fermi gas*, J. Low. Temp. Phys. 175:279–286 (2014).

[63] M. Bauer, M. M. Parish, T. Enss, *Universal equation of state and pseudogap in the two-dimensional Fermi gas*, Phys. Rev. Lett. **112**, 135302 (2014).

[64] R. Hanai, Y. Ohashi, *Heteropairing and component-dependent pseudogap phenomena in an ultracold Fermi gas with different species with different masses*, Phys. Rev. A **90**, 043622 (2014).

[65] A. Cichy, R. Micnas, *The spin-imbalanced attractive Hubbard model in $d = 3$: Phase diagrams and BCS-BEC crossover at low filling*, Ann. Phys. **347**, 207 (2014).

[66] F. Palestini, G. C. Strinati, *Temperature dependence of the pair coherence and healing lengths for a fermionic superfluid throughout the BCS-BEC crossover*, Phys. Rev. B **89**, 224508 (2014).

[67] F. Marsiglio, P. Pieri, A. Perali, F. Palestini, G. C. Strinati, *Pairing effects in the normal phase of a two-dimensional Fermi gas*, Phys. Rev. B **91**, 054509 (2015).

[68] H. Tajima, P. van Wyk, R. Hanai, D. Kagamihara, D. Inotani, M. Horikoshi, Y. Ohashi, *Strong-coupling corrections to ground-state properties of a superfluid Fermi gas*, Phys. Rev. A **95**, 043625 (2017).

[69] H. Tajima, S. Uchino, *Many Fermi polarons at nonzero temperature*, New J. Phys. **20** 073048 (2018).

[70] L. Pisani, A. Perali, P. Pieri, and G. C. Strinati, *Entanglement between pairing and screening in the Gorkov-Melik-Barkhudarov correction to the critical temperature throughout the BCS-BEC crossover*, Phys. Rev. B **97**, 014528 (2018).

[71] L. Pisani, P. Pieri, and G. C. Strinati, *Gap equation with pairing correlations beyond the mean-field approximation and its equivalence to a Hugenholtz-Pines condition for fermion pairs*, Phys. Rev. B **98**, 104507 (2018).

[72] B. Frank, J. Lang, W. Zwerger, *Universal phase diagram and scaling functions of imbalanced Fermi gases*, J. Exp. Th. Phys. **127**, 812–825 (2018).

[73] H. Hu, B. C. Mulkerin, J. Wang, X.-J. Liu, *Attractive Fermi polarons at nonzero temperatures with a finite impurity concentration*, Phys. Rev. A **98**, 013626 (2018).

[74] P. van Wyk, H. Tajima, D. Inotani, A. Ohnishi, and Y. Ohashi, *Superfluid Fermi atomic gas as a quantum simulator for the study of neutron-star equation of state in the low-density region*, Phys. Rev. A **97**, 013601 (2018).

[75] M. Pini, P. Pieri, and G. C. Strinati, *Fermi gas throughout the BCS-BEC crossover: Comparative study of t-matrix approaches with various degrees of self-consistency*, Phys. Rev. B **99**, 094502 (2019).

[76] B. C. Mulkerin, J. Wang, X.-J. Liu, *Breakdown of the Fermi polaron description near Fermi degeneracy at unitarity*, Ann. Phys. **407**, 29-45 (2019).

[77] M. Pini, P. Pieri, M. Jäger, J. Hecker Denschlag, G. C. Strinati, *Pair correlations in the normal phase of an attractive Fermi gas*, arXiv:1912.04802.

[78] J. Carlson, S. Reddy, *Asymmetric two-component fermion systems in strong coupling*, Phys. Rev. Lett. **95**, 060401 (2005).

[79] C. Lobo, A. Recati, S. Giorgini, and S. Stringari, *Normal state of a polarized Fermi gas at unitarity*, Phys. Rev. Lett. **97**, 200403 (2006).

[80] A. Bulgac, J. E. Drut, P. Magierski, *Quantum Monte Carlo simulations of the BCS-BEC crossover at finite temperature*, Phys. Rev. A **78**, 023625 (2008).

[81] A. Bulgac, M. McNeil Forbes, *Unitary Fermi supersolid: The Larkin-Ovchinnikov phase*, Phys. Rev. Lett. **101**, 215301 (2008).

[82] S. Pilati, S. Giorgini, *Phase separation in a polarized Fermi gas at zero temperature*, Phys. Rev. Lett. **100**, 030401 (2008).

[83] P. Magierski, G. Wlazłowski, A. Bulgac, J. E. Drut, *Finite-temperature pairing gap of a Unitary Fermi gas by Quantum Monte Carlo calculations*, Phys. Rev. Lett. **103**, 210403 (2009).

[84] P. Magierski, G. Wlazłowski, A. Bulgac, *Onset of a pseudogap regime in ultracold Fermi gases*, Phys. Rev. Lett. **107**, 145304 (2011).

[85] J. E. Drut, T. A. Lähde, G. Wlazlowski, P. Magierski, *Equation of state of the unitary Fermi gas: An update on lattice calculations*, Phys. Rev. A **85**, 051601(R) (2012).

[86] A. Bulgac, *The unitary Fermi gas: from Monte Carlo to density functionals*, in: W. Zwerger (Ed.), *The BCS-BEC Crossover and the Unitary Fermi Gas*, Vol. 863 of Lecture Notes in Physics pp. 305–374 (Springer-Verlag, Berlin, Heidelberg, 2012).

[87] J. Carlson, S. Gandolfi, A. Gezerlis, *Quantum Monte Carlo approaches to nuclear and atomic physics*, Prog. Theor. Exp. Phys. **2012** 01A209 (2012).

[88] L. Rammelmüller, W. J. Porter, J. E. Drut, J. Braun, *Surmounting the sign problem in nonrelativistic calculations: A case study with mass-imbalanced fermions*, Phys. Rev. D **96**, 094506 (2017).

[89] L. Rammelmüller, A. C. Loheac, J. E. Drut, J. Braun, *Finite-temperature equation of state of polarized fermions at unitarity*, Phys. Rev. Lett. **121**, 173001 (2018).

[90] N. Prokof'ev, B. Svistunov, *Bold diagrammatic Monte Carlo: A generic sign-problem tolerant technique for polaron models and possibly interacting many-body problems*, Phys. Rev. B **77**, 125101 (2008).

[91] E. Burovski, E. Kozik, N. Prokof'ev, B. Svistunov, M. Troyer, *Critical temperature curve in BEC-BCS crossover*, Phys. Rev. Lett. **101**, 090402 (2008).

[92] J. Vlietinck, J. Ryckebusch, K. Van Houcke, *Quasiparticle properties of an impurity in a Fermi gas*, Phys. Rev. B **87**, 115133 (2013).

[93] K. Van Houcke, F. Werner, E. Kozik, N. Prokof'ev, B. Svistunov, *Contact and momentum distribution of the unitary Fermi gas*, Phys. Rev. Lett. **121**, 130406 (2018).

[94] K. Van Houcke, F. Werner, N. Prokof'ev, B. Svistunov, *Diagrammatic Monte Carlo algorithm for the resonant Fermi gas*, Phys. Rev. B **99**, 035140 (2019).

[95] K. Gubbels, H. Stoof, *Renormalization group theory for the imbalanced Fermi gas*, Phys. Rev. Lett. **100** (2008) 140407.

[96] S. Diehl, S. Floerchinger, H. Gies, J. Pawlowkski, C. Wetterich, *Functional renormalization group approach to the BCS-BEC crossover*, Annalen der Physik 522, 615–656 (2010).

[97] Y. Nishida, D. Son, *Unitary Fermi gas, ϵ expansion, and nonrelativistic conformal field theories*, in: W. Zwerger (Ed.), *The BCS-BEC Crossover and the Unitary Fermi Gas*, Vol. 863 of Lecture Notes in Physics, pp. 305–374 (Springer-Verlag, Berlin, 2012).

[98] X.-J. Liu, H. Hu, P. D. Drummond, *Virial expansion for a strongly correlated Fermi gas*, Phys. Rev. Lett. **102**, 160401 (2009).

[99] X. Leyronas, *Virial expansion with Feynman diagrams*, Phys. Rev. A **84**, 053633 (2011).

[100] X.-J. Liu, *Virial expansion for a strongly correlated Fermi system and its application to ultracold atomic Fermi gases*, Phys. Rep. **524** (2013) 37–83.

[101] W. Zwerger (Ed.), *The BCS-BEC Crossover and the Unitary Fermi Gas*, Vol. 863 of Lecture Notes in Physics (Springer-Verlag, Berlin, Heidelberg, 2012).

[102] G. C. Strinati, P. Pieri, G. Röpke, P. Schuck, and M. Urban, *The BCS-BEC crossover: From ultracold Fermi gases to nuclear systems*, Phys. Rep. **738**, 1 (2018).

[103] V. M. Galitskii, *The energy spectrum of a non-ideal Fermi gas*, Sov. Phys. JETP **7**, 104 (1958) [Zh. Eksp. Teor. Fiz. **34**, 151 (1958)].

[104] C. Lobo, I. Carusotto, S. Giorgini, A. Recati, S. Stringari, *Pair correlations of an expanding superfluid Fermi gas*, Phys. Rev. Lett. **97**, 100405 (2006).

[105] T. Paintner, D. K. Hoffmann, M. Jäger, W. Limmer, W. Schoch, B. Deissler, M. Pini, P. Pieri, G. C. Strinati, C. Chin, J. Hecker Denschlag, *Pair fraction in a finite-temperature Fermi gas on the BEC side of the BCS-BEC crossover*, Phys. Rev. A **99**, 053617 (2019).

[106] J. M. Luttinger, *Fermi surface and some simple equilibrium properties of a system of interacting fermions*, Phys. Rev. **119**, 1153 (1960).

[107] P. Pieri, G. C. Strinati, *Luttinger theorem and imbalanced Fermi systems*, Eur. Phys. J. B 90: 68 (2017).

[108] A. L. Fetter and J. D. Walecka, *Quantum Theory of Many-Particle Systems* (McGraw-Hill, New York, 1971).

[109] L. D. Landau, E. M. Lifshitz, *Quantum mechanics, non-relativistic theory*, Course of Theoretical Physics Vol. 3 (Pergamon press, Oxford, 1991).

[110] D. J. Thouless, *Perturbation theory in statistical mechanics and the theory of superconductivity*, Ann. Phys. **10**, 553 (1960).

[111] V. N. Popov, *Functional Integrals and Collective Excitations* (Cambridge Univ. Press, Cambridge, 1987).

[112] G. Baym, L. P. Kadanoff, *Conservation laws and correlation functions*, Phys. Rev. **124**, 287 (1961).

[113] G. Baym, *Self-consistent approximations in many-body systems*, Phys. Rev. **127**, 1391 (1962).

[114] S. Tan, *Energetics of a strongly correlated Fermi gas*, Ann. Phys. **323**, 2952 (2008).

[115] S. Tan, *Large momentum part of a strongly correlated Fermi gas*, Ann. Phys. **323**, 2971 (2008).

[116] S. Tan, *Generalized virial theorem and pressure relation for a strongly correlated Fermi gas*, Ann. Phys. **323**, 2987 (2008).

[117] E. Braaten, *Universal relations for fermions with large scattering length*, in *The BCS-BEC Crossover and the Unitary Fermi Gas*, W. Zwerger Ed., Lecture Notes in Physics Vol. 836, p. 193–230 (Springer-Verlag, Berlin, Heidelberg, 2012).

[118] B. O. Frank, *Thermodynamics and transport in Fermi gases near unitarity*, Ph.D. thesis, Technische Universität München (2018).

[119] J. R. Schrieffer, *Theory of Superconductivity* (Benjamin, New York, 1964).

[120] G. C. Strinati, *Application of the Green's functions method to the study of the optical properties of semiconductors*, La Rivista del Nuovo Cimento **11** (1988).

[121] N. Andrenacci, P. Pieri, G. C. Strinati, *Evolution from BCS superconductivity to Bose-Einstein condensation: Current correlation function in the broken symmetry phase*, Phys. Rev. B **68**, 144507 (2003).

[122] M. J. H. Ku, A. T. Sommer, L. W. Cheuk, M. W. Zwierlein, *Revealing the superfluid lambda transition in the universal thermodynamics of a unitary Fermi gas*, Science **335** 563–567 (2012).

[123] A. M. Clogston, *Upper limit for the critical field in hard superconductors*, Phys. Rev. Lett. **9**, 266–267 (1962).

[124] B. S. Chandrasekhar, *A note on the maximum critical field of high-field superconductors*, Appl. Phys. Lett. **1**, 7–8 (1962).

[125] G. Sarma, *On the influence of a uniform exchange field acting on the spins of the conduction electrons in a superconductor*, J. Phys. Chem. Solids **24**, 1029 (1963).

[126] L. P. Gor'kov, T. M. Melik-Barkhudarov, *Contribution to the theory of superfluidity in an imperfect Fermi gas*, Sov. Phys. JETP **13**, 1018 (1961) [Zh. Eksp. Teor. Fiz. **40**, 1452 (1961)].

[127] G. Baym, J.-P. Blaizot, M. Holzmann, F. Laloë, D. Vautherin, *The transition temperature of the dilute interacting Bose gas*, Phys. Rev. Lett. **83**, 1703 (1999).

[128] D. S. Petrov, C. Salomon, G. V. Shlyapnikov, *Scattering properties of weakly bound dimers of fermionic atoms*, Phys. Rev. A **71**, 012708 (2005).

[129] H. J. Vidberg, J. W. Serene, *Solving the Eliashberg equations by means of N-point Padé approximants*, J. Low Temp. Phys. **29**, 179 (1977).

[130] K. S. D. Beach, R. J. Gooding, F. Marsiglio, *Reliable Padé analytical continuation method based on a high-accuracy symbolic computation algorithm*, Phys. Rev. B **61**, 5147 (2000).

[131] J. Shött, I. L. M. Locht, E. Lundin, O. Grånäs, O. Eriksson, I. Di Marco, *Analytic continuation by averaging Padé approximants*, Phys. Rev. B **93**, 075104 (2016).

[132] P. Nozières, *Theory of Interacting Fermi Systems* (Benjamin, New York, 1964).

[133] A. Abrikosov, L. P. Gorkov, E. Dzyaloshinski, *Methods of Quantum Field Theory in Statistical Physics* (Dover, New York, 1975).

[134] S. Nascimbène, N. Navon, S. Pilati, F. Chevy, S. Giorgini, A. Georges, C. Salomon, *Fermi-liquid behavior of the normal phase of a strongly interacting gas of cold atoms*, Phys. Rev. Lett. **106**, 215303 (2011).

[135] S. Jensen, C. N. Gilbreth, Y. Alhassid, *The pseudogap regime in the unitary Fermi gas*, Eur. Phys. J. Special Topics **227**, 2241–2261 (2019).

[136] B. Mukherjee, P. B. Patel, Z. Yan, R. J. Fletcher, J. Struck, M. W. Zwierlein, *Spectral response and contact of the Unitary Fermi gas*, Phys. Rev. Lett. **122**, 203402 (2019).

[137] M. Grumet, P. Liu, M. Kaltac, J. Kliměs, G. Kresse, *Beyond the quasiparticle approximation: Fully self-consistent GW calculations*, Phys. Rev. B **98**, 155143 (2018).

[138] N. Marom, F. Caruso, X. Ren, O. T. Hofmann, T. Körzdörfer, J. R. Chelikowsky, A. Rubio, M. Scheffler, P. Rinke, *Benchmark of GW methods for azabenzenes*, Phys. Rev. B **86**, 245127 (2012).

[139] P. F. Loos, P. Romaniello, and J. A. Berger, *Green functions and self-consistency: insights from the spherium model*, J. Chem. Theory Comput. **14**, 3071 (2018).

[140] A. L. Kutepov, *Vertex corrections in self-consistent $GW\Gamma$ calculations: Ground state properties of vanadium*, arXiv:1809.06654.

[141] A. M. Lewis, T. C. Berkelbach *Vertex corrections to the polarizability do not improve the GW approximation for molecules*, J. Chem. Theory Comput. **15**, 5, 2925-2932 (2019).

[142] B. Mukherjee, Z. Yan, P. B. Patel, Z. Hadzibabic, T. Yefsah, J. Struck, M. W. Zwierlein, *Homogeneous atomic Fermi gases*, Phys. Rev. Lett. **118**, 123401 (2017).

[143] Z. Yan, P. B. Patel, B. Mukherjee, R. J. Fletcher, J. Struck, M. W. Zwierlein, *Boiling a Unitary Fermi liquid*, Phys. Rev. Lett. **122**, 093401 (2019).

[144] L. A. Sidorenkov, M. K. Tey, R. Grimm, Y.-H. Hou, L. Pitaevskii, S. Stringari, *Second sound and the superfluid fraction in a Fermi gas with resonant interactions*, Nature **498**, 78–81 (2013).

[145] S. Giorgini, L. P. Pitaevskii, and S. Stringari, *Condensate fraction and critical temperature of a trapped interacting Bose gas*, Phys. Rev. A **54**, R4633(R) (1996).

[146] J. Friedel, *The distribution of electrons round impurities in monovalent metals*, Philos. Mag. **43**, 153 (1952).

[147] N. Andrenacci, P. Pieri, G. C. Strinati, *Size shrinking of composite bosons for increasing density in the BCS to Bose-Einstein crossover*, Eur. Phys. J. B **13**, 637–642 (2000).

[148] M. Randeria, *Pre-pairing for condensation*, Nat. Phys. **6**, 561 (2010).

[149] W. Ketterle, M. Zwierlein, *Making, probing and understanding ultracold Fermi gases*, in *Ultra-cold Fermi gases*, International School of Physics "Enrico Fermi", Vol. Course CLXIV, edited by M. Inguscio, W. Ketterle, and C. Salomon (IOS Press, Amsterdam, 2007).

[150] G. B. Partridge, K. E. Strecker, R. I. Kamar, M. W. Jack, and R. G. Hulet, *Molecular probe of pairing in the BEC-BCS crossover*, Phys. Rev. Lett. **95**, 020404 (2005).

[151] M. Bartenstein, A. Altmeyer, S. Riedl, R. Geursen, S. Jochim, C. Chin, J. Hecker Denschlag, R. Grimm, A. Simoni, E. Tiesinga, C. J. Williams, P. S. Julienne, *Precise determination of ^{6}Li cold collision parameters by radio-frequency spectroscopy on weakly bound molecules*, Phys. Rev. Lett. **94**, 103201 (2005).

[152] G. Zürn, T. Lompe, A. N. Wenz, S. Jochim, P. S. Julienne, J. M. Hutson, *Precise characterization of ^{6}Li Feshbach resonances using trap-sideband-resolved RF spectroscopy of weakly bound molecules*, Phys. Rev. Lett. **110**, 135301 (2013).

[153] C. Chin and R. Grimm, *Thermal equilibrium and efficient evaporation of an ultracold atom-molecule mixture*, Phys. Rev. A **69**, 033612 (2004).

[154] P. Fulde, R. A. Ferrell, *Superconductivity in a strong spin-exchange field*, Phys. Rev. **135**, A550–A563 (1964).

[155] A. I. Larkin, Y. N. Ovchinnikov, *Nonuniform state of superconductors*, Sov. Phys. JETP **20**, 762–769 (1965), [Zh. Eksp. Teor. Fiz. **47**, 1136-1146 (1964)].

[156] C. Mora, R. Combescot, *Transition to Fulde-Ferrell-Larkin-Ovchinnikov phases in three dimensions: A quasiclassical investigation at low temperature with Fourier expansion*, Phys. Rev. B **71**, 214504 (2005).

[157] M. W. Zwierlein, A. Schirotzek, C. H. Schunck, W. Ketterle, *Fermionic superfluidity with imbalanced spin populations*, Science **311**, 492–496 (2006).

[158] G. B. Partridge, W. Li, R. I. Kamar, Y.-a. Liao, R. G. Hulet, *Pairing and phase separation in a polarized Fermi gas*, Science **311**, 503–505 (2006).

[159] Y.-I. Shin, C. H. Schunck, A. Schirotzek, W. Ketterle, *Phase diagram of a two-component Fermi gas with resonant interactions*, Nature **451**, 689–693 (2008).

[160] Y.-I. Shin, *Determination of the equation of state of a polarized Fermi gas at unitarity*, Phys. Rev. A **77**, 041603(R) (2008).

[161] Y.-I. Shin, A. Schirotzek, C. H. Schunck, W. Ketterle, *Realization of a strongly interacting Bose-Fermi mixture from a two-component Fermi gas*, Phys. Rev. Lett. **101**, 070404 (2008).

[162] N. Navon, S. Nascimbéne, F. Chevy, C. Salomon, *The equation of state of a low-temperature Fermi gas with tunable interactions*, Science **328**, 729 (2010).

[163] B. A. Olsen, M. C. Revelle, J. A. Fry, D. E. Sheehy, R. G. Hulet, *Phase diagram of a strongly interacting spin-imbalanced Fermi gas*, Phys. Rev. A **92**, 063616 (2015).

[164] H. A. Radovan, N. A. Fortune, T. P. Murphy, S. T. Hannahs, E. C. Palm, S. W. Tozer, D. Hall, *Magnetic enhancement of superconductivity from electron spin domains*, Nature **425**, 51–55 (2003).

[165] Y. Matsuda, H. Shimahara, *Fulde-Ferrell-Larkin-Ovchinnikov state in heavy fermion superconductors*, J. Phys. Soc. Jpn. **76**, 051005 (2007).

[166] Y.-a Liao, A. S. C. Rittner, T. Paprotta, W. Li, G. B. Partridge, R. G. Hulet, S. K. Baur, E. J. Mueller, *Spin-imbalance in a one-dimensional Fermi gas*, Nature **467**, 567–569 (2010).

[167] D. E. Sheehy, L. Radzihovsky, *BEC-BCS crossover, phase transitions and phase separation in polarized resonantly-paired superfluids*, Ann. Phys. **322** (2007).

[168] P. Massignan, M. Zaccanti, G. M. Bruun, *Polarons, dressed molecules and itinerant ferromagnetism in ultracold Fermi gases*, Rep. Prog. Phys. **77**, 034401 (2014).

[169] A. Schirotzek, C.-H. Wu, A. Sommer, M. W. Zwierlein, *Observation of Fermi polarons in a tunable Fermi liquid of ultracold atoms*, Phys. Rev. Lett. **102**, 230402 (2009).

[170] S. Nascimbène, N. Navon, K. J. Jiang, L. Tarruell, M. Teichmann, J. McKeever, F. Chevy, C. Salomon, *Collective oscillations of an imbalanced Fermi gas: axial compression modes and polaron effective mass*, Phys. Rev. Lett. **103**, 170402 (2009).

[171] F. Chevy, *Universal phase diagram of a strongly interacting Fermi gas with unbalanced spin populations*, Phys. Rev. A **74**, 063628 (2006).

[172] C. Mora, F. Chevy, *Ground state of a tightly bound composite dimer immersed in a Fermi sea*, Phys. Rev. A **80**, 033607 (2009).

[173] M. Punk, P. T. Dumitrescu, W. Zwerger, *Polaron-to-molecule transition in a strongly imbalanced Fermi gas*, Phys. Rev. A, **80**, 053605 (2009).

[174] M. Abramowitz, I. A. Stegun, *Handbook of Mathematical Functions* (Dover, New York, 1972), Chap. 7.

[175] L. G. Ferreira, *Theory and method for accelerating the convergence of self-consistent electronic structure calculations*, J. Comp. Phys. **36**, 198 (1980).

[176] N. M. Hugenholtz, D. Pines, *Ground-state energy and excitation spectrum of a system of interacting bosons*, Phys. Rev. **116**, 489 (1959).

[177] L. Pitaevskii, S. Stringari, *Bose-Einstein Condensation* (Clarendon Press, Oxford, 2003).

[178] C. J. Pethick, H. Smith, *Bose-Einstein Condensation in Dilute Gases* (Cambridge Univ. Press, Cambridge, 2008).

[179] L. D. Landau and E. M. Lifshitz, *Statistical Physics*, Course of Theoretical Physics Vol. 5 (Butterworth-Heinemann, Oxford, 1999), Chap. X.

Acknowledgements

I gratefully acknowledge my supervisors, Prof. Pierbiagio Pieri and Prof. Giancarlo Calvanese Strinati, for the opportunity to work in the field of research I love, for their continuous support along the course of this whole Ph.D., and for the company during the many late evening meetings and dinners together.

I also sincerely thank Prof. Johannes Hecker Denschlag and his grad student Manuel Jäger for the hospitality, the stimulating discussions and the fruitful collaboration born during my period of stay in Ulm.

Finally, I thank Prof. Leonardo Fallani for the support and for the realization of the collaboration between the universities of Firenze and Camerino, without which this Ph.D. would not have been possible.